



HAL
open science

Molecular dynamics in complex polymer systems : from anisotropy to confinement effects

Xavier Monnier

► **To cite this version:**

Xavier Monnier. Molecular dynamics in complex polymer systems : from anisotropy to confinement effects. Materials Science [cond-mat.mtrl-sci]. Normandie Université, 2017. English. NNT : 2017NORMR021 . tel-01622112

HAL Id: tel-01622112

<https://theses.hal.science/tel-01622112>

Submitted on 24 Oct 2017

HAL is a multi-disciplinary open access archive for the deposit and dissemination of scientific research documents, whether they are published or not. The documents may come from teaching and research institutions in France or abroad, or from public or private research centers.

L'archive ouverte pluridisciplinaire **HAL**, est destinée au dépôt et à la diffusion de documents scientifiques de niveau recherche, publiés ou non, émanant des établissements d'enseignement et de recherche français ou étrangers, des laboratoires publics ou privés.



Normandie Université

THESE

Pour obtenir le diplôme de doctorat

Spécialité : Physique

Préparée au sein de l'Université de Rouen Normandie

Etude de la mobilité moléculaire dans des systèmes polymères complexes anisotropes et confinés

Présentée et soutenue par
Xavier MONNIER

Thèse soutenue publiquement le 3 Octobre 2017
devant le jury composé de

Mme. Aline AUROUX	Directrice Recherche CNRS. IRCELYON, Université Lyon 1	Rapporteur
M. Guillaume VIGNAUD	Dr. HDR. IRDL, Université Bretagne Sud	Rapporteur
Mme. Valérie GAUCHER	Pr. UMET, Université Lille 1	Président
M. Franck COLLAS	Dr., Entreprise Mettler Toledo	Examineur
Mme. Allisson SAITER	Dr. HDR. GPM, Université de Rouen Normandie	Co-directeur de thèse
M. Eric DARGENT	Pr. GPM, Université de Rouen Normandie	Directeur de thèse

Thèse dirigée par Dr. Allisson SAITER et Pr. Eric DARGENT, Groupe Physique des Matériaux (GPM)





Normandie Université

PhD THESIS

In view to obtain the degree of Doctor of Philosophy in Science

Specialty: Physics

Submitted to the Faculty of Science – University of Rouen Normandie in partial fulfilment of the requirements for the degree

Molecular dynamics in complex polymer systems : from anisotropy to confinement effects

Presented and defended by
Xavier MONNIER

Defended the October, 3rd 2017
in front of the dissertation committee composed of

Mme. Aline AUROUX	Directrice Recherche CNRS. IRCELYON, Université Lyon 1	Reviewer
M. Guillaume VIGNAUD	Dr. HDR. IRDL, Université Bretagne Sud	Reviewer
Mme. Valérie GAUCHER	Pr. UMET, Université Lille 1	President
M. Franck COLLAS	Dr., Entreprise Mettler Toledo	Examiner
Mme. Allisson SAITER	Dr. HDR. GPM, Université de Rouen Normandie	Co-supervisor
M. Eric DARGENT	Pr. GPM, Université de Rouen Normandie	Supervisor

Supervised by Dr. Allisson SAITER et Pr. Eric DARGENT, “Groupe Physique des Matériaux” (GPM)



ACKNOWLEDGMENTS

The following manuscript deals with the entire work performed during my PhD thesis from 2014 to 2017. Nevertheless, it would be reducing and wrong to only associate myself to this work. Indeed, first of all it comes from different collaborations (locals, nationals and internationals) in which I have been involved. In addition, it is also the results of various fruitful discussions: discussions in the laboratory with a good work atmosphere; discussions from interesting conferences; but also discussions from phone or Skype. At the end, this work has only been possible thanks to availability, kindness, interest, support, passion, trust, friendship and love, of many people I interacted with during the last three years.

For all these reasons, I just want to thank them all.

JOHN M. HUTCHINSON, VINCE, LAURENT DELBREILH, ANTONELLA ESPOSITO, BOOLI, GUILLAUME VIGNAUD (REVIEWER), JORGE ARTURO SOTO PUENTE, AGNÈS, GÉRARD, NICOLAS DELPOUVE, JÉRÔME, ALEXANDRE DHOTEL, RANKO RICHERT, ERIC DARGENT (SUPERVISOR), BIDUR RIJAL, MARIE-ROSE GARDA, ROUKI, CRIS, ERIC DONTZOFF (HONEY FOREVER), QUENTIN VIEL, PAPY, BENJAMIN SCHAMMÉ, NICOLAS COUV RAT, NAGIHAN VAROL, FRANCK COLLAS (EXAMINER), LAURENT MEURET, TOMB RAIDER, CLÉMENT FOSSE, VALÉRIE GAUCHER (EXAMINER), SÉLIM ZAHOUR, STEVEN ARAUJO (PHD BRO AND MORE), FLORIAN BATTEUX, LAURENCE CHEVALIER, MAT BEN'S (THE CRAZY DUDE), AURÉLIEN, SAFA MBAREK, MARIE-ANGE DERUE, MARIE-CHRISTINE, LAURE PARIS, ALLISSON SAITER (SUPERVISOR), MIGUEL KPAKPO, LUCIA FERNANDEZ-BALLESTER, DENIS LOURDIN, NEIL BASSON, PETER E. MALLON, CLAIRE DEBREUX (PRESIDENT OF THE PRESIDENTS), ALINE AUROUX (REVIEWER), HONG KONG FOU FOU, DANIELE CANGIALOSI, SAREH MAHMOUDIAN MOGHADDAM, CHRISTOPH SCHICK, LA FOLLE COCHE, L'HOMME MAÏS (WOULD I SAY L'HOMME POULE), MARIE-SYLVIE KAËLIN, MARJO, WIL'S, YANNICK, NATH (THANK YOU FOR THE IBIS NIGHTS), AURÉLIE BOURDET, LINLIN, MATHILDE, MOULE, TIMMY, ROMAIN VINCENT

**T H A N K
Y O U T O**

...

TABLE OF CONTENTS

INTRODUCTION	1
CHAPTER I	
STATE OF THE ART	7
I.1 Glass transition and glassy state	8
I.2 Non-exhaustive phenomenology of the glass transition	11
I.2.1 Free-volume model	11
I.2.2 Configurational-entropy theory	12
I.3 Molecular dynamics and relaxation phenomena: from glass-forming liquids to glassy polymers	13
I.3.1 Glass-forming liquid in general.....	13
I.3.2 Glassy polymers in particular	14
I.3.3 From Arrhenius to non-Arrhenius temperature dependence	15
I.3.4 The approach of Donth.....	18
I.4 Structural relaxation in the glassy state	19
I.4.1 Concept of physical aging	19
I.4.2 Concept of fictive temperature	21
I.4.3 Non-exponential behavior of the relaxation times	23
I.5 Crystallization of polymers	24
I.5.1 From conventional to unconventional crystallizations	24
I.5.2 Crystallization vs. vitrification	26
I.6 Structural anisotropy	26
I.6.1 Flow induced crystallization	28
I.6.2 Electrospinning	29
I.6.3 Polylactide	31
REFERENCES	32
CHAPTER II	
EXPERIMENTAL SECTION	41
II.1 Materials	42
II.1.1 Poly(lactide) (PLA) and acetyl tributyl citrate (ATBC).....	42
II.1.2 Flow induced crystallization	42
II.1.3 Electrospinning	45
II.2 Characterization methods	46
II.2.1 Structural and morphological analyses	46
II.2.2 Thermal analysis	51
II.3 Theories, models and concepts: experimental methodologies	57
II.3.1 Estimation of the cooperative rearrangement sizes	57
II.3.2 Estimation of the enthalpy recovery	59
II.3.3 Estimation of the fictive temperature	60
REFERENCES	61

CHAPTER III

GLASS TRANSITION PROPERTIES AND STRUCTURAL RELAXATION OF WHOLLY AMORPHOUS PLA BY STANDARD DSC AND FSC	65
III.1 Glass transition and fictive temperature	66
III.2 Thermal lag considerations	68
III.2.1 Thermal lag: dynamic and static.....	68
III.2.2 Deviation from the VFTH law	70
III.3 From low to high enthalpy PLA glasses	74
III.4 Parameters influencing the structural relaxation kinetics	77
III.4.1 Cooling rate	77
III.4.2 Sample geometries	79
III.5 Structural relaxation of wholly amorphous PLA over 6 decades	83
III.6 Conclusion	88
R E F E R E N C E S	89

CHAPTER IV

STRUCTURAL ANISOTROPY INVESTIGATIONS THROUGH PLA FLOW INDUCED CRYSTALLINE STRUCTURES: MOLECULAR DYNAMICS FROM LOCAL TO SEGMENTAL SCALES	93
IV.1 Conventional vs. unconventional crystallization	94
IV.1.1 Impact of the crystal nuclei precursors.....	94
IV.1.2 From isotropic to anisotropic crystalline morphology.....	96
IV.2 Thermal and microstructural properties	98
IV.3 Characteristic length at the glass transition	100
IV.4 Structural relaxation below the glass transition	103
IV.5 From local to segmental molecular motions	109
IV.6 Conclusion	110
R E F E R E N C E S	112

CHAPTER V

STRUCTURAL ANISOTROPY INVESTIGATIONS THROUGH ELECTROSPUN AMORPHOUS PLASTICIZED PLA FIBERS	117
V.1 As-spun fibers: Morphological aspects	118
V.2 Macromolecular organizations	118
V.2.1 Wide Angle X-ray Scattering (WAXS)	118
V.2.2 Modulated Temperature Differential Scanning Calorimetry (MT-DSC).....	126
V.3 Molecular Dynamics	135
V.4 Conclusions	140
R E F E R E N C E S	141

C O N C L U S I O N A N D P R O S P E C T S	145
S C I E N T I F I C C O M M U N I C A T I O N S	151

“Tell me and I forget.
Teach me and I remember.
Involve me and I learn.”

Benjamin Franklin (1706 - 1790)

INTRODUCTION

For a long time, one of the major issue, and challenge, in the field of material science is the understanding of the glass transition phenomenon occurring in glass-forming liquids. Upon sufficient fast cooling, any glass-forming liquids vitrify. The molecular motions involved during the vitrification display complex behaviors and interactions. In the past, numerous models and concepts have been proposed to theorize that intriguing phenomenon. Nevertheless, none of them successfully describes the whole aspects. The difficulties lie on the temperature, the time and the structure dependence of the relaxation phenomena involved.

With regard to polymer science, various investigations have been done to characterize the molecular dynamics as a function of time and temperature. In addition, investigations of the molecular dynamics have also focused on the influence of the structure. Especially in the past few years, molecular dynamic characterizations have been reported for nano-composite polymers, nano-sphere polymers, multilayer polymers, plasticized polymers, and crystallized polymers among others. Among them, numerous works and PhD thesis have been achieved in the EIRCAP team of the GPM laboratory (former AMME-LECAP laboratory). First of all, Mickaël Arnoult[†] has investigated the molecular dynamics in two different polyesters - poly(ethylene terephthalate) (PET) and polylactide (PLA) - in order to focus on the difference of intra- and inter-molecular interactions only. Then, Hugues Couderc[‡] has investigated the influence of the confinement effects of intercalated nano-fillers (montmorillonite) on the amorphous phase through poly(ethylene 1,4-cyclohexylenedimethylene terephthalate glycol) (PET_g) nano-composites. In the same time, influence of the confinement by the crystals has been investigated in PLA during the PhD thesis of Nicolas Delpouve[‡]. Another kind of confinement has also been investigated on amorphous systems through the PhD thesis of Khadidja Arabeche[‡] on multilayer films of polycarbonate/poly(methyl methacrylate) with thickness going from micro- to nano-meters. Later, structural anisotropy has also been investigated on the PhD thesis of Florian Hamonic[‡] by strain induced crystallization of semi-crystalline and amorphous polyesters: PET and PET_g, respectively.

From those different investigations, the common result is the decreasing of the molecular motion due to the geometrical restrictions. The crystals, the intercalated fillers or

the nanometric thickness of the multilayer films induce a confinement effects, which disrupt the molecular dynamics. Such behavior has also been observed on non-crystalline stretched PET_g by Florian Hamonic. PET_g chains organize in an oriented and constrained structure upon drawing, and chains packing constrain their own motions. Therefore, molecular dynamics are also disrupted in spite of the non-crystalline nature of the system. In that context, a question may arise. Would the structural anisotropy depict the same influence on the molecular dynamics when the anisotropy would be induced to the system prior to its crystallization and vitrification? From literature, it is well know that flow induced in the melt prior to crystallization leads to anisotropic semi-crystalline structures. In addition, the process of electrospinning may provide non-crystalline fibers with high orientation of the polymer chains. Therefore, how such structures and morphologies could affect the molecular dynamics? In addition of the numerous geometrical effects introduced above, is there any influence of the crystalline morphology? Is there any influence of the molecular orientation?

Consequently, molecular dynamics have been investigated on flow induced crystalline structures as well as electrospun fibers, which provide crystalline and non-crystalline complex polymer systems subjected to structural anisotropy prior to crystallization and vitrification, respectively. The entire works have been done by using PLA to assess and dissociate the influences of the crystalline morphology and the molecular orientation. For both systems, characterizations of the microstructure and the morphology have been carefully done prior to the characterizations of the molecular dynamics. The aim of such characterizations has been to confirm the structural anisotropy nature induced by the process. Thus, a correct, as well as a better, understanding of the molecular motions phenomena have been possible. In that regard, a focus has been specially done on a recent commercialized thermal analysis technique through wholly amorphous PLA: fast scanning calorimetry (FSC). Funding by the region Normandy for the ACDC project, this technique allows the characterization of microstructures and molecular dynamics at the micro-scale, namely the typical length-scale of the systems investigated in this study, which was impossible in the past. The work and the results have been structured as follow:

- The first chapter introduces the glass transition phenomenon. The properties of the glass-forming liquids are discussed as well as the different theories and concepts related. They allow to understand and interpret the molecular dynamics as well as the

relaxation phenomena involved in the glass-forming liquids and the glassy state. Focus is also done on the specificities of polymer glasses. Subsequently, crystallization of polymers are depicted to highlight the environmental and the structural influences on the molecular dynamics of the amorphous phase. Finally, influences of the structure and confinement effects on the molecular dynamics of various polymeric systems are detailed. In this way, structural anisotropy is displayed in order to precisely justify the motivation of this work.

- The second chapter presents the materials used as well as the experimental set-up - flow induced crystallization and electrospinning - in order to investigate the influence of the structural anisotropy on the molecular dynamics of the amorphous phase. The characterization methods used in this work are also briefly described.
- The third chapter of this work focuses on the glass transition and the physical aging of wholly amorphous PLA through differential scanning calorimetry (DSC) and FSC. Both techniques are compared in order to highlight the respective benefits and drawbacks of FSC. The aim of those investigations is to understand the influence of the scanning rates, and the sample geometries, on the glass transition as well as the kinetics of the physical aging. Molecular dynamics have been used by means of FSC in order to investigate the influence of the structural anisotropy on the amorphous phase of the flow induced crystalline structures in the following chapter. Consequently, this section highlights the interests of the FSC and shows some perspectives opened by this new technique on complex polymer systems.
- The fourth chapter of this work deals with the influence of the structural anisotropy induced during the processing on semi-crystalline systems: flow induced crystallization. Special attention have been done on the characterization of the semi-crystalline morphology as well as the thermal and microstructural properties through polarized optical microscope, scanning electronic microscope and obviously FSC. Molecular dynamics have been characterized at the glass transition through the approach of Donth, as well as in the glassy state, through the phenomenon of structural relaxation.

- The last chapter approaches the influence of the structural anisotropy induced during the processing on non-crystalline systems: electrospinning. Special attention have been done on the characterization of the macromolecular organization prior to characterize the molecular dynamics. An interpretation is given to highlight the role of the weak inter-molecular interactions.

This research work, financially supported by the Normandy Region (FRANCE), was conducted at the “Groupe Physique des Matériaux” (GPM - UMR CNRS 6634) from the University of Rouen Normandy. In order to achieve electrospinning and flow induced crystallization, collaborations with Pr. P. E. Mallon from the University of Stellenbosch (South Africa) and Dr. L. Fernandez-Ballester from the University of Nebraska-Lincoln (USA) have been fruitful.

[†] **Mickaël Arnoult:** “*Contribution à l’étude des dynamiques moléculaires associées aux cinétiques de relaxation sous contrainte dans les polymères semicristallins : étude expérimentale et simulation numérique*”. **2007**

[‡] **Hugues Couderc:** “*Nanocomposites : polyester amorphe-montmorillonite. Influence des nanoparticules sur les dynamiques des relaxations moléculaires*”. **2008**

[‡] **Nicolas Delpouve:** “*Etude de la microstructure et des phénomènes de relaxation dans un biopolyester: le poly(acide lactique)*”. **2009**

[‡] **Khadidja Arabeche:** “*Etude de la mobilité moléculaire dans des systèmes amorphes complexes: multicouches de polycarbonate de bisphenol A (PC)/Polyméthacrylate de méthyle (PMMA) de l’échelle microscopique à l’échelle nanoscopique*”. **2011**

[‡] **Florian Hamonic:** “*Etude de la mobilité moléculaire dans des polyesters synthétiques : mise en évidence de l’anisotropie*”. **2012**

CHAPTER I

State of the art

CONTENTS

I.1 Glass transition and glassy state	8
I.2 Non-exhaustive phenomenology of the glass transition	11
I.3 Molecular dynamics and relaxation phenomena: from glass-forming liquids to glassy polymers	13
I.4 Structural relaxation in the glassy state	19
I.5 Crystallization of polymers	24
I.6 Structural anisotropy	26
References.....	32

This first chapter introduces the glass transition phenomenon. To begin with, the properties of the glass-forming liquids are discussed. Then, different theories and concepts are also presented in order to understand and interpret the molecular dynamics as well as the relaxation phenomena involved in the glass-forming liquids and the glassy state. Focus is also done on the specificities of polymer glasses. Subsequently, crystallization of polymers are depicted to highlight the environmental and the structural influences on the molecular dynamics of the amorphous phase. Finally, structural anisotropy is displayed in order to justify the motivation of this work.

I.1 Glass transition and glassy state

Glasses are disordered materials. They display short-range ordering over only few molecular dimensions. Thus, at the molecular scale they present a liquid-like structure. Nevertheless, even if they lack the periodicity of crystals, they mechanically behave like solids. Conventionally, it is expected that any liquids are able to form glasses if the cooling rate applied is sufficient to avoid crystallization of the material, among the numerous ways to vitrify [1]. Called glass-forming liquids, those materials exhibit very different chemical nature. They include oxides [2][3], chalcogenides [4][5][6], halides [7][8], ionic liquids [9][10], organic compounds [11][12][13], polymers [14][15][16], metal alloys [17][18][19] as well as metal-metalloid alloys [20]. The cooling rate applied to achieve a glass is then nature-specific [21]. Independently of their natures, when any glass-forming liquid is cooled down fast enough, its viscosity η increases and reaches a value close to 10^{12} Pa.s at a temperature which defines the well-known glass transition temperature T_g . The formation of the glassy state is the resulting effect of the impossibility of the liquid to equilibrate in the available time imposed by the cooling rate. The viscosity upon cooling being too significant the molecular motion is stopped. This dynamic phenomenon is the so-called α -relaxation. As a consequence, going through the glass transition, the thermodynamic properties (volume, enthalpy, entropy...) of the glass formed go out of equilibrium. A glass is then a non-equilibrium state.

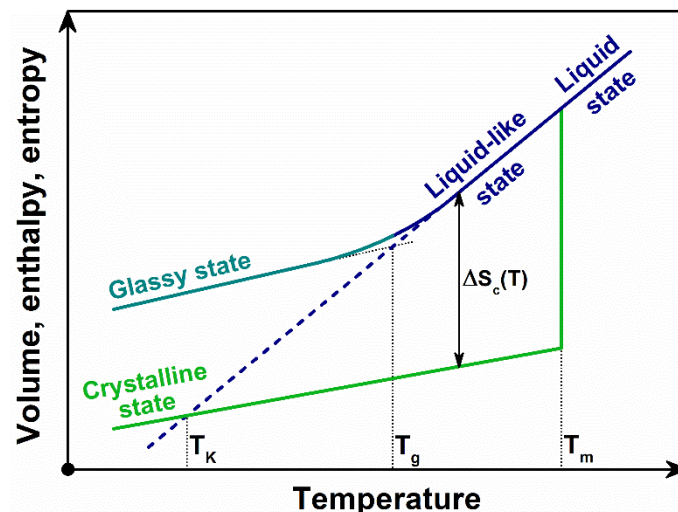


Figure I.1.1: Schematic illustration of the temperature dependence of the thermodynamic properties (volume, enthalpy or entropy) of a glass-forming liquid. T_K : Kauzmann's temperature. T_g : glass transition temperature. T_m : melting temperature. ΔS_c : configurational entropy $\Delta S_c = S_{\text{liquid}} - S_{\text{crystal}}$. Dotted line: thermodynamic equilibrium.

Figure I.1.1 depicts the variation of volume, enthalpy or entropy as a function of temperature leading to the formation of an amorphous solid, namely a glass. If the glass-forming liquid is sensitive to crystallization, the thermodynamic properties of the crystalline state, slowly increase upon heating (green line). At the melting temperature T_m an abrupt discontinuity of the thermodynamic properties turn crystals into liquid state through a first-order transition (green line). At high temperature in the liquid state, the glass-forming liquid is in equilibrium. The viscosity is low (around 10^{-1} Pa.s) and the molecular motion is high. Then, upon sufficient cooling rate to prevent crystallization, the system is in a metastable state below the melting temperature: the liquid-like state. The liquid-like state follows the general trend of the liquid state (blue line). Upon cooling, the viscosity increases and the molecular motion decreases. The thermodynamic properties gradually decrease up to change in slope at the glass transition where the glass-forming liquid vitrifies (cyan line) [22][23]. The resulting material is a glass. In contrast to melting, the vitrification occurs over a relative wide temperature interval [21]. The intersection of the liquid and glassy lines of the thermodynamic properties vs. temperature curve defines the glass transition temperature T_g (another common definition of T_g).

It is worth mentioning that the glass transition phenomenon, from a physical point of view, prevents from the Kauzmann's paradox [24]. Indeed, as pointed out by Kauzmann, the heat capacity, at constant pressure, of the liquid is higher than solid, namely the crystals. Thus, decrease of the temperature leads the liquid to decrease its entropy faster than the enthalpy of the crystals. However, if the material is sensitive to crystallization, the entropy of the equilibrium liquid S_{liquid} would be equal to the entropy of the crystals S_{crystal} at a temperature T_K , termed Kauzmann's temperature. Besides, a further decrease of temperature would lead to $\Delta S_c < 0$ (dashed line). Such inequality is a violation of the third law of thermodynamics [25]. This context refers to the Kauzmann's paradox, and allows to illustrate the origin of the glass transition phenomenon.

As explained above, the vitrification results from the impossibility of the liquid to equilibrate in the available time imposed upon cooling. However, the cooling rate β_c is defined as the first derivative of the temperature T by time t :

$$\beta_c = \frac{dT}{dt} \quad (1.1.1)$$

By assuming the cooling as a series of temperature steps, it gives information on the time t spent at each temperature T :

$$t = \frac{T}{\beta_c} \quad (1.1.2)$$

Consequently, higher the cooling rate, shorter the time spent at each temperature. In the same way, lower the cooling rate, longer the time spent at each temperature. This interpretation allows to introduce the notion of relaxation time τ , namely the time required by the system to recover equilibrium after external perturbations (thermic, mechanic, electric...) [21]. Therefore, upon cooling the liquid falls out of equilibrium when the time spent at each temperature becomes smaller than the relaxation time. The system does not succeed to remain in equilibrium by lack of time. This phenomenon shows the temperature dependence of the relaxation time. Even more, it highlights the significant and intriguing interest of the glass transition phenomenon, which is based on the fact that various glass-forming liquids of different chemical nature involving ionic interactions, van der Waals forces, hydrogen bonds, covalent bonds or metallic bonds, share that particular common property, among others as quoted above (liquid-like structure, solid-like mechanic behavior...).

Due to the temperature dependence, the vitrification can be more or less delayed by using lower cooling rates. If the cooling rate is too high, the rearrangement of the molecules will be low and the molecules will “freeze” more quickly. If the cooling rate is low, the rearrangement of the molecules will be facilitate and the molecules will “freeze” less rapidly. As depicted in Figure I.1.2, the glass transition temperature is cooling rate dependent. Fast cooling rate will lead to high glass transition temperature values, when slow cooling rate will provide low glass transition temperature values. This dependence with the applied cooling rate has been widely observed through experiments [26][27][28] and finally brings out the kinetic nature of the glass transition, namely its frequency dependence.

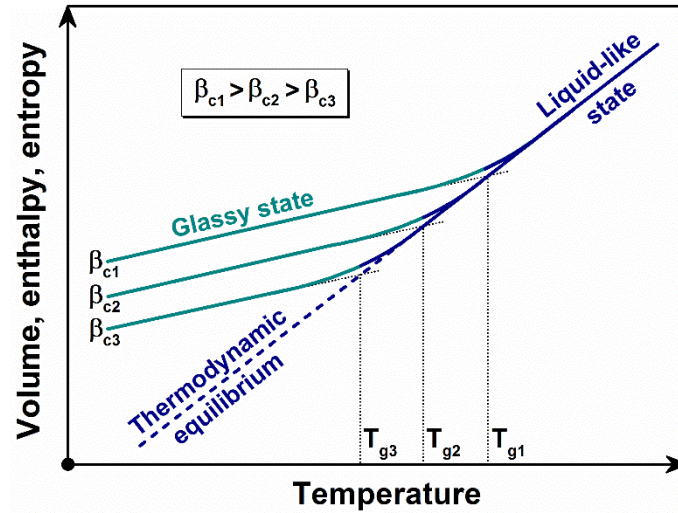


Figure 1.1.2: Schematic illustration of the temperature dependence of the thermodynamic properties (volume, enthalpy or entropy) of a glass-forming liquid upon three different cooling rates: $\beta_{c1} > \beta_{c2} > \beta_{c3}$. T_{g1} , T_{g2} and T_{g3} are the respective glass transition temperatures.

I.2 Non-exhaustive phenomenology of the glass transition

For the last century, numerous theories, models or approaches have been established to explain the fundamental nature of the glass transition in glass-forming liquids. It is worth mentioning that most of the concepts used nowadays originate from the sixties (defect-diffusion approaches [29], free-volume model [30][31], configurational-entropy theory [32][33]) up to eighties (energy-landscape picture [34], mode-coupling theory [35][36], random first-order transition theory [37][38], concept of kinetic constraints [39][40], geometric frustration concept [41][42]). The validity of those different theoretical descriptions have been widely discussed and reviewed [1][21][43][44][45][46]. However, the glass transition phenomenon remains unsolved. Indeed, none of the various models describes successfully all the aspects of that phenomenon briefly introduced in the previous section.

Nevertheless, two concepts are briefly approached, as they are used in this work for interpretations: free-volume model [30][31] and configurational-entropy theory [32][33].

I.2.1 Free-volume model

Historically, Eyring and coworkers were the first to highlight the importance of volume in the glass-forming liquids in 1941 [47]. They suggested that lower the viscosity of the liquid, higher the number of holes present in the liquid.

In that assumption, Cohen and Turnbull [30][31] have argued that redistribution of free volume in viscous liquids occurs without any expense of local energy and that molecular motions is related to the mobility of voids having a volume large enough to hold a molecule through the redistribution of free volume. In viscous liquids, a molecule is surrounded by neighbors, which define a “cage”. In that cage, the volume exceeding the volume taken by the molecule is then defined as local free volume v_f . Thus, molecules need free volume in their vicinity to rearrange. However, as viscosity increases as temperature cools down, less free volume is available to rearrange molecules. This leads to an expression of the viscosity, also known as the Doolittle equation [48]:

$$\eta(T) = A \cdot \exp\left(\frac{B}{v_f(T)}\right) \quad (1.2.1)$$

where A and B are fitting parameters. This decrease of free volume upon cooling explains the slowing down of the molecular motions towards glass transition. Consequently, the free volume model can be used to describe the temperature dependence of relaxation processes. However, the free volume concept rests on hard-sphere picture in which thermal activation does not play a role. Therefore, the concept can be criticized as it does not take into account the role of all thermodynamic aspects, such as entropy.

1.2.2 Configurational-entropy theory

The configurational-entropy theory is based on the idea that slowing down of the relaxation time with decreasing temperature towards glass transition is associated to the decline of available configurations related to configurational entropy ΔS_c [49]. Thus, Adam and Gibbs suggested in 1965 that relaxation processes involved in glass-forming liquids upon cooling take place through cooperative rearrangements of molecular groups [33]. In other words, the motion of such groups are only possible if a given number of neighboring molecular groups are also in motion. They argued that the number of molecular groups involved in those cooperative rearrangements increases as the temperature decreases. In addition, the size of the so-called cooperative rearranging region (CRR), are defined as the smallest region which can be subjected to a new configuration without requiring any simultaneous configurational change on and outside its limit. Those subsystems are assumed to relax independently of the others.

The CRR size increases as temperature decreases, namely the configurational ΔS_c entropy decreases. Consequently, by assuming that the energy barrier to overcome in order to relax is proportional to the size of the region, the temperature dependence of the relaxation times τ of glass-forming liquids approaching the glass transition is then described by the following equation:

$$\tau(T) = \tau_0 \cdot \exp\left(\frac{C}{T\Delta S_c(T)}\right) \quad (1.2.2)$$

where τ_0 and C are constants.

As for the free volume model, criticisms may also arise. Especially, one major criticism comes from the configurational entropy definition. It is based on the fact that the glass has the same “fast” contribution to the entropy than the crystal at the same temperature. Though, as pointed out by Goldstein, this assumption is not always realistic because the glass may have significant contributions to the “fast” specific heat from anharmonic vibrations (no periodic motions) and secondary relaxations, not present in the crystal [50].

I.3 Molecular dynamics and relaxation phenomena: from glass-forming liquids to glassy polymers

In the previous sections, we have highlighted the temperature dependence of the relaxation time of glass-forming liquids upon cooling. The molecular motions are impeded as approaching the glassy state, resulting in the glass transition phenomenon. Combined to the temperature dependence, the frequency dependence of the vitrification has also been evidenced through the cooling rate dependence. In addition, few models attempting to describe this phenomenon have been approached. However, the molecular dynamics and the relaxation phenomena bring complexity to theorize this intriguing phenomenon.

I.3.1 Glass-forming liquid in general

The slowing down of the molecular motions extends the relaxation times from picoseconds in the liquid state to almost one hundred seconds at the glass transition. It becomes longer and longer as the deep glassy state is reached. Such molecular dynamics are related to the main relaxation process, the α -relaxation, and are characterized by an Arrhenius

to a non-Arrhenius behavior of the relaxation times when reaching the glass transition [51]. Even if the glass formed looks “frozen” on the laboratory time scale, molecular motions still exist below the glass transition. Indeed, α -relaxation processes become significantly slow and longer than the experimental observation time scale. Such motions are believed to take place in the form of a rearrangement of molecules defined as “relaxing unit”, “quasi-independent unit”, “thermokinetic structure”, “molecular domain”, “dynamically correlated domain” or “cooperative rearranging region” according to the numerous model previously introduced.

In addition, fast local motions take place at different scales and are dimly dependent of the environment. They are characterized by an Arrhenius behavior [51]. Motions related to δ, γ -relaxations have to be distinguished from β -relaxations. The first ones display very short relaxation times. Such motions come out from vibrations or rotations of atoms or molecules. In contrast, the last one is also affected by local motions. However, its contribution to the cooperative rearrangement still remains under debates in literature [52][53].

I.3.2 Glassy polymers in particular

In addition to the generalities approached in the previous section with regard to glass forming-liquids in general, glassy polymers display specific properties. Due to the extremely long macromolecular chains, the complex molecular architecture results in disorder and entanglement involving inter- or intra-molecular interactions. More specially, chain motions may be influenced by chain flexibility, steric hindrance, polarity, geometric factors, molecular weight, crosslinking or crystallization. Therefore, the molecular motions and the relaxation may arise from various interactions:

- covalent bonds along the main macromolecular chains are strong bonds setting the configuration of the system. The energy of such bond is around $300 \text{ kJ}\cdot\text{mol}^{-1}$.
- weak bonds lead to cohesion of the system. They are about 10 to 100 less energy. Interactions related to electronegativity differences such as hydrogen bonds have to be distinguished from the Van der Waals interactions.

It is then possible to differentiate two other kinds of molecular motions: one related to the movement of long macromolecular chain segments and another one associated to the local motions of molecules or groups of molecules within the macromolecular chain.

I.3.3 From Arrhenius to non-Arrhenius temperature dependence

Despite the numerous concepts and theories proposed, the combination of relaxation phenomena still remains challenging in order to understand the molecular dynamics in glass-forming liquids. One of the most challenging is the explanation of the Arrhenius to non-Arrhenius temperature dependence of the α -relaxation as approaching the glass transition. Experimentally, complementary techniques have been used to study and assess the relaxations of glass-forming liquids either above or below the glass transition: differential scanning calorimetry (DSC), modulated temperature differential scanning calorimetry (MT-DSC), fast scanning calorimetry (FSC), dynamic mechanical analysis (DMA), broadband dielectric spectroscopy (BDS), nuclear magnetic resonance (NMR) spectroscopy, positron annihilation lifetime spectroscopy (PALS), neutron scattering (NS) among others. Through a wide range of frequencies (rate and time of solicitations), they allow to investigate the temperature dependence of the relaxation time and the molecular dynamics as schematically represented in Figure I.3.1.

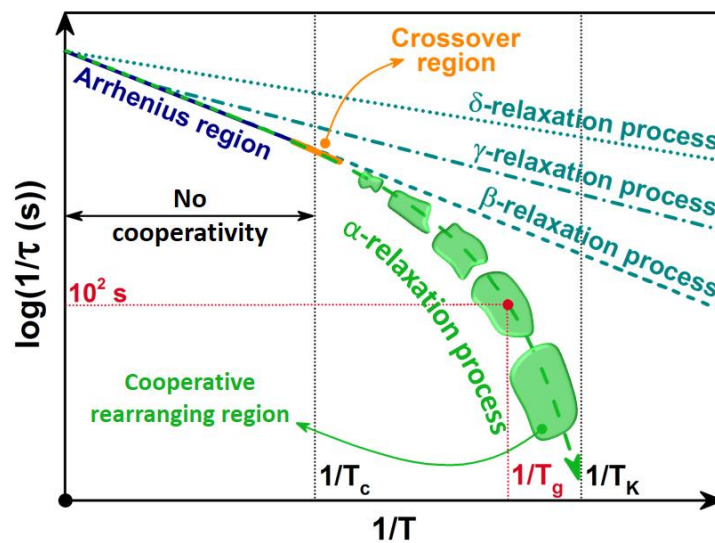


Figure I.3.1: Schematic illustration of the temperature dependence of the $\alpha, \beta, \gamma, \delta$ -relaxation processes of a glass-forming liquid upon cooling. T_c corresponds to the cross-over temperature where α - and β -relaxations merge. T_g is the glass transition temperature where relaxation times reach hundred seconds. T_K defines the Kauzmann's temperature.

From very high temperatures to the so-called cross-over temperature T_c [54], the relaxation times related to $\alpha, \beta, \gamma, \delta$ -relaxation processes of a glass-forming liquid upon cooling exhibits an Arrhenius temperature dependence:

$$\tau(T) = \tau_{\infty} \cdot \exp\left(\frac{E_a}{k_B T}\right) \quad (1.3.1)$$

with τ_{∞} the relaxation time at infinite temperature, E_a the activation energy and k_B the Boltzmann constant ($k_B = 1.38 \cdot 10^{-23} \text{ J.K}^{-1}$). The relaxation processes are spatially homogeneous. The activation energy is related to the energy needed to overcome the barrier leading to molecular motions. Thus, the motions associated to δ - and γ -relaxations display low activation energies due to their localized nature. With regard to β - and α -relaxations, their activation energies merge together. The nature of such relaxation still remains unclear, but present higher energy activations. However, while the temperature reaches the cross-over temperature T_c a distinction can be made: the β -relaxation still describes an Arrhenius behavior whereas it vanishes with regard to the α -relaxation. At the cross-over temperature, the α -relaxation becomes cooperative, as introduced by the theory of Adam and Gibbs. The feature slowing down of glass-forming liquid between T_c and T_K highlights the non-Arrhenius behavior, also termed super-Arrhenius behavior, of the α -relaxation. This deviation from the Arrhenius behavior is well described by the empirical Vogel-Fulcher-Tamman (VFT) equation [55][56]:

$$\tau_{\alpha}(T) = \tau_{\infty} \cdot \exp\left(\frac{A}{T - T_V}\right) \quad (1.3.2)$$

where τ_{∞} is the relaxation time at infinite temperature, A is a fitting parameter and T_V is a characteristic temperature below T_g , the so-called Vogel temperature. T_V is a hypothetical thermodynamic temperature where cooperative rearrangement are assumed to be almost non-existent. Finally, as the temperature decreases and digresses from T_c , the cooperative rearrangements increase through bigger and bigger CRR.

Any glass-forming liquids exhibit the temperature dependence of their relaxation times. However, according to their chemical nature or their structures, glass-forming liquids can display a deviation more or less pronounced from the Arrhenius to the non-Arrhenius behavior. In that purpose, Angell introduced the notion of fragility in order to classify the degree of departure from the Arrhenius behavior [57][58]. Such a parameter estimates the dynamic properties of a glass-forming liquid and the changes in its molecular motion as approaching the glass transition. In other words, it characterizes the steepness of the

temperature variation of viscosity or relaxation time towards glass transition, as highlighted so far. Thus, the fragility index m is expressed as follow:

$$m = \left[\frac{d(\log \tau)}{d\left(\frac{T_g}{T}\right)} \right]_{T=T_g} \quad (1.3.3)$$

in which τ is the relaxation time, T the temperature and T_g the glass transition temperature. Through the value of m , the glass-forming liquids are then classified into “strong” or fragile” category. Strong liquids display low value of m , when fragile liquids depict high value of m ($16 \leq m \leq 200$). Strong liquids behave nearly in Arrhenius fashion, whereas fragile liquids show marked deviation from Arrhenius behavior as depicted by the Angell’s plot in Figure I.3.2.

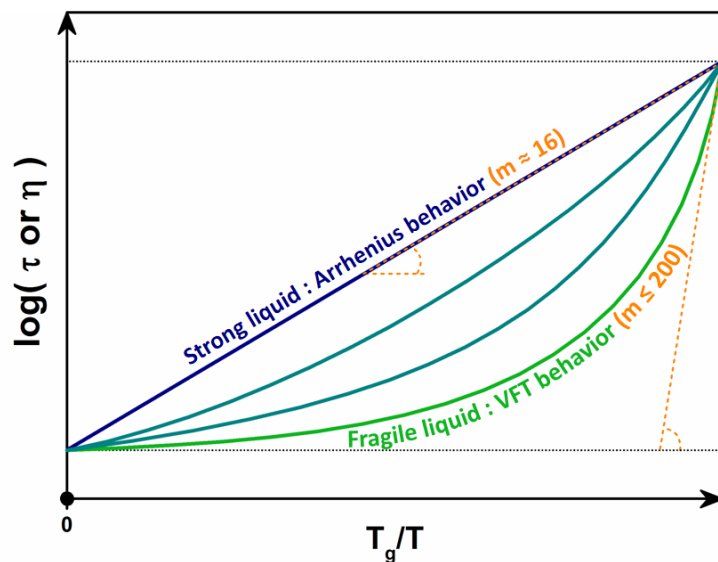


Figure I.3.2: Angell’s plot showing the variations of relaxation time τ , or viscosity η , as a function of normalized temperature T_g/T . It defines the two main classes of glass-forming liquids from strong liquids (Arrhenius behavior: blue line) to fragile liquids (VFT behavior: green line). Glass-forming liquids with intermediate values of fragility index m are also display (cyan lines). Steepness at T_g for the strong and fragile liquid are also presented with m value of 16 and 200, respectively (orange dashed lines).

I.3.4 The approach of Donth

In addition to the empirical VFT equation and the Angell's fragility concept, which allow to characterize the Arrhenius to non-Arrhenius behavior of the α -relaxation process, numerous approaches [59][60][61][62] also exist in order to estimate the size or the number of structural units involved in the cooperative rearrangements, the so-called CRR. One of the most popular is the approach of Donth [63][64]. This approach is based on the theory of Adam and Gibbs: the configurational-entropy theory introduced in the section I.2.2. As explained, a CRR is an independent and distinguishable subsystem with these own thermodynamic fluctuations: relaxation time, relaxation temperature, glass transition temperature. Therefore, going through the glass transition, the glass-forming liquid displays a broad distribution of relaxation times τ_α as well as a broad distribution of dynamic glass transition temperatures $T_{g\alpha}$ related to each CRR. From this postulate, Donth associates the fluctuating time of the molecular motions related to their relaxation times with the fluctuating temperature. In this way, this thermodynamic approach relates the CRR, or cooperativity length $\xi_{T\alpha}$, to the dynamic heterogeneity deduced from the temperature fluctuation associated with the glass transition. It provides a picture of the relaxation time at the glass transition which is directly observable through calorimetric measurements, either from DSC or MT-DSC. The cooperativity volume $\xi_{T\alpha}^3$ at the average dynamic glass transition temperature T_α can be then estimated from the following equation:

$$\xi_{T\alpha}^3 = \frac{(1/C_p)_{\text{Glass}} - (1/C_p)_{\text{Liquid}}}{\rho(\delta T)^2} k_B T_\alpha^2 \quad (I.3.4)$$

with k_B the Boltzmann constant, δT the average temperature fluctuation related to the dynamic glass transition of a CRR, ρ the density of the relaxing system, and C_p the heat capacity at constant pressure.

In the last two decades, the approach of Donth has been widely used in order to estimate the cooperativity length at the glass transition in various glass-forming liquids such as chalcogenied glasses [65], organic compound glasses [66][67] or polymer glasses [68][69] among others. With regard to polymer science, two causes for cooperativity changes have been observed so far. The first relates to changes in thermodynamic variables such as

temperature, and the second to structural modifications of the material. In the first case, it is well known that the cooperativity length increases when the temperature decreases from the crossover temperature, for which the cooperativity arises, to the glass transition temperature. It is the behavior described in Figure I.3.1. In the second case, the approach of Donth has widely been used to investigate the decrease of cooperativity for two kinds of structural hindrances namely external and internal hindrances. External hindrances are related to geometrical restrictions like the confinement between nanolayers [70][71] or the addition of additives such as fillers [72] or plasticizer [73]. On the other hand, internal hindrances are related to the material itself, in other words its microstructural modifications such as spherulitic crystallization [74][75][76] or orientation/crystallization of the amorphous phase induced by drawing [77][78][79]. In literature, it is now assumed that the cooperativity length is correlated with the nature and the number of inter-chain interactions. In regard to this hypothesis, the decrease of the cooperativity length related to structural hindrances could be interpreted as the consequence of inter-chain bond breaking.

I.4 Structural relaxation in the glassy state

In the previous sections, we have highlighted the temperature dependence of the α -relaxation process in glass-forming liquids through the Arrhenius to the non-Arrhenius behavior, as well as the increase of the cooperative rearrangement sizes involved, upon cooling. However, while approaching the glass transition - and below - another phenomenon takes place: the structural relaxation.

I.4.1 Concept of physical aging

Such phenomenon is clearly visible through the concept of physical aging [23][80][81][82]. Indeed, even if a glass looks “frozen” on the laboratory time scale, molecular motions still exist below the glass transition temperature. Therefore, if a glass-forming liquid is held below its respective glass transition temperature, the thermodynamic properties of the system will slowly evolve towards equilibrium, as depicted in Figure I.4.1.A. The glass looks for decreasing its excess of thermodynamic properties without leading to crystallization. A lower energetic state is reached while maintaining a disordered state.

In the recent years, understanding of the glassy state nature, and its physical aging, still supports the focus of many researchers on a variety of glass-forming liquids such as metallic glasses [83], small organic glasses [13], chalcogenide glasses [84], colloidal glasses [85][86] or polymer glasses [87][88]. Investigations of physical aging is a major issue in order to understand the structural relaxation processes on the physical properties evolution. From the free-volume model presented in section 1.2.1, it has been proposed from various investigations that the driving forces of the physical aging, leading to the decrease of the thermodynamic properties towards equilibrium are related to a free volume hole diffusion towards surfaces [89][90][91][92]. Those surfaces may be the external ones of the system or the internal ones tied to the creation of low density regions induced by the cooling rate. Therefore, through structural relaxation, molecular motions can be investigated.

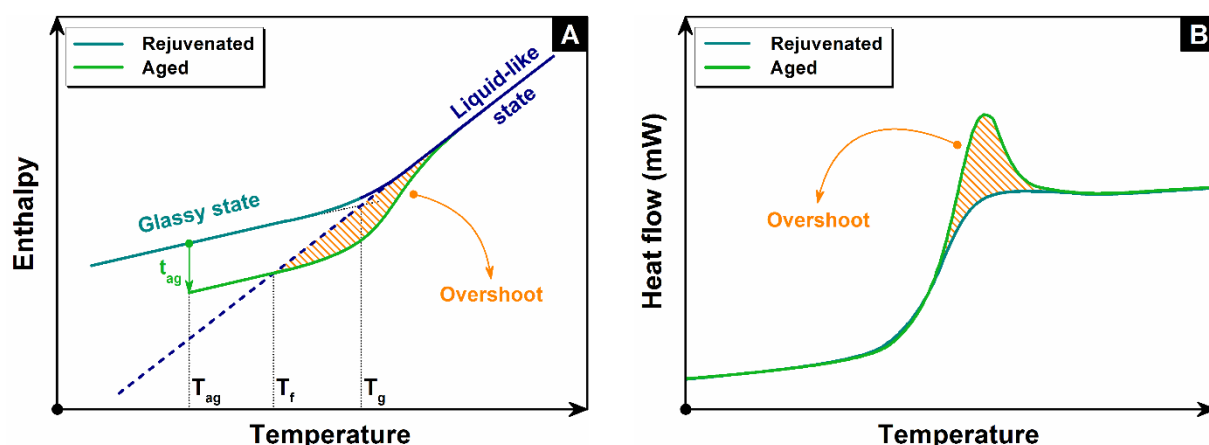


Figure I.4.1: Schematic illustration of the temperature dependence of the enthalpy of a glass-forming liquid upon physical aging (A) and the respective DSC heat flows of the rejuvenated and the aged scans as a function of temperature (B). Cyan and green lines represent the rejuvenated and the aged scans, respectively. The blue dashed line depicts the thermodynamic equilibrium. T_g : glass transition temperature. T_{ag} : aging temperature. t_{ag} : aging time. T_f : fictive temperature (concept introduced below).

The kinetics of physical aging can be investigated by means of calorimetric investigations. In figure I.4.1.A, the lower energetic state reached delays the recovery to the liquid-like state upon subsequent heating (orange hatched area). Thus, when held isothermally below the glass transition temperature, the subsequent heating will display a peak superimposed to the glass transition by DSC or FSC. The delay leads, in figure I.4.1.B, to a peak (the overshoot) which is related to the enthalpy recovery and gives insight on the excess of energy released upon aging for an aging duration. Usually, enthalpy recovery of a

glass, aged at a temperature T_{ag} during a time t_{ag} , is calculated by integrating the difference between the scans of aged and rejuvenated sample, according to the following equation [80]:

$$\Delta H(T_{ag}, t_{ag}) = \int_{T_1}^{T_2} [C_p^a(T) - C_p^r(T)] \cdot dT \quad (1.4.1)$$

in which $C_p^a(T)$ and $C_p^r(T)$ are the heat capacity of the aged and the rejuvenated sample, respectively, and T_1 and T_2 are arbitrary temperatures below and above the glass transition temperature T_g , respectively. For an infinite time, it is believed that equilibrium is reached. The expected total enthalpy loss ΔH_∞ extrapolated from the equilibrium melt depends on the aging temperature T_{ag} , as well as the glass transition temperature T_g and the heat capacity step ΔC_p of the sample, as depicted from the following relation:

$$\Delta H_\infty = \Delta C_p \cdot (T_g - T_{ag}) \quad (1.4.2)$$

1.4.2 Concept of fictive temperature

The phenomenon of structural relaxation can also be depicted through the concept of fictive temperature T_f , as depicted in Figure I.4.1.A. This concept has been introduced by Tool in 1931 [93]. It allows to characterize the non-equilibrium state related to the vitrification. Tool defines T_f as the temperature at which any properties, related to the structural relaxation, are at the equilibrium state. As presented in Figure I.4.1.A, T_f is measured when the thermodynamic properties, here the enthalpy, intercept the thermodynamic equilibrium. Thus, by measuring the fictive temperature as a function of aging time, kinetics of the structural relaxation can be investigated. When the fictive temperature measured reaches the aging temperature value, the thermodynamic equilibrium is reached: $T_f = T_{ag}$.

The concept of fictive temperature is also used in order to investigate the kinetic nature of the glass transition through the cooling rate dependence of the glass-forming liquids, introduced in section I.1. The resulting kinetic effects are observed upon heating from the glassy state to the liquid-like state, as the response upon heating depends on the previous thermal history of the material, as shown in Figure I.4.2. Figure I.4.2 displays the enthalpy response observed upon heating after cooling the glass-forming liquids at different rates. Firstly, a glass has been formed at β_{c1} . Then, by heating at the same rate $|\beta_{c1}| = \beta_{h1}$, the

enthalpy recovers the equilibrium in the liquid-like state on the same line. Secondly, a glass has been formed at β_{c2} lower than β_{c1} . Thus, the glass transition temperature depicts a lower value. Then, by heating the glass formed at a scanning rate β_{h1} higher than the cooling rate, the enthalpy recovers the equilibrium in the liquid-like state on a different line (green line). The glassy state presents a lower molecular motion upon heating. Therefore, the recovery is delayed due to the structural relaxation leading to overshoot (orange hatched area). Higher the difference between the cooling and the heating rates, higher the magnitude of the overshoot. As for physical aging, the resulting effect of structural relaxation related to the difference between the cooling and the heating rates is a peak superimposed to the glass transition upon heating when investigated by DSC or FSC. From calorimetric investigations, the fictive temperature T_f is measured using the Moynihan's equation [94]:

$$\int_{T_1}^{T_f} (C_{p,liquid} - C_{p,glass}) \cdot dT = \int_{T_1}^{T_2} (C_p - C_{p,glass}) \cdot dT \quad (1.4.3)$$

in which T_1 and T_2 are arbitrary temperatures well above and well below the glass transition, respectively. C_p is the heat capacity of the sample at constant pressure, when $C_{p,liquid}$ and $C_{p,glass}$ are the extrapolated liquid and glassy heat capacity lines of the sample, respectively.

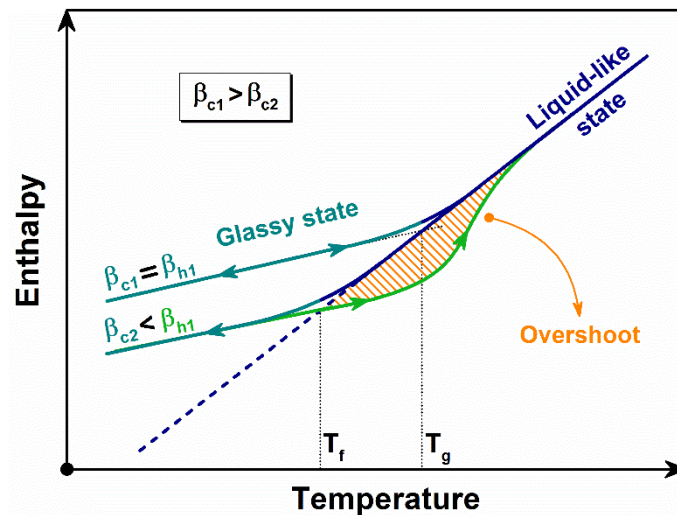


Figure 1.4.2: Schematic illustration of the temperature dependence of the enthalpy by cooling down a glass-forming liquid at two different rates β_{c1} and β_{c2} , and then heating up at the same rate β_{h1} . When the cooling and heating rates are different an overshoot (orange hatched area) is observed. The recovery towards equilibrium is delayed (green curve). The blue dashed line depicts the thermodynamic equilibrium. T_g : glass transition temperature. T_f : fictive temperature.

I.4.3 Non-exponential behavior of the relaxation times

Below the glass transition, the phenomenon of structural relaxation takes place, as highlighted above. The kinetics of structural recovery have been well formulated through the Tool-Narayanaswamy-Moynihan (TNM) [94] or Kovacs-Aklonis-Hutchinson-Ramos (KAHR) [95] models. In addition of the temperature dependence depicted in the previous sections, these models also bring out the structure dependence of the relaxation time.

A common representation of the temperature and structure dependence for the relaxation time relies on the Tool's concept of fictive temperature T_f introduced in the previous sections I.4.2 [96]:

$$\tau(T, T_f) = \tau_0 \cdot \exp\left(\frac{x \cdot \Delta h^*}{R \cdot T} + \frac{(1-x) \cdot \Delta h^*}{R \cdot T_f}\right) \quad (1.4.4)$$

where τ_0 is the relaxation time in equilibrium at an infinitely high temperature, T the temperature, Δh^* the activation energy of the relaxation phenomena and x a constant of the material ($0 \leq x \leq 1$) defining the relative contributions of temperature and structure to the relaxation time. The equation shows the non-linearity of the relaxation time, as already observed from the Arrhenius to non-Arrhenius behavior of the α -relaxation. However, from the configurational-entropy theory, each CRR has its own relaxation time. Thus, a broad distribution of relaxation times τ exists, and is well described through a stretched exponential function ϕ , also known as Kohlraush-Williams-Watt (KWW) function [97]:

$$\phi(t) = \exp(-(t/\tau)^\beta) \quad (1.4.5)$$

with β the stretch exponent ($0 \leq \beta \leq 1$) defining the distribution of the relaxation times. It is inversely proportional to the width of a corresponding distribution of relaxation times. Therefore, in addition of the non-linearity as a function of temperature, the relaxation times also depict a non-exponential behavior as a function of time upon isothermal.

I.5 Crystallization of polymers

As introduced in this chapter, the phenomenon of crystallization can also occur in glass-forming liquids, in addition to vitrification. Therefore, this section focuses on the different aspects of crystallization with regard to polymers.

I.5.1 From conventional to unconventional crystallizations

The Lauritzen-Hoffman concept based on the nucleation theory leading to the formation of stable crystal nuclei which then are followed by their own growth is widely accepted to describe the crystallization phenomenon of polymers [98][99][100][101]. Thus, when polymers crystallize, macromolecular chains that initially are in 3D random coil conformations turn into crystalline lamellae with a thickness of the order of tens of nanometers. Those crystalline lamellae are alternately separated by amorphous regions with some chain folding which can connect them together. One possible representation in two dimensions is depicted in Figure I.5.1. The polymers pass from one disordered state to a partially ordered state between crystalline and amorphous regions. Therefore, following their crystallization, polymers are always semi-crystalline.

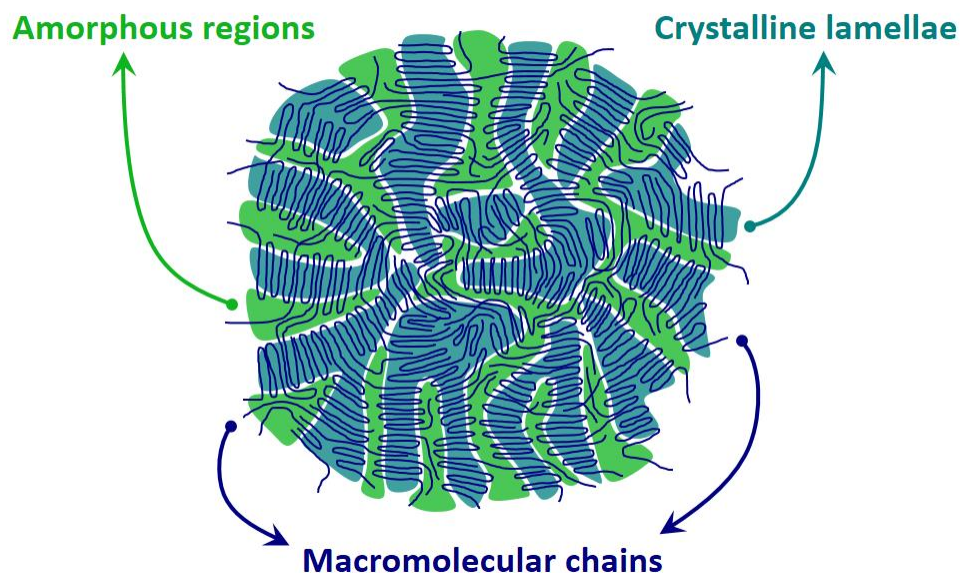


Figure I.5.1: Schematic illustration of the crystalline lamellae and the amorphous regions competition arising from quiescent crystallization. Blue lines: macromolecular chains. Green area: amorphous regions. Cyan area: crystalline lamellae.

Semi-crystalline polymers can be obtained by either conventional or unconventional crystallization pathways. Crystallization is conventional when the process is only thermally activated (quiescent crystallization), whether performed upon cooling from the melt or upon heating from the glassy state to a given temperature [102][103][104]. Quiescent crystallization is also possible in the presence of nucleating agents, which allow tailoring crystal morphology and lamellae orientation [105]. Under conventional crystallization, crystalline lamellae are organized into three dimensional superstructures, the so-called spherulites. The growth direction is always corresponding to a crystallographic direction and oriented radially. Upon polarized optical microscopy, spherulites display a cross-shaped extinction, the so-called Maltese cross, as observed in Figure I.5.2.

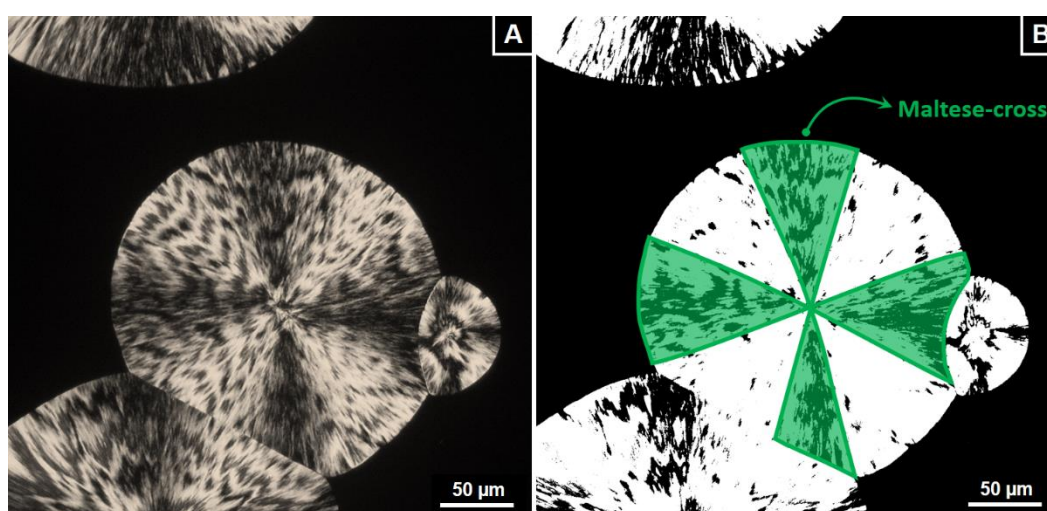


Figure I.5.2: Polarized optical microscope picture of polylactide spherulites crystallized at 130 °C after 200 min. (A) Raw picture. (B) Thresholded picture in order to highlight the Maltese-cross (green area).

Unconventional crystallization emerges from specific conditions, such as memory effect [106], cross-nucleation [107][108] or thermo-mechanical history [109][110]. Memory effect arises from melt domain with residual order from previous crystallites or entangled polymer chains that remain above the melting temperature. Therefore, the melt displays a kind of “memory” that will affect a subsequent crystallization. Cross-nucleation arises from the heterogeneous nucleation of one polymorph by another without requiring a polymorphic transformation. Finally, thermo-mechanical history can lead to strain induced crystallization (stress induced above the glass transition temperature) or flow induced crystallization (stress induced above the melting temperature).

I.5.2 Crystallization vs. vitrification

Semi-crystalline polymers come out from a competition between crystallization and vitrification. The result is the formation of nano-phasic structures [111]. For decades now, most semi-crystalline polymers are described in the literature by a three-phase model [112][113][114][115]. Between the crystalline and the amorphous phases, an incomplete decoupling may exist that defines an additional fraction [116][117]. Such a fraction is due to the fact that polymer chains are much longer than the typical dimensions of polymer crystal [118][119]. This fraction has been called the rigid amorphous fraction (RAF) and is commonly defined by opposition to the unconstrained amorphous phase, the mobile amorphous fraction (MAF), as its mobility is drastically restricted because of the geometrical constraints at the interface with the crystals [120][121]. In addition to the three-phase model, a distinction may be done regarding the mobile amorphous fraction. In the past few years, constrained and unconstrained mobile amorphous fractions (CMAF and UCMAF), also depicted as intra- and inter-spherulitic amorphous phase respectively, have been reported for semi-crystalline polyesters, such as PET [122] and PLA [76][123], as revealed by DSC measurements through the concept of cooperative rearranging regions [75] as well as structural relaxation (i.e. physical aging) [124]. Consequently, the presence of crystals affects the molecular dynamics of the mobile amorphous fraction.

I.6 Structural anisotropy

The influence of the molecular dynamics of the amorphous phase in complex polymer systems have been widely discussed in the past few years. Especially, as rapidly highlighted in the section I.3.4 with the approach of Donth, the decrease of cooperativity have been observed for two kinds of structural hindrances, namely external and internal hindrances.

External hindrances are related to geometrical restrictions such as confinement. For examples, Tran et al. have discussed the decrease of cooperativity in syndiotactic poly(methyl methacrylate) confined between layers of organophilic montmorillonite [71]. They assigned such decrease to a restriction of the possible conformation in the confined state due the nature of the interfacial interactions. In the same way, Arabeche et al. have shown in confined nano-layers polycarbonate/poly(methyl methacrylate) a significant decrease of the

cooperativity due to the annihilation of π -stacking in polycarbonate [70]. In isochorically confined polymer glasses, decrease of the cooperativity has also been evidenced by Zhang et al. due to the reduction of the number of segmental units required to move cooperatively [125]. In addition, external hindrances are also related to additives such as fillers and plasticizer [73] or donor-acceptor groups [126]. To contrast, fillers can play role of confiner when they are intercalated, as described above. However, fillers can also improve the molecular motion when they are exfoliated [127][128]. Indeed, in this configuration the fillers increase the cooperativity due to different interfacial interactions. Finally, through plasticizer or donor-acceptor groups, the molecular dynamics have been evidenced to be less cooperative when covalent bonds become predominant over weak bonds such as Van der Waals bonds. Dorbicau et al. have concluded in the case of plasticized polylactide that interactions between PLA chains are hindered by the breaking of macromolecular interactions due to intercalations of plasticizer molecules. With regard to donor-acceptor groups, Grigoras et al. have created more intra- than inter-molecular electron transfers on a series of statistical methacrylate copolymers. They have highlighted the decrease of cooperativity when decreasing the weak bond interactions.

On the other hand, internal hindrances are related to the materials itself, in other words its microstructural modifications such as cross-linking [129], as well as spherulitic crystallization [69][75][74] or structural anisotropy related to orientation/crystallization of the amorphous phase induced by drawing above the glass transition [77][78][79][130][131]. With regard to cross-linking effects, Sasaki et al. have shown a decrease of the cooperativity as the degree of cross-link, namely the rigidity of the network, increases. To draw a parallel with external hindrances, the molecular dynamics become less cooperative when covalent bonds become predominant. The same behavior is also observed upon conventional or unconventional crystallization, as highlighted above with the competition between crystallization and vitrification. Upon quiescent crystallization, Delpouve et al. have shown for PLA a decrease of the cooperativity as increasing the degree of crystallinity [74][75]. The mobile amorphous fraction becomes constrained due to the confinement effect of the crystalline lamellae. In the same way, strain induced crystallization of PLA [78] and PET [131] display a decrease of the cooperativity due to the confinement effects of the crystals. Finally, Hamonic et al. have investigated the strain induced crystallization of PET_g due to its low ability

to crystallize. Thus, upon drawing they have investigated molecular dynamics in non-crystalline but oriented system. However, they have also observed a decrease of the cooperativity even if crystallization has been inhibited [79]. They assigned such behavior to the presence of large amount of RAF, which originates from the disordered nature of the PET_g. Even if the confinement effect of the crystal is avoided, PET_g chains still organize in an oriented and constrained structure where chains packing constrain their conformations.

Therefore, molecular dynamics, and especially cooperativity, depend on the molecular interactions between the macromolecular chains, which themselves depend on the environment or the structural hindrances of the system. In this context, it is clear that molecular dynamics are structure dependent. Nevertheless, questions still rise: what is the role of the structural anisotropy on the molecular dynamics with regard to crystalline and non-crystalline complex polymer systems prior to crystallization and vitrification? What is the role of crystalline morphology? What is the role of the molecular orientation?

In that respect, two original sample preparations have been used in this work in order to investigate the molecular dynamics involved in systems subjected to such structural anisotropy.

I.6.1 Flow induced crystallization

Over the last few decades, numerous works have been done on the initial stages of flow-induced crystallization [132][133][134][135][136][137][138][139] as well as on the final oriented semi-crystalline microstructure [140][141][142][143][144][145]. The flow in the melt results in a local alignment of chain segments inducing metastable quasi-crystalline aggregates. Such aggregates are also depicted as crystal nucleation precursors, and their number and lifetime are time and temperature dependent. The most significant consequences are the acceleration of the crystallization kinetics, and the modification of the crystalline morphology from isotropic spherulites to anisotropic flow-induced crystalline structures, as depicted in Figure I.6.1 with the so-called shish kebab superstructure. As a result, the structural anisotropy induced significantly impacts the final physical properties of the materials. The highly oriented morphology confers greater density, modulus, hardness as well as lower permeability and thermal expansion coefficient [146][147][148][149].

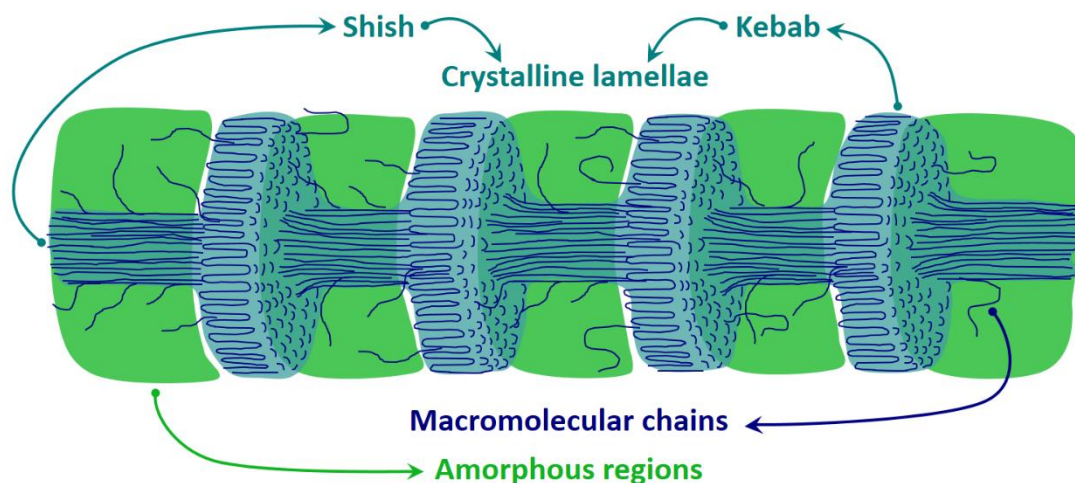


Figure I.6.1: Schematic illustration of the shish-kebab superstructure in semi-crystalline polymers. From the melt flow, the crystal nucleation precursors allow the crystallization of the shish. Then, kebabs crystallize transversally from the shish. The shish and the kebabs are made of crystalline lamellae (cyan area), which are surrounded by amorphous regions (green area).

Flow-induced crystallization has been mostly investigated on polypropylene because of industrial interests. Recently, essentially because of environmental concerns, several studies have also been reported about flow-induced crystalline structures in polylactide (PLA) [150][151][152][153][154][155][156][157][158], a bio-sourced and biodegradable thermoplastic polyester. Conventional crystallization of PLA leads to the concomitant formation of highly ordered α crystals and less ordered δ crystals [159][160]. It is established that quiescent crystallization performed at temperatures higher than 120 °C leads to α crystals, whereas at temperatures below 100 °C δ crystals are obtained. In the intermediate range of temperature, the concomitant crystallization of both α and δ crystals occurs [161][162]. The control over the crystalline structures formed in PLA in the presence of shear or elongational flows has been mainly investigated in order to improve physical properties, such as oxygen barrier [163] or mechanical properties [164]. To highlight the interest of flow-induced crystalline structures on PLA, it might also be mentioned that such structures are also mimicked on composite materials [165][166], or by adding nucleating agent [167][168] as well as nano-fibrils [169].

I.6.2 Electrospinning

Electrospinning is a simple technique to implement in order to produce polymer fibers with diameters ranging from the micro- to the nano-scale [170][171][172]. The technique has emerged as a useful technique to produce micro- and nano-fibers that have found wide

applications in fields such as tissue engineering [173], biomedical [174], filtration [175], or electronic [176]. Despite the simplicity of the technique, many factors influence the fiber morphology including the solution flow rate, the distance between the syringe and the collector, solution concentration and the spinning voltage among others. In addition, very complex processes are involved that influences the fiber structure including the very rapid solvent evaporation as well as the mechanical and electrical forces which induce an orientation of the macromolecular chains along the fiber axis [171]. For these reasons, electrospinning can lead to complicated internal microstructures related to the structural anisotropy. It has been observed that electrospinning retards or inhibits the crystallization of many polymers such as PLA [177][178]. Due to the very rapid solvent evaporation from the syringe to the collector, the macromolecular chains do not have sufficient time to move and crystallize during the process. However, even if electrospun fibers can depict a low degree of crystallinity, they clearly display a high orientation of their macromolecular chains aligned with the fiber axis. Indeed, under the effect of the electric field the macromolecular chains are subjected to an elongation strain and a shear force. Zong et al. initially reported that electrospun fibers of PLA exhibit highly oriented chains although they are non-crystalline [177]. Recently Ma et al. confirmed this result by showing that the electrospinning carried on free-end fibers of PLA leads to the formation of an original microstructure where the amorphous phase is oriented with evidence of a mesophase but without the formation of any crystals [178]. Thus, electrospun fibers of PLA can display a short-range ordering phase related to structural anisotropy.

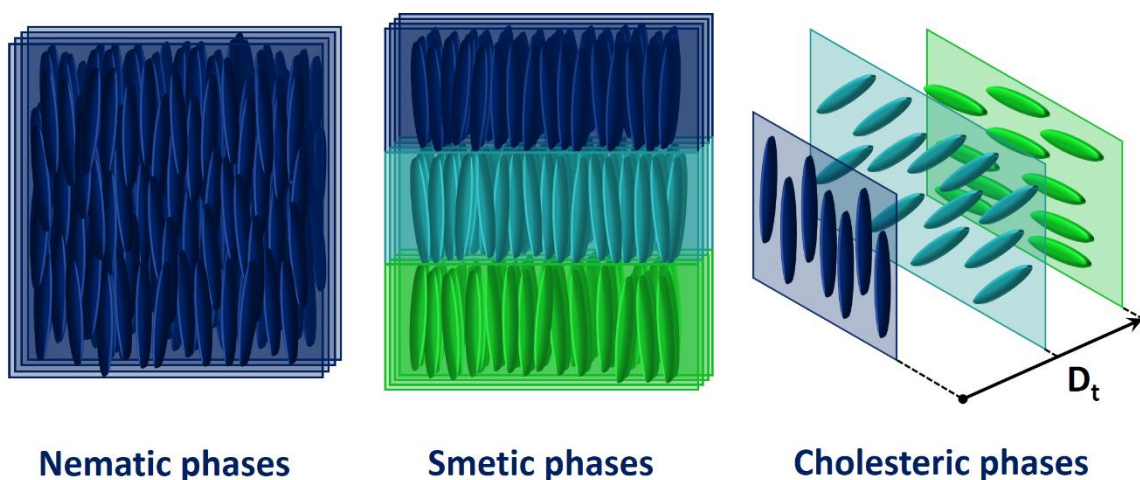


Figure 1.6.2: Schematic illustration of the mesomorphic phases: **(left)** nematic phases; **(center)** smectic phases; **(right)** cholesteric phases.

The nature of the mesophase has not been evidenced. However, for more clarity and discussion, the three different mesomorphic phases existing, and historically arising from liquid crystal phases, are presented in Figure I.6.2 [179]. Mesophase is a distinct phase in-between ordered and isotropic states leading to structural anisotropy. First, nematic phases are characterized by molecules that have no positional order but they are oriented in the same direction. Secondly, smectic phases also present the general orientation of the nematic phases, but in addition they align themselves in layers. Finally, cholesteric phases are defined as stacks of 2D nematic-like layers twisted from each other with respect to those above and below. Thus, along four twist distances D_t , two 2D nematic-like layers present the same orientation. Therefore, mesophase depicted in electrospun fibers of PLA might display one of those three anisotropic phases.

I.6.3 Polylactide

PLA is a semi-crystalline polymer leading to crystallization and vitrification. In addition, PLA can display crystalline and non-crystalline structures subjected to structural anisotropy. That is why, this work focuses on PLA. It only lies on the possibility of the processes (flow induced crystallization and electrospinning) to design a polymer where crystalline and non-crystalline phase can be achieved with regard to structural anisotropy prior to crystallization and vitrification. Therefore, the molecular dynamics of the amorphous phase in such anisotropic complex systems can be achieved.

REFERENCES

- [1] C. A. Angell, *Science* **267**, 1924 (1995).
- [2] H. Dislich, *Angew. Chem. Int. Ed. Engl.* **10**, 363 (1971).
- [3] B. A. Shakhmatkin, N. M. Vedishcheva, M. M. Shultz, and A. C. Wright, *J. Non-Cryst. Solids* **177**, 249 (1994).
- [4] M. Tatsumisago, B. L. Halfpap, J. L. Green, S. M. Lindsay, and C. A. Angell, *Phys. Rev. Lett.* **64**, 1549 (1990).
- [5] K. Chebli, J. M. Saiter, J. Grenet, A. Hamou, and G. Saffarini, *Phys. B Condens. Matter* **304**, 228 (2001).
- [6] A. Kozdras, R. Golovchak, O. Shpotyuk, S. Szymura, A. Saiter, and J.-M. Saiter, *J. Mater. Res.* **26**, 2420 (2011).
- [7] J. D. Mackenzie, *J. Chem. Phys.* **32**, 1150 (1960).
- [8] J. D. Mackenzie, W. K. Murphy, *J. Chem. Phys.* **33**, 366 (1960).
- [9] J. S. Wilkes, *Green Chem.* **4**, 73 (2002).
- [10] W. Xu, E. I. Cooper, and C. A. Angell, *J. Phys. Chem. B* **107**, 6170 (2003).
- [11] S. E. B. Petrie, *J. Polym. Sci. Part -2 Polym. Phys.* **10**, 1255 (1972).
- [12] S. F. Swallen, K. L. Kearns, M. K. Mapes, Y. S. Kim, R. J. McMahon, M. D. Ediger, T. Wu, L. Yu, and S. Satija, *Science* **315**, 353 (2007).
- [13] B. Schammé, M. Mignot, N. Couvrat, V. Tognetti, L. Joubert, V. Dupray, L. Delbreilh, E. Dargent, and G. Coquerel, *J. Phys. Chem. B* **120**, 7579 (2016).
- [14] A. Saiter, C. Devallencourt, J. M. Saiter, and J. Grenet, *Eur. Polym. J.* **37**, 1083 (2001).
- [15] A. Schönhals, H. Goering, C. Schick, B. Frick, and R. Zorn, *Colloid Polym. Sci.* **282**, 882 (2004).
- [16] R. D. Priestley, C. J. Ellison, L. J. Broadbelt, and J. M. Torkelson, *Science* **309**, 456 (2005).
- [17] Á. Molnár, G. V. Smith, and M. Bartók, in *Adv. Catal.*, edited by H. P. and P. B. W. D.D. Eley (Academic Press, 1989), pp. 329–383.
- [18] M. F. Ashby and A. L. Greer, *Scr. Mater.* **54**, 321 (2006).
- [19] A. L. Greer and E. Ma, *MRS Bull.* **32**, 611 (2007).
- [20] U. Köster, U. Schünemann, M. Blank-Bewersdorff, S. Brauer, M. Sutton, and G. B. Stephenson, *Mater. Sci. Eng. A* **133**, 611 (1991).
- [21] P. G. Debenedetti, T. M. Truskett, C. P. Lewis, and F. H. Stillinger, in edited by B.-A. in *C. Engineering* (Academic Press, 2001), pp. 21–79.
- [22] A. J. Kovacs, in *Fortschritte Hochpolym.-Forsch.* (Springer Berlin Heidelberg, 1964), pp. 394–507.
- [23] L. C. E. Struik, *Polym. Eng. Sci.* **17**, 165 (1977).
- [24] W. Kauzmann, *Chem. Rev.* **43**, 219 (1948).
- [25] H. B. Callen, *Thermodynamics and an introduction to thermo-statistics*, Wiley, 1985.
- [26] S. Weyer, H. Huth, and C. Schick, *Polymer* **46**, 12240 (2005).
- [27] A. Dhotel, B. Rijal, L. Delbreilh, E. Dargent, and A. Saiter, *J. Therm. Anal. Calorim.* **121**, 453 (2015).
- [28] S. Gao and S. L. Simon, *Thermochim. Acta* **603**, 123 (2015).
- [29] S.H. Glarum, *J. Chem. Phys.* **33**, 639 (1960).
- [30] M. H. Cohen, D. Turnbull, *J. Chem. Phys.* **31**, 1164 (1959).
- [31] D. Turnbull, M. H. Cohen, *J. Chem. Phys.* **34**, 120 (1961).
- [32] J. H. Gibbs, E. A. DiMarzio, *J. Chem. Phys.* **28**, 373 (1958).
- [33] G. Adam, J. H. Gibbs, *J. Chem. Phys.* **43**, 139 (1965).

- [34] F. H. Stillinger and T. A. Weber, *Phys. Rev. A* **28**, 2408 (1983).
- [35] U. Bengtzelius, W. Gotze, and A. Sjolander, *J. Phys. C Solid State Phys.* **17**, 5915 (1984).
- [36] E. Leutheusser, *Phys. Rev. A* **29**, 2765 (1984).
- [37] Y. Singh, J. P. Stoessel, and P. G. Wolynes, *Phys. Rev. Lett.* **54**, 1059 (1985).
- [38] T. R. Kirkpatrick and P. G. Wolynes, *Phys. Rev. A* **35**, 3072 (1987).
- [39] R. G. Palmer, D. L. Stein, E. Abrahams, and P. W. Anderson, *Phys. Rev. Lett.* **53**, 958 (1984).
- [40] G. H. Fredrickson and H. C. Andersen, *Phys. Rev. Lett.* **53**, 1244 (1984).
- [41] D. R. Nelson and M. Widom, *Nucl. Phys. B* **240**, 113 (1984).
- [42] S. Sachdev and D. R. Nelson, *Phys. Rev. B* **32**, 1480 (1985).
- [43] M. D. Ediger, C. A. Angell, and S. R. Nagel, *J. Phys. Chem.* **100**, 13200 (1996).
- [44] K. L. Ngai, *J. Non-Cryst. Solids* **275**, 7 (2000).
- [45] A. Cavagna, *Phys. Rep.* **476**, 51 (2009).
- [46] L. Berthier and G. Biroli, in *Encycl. Complex. Syst. Sci.*, edited by R. A. M. Ph. D (Springer New York, 2009), pp. 4209–4240.
- [47] WE Roseveare, RE Powell, H Eyring, *J. Appl. Phys.* **12**, 669 (1941).
- [48] A. K. Doolittle, *J. Appl. Phys.* **22**, 1471 (1951).
- [49] J. D. Mackenzie, *Modern Aspects of the Vitreous State*. (Butterworths, London, 1960).
- [50] M. Goldstein, *J. Chem. Phys.* **64**, 4767 (1976).
- [51] J. Rault, *J. Non-Cryst. Solids* **271**, 177 (2000).
- [52] H. W. Starkweather, *Macromolecules* **14**, 1277 (1981).
- [53] G. P. Johari, *J. Non-Cryst. Solids* **307–310**, 317 (2002).
- [54] W. Gotze and L. Sjogren, *Rep. Prog. Phys.* **55**, 241 (1992).
- [55] G. S. Fulcher, *J. Am. Ceram. Soc.* **8**, 339 (1925).
- [56] G. Tammann and W. Hesse, *Z. Für Anorg. Allg. Chem.* **156**, 245 (1926).
- [57] C. A. Angell, *J. Non-Cryst. Solids* **73**, 1 (1985).
- [58] C. A. Angell, *J. Non-Cryst. Solids* **131**, 13 (1991).
- [59] E. Hempel, G. Hempel, A. Hensel, C. Schick, and E. Donth, *J. Phys. Chem. B* **104**, 2460 (2000).
- [60] L. Berthier, G. Biroli, J.-P. Bouchaud, L. Cipelletti, D. E. Masri, D. L'Hôte, F. Ladieu, and M. Pierno, *Science* **310**, 1797 (2005).
- [61] L. Hong, P.D. Gujrati, V.N. Novikov and A.P. Sokoloc, *J. Chem. Phys.* **131**, 194511 (2009).
- [62] M. D. Ediger, P. Harrowell, *J. Chem. Phys.* **137**, 080901 (2012).
- [63] E. Donth, *J. Non-Cryst. Solids* **53**, 325 (1982).
- [64] E. Donth, *Acta Polym.* **50**, 240 (1999).
- [65] A. Saiter, J.-M. Saiter, R. Golovchak, M. Shpotyuk, and O. Shpotyuk, *J. Phys. Condens. Matter* **21**, 075105 (2009).
- [66] M. Nakanishi and R. Nozaki, *Phys. Rev. E* **84**, 011503 (2011).
- [67] S. Pawlus, A. Grzybowski, M. Paluch, and P. Włodarczyk, *Phys. Rev. E* **85**, 052501 (2012).
- [68] E. Bouthegourd, A. Esposito, D. Lourdin, A. Saiter, and J. M. Saiter, *Phys. B Condens. Matter* **425**, 83 (2013).
- [69] A. Saiter, N. Delpouve, E. Dargent, and J. M. Saiter, *Eur. Polym. J.* **43**, 4675 (2007).
- [70] K. Arabeche, L. Delbreilh, R. Adhikari, G. H. Michler, A. Hiltner, E. Baer, and J.-M. Saiter, *Polymer* **53**, 1355 (2012).
- [71] T. A. Tran, S. Saïd, and Y. Grohens, *Macromolecules* **38**, 3867 (2005).
- [72] G. P. Kar, P. Xavier, and S. Bose, *Phys. Chem. Chem. Phys.* **16**, 17811 (2014).

- [73] L. Dobircau, N. Delpouve, R. Herbinet, S. Domenek, L. Le Pluart, L. Delbreilh, V. Ducruet, and E. Dargent, *Polym. Eng. Sci.* **55**, 858 (2015).
- [74] N. Delpouve, A. Saiter, and E. Dargent, *Eur. Polym. J.* **47**, 2414 (2011).
- [75] N. Delpouve, A. Saiter, J. F. Mano, and E. Dargent, *Polymer* **49**, 3130 (2008).
- [76] N. Delpouve, M. Arnoult, A. Saiter, E. Dargent, and J.-M. Saiter, *Polym. Eng. Sci.* **54**, 1144 (2014).
- [77] F. Hamonic, A. Saiter, and E. Dargent, *Mater. Lett.* **128**, 12 (2014).
- [78] N. Delpouve, L. Delbreilh, G. Stoclet, A. Saiter, and E. Dargent, *Macromolecules* **47**, 5186 (2014).
- [79] F. Hamonic, D. Prevosto, E. Dargent, and A. Saiter, *Polymer* **55**, 2882 (2014).
- [80] I. M. Hodge, *J. Non-Cryst. Solids* **169**, 211 (1994).
- [81] I. M. Hodge, in (1996), p. 195.
- [82] J. M. Hutchinson, *Prog. Polym. Sci.* **20**, 703 (1995).
- [83] Z. Evenson, T. Koschine, S. Wei, O. Gross, J. Bednarcik, I. Gallino, J. J. Kruzic, K. Rätzke, F. Faupel, and R. Busch, *Scr. Mater.* **103**, 14 (2015).
- [84] R. Golovchak, A. Kozdras, V. Balitska, and O. Shpotyuk, *J. Phys. Condens. Matter* **24**, 505106 (2012).
- [85] R. Golovchak, J. Oelgoetz, M. Vlcek, A. Esposito, A. Saiter, J.-M. Saiter, and H. Jain, *J. Chem. Phys.* **140**, 054505 (2014).
- [86] X. Peng and G. B. McKenna, *Phys. Rev. E* **93**, 042603 (2016).
- [87] C. Lixon Buquet, F. Hamonic, A. Saiter, E. Dargent, D. Langevin, and Q. T. Nguyen, *Thermochim. Acta* **509**, 18 (2010).
- [88] D. Cangialosi, A. Alegría, and J. Colmenero, *Prog. Polym. Sci.* **54–55**, 128 (2016).
- [89] Y. Huang and D. R. Paul, *Polymer* **45**, 8377 (2004).
- [90] Y. Huang and D. R. Paul, *Macromolecules* **39**, 1554 (2006).
- [91] K. D. Dorkenoo and P. H. Pfromm, *J. Polym. Sci. Part B Polym. Phys.* **37**, 2239 (1999).
- [92] D. Cangialosi, M. Wübbenhorst, J. Groenewold, E. Mendes, H. Schut, A. van Veen, and S. J. Picken, *Phys. Rev. B* **70**, 224213 (2004).
- [93] A. Q. Tool and C. G. Eicitlin, *J. Am. Ceram. Soc.* **14**, 276 (1931).
- [94] C. T. Moynihan, P. B. Macedo, C. J. Montrose, C. J. Montrose, P. K. Gupta, M. A. DeBolt, J. F. Dill, B. E. Dom, P. W. Drake, A. J. Easteal, P. B. Elterman, R. P. Moeller, H. Sasabe, and J. A. Wilder, *Ann. N. Y. Acad. Sci.* **279**, 15 (1976).
- [95] A. J. Kovacs, J. J. Aklonis, J. M. Hutchinson, and A. R. Ramos, *J. Polym. Sci. Polym. Phys. Ed.* **17**, 1097 (1979).
- [96] A. Q. Tool, *J. Am. Ceram. Soc.* **29**, 240 (1946).
- [97] G. Williams and D. C. Watts, *Trans. Faraday Soc.* **66**, 80 (1970).
- [98] M. Muthukumar, in *Interphases Mesophases Polym. Cryst. III*, edited by G. Allegra (Springer Berlin Heidelberg, 2005), pp. 241–274.
- [99] P. D. Olmsted, W. C. K. Poon, T. C. B. McLeish, N. J. Terrill, and A. J. Ryan, *Phys. Rev. Lett.* **81**, 373 (1998).
- [100] G. Strobl, *Prog. Polym. Sci.* **31**, 398 (2006).
- [101] A. Toda, R. Androsch, and C. Schick, *Polymer* **91**, 239 (2016).
- [102] X. F. Lu and J. N. Hay, *Polymer* **42**, 9423 (2001).
- [103] H. Li and M. A. Huneault, *Polymer* **48**, 6855 (2007).
- [104] H. Chen, M. Pyda, and P. Cebe, *Thermochim. Acta* **492**, 61 (2009).
- [105] H. Bai, C. Huang, H. Xiu, Q. Zhang, and Q. Fu, *Polymer* **55**, 6924 (2014).

- [106] B. O. Reid, M. Vadlamudi, A. Mamun, H. Janani, H. Gao, W. Hu, and R. G. Alamo, *Macromolecules* **46**, 6485 (2013).
- [107] D. Cavallo, L. Gardella, G. Portale, A. J. Müller, and G. C. Alfonso, *Polymer* **54**, 4637 (2013).
- [108] D. Cavallo, L. Gardella, G. Portale, A. J. Müller, and G. C. Alfonso, *Macromolecules* **47**, 870 (2014).
- [109] Z. Wang, Z. Ma, and L. Li, *Macromolecules* **49**, 1505 (2016).
- [110] S. A. Jabarin, *Polym. Eng. Sci.* **32**, 1341 (1992).
- [111] B. Wunderlich, *Prog. Polym. Sci.* **28**, 383 (2003).
- [112] M. L. Di Lorenzo and M. C. Righetti, *Polymer* **49**, 1323 (2008).
- [113] M. C. Righetti and E. Tombari, *Thermochim. Acta* **522**, 118 (2011).
- [114] T. L. Nguyen, F. Bédoui, P.-E. Mazeran, and M. Guigon, *Polym. Eng. Sci.* **55**, 397 (2015).
- [115] M. Kattan, E. Dargent, and J. Grenet, *Polymer* **43**, 1399 (2002).
- [116] J. Lin, S. Shenogin, and S. Nazarenko, *Polymer* **43**, 4733 (2002).
- [117] I. Kolesov and R. Androsch, *Polymer* **53**, 4770 (2012).
- [118] R. Androsch and B. Wunderlich, *Polymer* **46**, 12556 (2005).
- [119] A. Esposito, N. Delpouve, V. Causin, A. Dhotel, L. Delbreilh, and E. Dargent, *Macromolecules* **49**, 4850 (2016).
- [120] M. C. Righetti, D. Prevosto, and E. Tombari, *Macromol. Chem. Phys.* **217**, 2013 (2016).
- [121] Q. Ma, G. Georgiev, and P. Cebe, *Polymer* **52**, 4562 (2011).
- [122] N. M. Alves, J. F. Mano, E. Balaguer, J. M. Meseguer Dueñas, and J. L. Gómez Ribelles, *Polymer* **43**, 4111 (2002).
- [123] Y. Wang and J. F. Mano, *J. Appl. Polym. Sci.* **100**, 2628 (2006).
- [124] Y. Wang, J. L. Gómez Ribelles, M. Salmerón Sánchez, and J. F. Mano, *Macromolecules* **38**, 4712 (2005).
- [125] C. Zhang, Y. Guo, and R. D. Priestley, *ACS Macro Lett.* **3**, 501 (2014).
- [126] C. V. Grigoras and A. G. Grigoras, *J. Therm. Anal. Calorim.* **103**, 661 (2011).
- [127] A. Saiter, D. Prevosto, E. Passaglia, H. Couderc, L. Delbreilh, and J. M. Saiter, *Phys. Rev. E* **88**, 042605 (2013).
- [128] A. Saiter, N. Delpouve, E. Dargent, W. Oberhauser, L. Conzatti, F. Cicogna, and E. Passaglia, *Eur. Polym. J.* **78**, 274 (2016).
- [129] T. Sasaki, T. Uchida, and K. Sakurai, *J. Polym. Sci. Part B Polym. Phys.* **44**, 1958 (2006).
- [130] N. Delpouve, C. Lixon, A. Saiter, E. Dargent, and J. Grenet, *J. Therm. Anal. Calorim.* **97**, 541 (2009).
- [131] C. Lixon, N. Delpouve, A. Saiter, E. Dargent, and Y. Grohens, *Eur. Polym. J.* **44**, 3377 (2008).
- [132] F. Azzurri and G. C. Alfonso, *Macromolecules* **38**, 1723 (2005).
- [133] R. H. Somani, L. Yang, L. Zhu, and B. S. Hsiao, *Polymer* **46**, 8587 (2005).
- [134] F. Azzurri and G. C. Alfonso, *Macromolecules* **41**, 1377 (2008).
- [135] Y. Hayashi, G. Matsuba, Y. Zhao, K. Nishida, and T. Kanaya, *Polymer* **50**, 2095 (2009).
- [136] F. Su, W. Zhou, X. Li, Y. Ji, K. Cui, Z. Qi, and L. Li, *Macromolecules* **47**, 4408 (2014).
- [137] F. G. Hamad, R. H. Colby, and S. T. Milner, *Macromolecules* **48**, 7286 (2015).
- [138] L. Balzano, Z. Ma, D. Cavallo, T. B. van Erp, L. Fernandez-Ballester, and G. W. M. Peters, *Macromolecules* **49**, 3799 (2016).
- [139] J. Fan, Q. Zhang, D. Hu, Q. Ren, and J. Feng, *Phys. Chem. Chem. Phys.* **18**, 8926 (2016).
- [140] B. Monasse, *J. Mater. Sci.* **27**, 6047 (1992).
- [141] C. Duplay, B. Monasse, J.-M. Haudin, and J.-L. Costa, *Polym. Int.* **48**, 320 (1999).

- [142] Li and W. H. de Jeu, *Macromolecules* **36**, 4862 (2003).
- [143] J. Ju, Z. Wang, F. Su, Y. Ji, H. Yang, J. Chang, S. Ali, X. Li, and L. Li, *Macromol. Rapid Commun.* **37**, 1441 (2016).
- [144] P. C. Roozmond, T. B. van Erp, and G. W. M. Peters, *Polymer* **89**, 69 (2016).
- [145] F. G. Hamad, R. H. Colby, and S. T. Milner, *Macromolecules* **49**, 5561 (2016).
- [146] M. Fujiyama, T. Wakino, and Y. Kawasaki, *J. Appl. Polym. Sci.* **35**, 29 (1988).
- [147] M. R. Kantz, H. D. Newman, and F. H. Stigale, *J. Appl. Polym. Sci.* **16**, 1249 (1972).
- [148] S. Liedauer, G. Eder, and H. Janeschitz-Kriegl, *Int. Polym. Process.* **10**, 243 (1995).
- [149] P. G. Andersen and S. H. Carr, *Polym. Eng. Sci.* **18**, 215 (1978).
- [150] S. Yamazaki, M. Itoh, T. Oka, and K. Kimura, *Eur. Polym. J.* **46**, 58 (2010).
- [151] S. Huang, H. Li, S. Jiang, X. Chen, and L. An, *Polymer* **52**, 3478 (2011).
- [152] H. Tang, J.-B. Chen, Y. Wang, J.-Z. Xu, B. S. Hsiao, G.-J. Zhong, and Z.-M. Li, *Biomacromolecules* **13**, 3858 (2012).
- [153] H. Xu, L. Xie, and M. Hakkarainen, *ACS Sustain. Chem. Eng.* **3**, 1443 (2015).
- [154] H. Xu, G.-J. Zhong, Q. Fu, J. Lei, W. Jiang, B. S. Hsiao, and Z.-M. Li, *ACS Appl. Mater. Interfaces* **4**, 6774 (2012).
- [155] Y. Zhong, H. Fang, Y. Zhang, Z. Wang, J. Yang, and Z. Wang, *ACS Sustain. Chem. Eng.* **1**, 663 (2013).
- [156] J. Bojda and E. Piorkowska, *Polym. Test.* **50**, 172 (2016).
- [157] N. Najafi, M.-C. Heuzey, P. Carreau, and D. Theriault, *Rheol. Acta* **54**, 831 (2015).
- [158] X.-L. Xie, Z.-H. Sang, J.-Z. Xu, G.-J. Zhong, Z.-M. Li, X. Ji, R. Wang, and L. Xu, *Polymer* **110**, 196 (2017).
- [159] J. Zhang, Y. Duan, H. Sato, H. Tsuji, I. Noda, S. Yan, and Y. Ozaki, *Macromolecules* **38**, 8012 (2005).
- [160] K. Wasanasuk and K. Tashiro, *Polymer* **52**, 6097 (2011).
- [161] T.-Y. Cho and G. Strobl, *Polymer* **47**, 1036 (2006).
- [162] M. Cocca, M. L. D. Lorenzo, M. Malinconico, and V. Frezza, *Eur. Polym. J.* **47**, 1073 (2011).
- [163] H. Bai, C. Huang, H. Xiu, Q. Zhang, H. Deng, K. Wang, F. Chen, and Q. Fu, *Biomacromolecules* **15**, 1507 (2014).
- [164] H. Xu, L. Xie, X. Jiang, X.-J. Li, Y. Li, Z.-J. Zhang, G.-J. Zhong, and Z.-M. Li, *J. Phys. Chem. B* **118**, 812 (2014).
- [165] H. Xu, L. Xie, Y.-H. Chen, H.-D. Huang, J.-Z. Xu, G.-J. Zhong, B. S. Hsiao, and Z.-M. Li, *ACS Sustain. Chem. Eng.* **1**, 1619 (2013).
- [166] H. Xu, L. Xie, X. Jiang, M. Hakkarainen, J.-B. Chen, G.-J. Zhong, and Z.-M. Li, *Biomacromolecules* **15**, 1676 (2014).
- [167] H. Bai, W. Zhang, H. Deng, Q. Zhang, and Q. Fu, *Macromolecules* **44**, 1233 (2011).
- [168] Y. Fan, J. Zhu, S. Yan, X. Chen, and J. Yin, *Polymer* **67**, 63 (2015).
- [169] L. Xie, H. Xu, B. Niu, X. Ji, J. Chen, Z.-M. Li, B. S. Hsiao, and G.-J. Zhong, *Biomacromolecules* **15**, 4054 (2014).
- [170] G. M. Bayley and P. E. Mallon, *Polymer* **53**, 5523 (2012).
- [171] N. Bhardwaj and S. C. Kundu, *Biotechnol. Adv.* **28**, 325 (2010).
- [172] R. Neppalli, V. Causin, E. M. Benetti, S. S. Ray, A. Esposito, S. Wanjale, M. Birajdar, J.-M. Saiter, and A. Marigo, *Eur. Polym. J.* **50**, 78 (2014).
- [173] G. Liao, S. Jiang, X. Xu, and Y. Ke, *Mater. Lett.* **82**, 159 (2012).
- [174] I. Keun Kwon, S. Kidoaki, and T. Matsuda, *Biomaterials* **26**, 3929 (2005).
- [175] K. Yoon, K. Kim, X. Wang, D. Fang, B. S. Hsiao, and B. Chu, *Polymer* **47**, 2434 (2006).

- [176] W. Serrano, A. Meléndez, I. Ramos, and N. J. Pinto, *Polymer* **55**, 5727 (2014).
- [177] X. Zong, K. Kim, D. Fang, S. Ran, B. S. Hsiao, and B. Chu, *Polymer* **43**, 4403 (2002).
- [178] P. Cebe, B. P. Partlow, D. L. Kaplan, A. Wurm, E. Zhuravlev, and C. Schick, *Thermochim. Acta* **615**, 8 (2015).
- [179] E. B. Priestley, in *Introd. Liq. Cryst.*, edited by E. B. Priestley, P. J. Wojtowicz, and P. Sheng (Springer US, 1975), pp. 1–13.

CHAPTER II

Experimental section

CONTENTS

II.1 Materials	42
II.2 Characterization methods	46
II.3 From theories, models and concepts: experimental methodologies	57
References.....	61

This second chapter presents the materials used in order to investigate the influence of the structural anisotropy on the molecular dynamics of the amorphous phase. Presentations of the experimental set-up regarding the electrospinning and the flow induced crystallization are done. Finally, the characterization methods used in this work are briefly described.

II.1 Materials

In this work, influence of the structural anisotropy or molecular orientation on the molecular dynamics of amorphous phase have been investigated through poly(lactide) (PLA), as well as plasticized PLA. To do so, two original sample preparations have been used as presented in the chapter I: flow induced crystallization and electrospinning.

II.1.1 Poly(lactide) (PLA) and acetyl tributyl citrate (ATBC)

Semi-crystalline PLA pellets (grade 4042D) were provided by Natureworks. The content of L-lactide and D-lactide were about 96% and 4% respectively. The number-average and weight-average molecular weights were $M_n = 116$ kDa and $M_w = 188$ kDa respectively, as measured by Gel Permeation Chromatography.

Acetyl tributyl citrate (ATBC, CAS Number 77-90-7) plasticizer was purchased from sigma Aldrich (France). PLA and ATBC were dried at 80 °C under vacuum for 12 h. Blending to PLA was performed with an internal mixer (Haake Rhecord 9000) at 160 °C and 60 rpm for 15 min. After a subsequent drying step (4 h at 80 °C under vacuum) bulk samples were obtained. The measure of density leads to a constant value equal to 1.25 independent of the plasticizer content.

II.1.2 Flow induced crystallization

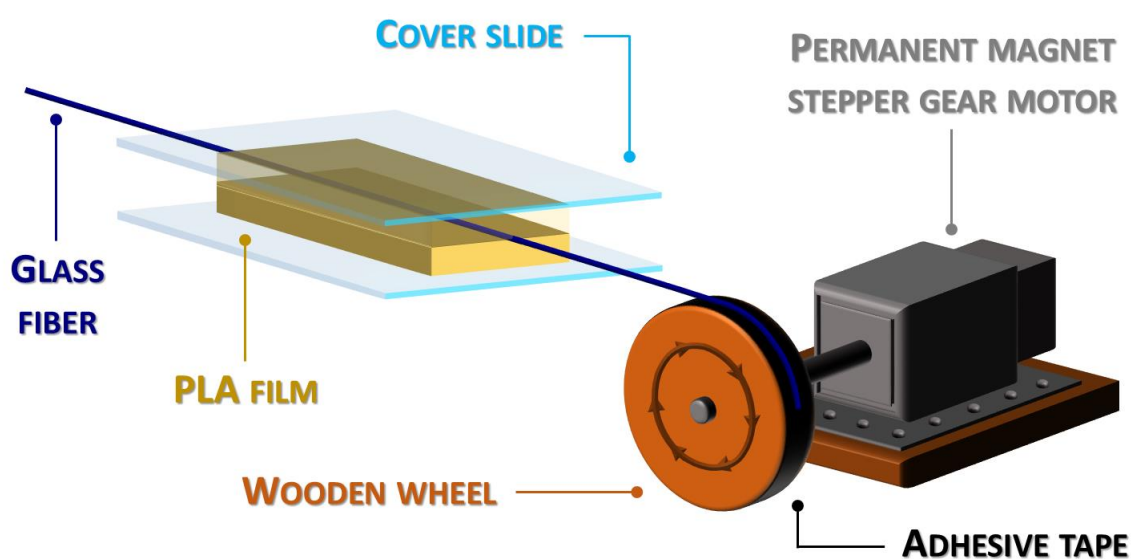


Figure II.1.1: Schematic representation of the home made fiber pulling device.

The PLA pellets were dried overnight in an oven at 60 °C in order to avoid any degradation prior to use. The dried pellets were then thermo-molded at a pressure of 1 bar and a temperature of 180 °C between two hot plates during 5 min by using a manual hydraulic press ATLAS™ SPECAC. The temperature was selected below the equilibrium melting temperature T_m^0 (ranging from 199 °C to 207 °C [1]) and above the melting temperature T_m (ranging from 160 to 170 °C [2][3][4]) of PLA. The sample was then quickly quenched in cold water and finally dried. Thickness of the obtained films were ranging from 200 to 300 μm thick. A single glass fiber with a diameter of $17 \pm 1 \mu\text{m}$ was sandwiched between two PLA films. The whole system was then placed between two microscope cover-slides. A homemade fiber pulling device, made of a permanent magnet stepper gear motor TGM24 series from Anaheim Automation and a wooden wheel with an adhesive tape, was used to pull the fiber through the molten polymer at a constant linear velocity of $10 \text{ mm}\cdot\text{s}^{-1}$ during 1 s. Illustration of the home made system is depicted in Figure II.1.1.

The shear stress at the interface fiber/molten polymer was estimated to be close to 1000 s^{-1} , according to Monasse et al. [5]. The different steps of the fiber pulling procedure are described as follow. First, the as-prepared sandwich was transferred into a Mettler FP 82 hot stage to control thermal conditions. In the hot stage, an isotherm at $T_e = 180 \text{ °C}$ during $t_e = 5 \text{ min}$ was applied to erase the thermal and mechanical histories of the sandwich preparation. Then, the system was cooled down to a pull-out temperature T_{po} and held during $t_e = 5 \text{ min}$ before to pull-out the fiber from the molten polymer. From this point two protocols have to be distinguished: one for the precursor's relaxation investigations and another one for the amorphous phase investigations.

- In order to investigate the relaxation of the shear induced precursors, six T_{po} were used: 157.5 °C, 160 °C, 162.5 °C, 165 °C, 167.5 °C and 170 °C. After the shear stress was applied, the sample was held during a relaxation time ranging from few seconds to few hours. Then, the sample was directly quenched to the crystallization temperature $T_c = 130 \text{ °C}$ in order to observe spherulitic or flow induced crystallization, namely the indirect relaxation of the precursors. Figure II.1.2 depicts the applied thermo-mechanical history as a function of time for the precursor's relaxation investigations.

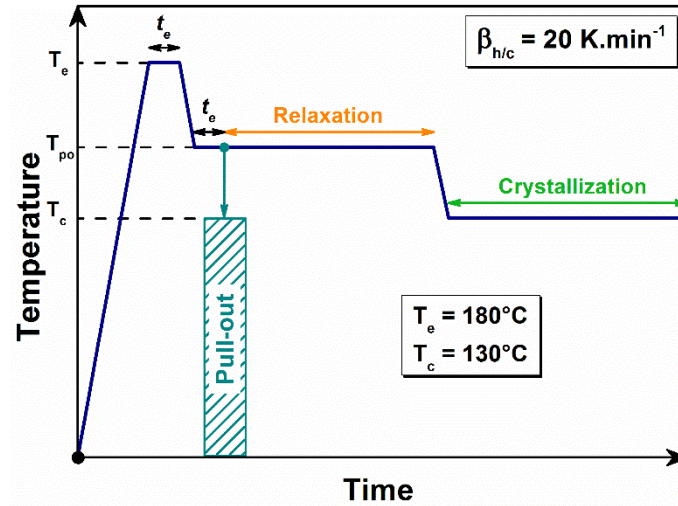


Figure II.1.2: Diagram of the applied thermo-mechanical history for the precursor's relaxation investigations vs. time.

- Prior to quiescent crystallization, shear precursors were induced at $T_{po} = 150^\circ\text{C}$. After the shear stress was applied, the sample was directly quenched to the crystallization temperature $T_c = 130^\circ\text{C}$ in order to avoid any relaxation of the crystal nucleation precursors induced by the shear. The isothermal crystallization took place during 90 min. Figure II.1.3 depicts the applied thermo-mechanical history as a function of time for the amorphous phase investigations in flow-induced crystalline structures.

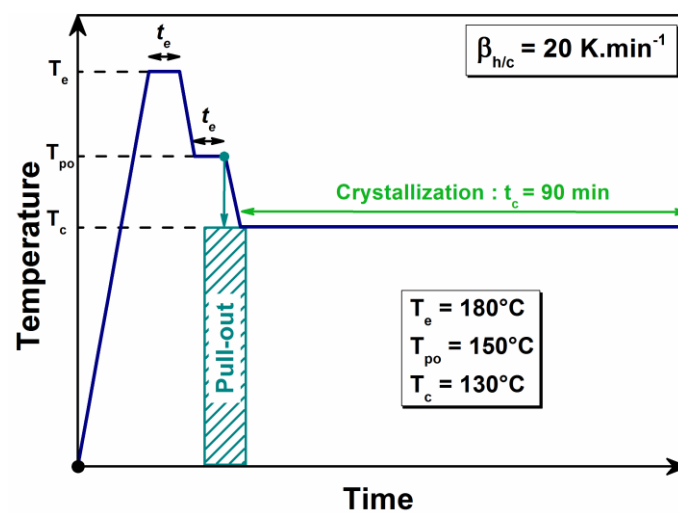


Figure II.1.3: Diagram of the applied thermo-mechanical history for the amorphous phase investigations vs. time.

II.1.3 Electrospinning

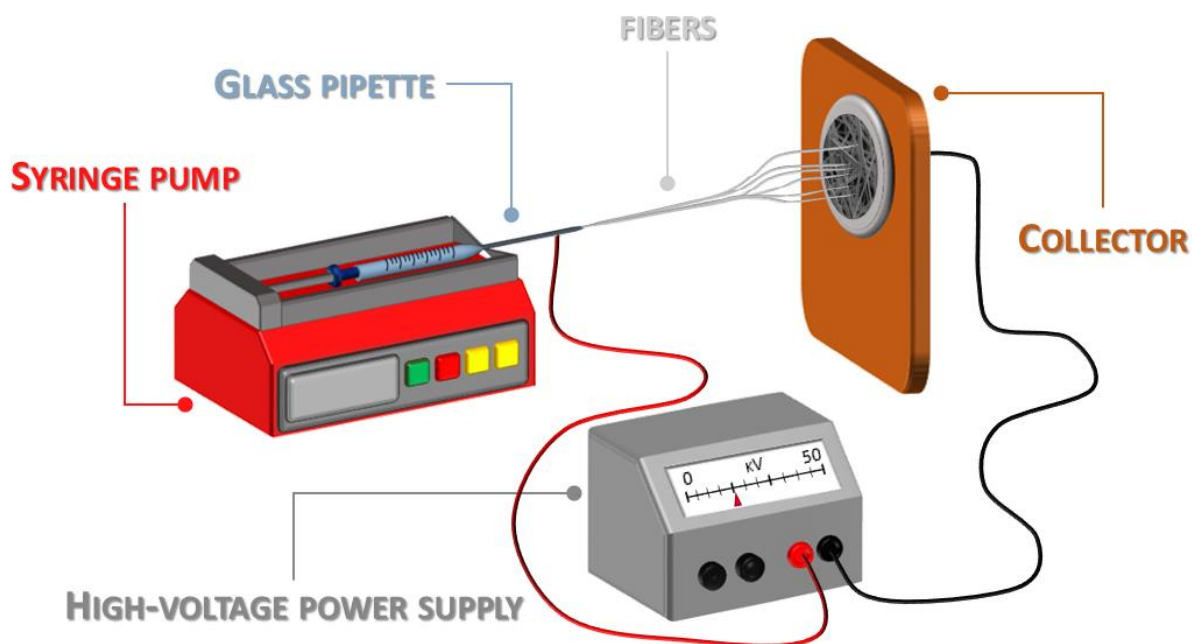


Figure II.1.4: Schematic representation of the home made electrospinning set-up.

The polymer solutions, PLA and plasticized PLA, were prepared in mix solvent of chloroform and acetone (chloroform:acetone = 2:1 in volume), both purchased from sigma Aldrich (South Africa). Plasticized and non-plasticized PLA were dissolved in the mix solvent and stirred using a magnetic stir bar at room temperature until homogenization of the solution. The required amounts of polymer were figured out to give a concentration solution of 8 wt% in PLA. Then, the polymer solution was placed in a horizontally glass pipette with a capillary around 1 mm diameter. At 5 cm from the needle, a petri-dish covered by an aluminum foil took place as a collector. The needle and the collector were connected to a high-voltage power supply which can generate a voltage up to 50 kV. The electric field applied was 1 kV.cm^{-1} . The flow rate was controlled by a pump at 0.04 mL.min^{-1} . Illustration of the home made electrospinning set-up is depicted in Figure II.1.4. The electrospinning process took place under controlled atmospheric conditions at $25 \pm 2 \text{ }^\circ\text{C}$ and $35 \pm 4\%$ relative humidity. The thickness of the final as-spun fibers mat was less than 1 mm.

II.2 Characterization methods

The complementary use of two kinds of experimental techniques were used in this work. First, a set of characterization methods related to the analysis of the structure and the morphology of the investigated materials were employed. These techniques were used to identify structural anisotropy or molecular orientation from the micro- to the nano-scale. Then, dynamic methods, especially thermal analyses, were used in order to understand the fundamental mechanism leading to short- and/or long-range mobility of molecules when subjected to confinement and/or structural anisotropy.

II.2.1 Structural and morphological analyses

II.2.1.1 Polarized optical microscopy (POM) with hot stage

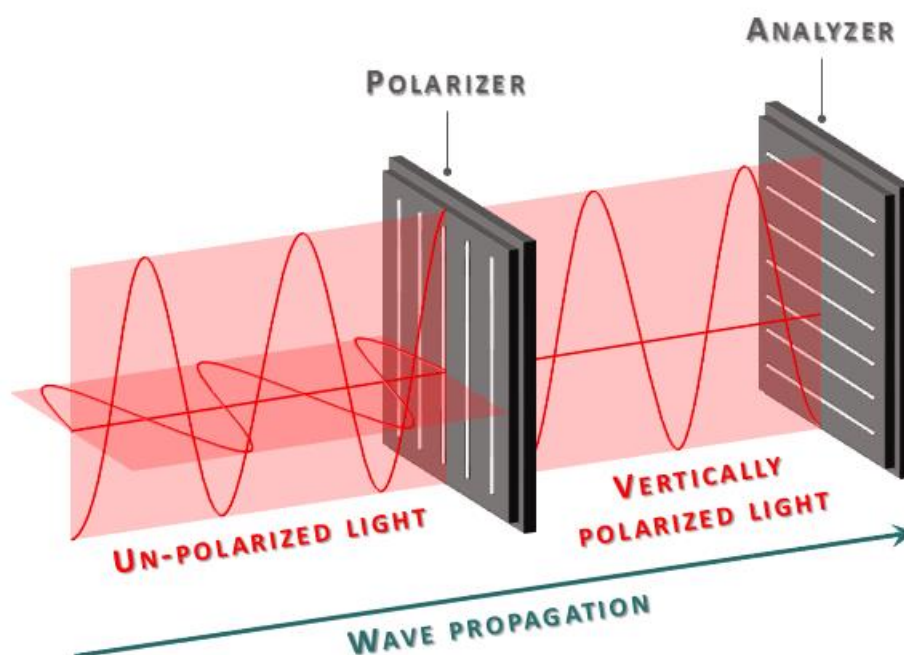


Figure II.2.1: Schematic representation of a light wave passing through crossed polarizers.

Polarized optical microscopy (POM) is a simple technique to observe anisotropic structures at the micro-scale. In addition to the conventional optical microscope which uses visible light and a system of lenses, POM involves polarized light. Thus, experimental setup is similar to a conventional optical microscope with two additional polarizing filters: a first one between the light source and the analyzed sample, named polarizer, and a second one between the sample and the eyepiece or camera, named analyzer. These filters are used to

restrict electro-magnetic field vectors constituting visible light to a single plane, as shown in Figure II.2.1. As a results, all electro-magnetic field vectors are vibrating in the same plane. The light is then polarized.

In a cross polarization setup, the analyzer is oriented perpendicularly to the first polarizer. This position aims to block remaining electro-magnetic field vectors. Consequently, when no sample is placed on the light field, the light polarized by the polarizer is blocked by the analyzer, resulting in no visible light in the eyepiece or the camera. However, when birefringent sample, such as anisotropic material, (whose refractive index depends on the polarization and propagation direction of light) is placed on the polarized light field, the restricted electro-magnetic field vectors coming through the sample are produced in many different perpendicular planes. Then, electro-magnetic field vectors that are parallel to the polarization direction of the analyzer can go through and be visualized in the eyepiece.

In this work, POM observations were performed by using a universal Nikon EPI-illuminator with Nikon M Plan x2.5 / x5 / x10 lenses connected with a digital sight camera system from Nikon Corporation, either in transmission or reflection mode. A Mettler FP82HT hot stage connected to a Mettler FP90 central processor was used as temperature controller during crystallization observations.

II.2.1.2 Scanning electron microscopy (SEM)

Scanning electron microscopy (SEM) is a kind of microscopy based on a finely focused beam of electrons to produce images of a sample placed in a vacuum chamber. Thanks to the particle-wave duality of electrons, the beam is accelerated and focused on a sample through anode, condenser and magnetic lenses, as presented in Figure II.2.2. The incident beam of electrons interacts with the sample surface. Thus, the sample area where the primary beam is focused leads to the ejection of other electrons including secondary electrons, back-scattered electrons or X-rays among others. Specific detectors are used according to their natures. The signals measured contain information about sample surface topography as well as sample composition.

In this work, two different electronic microscopes were used:

- A LEO1430VP-ZEISS scanning electron microscope (University of Stellenbosch) was used to observe morphology of electrospun fibers and measure their respective diameters, after being gold coated during 3 min.
- A Dual-BEAM LEO1530-ZEISS scanning electron microscope (GPM - University of Rouen Normandie) was used to obtain images of semi-crystalline structures after deposition of a 10 nm thick gold coating. Prior to gold coat, PLA semi-crystalline structures were first trimmed in the transversal direction by means of ultramicrotomy with an Ultracut UCT Leica-microsystem by using a dry-glass knife and etched by a water-methanol (1:2 by volume) solution containing 0.025 mol.L^{-1} of sodium hydroxide at room temperature during 24 h. Afterward, the etched sample was cleaned by using distilled water. Ultramicrotomy and electronic microscopy have been performed with Laurence Chevalier (GPM).

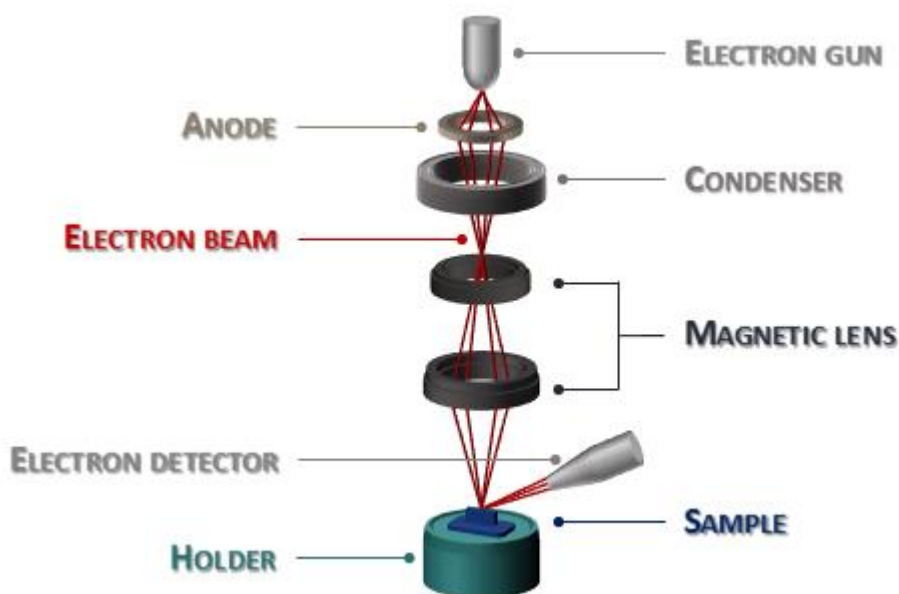


Figure II.2.2: Schematic representation of SEM analysis in a vacuum chamber.

II.2.1.3 Wide angle X-ray diffraction (WAXD)

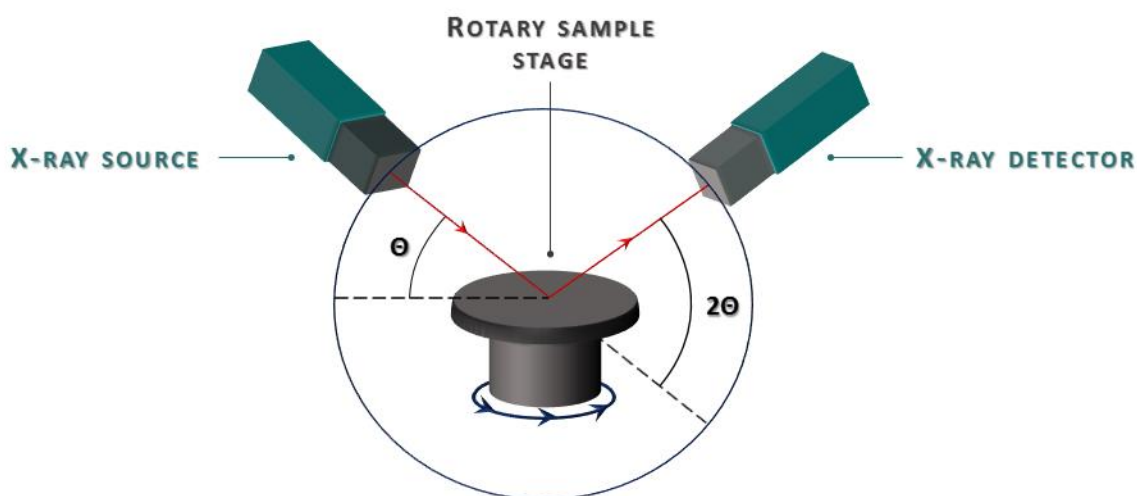


Figure II.2.3: Schematic representation of WAXD measurements with a Bragg-Brentano $\theta:2\theta$ geometry.

The diffraction of X-rays is a non-destructive analytical technique to determine the spatial organization of atoms or larger molecules in ordered structures. With regards to polymer science, such a technique allows to detect and quantify crystalline fractions in amorphous matrixes. As depicted in Figure II.2.3, the basic principle of WAXD is based on the bombarding of a sample with a X-ray beam and the measuring of intensity related to the diffracted rays as a function of the scattered angle 2θ . Regular or irregular arrangements of atoms or molecules lead X-rays to diffract or scatter, respectively, into many specific directions after elastic interactions with electronics clouds from the sample. As a consequence, high intensity diffraction peaks or low intensity halos are recorded, as presented in Figure II.2.4. In the case of diffraction peak, relation between angle of the recorded peaks and distance between crystalline layers can be done through the Bragg's law [6]:

$$n\lambda = 2d\sin(\theta) \quad (\text{II.2.1})$$

in which n is an integer called the order of diffraction, λ is the wavelength of incident X-ray beam, d is the spacing between diffracting planes in the crystalline lattice, and θ is the angle between the incident and the scattered rays.

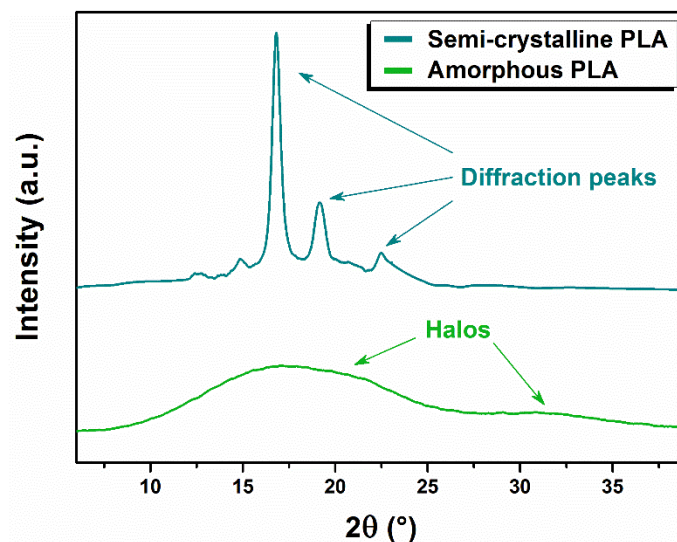


Figure II.2.4: WAXD patterns displaying diffraction peaks and halos as a function of 2θ for a semi-crystalline and a wholly amorphous PLA samples, respectively.

In this work, WAXD measurements were performed on a PANalytical X'Pert Pro diffractometer in Bragg-Brentano mode with X'Celerator detector (University of Stellenbosch). The generator was set up at 45 kV and 40 mA and the copper $\text{Cu K}\alpha$ radiation ($\lambda = 1.54 \text{ \AA}$) was selected. The system was equipped with a silicon-made sample holder on a spinner stage PW3064, and a goniometer PW3050/60 system. The silicon holder used is neutral (no diffraction peak) in order to avoid a baseline subtraction step. The distance from the sample to the detector was fixed at 14 cm. The measurements were run at room temperature from 5° to 45° at $0.04^\circ/\text{s}$ and with a rotational speed equal to one revolution per second.

II.2.2 Thermal analysis

II.2.2.1 Differential scanning calorimetry (DSC)

Differential scanning calorimetry (DSC) is a technique used to study thermal events, such as crystallizations, melting or oxidations, as well as evolution of materials, such as physical aging. During physical transitions, heat is either absorbed (endothermic) or released (exothermic). The basic principle is to quantify the difference in amount of heat required to increase the temperature of a sample and a reference. Thus, the apparatus determines the heat flow associated as a function of time and temperature through the measured temperature. Two kinds of calorimeter were used in this work, heat-flux and power-compensated calorimeters. With regard to DSC, the experiments were performed by using a heat-flux calorimeter DSC Q100 from Thermal Analysis Instruments.

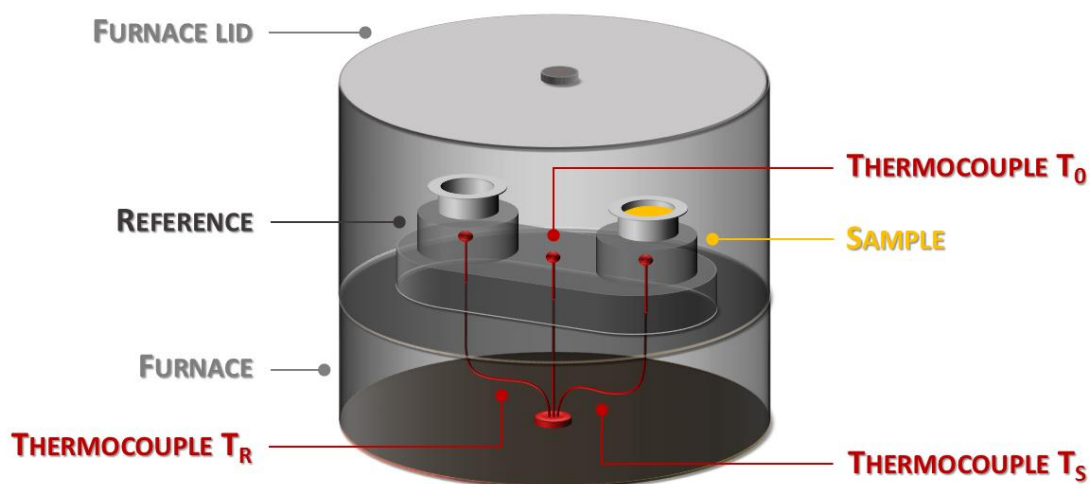


Figure II.2.5: Schematic representation of heat-flux DSC cells.

In standard DSC, the temperature ramp applied to the sample and the reference is linear:

$$T = T_i + \beta t \quad (II.2.2)$$

in which T is the temperature at the time t , T_i the initial temperature and β the scanning rate. The heat flow ϕ resulting in the heat transfer Q is expressed as follow:

$$\phi = \frac{dQ}{dt} = C \frac{dT}{dt} \quad (II.2.3)$$

where C is the heat capacity.

In heat-flux calorimeter, the sample and the reference are placed in a same furnace, as presented in Figure II.2.5. Then, a variation of temperature is applied to the entire furnace in order to transfer heat Q_S and Q_R onto the sample and the reference, respectively. Thus, exothermic or endothermic events of the sample engendered by the variations of temperature will lead to a temperature difference $\Delta T = T_S - T_R$ between the sample and the reference. The resulting heat flow can be simplified by a thermal equivalent of the Ohm's law:

$$\phi = Q_S - Q_R = \frac{\Delta T}{R} \quad (II.2.4)$$

in which R is the thermal resistance. The measurement principle of the heat-flux calorimeter DSC Q100 is based on the T_{zero}^{TM} technology. Such technology uses a more complex equations of the heat flow. Thermal resistances R_{SCP} and R_{RCP} , and heat capacities C_{SCP} and C_{RCP} of the sample and reference cell platforms, respectively, are taken into account in the heat flow expression. Thus, by measuring the temperatures T_S and T_R of the sample and the reference, respectively, as a function of a fixed temperature T_0 the measured heat flow is expressed as follow [7]:

$$\phi = -\frac{T_S - T_R}{R} + (T_0 - T_S) \left(\frac{1}{R_{SCP}} - \frac{1}{R_{RCP}} \right) + (C_{RCP} - C_{SCP}) \frac{dT_S}{dt} - C \frac{d\Delta T}{dt} \quad (II.2.5)$$

As a consequence, specific calibration procedures were used with the T_{zero}^{TM} technology. First, a constant heating rate experiment was performed without sample and pan, namely an empty furnace. A second constant heating rate experiment was performed with sapphire disks directly placed on the sample and reference platform. These experiments figure out the resistance and capacitance R_{RCP} , R_{SCP} , C_{RCP} and C_{SCP} of the cell platforms. Then, the calibration in temperature and energy were carried out using standard of indium, by matching the melting temperature ($T_m = 156.6 \text{ }^\circ\text{C}$) and enthalpy ($\Delta H_m = 28.6 \text{ J.g}^{-1}$) associated. A second standard, benzophenone ($T_m = 48.0 \text{ }^\circ\text{C}$), was used to calibrate the cell in a temperature range from $0 \text{ }^\circ\text{C}$ to $200 \text{ }^\circ\text{C}$. The calibration in temperature and energy have to be repeated if the scanning rate is changed. To ensure a good signal-to-noise ratio, masses of sample were ranged between 5 and 10 mg. Scanning rate was selected to promote the resolution of

investigated thermal events, namely 10 K.min⁻¹. All experiments were carried out under a nitrogen atmosphere.

II.2.2.2 Modulated temperature DSC (MT-DSC)

During standard DSC experiments, samples experience thermal reactions that change their physical and/or chemical properties during heating or cooling ramps. These reactions include glass transition, crystallization, melting, oxidation, as well as curing, evaporation and so on, as listed in the previous section. Those reactions may occur at the same time or in the same range of temperature. Thus, the respective heat flows are overlapped and cannot be distinguished from each other by standard DSC. According to Reading et al. [8], heat flow ϕ measured from standard DSC can be expressed as follow:

$$\phi = \frac{dQ}{dt} = C^* \beta + f(t,T) \quad (II.2.6)$$

where $f(t,T)$ represents the part of the heat flow related to the kinetic or non-reversing events called non-reversing heat flow ϕ_{NR} . The part related to the thermodynamic events, namely the reversing heat flow ϕ_R , is expressed by the product of the complex heat capacity and the scanning rate $C^* \beta$. Therefore, modulated temperature DSC (MT-DSC) is in line with standard DSC. Where linear temperature ramp is applied by standard DSC, Reading et al. [9] have proposed to super-impose a sinusoidal oscillation in order to dissociate the reversing and the non-reversing events by MT-DSC:

$$T = T_i + \beta t + A \sin(\omega t) \quad (II.2.7)$$

in which A is the modulation amplitude and ω the angular frequency of the temperature modulation with the period of oscillation $p = 2\pi/\omega$. Thus, the modulated heat flow ϕ is expressed as follow:

$$\phi = \frac{dQ}{dT} = C^* (\beta + A\omega \cos(\omega t)) \quad (II.2.8)$$

with C^* the complex heat capacity defined as:

$$C^* = \frac{A_{HF}}{A_{\beta}} = \frac{\omega A C^*}{\omega A} \quad (II.2.9)$$

where A_{β} and A_{HF} are the amplitudes of the heating rate modulation and of the heat flow modulation, respectively. The thermodynamic events are related to vibrational and translational motions of molecules. These motions are very fast and can easily follow any sample temperature modulations. On the contrary, the kinetic or non-reversing events cannot. They do not contribute to the modulated part of the heat flow. To sum up:

$$\phi_R = C^* \beta = \frac{A_{HF}}{A_{\beta}} \beta \quad (II.2.10)$$

$$\phi_{NR} = \frac{dQ}{dt} - C^* \beta \quad (II.2.11)$$

In addition, a phase lag φ exists between the calorimeter response function, namely the total heat flow, and the heating modulation. In this way, two apparent heat capacity components noted C' (the in-phase component related to ϕ_R) and C'' (the out-of-phase component related to ϕ_{NR}) can be calculated according to the following equations:

$$C' = |C^*| \cos(\varphi) \quad (II.2.12)$$

$$C'' = |C^*| \sin(\varphi) \quad (II.2.13)$$

The MT-DSC experiments were performed with a heat-flux calorimeter DSC Q100 from Thermal Analysis Instruments. The calibration of MT-DSC consists of DSC calibration (cf. previous paragraph) and an additional step to calibrate the heat capacity. This last step uses a sapphire as a standard because it does not undergo any transition in the temperature range scanned for polymer analysis. The heat capacity of sapphire as a function of temperature is stable and precisely known. This step of calibration has to be repeated if the amplitude, the scanning rate or the period of oscillation are changed. A calibration factor K_{C_p} is then calculated from the experimental and theoretical heat capacity values. This factor corrects the apparent heat capacity of the sample. This factor is averaged on the temperature range investigated:

$$K_{C_p}(T) = \frac{C_{P_{Sapphire, theoretical}}(T)}{C_{P_{Sapphire, experimental}}(T)} \quad (II.2.14)$$

In MT-DSC, different modes of temperature modulation exist [8]. As reported in Figure II.2.6, three modes exist: named heat-only, heat-iso and heat-cool. Heat-only is advised to

investigate the coupling of different thermal events such as glass transition and cold-crystallization or crystallization and melting. Heat-iso is advised to investigate melting. Heat-cool is advised to investigate the glass transition and the molecular mobility in this region.

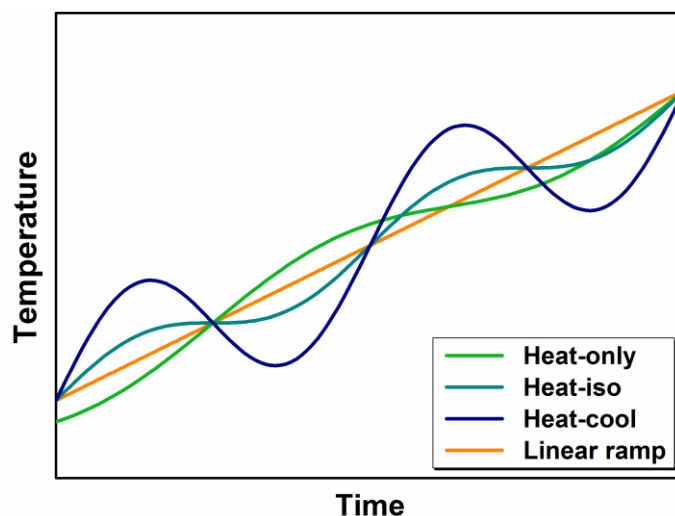


Figure II.2.6: Illustration of heating ramps in MT-DSC experiment with corresponding heat-only (green), heat-iso (cyan), heat-cool (blue) and linear ramp (orange) mode. The modulation amplitude, the period and the scanning rate are [0.318 K; 90 s; 2 K/min], [0.318 K; 60 s; 2 K/min], [1 K; 60 s; 2 K/min] for the three modes displayed, respectively.

In this work, heat-only mode was used to investigate the coupling between glass transition and cold crystallization in electrospun fibers. The experiments were performed with a modulation amplitude of 0.318 K, a period of 60 s and a scanning rate of 2 K.min⁻¹.

II.2.2.3 Fast scanning calorimetry (FSC)

As depicted in the previous section, the sample may experience concomitant thermal reactions during heating. Where temperature modulated ramp is applied by MT-DSC in order to dissociate the reversing and the non-reversing events, Schick and Mathot have proposed to use very high scanning rates in order to inhibit or delay thermal reactions, as well as observed very fast thermal reactions or crystallization processes by fast scanning calorimetry (FSC) [10]. Therefore, FSC is in line with MT-DSC. As for DSC, the basic principle of FSC is to quantify the difference in amount of heat required to increase the temperature of a sample and a reference. So far, FSC measurements are only done by a power-compensated calorimeter. The analyzed sample and the reference are placed in separated furnaces. A variation of temperature is then applied to both furnaces and heat is transferred to the sample and the reference. The difference in thermal power required to maintain the sample and the reference furnaces at the same temperature is finally measured. In this work, the experiments

were performed using a power compensation twin-type chip sensor, based on MEMS technology, fast scanning calorimeter Flash 1 DSC from Mettler Toledo. As presented in Figure II.2.7, the twin-type chip sensor based on MEMS technology is made of a sample and a reference sides. Both sides are independent furnaces. The MEMS chip sensor is mounted on a stable ceramic with electrical connections.

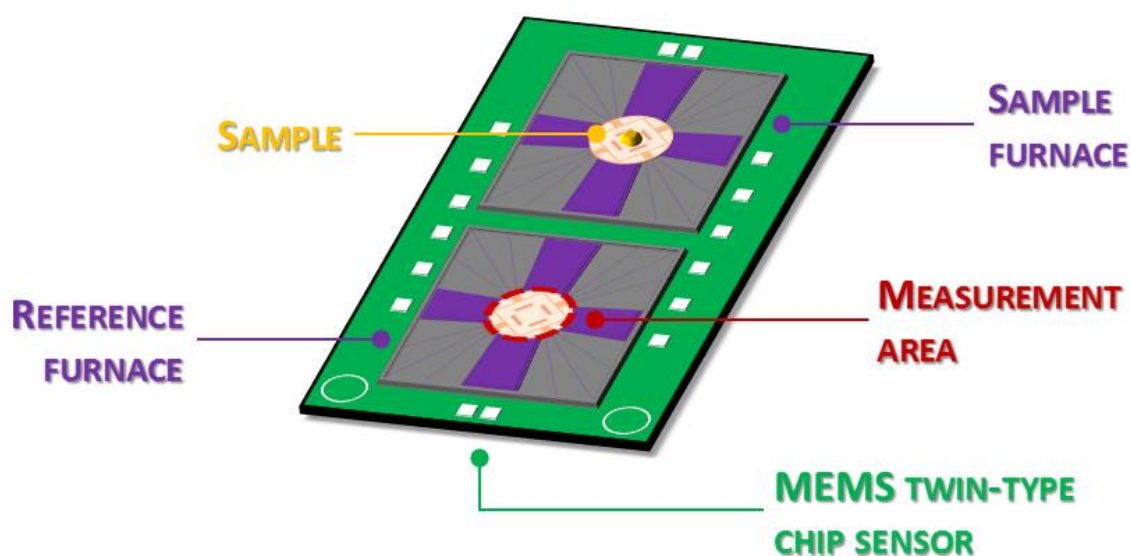


Figure II.2.7: Illustration of twin-type chip sensor based on MEMS technology.

Both, sample and reference, sides of the chip sensor are made of two thermal resistance heaters to apply the desired temperature program. The temperature resolution is determined by the time constant of the sensor which is about 1 millisecond, namely about thousand times less than standard DSC. The heat flow is measured through sixteen thermocouples, eight for each sides. They are arranged symmetrically in the form of a star around the measurement area on the sample and reference sides of the sensor. The measurement area of the chip is made of a silicon nitride and silicon dioxide coated with a thin layer of aluminum in order to provide homogeneous temperature distribution across the sensor. Samples are directly placed on the sensitive area of a MultiSTAR UFS 1 MEMS chip sensors. In this work, thin layer of silicone oil was used in order to improve the thermal contact between the sample and the chip. A Huber TC100 intra cooler was used to cool samples down to -90°C and operate high cooling rates. Samples were continuously flushed with a $20\text{ mL}\cdot\text{min}^{-1}$ nitrogen flow gas to avoid water condensation from the environment and to optimize the program temperature applied [11]. Sample mass was estimated from the step change in heat flow at the glass transition, by comparing the value of the heat capacity step ΔC_p from the one

obtained through FSC at $|\beta_{cl}| = \beta_h = 1500 \text{ K.s}^{-1}$ and the one obtained through standard DSC at $|\beta_{cl}| = \beta_h = 0.17 \text{ K.s}^{-1}$ equal to $0.51 \text{ J}/(\text{g.K})$ for a wholly amorphous PLA according to the literature [4][12]. Scanning rates were selected to promote the resolution of investigated thermal events ranging from 300 K.s^{-1} to 4000 K.s^{-1} .

The calibration of the Flash DSC 1 consists of conditioning and correction procedures. The conditioning procedure checks the proper behavior of the sensor. Potential memory effects from its production are erased by heating the sensor to the maximum temperature ($400 \text{ }^\circ\text{C}$). Then, the correction temperature is performed in order to correct the thermocouple signal with respect to the sensor support temperature. The correction is done by comparing the signal of the thermocouples with the temperature behavior of the heating resistances, which was determined during production.

In this work, two sample preparations were used with regards to the wholly amorphous and the flow induced crystalline or spherulitic PLA samples, respectively, prior to place on the measurement area of a MultiSTAR UFS 1 MEMS chip sensors:

- PLA were first thermo-molded in films of ten micron thick, at a pressure of 1 bar and a temperature of $180 \text{ }^\circ\text{C}$ between two hot plates by using a manual hydraulic press ATLASTM SPECAC. Then, films were quickly quenched in cold water. After a last drying step, the films were finally cut in small pieces with a surgical knife.
- Cross sections in the transversal direction of both, flow induced crystallization structure (cylindrical morphology) and spherulites, were obtained by means of ultramicrotomy. 500 nm thick-serial series were sectioned with an Ultracut UCT Leica-microsystem by using a dry-glass knife.

II.3 From theories, models and concepts: experimental methodologies

II.3.1 Estimation of the cooperative rearrangement sizes

As introduced in the previous chapter, the cooperativity volume $\xi_{T\alpha}^3$ at the average dynamic glass transition temperature T_α can be estimated from the equation I.3.4 [13][14][15].

II.3.1.1 By means of MT-DSC

Usually, the cooperativity sizes are directly extracted from MT-DSC experiments from the in-phase component C' and the out-of-phase component C'' of the complex heat capacity C^* , as depicted in Figure II.3.1.

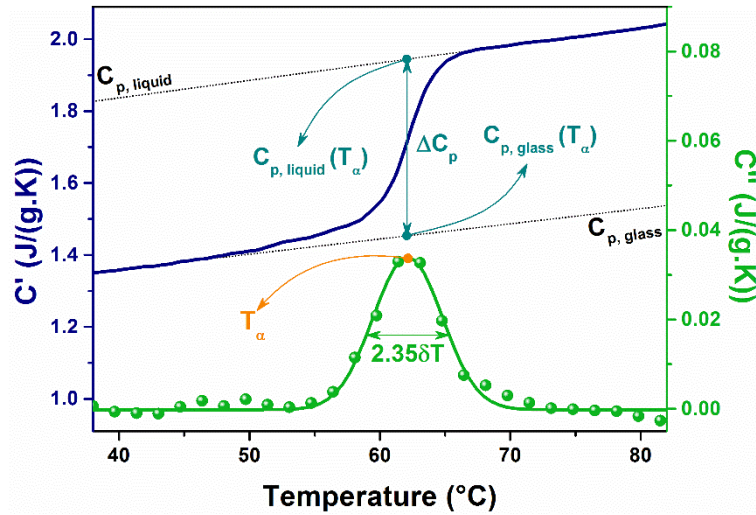


Figure II.3.1: MT-DSC in-phase component C' (blue line) and out-of-phase component C'' (green sphere) of the complex heat capacity C^* in the case of PLA glass transition as a function of temperature. Green line: Gaussian fit of the out-of-phase component C'' . The full width at half maximum of the Gaussian gives access to the average temperature fluctuation δT . The maximum of the Gaussian provides the average dynamic glass transition T_α . From the in-phase component C' , the $C_{p, \text{liquid}}(T_\alpha)$ and the $C_{p, \text{glass}}(T_\alpha)$ are extracted at T_α on the liquid dotted line ($C_{p, \text{liquid}}$) and the glass dotted line ($C_{p, \text{glass}}$), respectively.

II.3.1.2 By means of DSC or FSC: the “rule of thumb”

The experimental data required to estimate the cooperativity volume can also be extracted by means of DSC or FSC. In this case, the glass transition T_g and the heat capacity step ΔC_p are classically determined to extract the $C_{p, \text{liquid}}(T_g)$ and the $C_{p, \text{glass}}(T_g)$. The $C_{p, \text{liquid}}(T_g)$ and the $C_{p, \text{glass}}(T_g)$ intercept the liquid dotted line ($C_{p, \text{liquid}}$) and the glass dotted line ($C_{p, \text{glass}}$), respectively, at T_g . In order to estimate the average dynamic glass transition temperature δT , the following “rules of thumb” is used upon heating:

$$\delta T = \Delta T / 2.5 \quad (\text{II.3.1})$$

with ΔT the temperature interval where the $C_p(T)$ curve from DSC or FSC varies between 16 % and 84 % of the heat capacity step ΔC_p , as depicted in Figure II.3.2 [16]. This rule has been checked for several substances in literature [17].

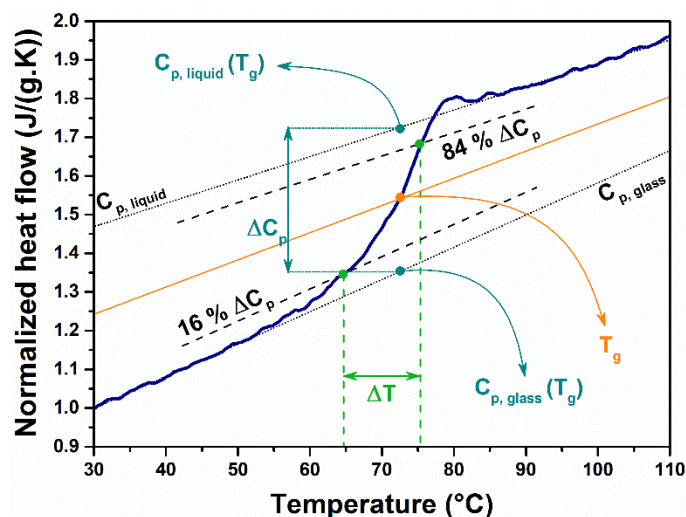


Figure II.3.2: FSC normalized heat flow of PLA glass transition. The extractions of data related to the cooperativity volume estimation are done through the “rule of thumb”.

II.3.2 Estimation of the enthalpy recovery

As graphically illustrated in Figure II.3.3, and presented in the previous chapter, the enthalpy recovery of a glass, aged at a temperature T_{ag} during a time t_{ag} , is calculated by integrating the difference between the scans of the aged and rejuvenated sample, according to the equation I.1.4 [18].

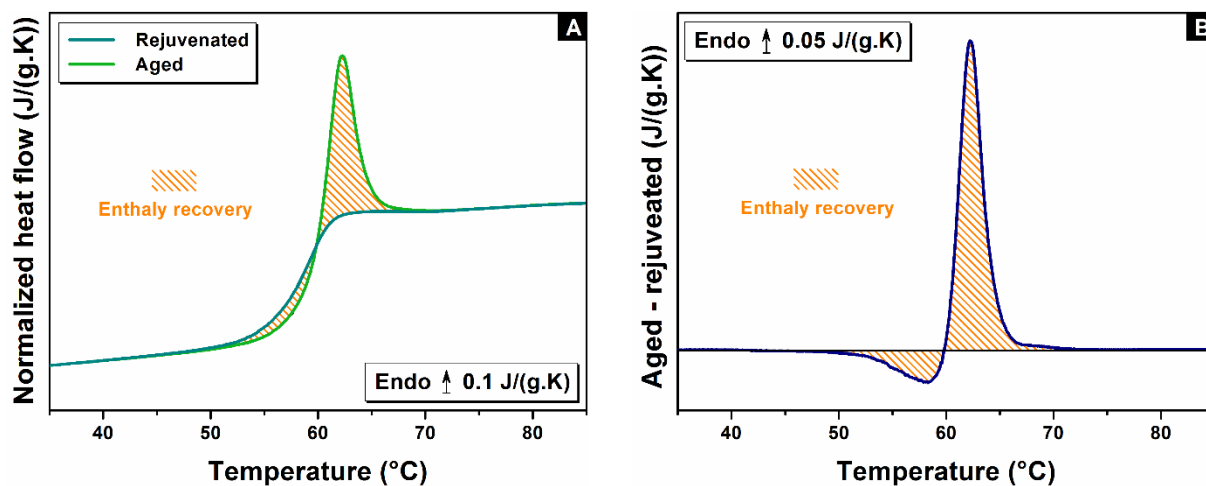


Figure II.3.3: Heat flows of rejuvenated (cyan line) and aged (green line) PLA (A). Subtraction of the aged heat flow to the rejuvenated heat flow (blue line) leading to the enthalpy recovery (orange hatched area) (B).

II.3.3 Estimation of the fictive temperature

The Tool's concept has been defined in the previous chapter [19]. From calorimetric investigations, the fictive temperature T_f is measured using the Moynihan's equation (equation I.4.3). Called areas matching method [20], T_f is extracted when the areas depicted in the Figure II.3.4 match together (green and cyan hatched areas).

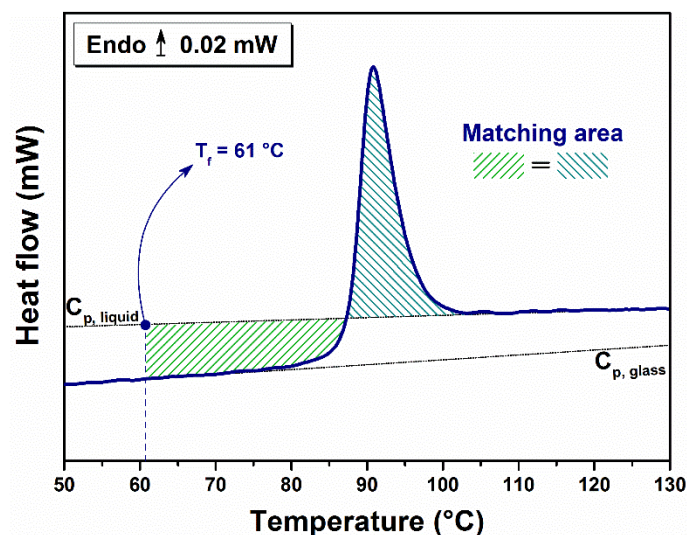


Figure II.3.4: FSC heat flow of PLA glass transition upon heating at $\beta_h = 1500 \text{K}\cdot\text{s}^{-1}$. Prior to heat up, the sample has been cooled down at $\beta_c = 0.17 \text{K}\cdot\text{s}^{-1}$ leading to the overshoot. By using the area matching method, the fictive temperature can be extracted.

REFERENCES

- [1] D. Garlotta, *J. Polym. Environ.* **9**, 63 (2001).
- [2] J. Zhang, Y. Duan, H. Sato, H. Tsuji, I. Noda, S. Yan, and Y. Ozaki, *Macromolecules* **38**, 8012 (2005).
- [3] J. Zhang, K. Tashiro, H. Tsuji, and A. J. Domb, *Macromolecules* **41**, 1352 (2008).
- [4] X. Monnier, N. Delpouve, N. Basson, A. Guinault, S. Domenek, A. Saiter, P. E. Mallon, and E. Dargent, *Polymer* **73**, 68 (2015).
- [5] B. Monasse, *J. Mater. Sci.* **27**, 6047 (1992).
- [6] W. H. Bragg and W. L. Bragg, *Proc. R. Soc. Lond. Ser. Contain. Pap. Math. Phys. Character* **88**, 428 (1913).
- [7] R. L. Danley, *Thermochim. Acta* **395**, 201 (2002).
- [8] M. Reading, B. K. Hanh, B. S. Crowe, *Method and apparatus for modulated differential analysis*. US5346306 A - September 13, 1994.
- [9] A. A. Lacey, D. M. Price, M. Reading, *Theory and practice of modulated temperature differential scanning calorimetry*. In *Modulated Temperature Differential Scanning Calorimetry*. Springer: 2006, pp 1-81.
- [10] C. Schick and V. Mathot, editors, *Fast Scanning Calorimetry* (Springer International Publishing, Cham, 2016).
- [11] V. Mathot, M. Pyda, T. Pijpers, G. Vanden Poel, E. van de Kerkhof, S. van Herwaarden, F. van Herwaarden, and A. Leenaers, *Thermochim. Acta* **522**, 36 (2011).
- [12] X. Cao, A. Mohamed, S. H. Gordon, J. L. Willett, and D. J. Sessa, *Thermochim. Acta* **406**, 115 (2003).
- [13] E. Donth, *J. Non-Cryst. Solids* **53**, 325 (1982).
- [14] E. Donth, *Acta Polym.* **35**, 120 (1984).
- [15] E. Donth, *Acta Polym.* **50**, 240 (1999).
- [16] E. Donth, *J. Polym. Sci. Part B Polym. Phys.* **34**, 2881 (1996).
- [17] E. Hempel, G. Hempel, A. Hensel, C. Schick, and E. Donth, *J. Phys. Chem. B* **104**, 2460 (2000).
- [18] I. M. Hodge, *J. Non-Cryst. Solids* **169**, 211 (1994).
- [19] A. Q. Tool and C. G. Eicitlin, *J. Am. Ceram. Soc.* **14**, 276 (1931).
- [20] C. T. Moynihan, P. B. Macedo, C. J. Montrose, C. J. Montrose, P. K. Gupta, M. A. DeBolt, J. F. Dill, B. E. Dom, P. W. Drake, A. J. Easteal, P. B. Elterman, R. P. Moeller, H. Sasabe, and J. A. Wilder, *Ann. N. Y. Acad. Sci.* **279**, 15 (1976).

CHAPTER III

Glass transition properties and structural relaxation of wholly amorphous PLA by standard DSC and FSC

Parts of this chapter are extracted from:

Physical aging in PLA through standard DSC and fast scanning calorimetry investigations

Xavier Monnier, Allisson Saiter, Eric Dargent

Thermochimica Acta 648 (2017) 13-22

CONTENTS

III.1 Glass transition and fictive temperature	66
III.2 Thermal lag considerations.....	68
III.3 From low to high enthalpy PLA glasses	74
III.4 Parameters influencing the structural relaxation kinetics.....	77
III.5 Structural relaxation of wholly amorphous PLA over 6 decades	83
III.6 Conclusion	88
References.....	89

The first experimental part of this work focuses on the glass transition and the structural relaxation of wholly amorphous PLA through DSC and FSC. Both techniques are compared in order to highlight the respective benefits and drawbacks of FSC. Influence of the scanning rate on the glass transition is first investigated. Different concept such as fictive temperature, thermal lags and structural relaxation have been used to characterize the influence of the scanning rate on the glass transition. The different parameters influencing the kinetics of the physical aging have been investigated. Consequently, this section shows the interests of FSC for physical aging investigations in complex polymer systems as related in the next chapter.

III.1 Glass transition and fictive temperature

Glass transition properties, and more exactly glass transition temperature, are of importance with regard to structural relaxation. In order to be able to compare physical aging, either from systems or from techniques, glass transition temperatures are the main parameters to know. As we have compared two thermal analysis techniques, standard DSC and FSC through wholly amorphous PLA, respective glass transitions have been first investigated.

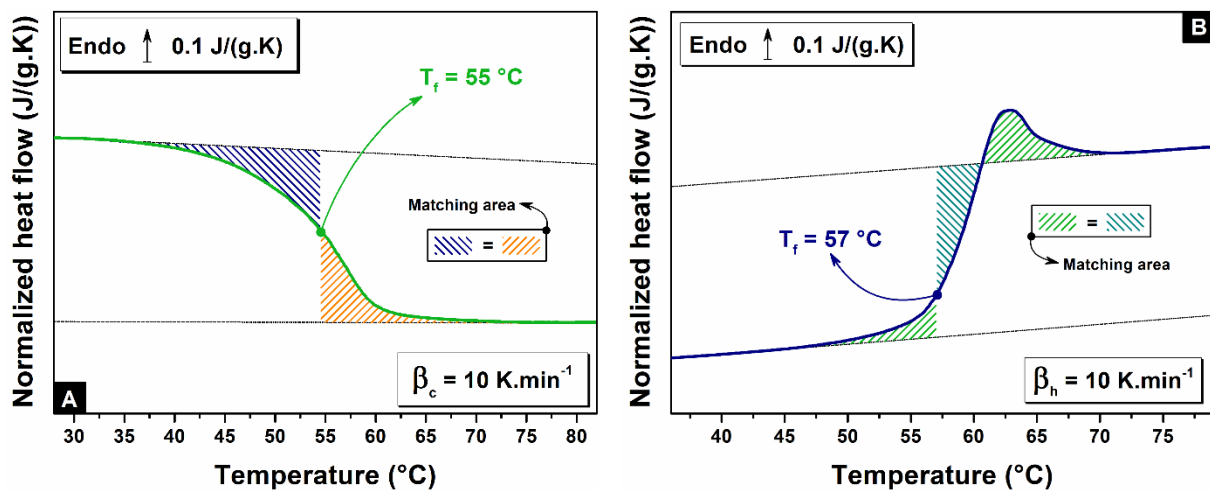


Figure III.1.1: Standard DSC normalized heat flow of 5 mg wholly amorphous PLA as a function of temperature, upon cooling (A) and heating (B), for scanning rate $|\beta_c| = \beta_h = 10 \text{ K.min}^{-1} = 0.17 \text{ K.s}^{-1}$.

Figure III.1.1 shows the normalized heat flows of 5 mg wholly amorphous PLA sample as a function of temperature in the glass transition domain. Measurements have been performed upon cooling (A) and then upon heating (B) with equal rates by standard DSC. In addition, Figure III.1.1.B depicts the procedure of the fictive temperature estimation based on the conventional area-matching method as proposed by Moynihan et al. [1]. Fictive temperatures of 55 °C and 57 °C are measured, respectively.

Figure III.1.2 displays the normalized heat flows as a function of temperature of 40 ng wholly amorphous PLA sample, measured upon cooling (A) and then upon heating (B) with equal rates ranging from 300 K.s^{-1} to 4000 K.s^{-1} by FSC. The heat capacity step at the glass transition is clearly observed independently of the scanning rates. By FSC experiments [2], as well as by standard or modulated temperature DSC experiments, the sensitivity (i.e. signal-to-noise ratio) of the heat flow is drastically dependent of the sample mass and the scanning rate [3]. Consequently, below 300 K.s^{-1} the sensitivity being too low, none heat flow has been

properly measured. On the contrary, the sensitivity becomes higher when the scanning rate increases, providing smoother heat flow signals as clearly shown in Figure III.1.2. Neither enthalpy relaxation nor thermal lag are observed upon cooling as shown in Figure III.1.2.A. On the contrary, endothermic peaks related to the enthalpy relaxation, and shifts of the glass transition related to the thermal lag, are observed upon heating, as depicted in Figure III.1.2.B.

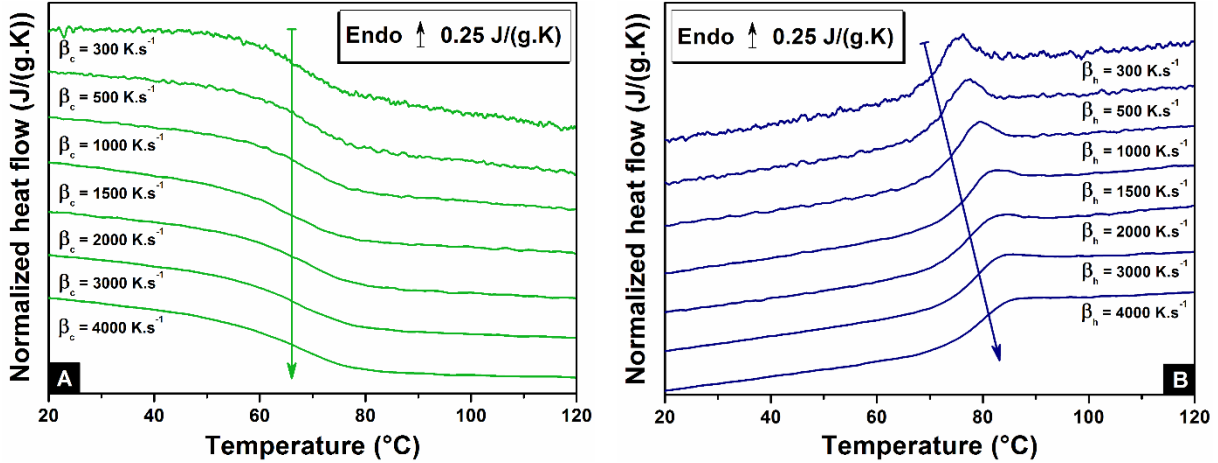


Figure III.1.2: FSC normalized heat flow of 40 ng wholly amorphous PLA as a function of temperature, upon cooling (A) and heating (B), for scanning rate $|\beta_c| = \beta_h$ ranging from 300 K.s^{-1} to 4000 K.s^{-1} . Arrows are guide for eyes.

In literature, it is well established that fictive temperatures depend on the applied cooling rate [4]. As clearly shown in Figure III.1.3, when the cooling rate applied to form the glass increases the fictive temperature increases by following a non-Arrhenius evolution. This curved evolution can be fitted with the Vogel-Fulcher-Tammann-Hesse (VFTH) equation [5]:

$$\log(|\beta_c|) = A_\beta - \frac{B}{T_f - T_V} \quad (\text{III.1.1})$$

where A_β is a constant, B a fitting parameter and T_V the so-called Vogel temperature, namely the extrapolated temperature when relaxation times τ tends towards infinite. When studying fictive temperature, the VFTH equation is a modified version arising from the Vogel-Fulcher-Tammann (VFT) - equation I.3.2 - introduced in the Chapter I [6]. By analogy to the equation I.3.3 presented in the Chapter I, the dynamic fragility m can be then defined as follow [7]:

$$m = \left[\frac{d(\log|\beta_c|)}{d\left(\frac{T_g}{T}\right)} \right]_{T=T_g} \quad (\text{III.1.2})$$

In this case, T_g is set as the fictive temperature measured at a cooling rate of $10 \text{ K}\cdot\text{min}^{-1}$, 330 K [7]. Therefore, from the equation III.1.1 and by assuming the VFTH behavior for the cooling rate dependency of the fictive temperatures, the equation III.1.2 becomes:

$$m = \frac{B \cdot T_g}{(T_g - T_0)^2} \quad (\text{III.1.3})$$

From the experimental data displayed in Figure III.1.3, and the equation III.3.1, a fitting parameter B of $118 \pm 10 \text{ K}$ and a Vogel temperature T_0 of $321 \pm 1 \text{ K}$ are obtained. These results lead to a dynamic fragility m value of 480 ± 42 . This value exceeds the range of values defined by Angell: $16 \leq m \leq 200$. Such value of m has physically no meaning and are correlated to thermal lags occurring in the sample due to the high scanning rates employed by FSC [8].

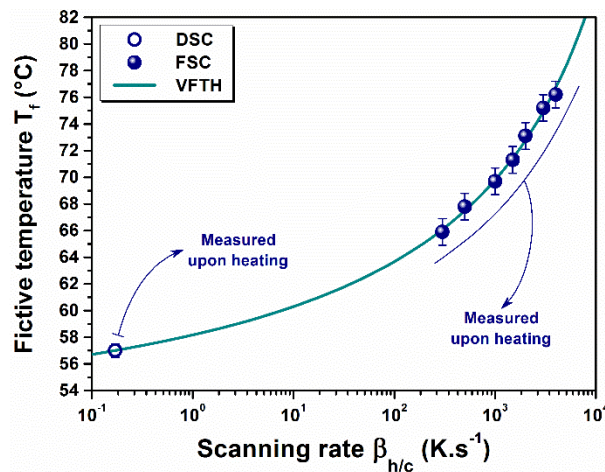


Figure III.1.3: Evolution of the fictive temperature as a function of the scanning rate $|\beta_c| = \beta_h$ determined from DSC (circle) and FSC (sphere). Solid line is VFTH fit to DSC and FSC data.

III.2 Thermal lag considerations

III.2.1 Thermal lag: dynamic and static

Fictive temperatures measured upon heating fit well to VFTH equation, as depicted in Figure III.1.3. However, as highlighted through the fragility concept, thermal lag occurs in FSC experiments leading to improper results [9]. The thermal lag is a shift of temperature due to the heat transfer delay between the heater and the sample. It is caused by the high scanning rates used, as well as the sample geometry. Thus, the temperature gradient leads to smearing effect. The measured thermal events appear to occur at higher temperature. The thermal lags related to the sample mass/dimension ratio and the scanning rate have been widely discussed [10][11], and corrected from the melting of an indium piece placed on the top of

the sample [12][13]. Recently, Schawe has proposed two thermal lag corrections (dynamic and static) in order to accurately measure the glass transition temperature by FSC experiments [8].

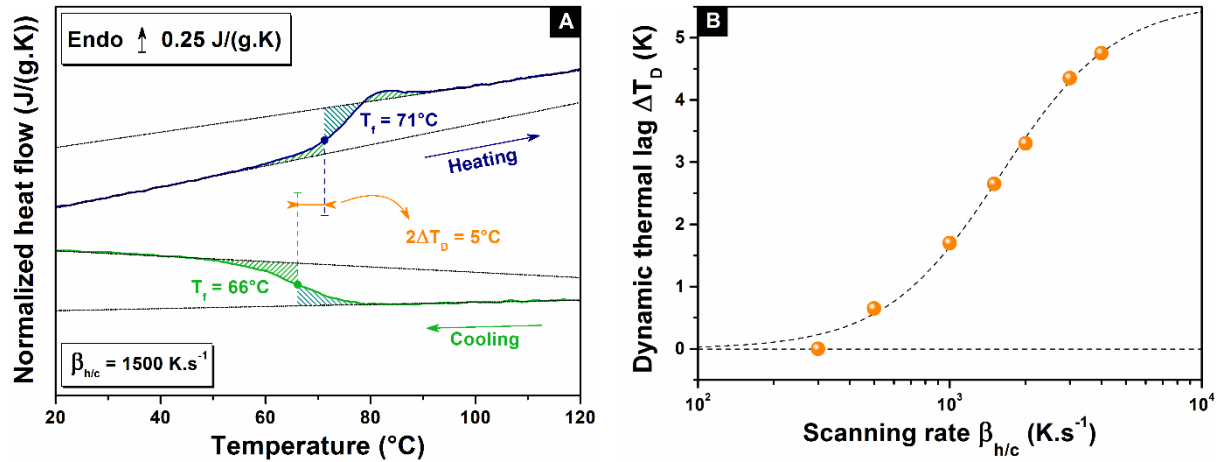


Figure III.2.1: (A) Estimation of dynamic thermal lag measured from the difference of fictive temperatures T_f upon heating and cooling at $\beta_h = |\beta_c| = 1500 \text{ K.s}^{-1}$. (B) Evolution of dynamic thermal lag as a function of the scanning rate $\beta_h = \beta_c$. Dashed lines are guide for eyes.

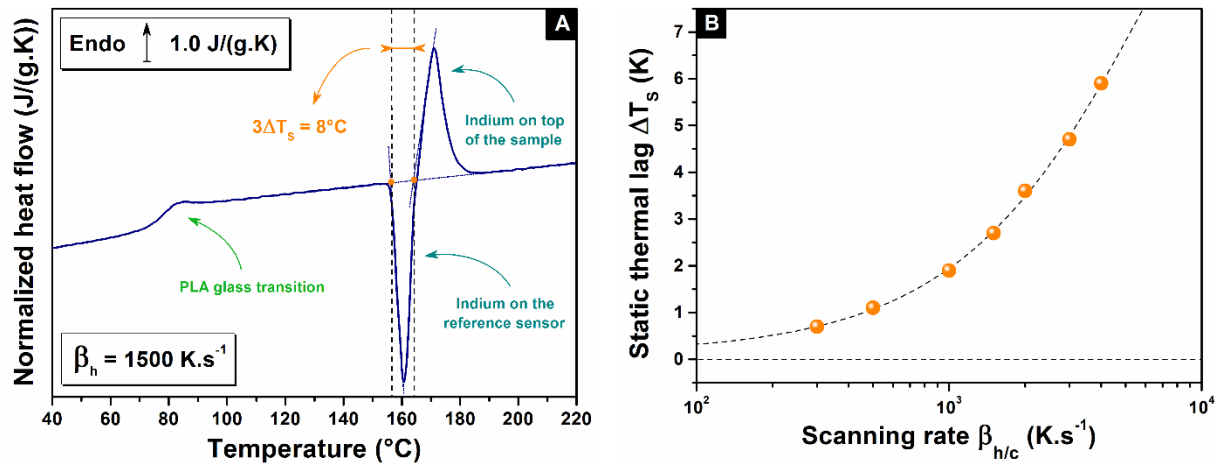


Figure III.2.2: (A) Estimation of static thermal lag measured from the third of the difference in the onset melting temperatures of an indium placed on top of the PLA and another one on the reference sensor. (B) Evolution of static thermal lag as a function of the scanning rate $\beta_h = |\beta_c|$. Dashed lines are guide for eyes.

Table III.2.1: Dynamic ΔT_D , static ΔT_S and thermal ΔT lag values, as well as the fictive temperatures T_f measured and corrected from heating, and measured from cooling for the different scanning rates $|\beta_c| = \beta_h$ investigated.

$\beta_h = \beta_c $ (K.s^{-1})	ΔT_D ($^{\circ}\text{C}$)	ΔT_S ($^{\circ}\text{C}$)	$\Delta T = \Delta T_D + \Delta T_S$ ($^{\circ}\text{C}$)	T_f from heating ($^{\circ}\text{C}$)	T_f corrected from heating ($^{\circ}\text{C}$)	T_f from cooling ($^{\circ}\text{C}$)
300	0.0	0.7	0.7	65.9	65.2	65.9
500	0.7	1.1	1.8	67.8	66.0	66.5
1000	1.7	1.9	3.6	69.7	66.1	66.3
1500	2.7	2.7	5.4	71.3	65.9	66.5
2000	3.3	3.6	6.9	73.1	66.2	66.7
3000	4.4	4.7	9.1	75.3	66.2	66.0
4000	4.8	5.9	10.7	76.6	65.6	66.5

Figure III.2.1.A depicts the procedure of the dynamic thermal lag determination related to the average values of the fictive temperatures measured from heating and cooling at $\beta_h = |\beta_c|$ [8]. Figure III.2.1.B shows the increase of dynamic thermal lag as a function of the scanning rate. At $|\beta_c| = \beta_h = 300 \text{ K}\cdot\text{s}^{-1}$, no dynamic thermal lag has been observed, when a dynamic thermal lag close to $5 \text{ }^\circ\text{C}$ is reached at $4000 \text{ K}\cdot\text{s}^{-1}$. Figure III.2.2.A relates the static thermal lag determined from the third of the difference in the onset melting temperatures of an indium placed on top of the PLA and another one on the reference sensor [8]. Figure III.2.2.B depicts the increase of static thermal lag as a function of the scanning rate. Even at the lower scanning rate, a static thermal lag smaller than $1 \text{ }^\circ\text{C}$ does exist due to the sample thickness. It expands to around $6 \text{ }^\circ\text{C}$ for a scanning rate of $4000 \text{ K}\cdot\text{s}^{-1}$. The different thermal lag values are summarized in Table III.2.1. They are consistent with the low mass and the scanning rates employed [4][12][14].

III.2.2 Deviation from the VFTH law

As observed in Figure III.1.3, the measured fictive temperature increases when the scanning rate increases. From the lowest to the highest scanning rate used, the fictive temperature increases of $10 \text{ }^\circ\text{C}$, from $65.9 \text{ }^\circ\text{C}$ up to $76.3 \text{ }^\circ\text{C}$. On the contrary, by standard DSC experiments performed at $0.17 \text{ K}\cdot\text{s}^{-1}$, the fictive temperature of PLA is equal to $57 \text{ }^\circ\text{C}$. Due to the smearing effects, gaps of $9 \text{ }^\circ\text{C}$ for $|\beta_c| = \beta_h = 300 \text{ K}\cdot\text{s}^{-1}$, up to $19 \text{ }^\circ\text{C}$ for $|\beta_c| = \beta_h = 4000 \text{ K}\cdot\text{s}^{-1}$, are measured between standard DSC and FSC experiments. Thanks to the dynamic and static thermal lag estimations, the raw fictive temperatures measured upon heating are corrected, depending on the scanning rate (see Table III.2.1). The fictive temperatures corrected do not depend in the scanning rate, and are close to an average value of $66 \text{ }^\circ\text{C}$. Table III.2.1 also depicts the fictive temperatures measured upon cooling, and as already noticed in Figure III.1.2.A, do not depend on the cooling rate. Thus, an average value of $T_{f1} = 66 \text{ }^\circ\text{C}$ is obtained upon cooling, matching with the average value of the corrected fictive temperatures measured upon heating. However, we may note the lack of dependence of the fictive temperature on the applied cooling rate is atypical, as depicted in Figure III.2.3. Indeed, as observed for PS or PET_g, the fictive temperature depends on the cooling rate applied [4][14]. Such result seems to be specific to PLA. Besides, it may also arise from improper thermal lag corrections. Consequently, how can we certify the thermal lag corrections?

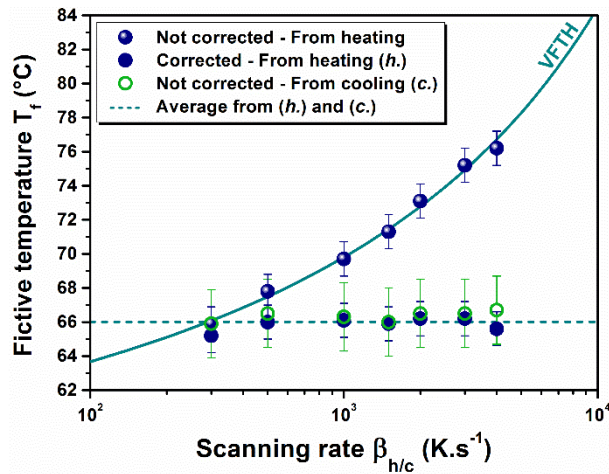


Figure III.2.3: Evolution of the fictive temperature as a function of the scanning rate $|\beta_c| = \beta_h$ determined from FSC. Fictive temperatures have been measured and not corrected upon heating (spheres) and cooling (circles), as well as measured and corrected upon heating (discs). Solid line is VFTH fit and dashed line is average of the fictive temperatures measured from the cooling, as well as measured and corrected from the heating.

In literature, it is well established that fictive temperature depends only on the applied cooling rate. Recently, Simon et al. have demonstrated the non-dependence of the heating rate on the fictive temperature on a wide range of scanning rate by means of FSC [4]. As a consequence, we have used this phenomenon to certify our thermal lag corrections. The fictive temperature measured upon cooling and heating by DSC at $|\beta_c| = \beta_h = 0.17 \text{ K.s}^{-1}$ are respectively $55 \text{ }^\circ\text{C}$ and $57 \text{ }^\circ\text{C}$. In addition, those values match with the ones reported in literature [15][16]. Thus, these values are taken as a reference in this investigation. By assuming the only dependence of the fictive temperature on the applied cooling rate, we have investigated the fictive temperature of wholly amorphous PLA cooled down at 0.17 K.s^{-1} . Figure III.2.4.A shows the heat flows upon cooling at $\beta_c = 0.17 \text{ K.s}^{-1}$ and heating at $\beta_h = 1500 \text{ K.s}^{-1}$ as an example. After the cooling (step 1), subsequent heating have been performed for the different heating rates used by FSC (step 2). The difference of scanning rate leads to endothermic relaxation peak superimposing to the glass transition. Then, the fictive temperature not corrected from the thermal lag have been measured for each heating rate investigated. The values are reported in Table III.2.2.

Table III.2.2: Fictive temperatures T_f measured and corrected from heating for the different heating rates β_h investigated when the glass is formed at $\beta_c = 0.17 \text{ K.s}^{-1}$. The thermal lag ΔT values are reminded.

β_h (K.s ⁻¹)	300	500	1000	1500	2000	3000	4000
T_f from heating (°C)	56.7	57.8	59.7	60.7	61.6	63.7	64.8
T_f corrected from heating (°C)	56.0	56.0	56.1	55.3	54.7	54.6	54.1
ΔT (°C)	0.7	1.8	3.6	5.4	6.9	9.1	10.7

Influence of the thermal lag is clearly observed. From the lowest to the highest heating rate used, the fictive temperature increases of 8 °C, from 56.7 °C up to 64.8 °C. As fictive temperatures depend only on the applied cooling rate, these results highlight once again the need for thermal lag corrections. The corrected fictive temperatures and the thermal lag values are also displayed in Table III.2.2. An average fictive temperature of 55 ± 1 °C is then obtained. This value match with the one measured upon cooling by DSC at $\beta_c = 0.17$ K.s⁻¹ as shown in Figure III.2.4.B. Consequently, the non-dependence of the fictive temperatures on the heating rates after thermal lag corrections is evidenced.

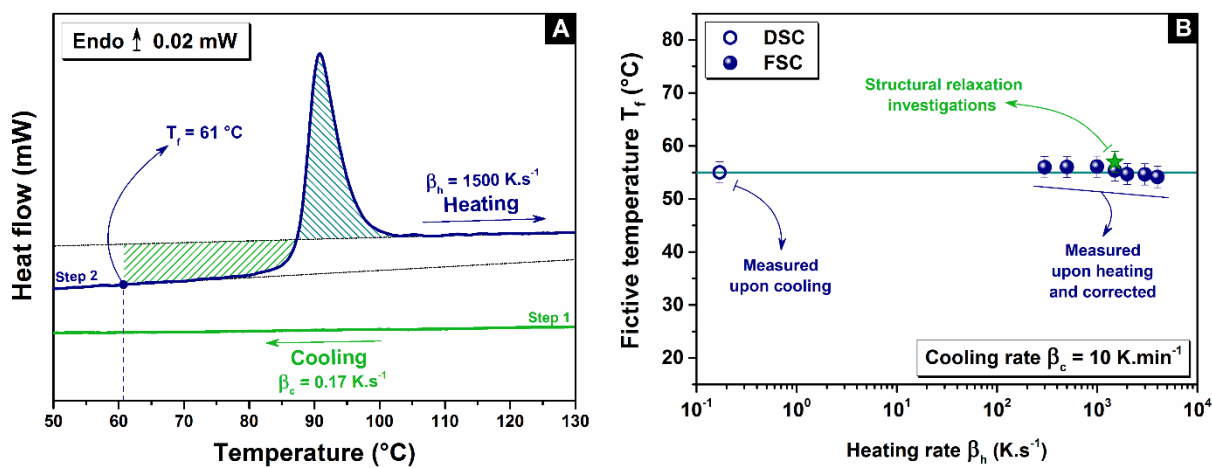


Figure III.2.4: (A) FSC heat flows of wholly amorphous PLA upon cooling at $\beta_c = 0.17$ K.s⁻¹ and heating at $\beta_h = 1500$ K.s⁻¹. (B) Evolution of the fictive temperature as a function of the heating rate β_h investigated after cooling the sample at $\beta_c = 0.17$ K.s⁻¹. Fictive temperatures have been measured and corrected upon heating (sphere) by FSC and measured upon cooling by DSC (circles). Solid line is average from the data obtained. The star refers to structural investigations discussed below.

Then, structural relaxation has also been used in order to confirm. Structural relaxation occurs only in the glassy state [17]. Thus, by performing physical aging at different temperature in the range of the glass transition domain, we can figure out what we call an onset temperature of structural relaxation T_{SR}^0 . It defines the temperature that allows structural relaxation when the sample is stored in its glassy state. It does not depend on any corrections. It is the only response of the material itself. Figure III.2.5.A shows normalized heat flows of wholly amorphous PLA, formed at $\beta_c = 0.17$ K.s⁻¹, rejuvenated and aged 10 min for aging temperatures ranging from 60 °C to 50 °C. After the physical aging, the subsequent heating has been performed at $\beta_h = 1500$ K.s⁻¹, leading to overshoot superimposed to the glass transition. Figure III.2.5.B reports the enthalpy recovery measured for the respective aging temperatures investigated. When shift of the structural relaxation peaks are observed, it means that the glassy state is reached. The value of T_{SR}^0 observed is 57 °C and matches with

the corrected fictive temperatures displayed in Figure III.2.4.B. The value of T_{SR}^O is above the fictive temperature T_f due to the broadening of the glass transition. These investigations lead us to certify the thermal lag corrections of this work. As a consequence, the non-dependence of the corrected fictive temperature with the applied cooling rate on PLA has been evidenced from the scanning rates investigated. However, in order to clarify this non-dependence behavior of the fictive temperature on the applied cooling rate used a final investigation has been done.

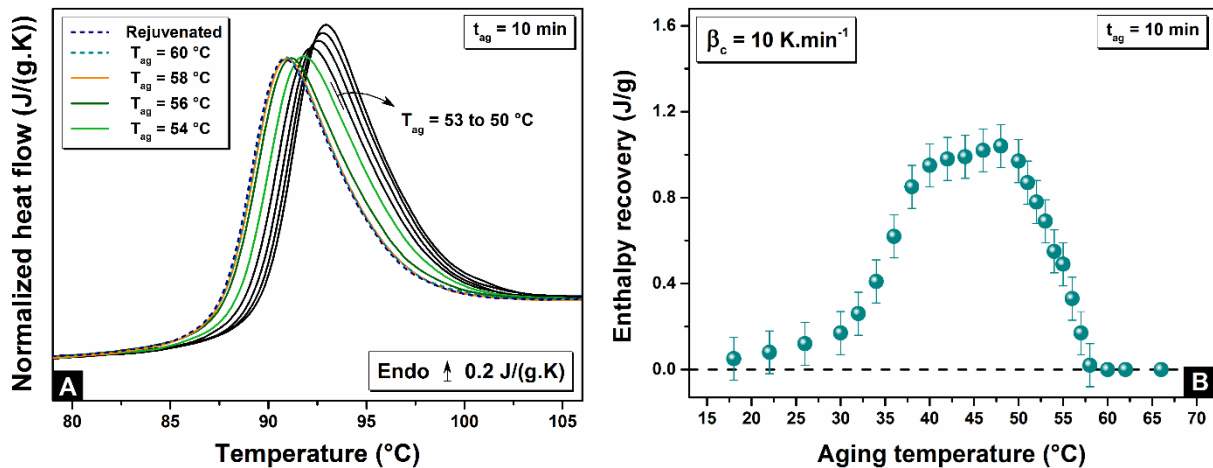


Figure III.2.5: (A) FSC normalized heat flows of wholly amorphous PLA formed at a cooling rate $\beta_c = 0.17$ K.s⁻¹ and then aged 10 min at different aging temperature ranging from 60 °C to 50 °C. The subsequent heating has been performed at $\beta_h = 1500$ K.s⁻¹. (B) Enthalpy recovery measured from each aging temperature investigated.

Figure III.2.6 shows investigation of fictive temperatures of PLA in a cooling rate range of four decades. Figure III.2.6.A displays FSC heat flows obtained at $\beta_h = 2000$ K.s⁻¹. An endothermic step of the specific heat capacity indicating the glass transition of the material is observed along with an endothermic relaxation peak. This latter peak progressively shifts towards higher temperatures, and its amplitude increases when the cooling rate used to form the glass is reduced. However for $\beta_c = [2000$ K.s⁻¹; 1500 K.s⁻¹; 1000 K.s⁻¹], the heat flows superimpose. Figure III.2.6.B depicts the fictive temperatures T_f measured and corrected from heating by FSC, as well as the fictive temperature T_f measured by DSC upon cooling (see Figure III.1.1.A). The fictive temperatures fit to VFTH equation up to $\beta_c = 500$ K.s⁻¹. From the equation III.3.1, a fitting parameter B of 261 ± 48 K and a Vogel temperature T_0 of 309 ± 1 K are obtained. These results lead to a dynamic fragility m value of 195 ± 49 from the equation III.1.3. This value is in the upper limit defining the fragility index. However, within the uncertainties the value is close to the values of 189 and 166 reported for wholly amorphous PLLA by Arnoult et

al. [18] and Mano et al. [19], respectively. Thus, by correcting the thermal lag, fragility index value with physical meaning are observed. In order to decrease the uncertainties, a combination of DSC, FSC as well as broadband dielectric spectroscopy should be performed on a wide range of scanning rates and frequencies, as already performed by Dhotel et al. on polystyrene (PS) and poly(ethylene 1,4-cyclohexylenedimethylene terephthalate glycol) [14].

Above $\beta_c = 500 \text{ K.s}^{-1}$, a fictive temperature of around $66 \text{ }^\circ\text{C}$ is measured. A lack of dependence of the fictive temperature on the applied cooling rate is then observed, as previously noticed from the thermal lag corrections. This final investigations complete the previous ones as it does not depend on any thermal lag corrections. The same thermal lag correction value has been subtracted to the raw fictive temperatures. It clearly shows that above a critical cooling rate the same fictive temperature is measured. It is worth mentioning that a similar behavior has been observed on PS by Dhotel et al. above 500 K.s^{-1} [14]. As a consequence, is the same glass formed above a critical cooling rate?

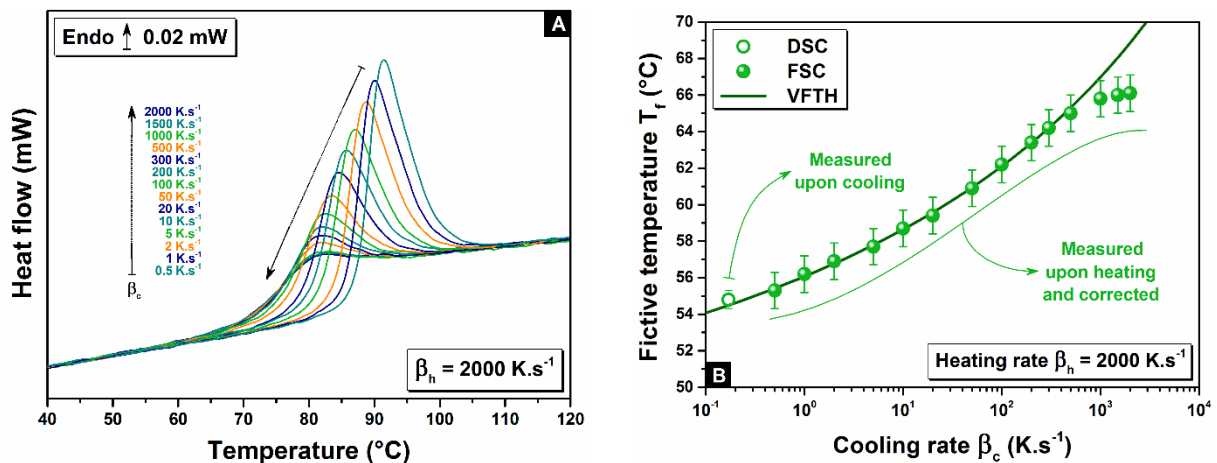


Figure III.2.6: (A) FSC heat flows of wholly amorphous PLA obtained at a heating rate $\beta_h = 2000 \text{ K.s}^{-1}$. The glassy PLA were formed at a cooling rate ranging from $\beta_c = 0.5 \text{ K.s}^{-1}$ to $\beta_c = 2000 \text{ K.s}^{-1}$. (B) Evolution of the fictive temperature as a function of the cooling rate β_c determined from DSC (circle) and FSC after thermal lag corrections induced by $\beta_h = 2000 \text{ K.s}^{-1}$ (sphere). Solid line is VFTH fit to DSC and FSC data.

III.3 From low to high enthalpy PLA glasses

For high cooling rates included between 300 K.s^{-1} and 4000 K.s^{-1} , a constant value of $T_{f1} = 66 \text{ }^\circ\text{C}$ has been determined by FSC after thermal lag corrections. It seems that the same PLA glass is formed from the different cooling rates used as depicted through the different investigations led in the previous section III.2. These results correlate with the work of Cangialosi et al. [20][21] by means of dielectric spectroscopy experiments. By cooling down

polycarbonate films at 60 and 100 K.s⁻¹, they observed similar relaxation patterns. To validate the assumption of a single PLA glass formed independently of the scanning rate used, physical aging were performed at $T_{ag} = T_g - 18\text{ }^\circ\text{C}$ (with $T_g = T_{f1} = 66^\circ\text{C}$ taking into account the thermal lag correction) for different aging times $t_{ag} = [1\text{ min}; 10\text{ min}; 100\text{ min}]$ by FSC.

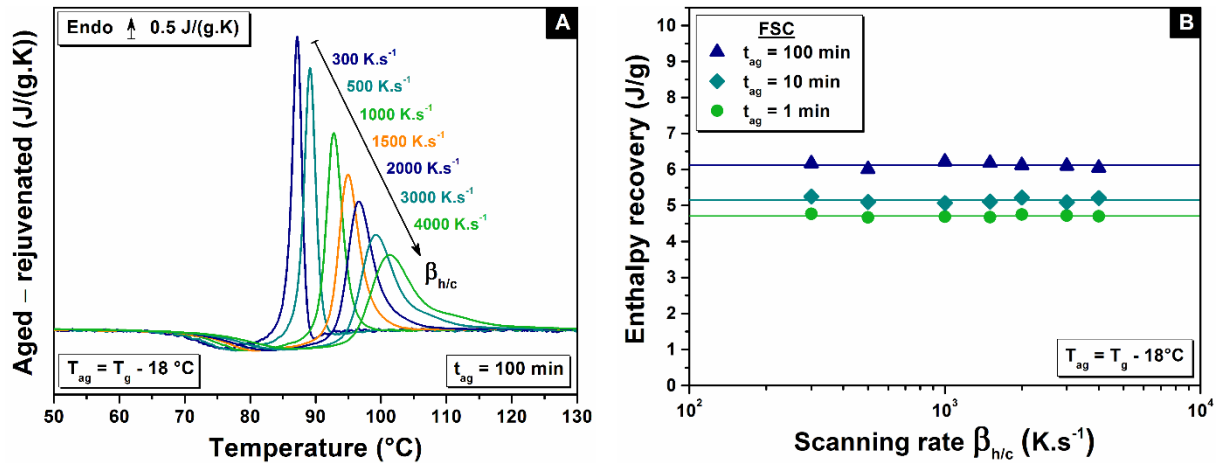


Figure III.3.1: Aging of PLA glasses at $T_{ag} = T_g - 18\text{ }^\circ\text{C}$ studied by FSC. **(A)** Normalized heat flow subtraction (aged - rejuvenated) for $t_{ag} = 100\text{ min}$. **(B)** Enthalpy recovery as a function of $\beta_{h/c}$ for $t_{ag} = 100\text{ min}$ (blue triangle), $t_{ag} = 10\text{ min}$ (cyan square) and $t_{ag} = 1\text{ min}$ (green disc).

For each scanning rate investigated $\beta_{h/c}$, Figure III.3.1.A displays the normalized heat flow subtraction (aged - rejuvenated) for PLA with $t_{ag} = 100\text{ min}$. Figure III.3.1.B presents the enthalpy recovery as a function of $\beta_{h/c}$ obtained for different t_{ag} . Due to the smearing effects, the peaks are shifted at higher temperatures when the scanning rates increase (Figure III.3.1.A). This is also observed for the other aging times investigated (Figure III.3.2). As shown in Figure III.3.1.B, the enthalpy recoveries measured do not depend on the scanning rate, and average values of 4.7, 5.2 and 6.1 J/g were measured for the three different aging times, respectively. As depicted above and highlighted in the case of polycarbonate cooled down at few tens degrees per seconds [20][21], the enthalpy recoveries measured from the physical aging in PLA glasses are the same independently of the scanning rate used to form the glass. Only the molecular dynamics involved are different, mainly due to the smearing effects of the technique itself [8]. To sum up, not only the same fictive temperature, but also the same enthalpy recovery, are measured from the glasses formed with the different scanning rates investigated. From various approaches, it is clear that only one glass is formed independently of the scanning rates.

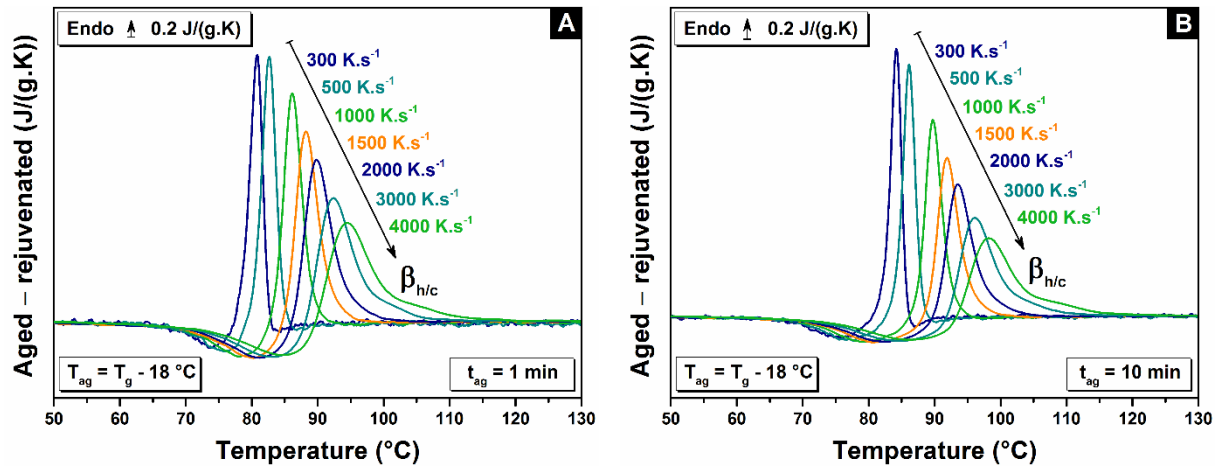


Figure III.3.2: FSC Normalized heat flow subtraction (aged - rejuvenated) of PLA glasses aged at $T_{ag} = T_g - 18$ °C for $t_{ag} = 1$ min (A) and $t_{ag} = 10$ min (B).

One can notice that the three aging times (i.e. 1, 10 and 100 min), investigated by FSC 18 °C below the glass transition T_g , depict higher values of the enthalpy recovery (4.7, 5.2 and 6.1 J/g respectively) compared to those measured by standard DSC [22][23]: in the same conditions (Figure III.3.3), enthalpy recoveries depict 0.1, 0.4 and 1.0 J/g respectively. Thus, an enthalpy recovery increase of 80 to 90 % is observed between FSC and standard DSC. How to explain this gap? Why the physical aging seems to be accelerated by FSC?

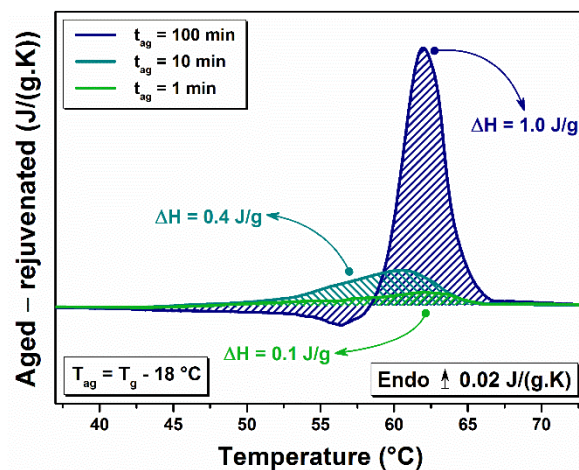


Figure III.3.3: DSC Normalized heat flow subtraction (aged - rejuvenated) of PLA glasses aged at $T_{ag} = T_g - 18$ °C for $t_{ag} = 100$ min (blue), $t_{ag} = 10$ min (cyan) and $t_{ag} = 1$ min (green). Hatched area represent the respective enthalpy recoveries measured.

III.4 Parameters influencing the structural relaxation kinetics

III.4.1 Cooling rate

In literature, accelerated physical aging are reported either for polymers subjected to quenching or medium cooling rates up to 100 K.s^{-1} [20][21][24][25][26] as well as for polymers with specific geometries, such as polymer thin films [27][28][29][30][31][32] or polymer nanocomposites [33][34][35]. In all cases, the mechanism of structural relaxation involved during the physical aging is correlated to a free volume hole diffusion towards surfaces. Those surfaces may be the external ones of the bulk, the internal ones tied to the creation of low density regions induced by a high cooling rate, or the interfaces between polymer and fillers. Consequently, in a first approach, it is obvious to correlate the gap in enthalpy recovery recorded in this work between FSC and standard DSC from the difference of the scanning rates used: up to six decades [8]. Such differences in cooling rate might induce low density regions, and so more free volume or enthalpy, in rapidly quenched samples as illustrated in Figure I.1.2.

FSC and standard DSC normalized heat flows of aged PLA during 1, 10 and 100 min 18 °C below their respective T_g are shown in Figure III.4.1. First, Figure III.4.1.A depicts aged curves from standard DSC. PLA sample was cooled down and heated up at $|\beta_c| = \beta_h = 0.17 \text{ K.s}^{-1}$. To erase influence of high cooling rates, FSC experiments with $\beta_c = 0.17 \text{ K.s}^{-1}$ and $\beta_h = 1500 \text{ K.s}^{-1}$ have been performed. The resulting curves are shown in Figure III.4.1.B. Finally, Figure III.4.1.C depicts aged curves from FSC when PLA samples have been cooled down and heated up at $|\beta_c| = \beta_h = 1500 \text{ K.s}^{-1}$. A classical behavior is observed when $|\beta_c| = \beta_h$: endothermic peaks related to the structural relaxation process superimpose to the glass transition. When $|\beta_c| \neq \beta_h$, endothermic peaks related to the structural relaxation process also superimpose to the glass transition, but in addition an overshoot due to the difference between β_c and β_h is observed. From standard DSC and FSC, the different enthalpy recoveries are determined and reported in Table III.4.1. By FSC or standard DSC, the same enthalpy recovery is measured when the samples are cooled down at 0.17 K.s^{-1} . On the contrary, for $\beta_c = 1500 \text{ K.s}^{-1}$ a

significant increase is observed. The idea that high cooling rates accelerate the aging process by FSC is evidenced.

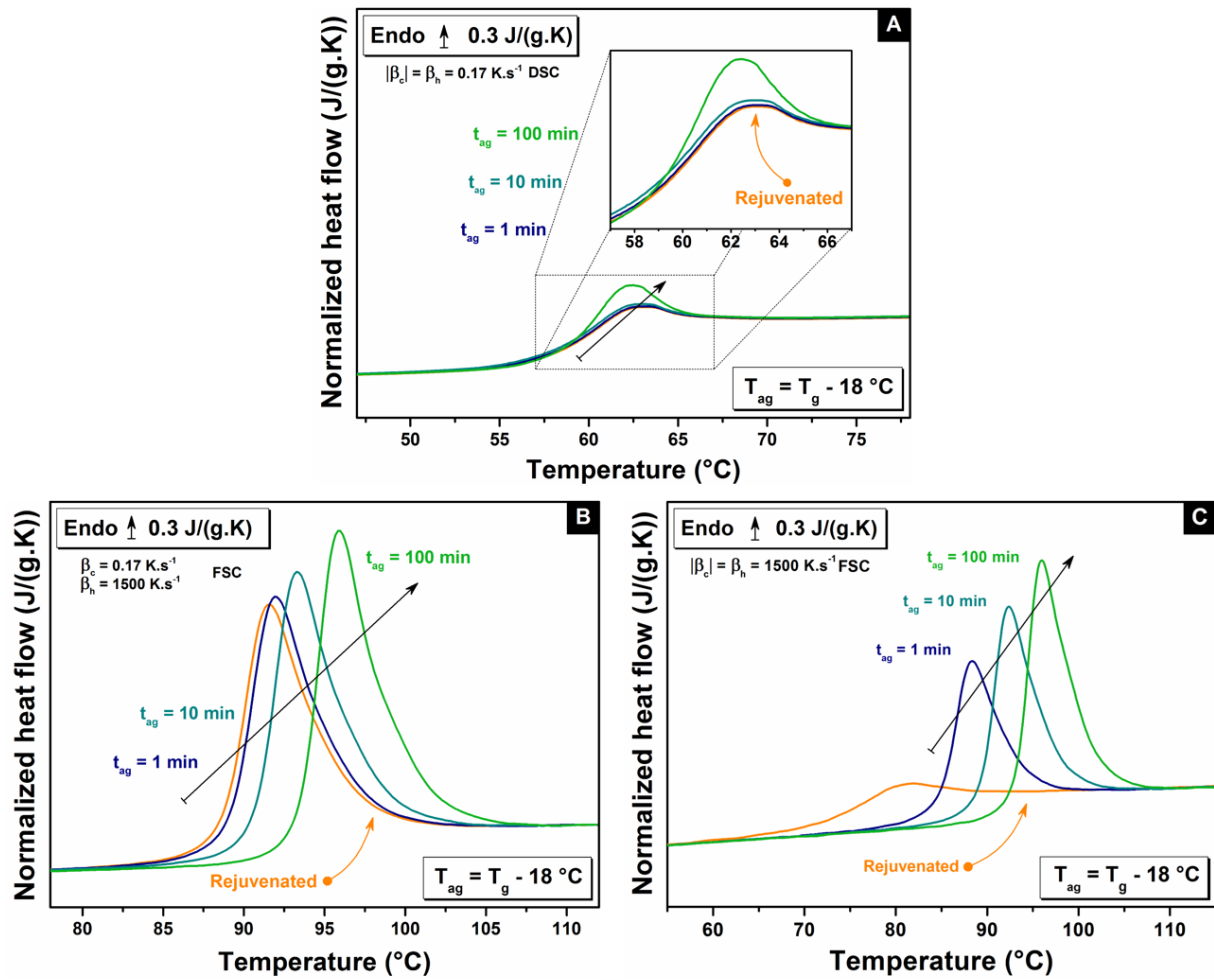


Figure III.4.1: Standard DSC and FSC normalized heat flows of amorphous PLA aged at $T_{ag} = T_g - 18 \text{ }^\circ\text{C}$ for three aging times $t_{ag} = [1; 10; 100 \text{ min}]$. **(A)** Standard DSC experiments were performed at a scanning rate of $|\beta_c| = \beta_h = 0.17 \text{ K.s}^{-1}$. **(B)** FSC experiments were performed at a scanning rate of $\beta_c = 0.17 \text{ K.s}^{-1}$ and $\beta_h = 1500 \text{ K.s}^{-1}$. $|\beta_c| \neq \beta_h$ explains the overshoot for the rejuvenated curve. **(C)** FSC experiments were performed at a scanning rate of $|\beta_c| = \beta_h = 1500 \text{ K.s}^{-1}$.

Table III.4.1: Enthalpy recovery values recorded from the amorphous PLA aged at $T_{ag} = T_g - 18 \text{ }^\circ\text{C}$ for three aging times $t_{ag} = [1; 10; 100 \text{ min}]$ by standard DSC at a cooling rate of $\beta_c = 0.17 \text{ K.s}^{-1}$ as well as by FSC at cooling rates of $\beta_c = 0.17 \text{ K.s}^{-1}$ and $\beta_c = 1500 \text{ K.s}^{-1}$. Values are recorded from the aging curves in Figure III.4.1.

t_{ag} (min)	Standard DSC ($\beta_c = 0.17 \text{ K.s}^{-1}$)	FSC ($\beta_c = 0.17 \text{ K.s}^{-1}$)	FSC ($\beta_c = 1500 \text{ K.s}^{-1}$)
1	0.1 ± 0.1	0.2 ± 0.2	4.4 ± 0.3
10	0.3 ± 0.2	0.5 ± 0.3	5.0 ± 0.5
100	0.8 ± 0.2	0.7 ± 0.3	6.2 ± 0.5

III.4.2 Sample geometries

In a second approach, the gap of enthalpy recovery observed initially between FSC and standard DSC might also be explained by the sample geometry, i.e. the ratio between the surface area and the volume noted SA:V. As the relaxation process involved during the physical aging is believed to be driven by a free volume hole diffusion towards surfaces, if the sample geometry is only considered, namely the external surfaces, accelerated aging process might be expected by FSC, as observed for polymer thin films [27][28][29][30] or polymer nano-composites [33][34][35], due to the few ng of sample analyzed, in other words due to an increase of SA:V value. Figure III.4.2 presents the enthalpy recoveries measured by FSC and standard DSC as a function of SA:V values related to different samples with different masses. As highlighted above in Table III.4.1, the same enthalpy recovery is measured from FSC and standard DSC when $\beta_c = 0.17 \text{ K.s}^{-1}$, independently of the SA:V values. In the same way, an increase of the enthalpy recovery is recorded for $\beta_c = 1500 \text{ K.s}^{-1}$. For example, the enthalpy recovery measured is around 1 J/g for a glass formed at $\beta_c = 0.17 \text{ K.s}^{-1}$ and aged 100 min, when it goes up to around 6 J/g for a glass formed at $\beta_c = 1500 \text{ K.s}^{-1}$ and aged during the same duration 100 min. However, as pointed out by Cangialosi et al., the thickness influencing the physical aging of polystyrene films is only measured from few microns down to nanometers (2 μm to 29 nm), in other words below a critical thickness L_c [36]. As the sample thickness investigated by our FSC experiments are ranging from 19 μm down to 2 μm , the same enthalpy recovery measured from standard DSC and FSC correlates with the idea that none influence of the SA:V (namely the thickness) is observed on the structural relaxation when the same cooling rate is used between both techniques. It attests that acceleration of the aging process observed by FSC is related to the high level of enthalpy, or free volume, induced by the high cooling rate available [24][37].

Even if the acceleration of the physical aging is now confirmed by FSC thanks to the high cooling rate used, we want to pay attention on the enthalpy recovery measured after an aging duration of 1 min with the 260 ng sample (series of points in the orange ellipse in Figure III.4.2).

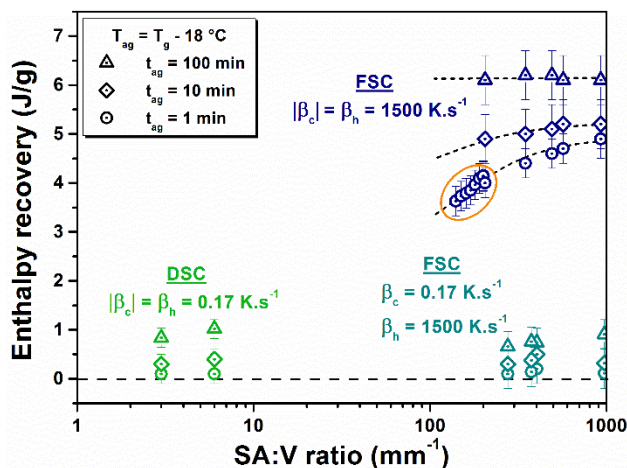


Figure III.4.2: Enthalpy recovery measured by FSC and standard DSC as a function of the SA:V ratio. By DSC, the glasses investigated were formed at $\beta_c = 0.17 \text{ K.s}^{-1}$. By FSC, the glasses were formed at $\beta_c = 1500 \text{ K.s}^{-1}$, as well as $\beta_c = 0.17 \text{ K.s}^{-1}$ to investigate the cooling rate influence.

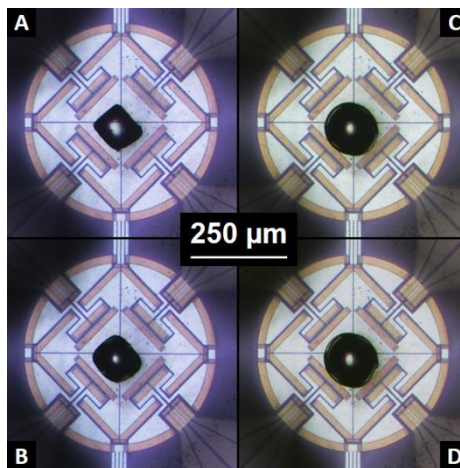


Figure III.4.3: Wetting evolution of 260 ng PLA sample. **(A)** After first heating at $\beta_h = 1500 \text{ K.s}^{-1}$ from $-50 \text{ }^\circ\text{C}$ to $230 \text{ }^\circ\text{C}$. **(B)** After 1 cycle. **(C)** After 7 cycles. **(D)** Chip stored overnight at room temperature and after 3 cycles (10 cycles in total).

Premelting by FSC experiments are usually done to improve the thermal contact between the sensor and the sample [8]. However, the sample changes from an uneven to an even shape, after preheating and melting, to reach a fine and stable geometry [38][39]. Such behaviors are depicted in Figure III.4.3. The sample shape evolves from a parallelepiped to a fine and stable disc after 10 cycles (1 cycle corresponds to two heat/cool ramps from $-50 \text{ }^\circ\text{C}$ to $230 \text{ }^\circ\text{C}$, as well as one physical aging step of 1 min $18 \text{ }^\circ\text{C}$ below T_g). By assuming a constant density, knowing the mass from calculation, and measuring the perimeter, we were able to figure out the thickness evolution induced from the different cycles, as well as the SA:V values. Table III.4.2 summarizes the different characteristic sizes after each cycle applied.

Table III.4.2: Evolution of the characteristic sizes of the 260 ng sample shape for the different temperature cycles applied.

Number of cycles	1	2	3	4	5	6	7	8	9	10
Surface on the sensor (.10 ² μm ²)	105	123	133	143	157	168	175	176	176	176
Perimeter (μm)	395	406	416	431	450	463	471	473	475	478
Thickness (μm)	19	17	15	14	13	12	12	12	12	12
Surface area to volume ratio (SA:V) (mm ⁻¹)	141	153	161	170	182	192	198	199	199	199

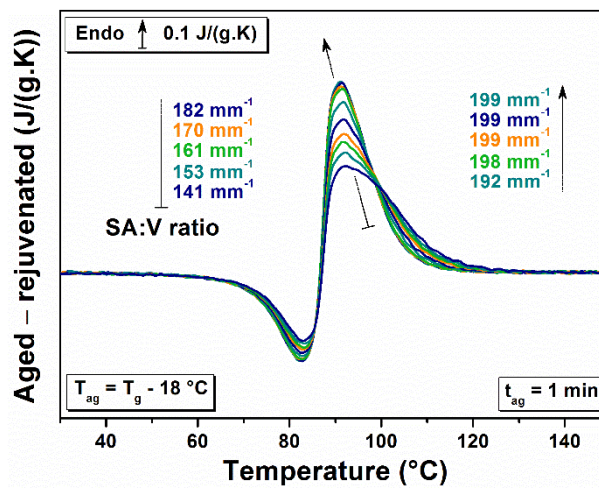
**Figure III.4.4:** FSC investigations of enthalpy recovery evolution as a function of SA:V for a 260 ng PLA sample aged at $T_{ag} = T_g - 18 \text{ }^\circ\text{C}$ with $t_{ag} = 1 \text{ min}$. The normalized heat flows subtraction (aged - rejuvenated) after different cycles at $|\beta_c| = \beta_n = 1500 \text{ K.s}^{-1}$ involves an evolution of SA:V leading to increase the relative enthalpy recovery χ_R as a function of SA:V.

Figure III.4.4 shows FSC investigations of enthalpy recovery evolution as a function of SA:V for the 260 ng PLA sample aged at $T_{ag} = T_g - 18 \text{ }^\circ\text{C}$ with $t_{ag} = 1 \text{ min}$. An increase of the amplitude of the endothermic peaks related to the physical aging is observed when the SA:V increases, even if the aging time remains constant. In order to quantify the SA:V influence on the aging process, we define a relative enthalpy recovery χ_R by the equation III.4.1:

$$\chi_R = \frac{\Delta H_{SA:V} - \Delta H_{141}}{\Delta H_{141}} \quad (\text{III.4.1})$$

where $\Delta H_{SA:V}$ and ΔH_{141} are the enthalpy recovery for a given SA:V value and the enthalpy recovery measured for SA:V equal to 141 mm^{-1} (cycle 1), respectively. An improvement close to 14 % of χ_R is observed when SA:V increases from 141 mm^{-1} to 199 mm^{-1} . This χ_R increase does correlate with the hypothesis that the diffusion of free volume holes to the surface is the driving forces of the physical aging [27][35]. As the final thickness dropped from $19 \text{ }\mu\text{m}$ to $12 \text{ }\mu\text{m}$ after 10 cycles, it is clear that the critical thickness L_c influencing the acceleration of the physical aging is cooling rate dependent. Indeed, thanks to the high cooling rate used by FSC, the thickness influencing the physical aging is superior to the critical one L_c observed by standard DSC in the case of polystyrene films [36]. This is an important result and we show here that the acceleration of physical aging could be observed for thicker sample presenting a high level of enthalpy. In addition, that series of points recorded from the 260 ng sample match with the trend of enthalpy recovery measured from the other samples presenting higher SA:V values (see \odot symbols in Figure III.4.2). An increase of 15 % is observed when the SA:V value increases from 200 mm^{-1} up to 1000 mm^{-1} . Such behavior is still depicted by aging time of 10 min, with an increase of 10 % in the enthalpy recovery. However, for longer aging times, namely $t_{ag} = 100 \text{ min}$, the enthalpy recoveries reached do not seem to be affected by the SA:V values. A constant value of enthalpy recovery close to 6 J/g is measured, independently of the SA:V values.

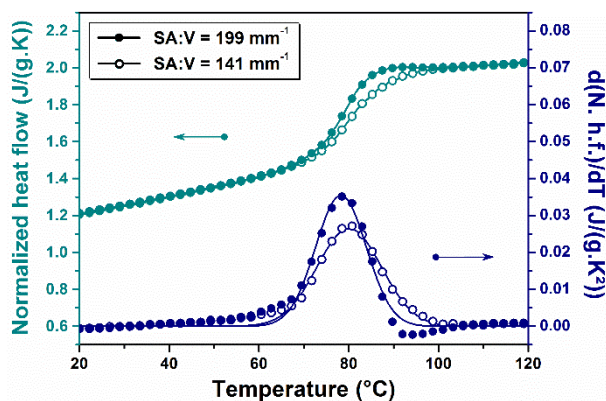


Figure III.4.5: Molecular dynamic investigations by FSC, as a function of SA:V value for a 260 ng fully amorphous PLA. Normalized heat flows and their derivatives of unaged sample at a scanning rate $|\beta_c| = \beta_h = 1500 \text{ K}\cdot\text{s}^{-1}$ with SA:V = 141 mm^{-1} (circles) and SA:V = 199 mm^{-1} (discs).

Moreover, one can notice that the endothermic peaks become less broadened when SA:V value increases (Figure III.4.4). Indeed, as shown in Figure III.4.5, a decrease of the width at the middle height observed on the derivative normalized heat flow curves for SA:V = 199

mm^{-1} , in comparison to a $\text{SA:V} = 141 \text{ mm}^{-1}$, could be related to a decrease of the heterogeneity in terms of molecular mobility at the glass transition [40]. However, as shown in literature by means of AC-chip calorimeter for thin polystyrene films [41], the dynamic glass transition is thickness independent down to 10 nm. As presented above, the recovery of equilibrium is driven by a free hole diffusion from the external interfaces towards the core. Consequently, samples with high SA:V value (199 mm^{-1}) will present more homogeneous recovery of equilibrium when heated up because the equilibration of the core will not be significantly delayed in comparison to the external interfaces. On the contrary, samples with small SA:V value (141 mm^{-1}) will present a delay, and thus will exhibit a more heterogeneous recovery of equilibrium as observed in Figure III.4.5. These observations evidence that the acceleration of physical aging observed is not related to the modification of the molecular mobility.

III.5 Structural relaxation of wholly amorphous PLA over 6 decades

Up to this point, the accelerated physical aging has been observed only in the case of glasses presenting a high level of enthalpy induced by the quenching. As highlighted above, a difference of 80 to 90 % in the enthalpy recovery is recorded between standard DSC and FSC, respectively between a cooling at 0.17 K.s^{-1} and 1500 K.s^{-1} . Consequently, from the high cooling rate of FSC, are the accelerated kinetics provide access to the whole structural relaxation?

Figure III.5.(1)-(2)-(3) displays standard DSC and FSC normalized heat flows of aged PLA up to 1000 min, $5 \text{ }^\circ\text{C}$, $8 \text{ }^\circ\text{C}$, $13 \text{ }^\circ\text{C}$, $18 \text{ }^\circ\text{C}$ and $23 \text{ }^\circ\text{C}$ below the respective T_g . The same endothermic relaxation peak evolutions, than those described in Figure III.4.1 are observed from FSC and standard DSC. In these three cases, endothermic relaxation peaks increase and shift towards high temperatures when the aging times increase, as classically observed for PLA [22][23][42][43] and other systems [44]. Besides, no variation of the glass transition, as well as of the heat capacity step, are detected from rejuvenated scans, either by FSC or standard DSC. In the case of $|\beta_c| = \beta_h$, endothermic peaks are more intense and broadened by FSC than those observed by standard DSC for a same aging duration. Besides, two opposite behaviors are observed when the aging temperature decreases. By standard DSC, the highest enthalpy recovery reached during the physical aging goes through a given temperature. Thus, $23 \text{ }^\circ\text{C}$

below the glass transition, namely below that given temperature, the enthalpy recovery measured in standard DSC drops due to a lack of mobility. On the contrary, by FSC the smaller the aging temperature, the higher the enthalpy recovery. By FSC, when $\beta_c = 0.17 \text{ K}\cdot\text{s}^{-1}$, the endothermic peaks are more intense and broadened due to the addition of the overshoot. However, the same phenomenon than the one observed in standard DSC is observed, namely a drop of the enthalpy recovery below a given temperature. Thus, the cooling rate does play a role on the structural relaxation process.

For standard DSC and FSC, Figure III.5.4 depicts the drops of the enthalpy during physical aging for the five aging temperatures investigated. The difference between the total enthalpy loss ΔH_∞ and the enthalpy recovery ΔH_{tag} at a given aging time displays different behaviors. Despite the different techniques used, similarities are also observed when the cooling rate is the same, as shown in Figure III.5.4.A. Indeed, by standard DSC and FSC, for $\beta_c = 0.17 \text{ K}\cdot\text{s}^{-1}$, the decays of the enthalpy during the physical aging are exactly the same in kinetics. It is worth mentioning that the few ng analyzed by FSC are totally representative of the bulk sample analyzed by DSC. Furthermore, we observe slower kinetics compared to glasses formed at $\beta_c = 1500 \text{ K}\cdot\text{s}^{-1}$. Thus, for given aging time and temperature, the enthalpy recovery reached is much lower. As an example, the total enthalpy loss is reached after 1 min 5 °C below T_g for a cooling rate of $\beta_c = 1500 \text{ K}\cdot\text{s}^{-1}$, when almost none structural relaxation is observed after 1 min 5 °C below T_g for a lower colling rate of $\beta_c = 0.17 \text{ K}\cdot\text{s}^{-1}$. Besides, the enthalpy recovery measurement is only possible for aging times down to 1 min, whereas with a glass cooled down at $\beta_c = 1500 \text{ K}\cdot\text{s}^{-1}$ the measurement of enthalpy recovery for shorter aging times down to 0.001 min is possible, due to the formation of a high fictive temperature glass having very short relaxation time [45]. The enthalpy recovery is driven by a single step decay. However, the decay follows a well-known stretched tendency. Such physical aging processes are classically observed for glassy polymers [33][46][47].

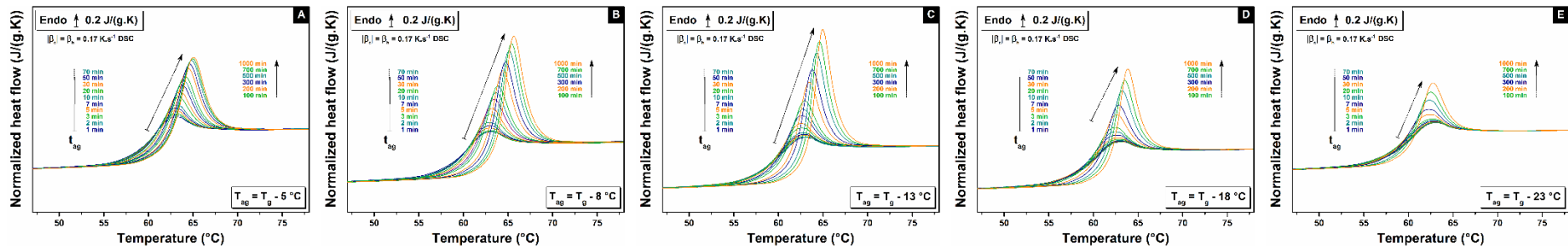


Figure III.5.1: Aged amorphous PLA investigations by standard DSC performed at a scanning rate of $|\beta_c| = \beta_h = 0.17 \text{ K.s}^{-1}$ for aging times ranging from 1 min to 1000 min. (A) $T_{ag} = T_g - 5 \text{ }^\circ\text{C}$ (B) $T_{ag} = T_g - 8 \text{ }^\circ\text{C}$ (C) $T_{ag} = T_g - 13 \text{ }^\circ\text{C}$ (D) $T_{ag} = T_g - 18 \text{ }^\circ\text{C}$ (E) $T_{ag} = T_g - 23 \text{ }^\circ\text{C}$.

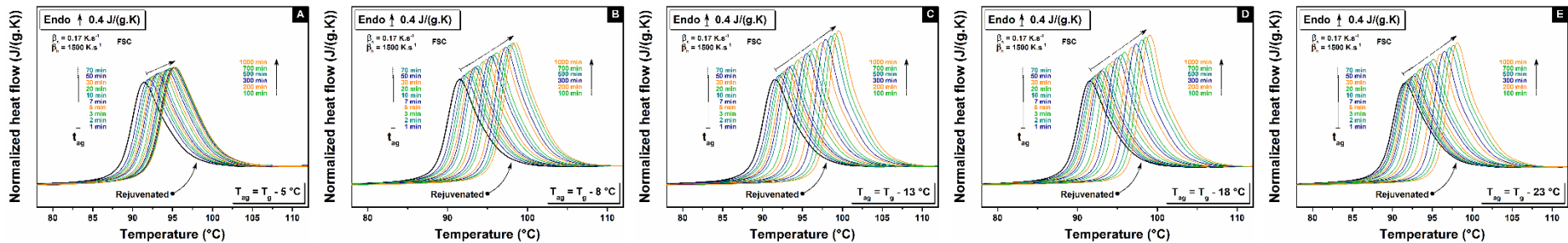


Figure III.5.2: Aged amorphous PLA investigations by FSC performed at a scanning rate of $\beta_c = 0.17 \text{ K.s}^{-1}$ and $\beta_h = 1500 \text{ K.s}^{-1}$ for aging times ranging from 1 min to 1000 min. (A) $T_{ag} = T_g - 5 \text{ }^\circ\text{C}$ (B) $T_{ag} = T_g - 8 \text{ }^\circ\text{C}$ (C) $T_{ag} = T_g - 13 \text{ }^\circ\text{C}$ (D) $T_{ag} = T_g - 18 \text{ }^\circ\text{C}$ (E) $T_{ag} = T_g - 23 \text{ }^\circ\text{C}$.

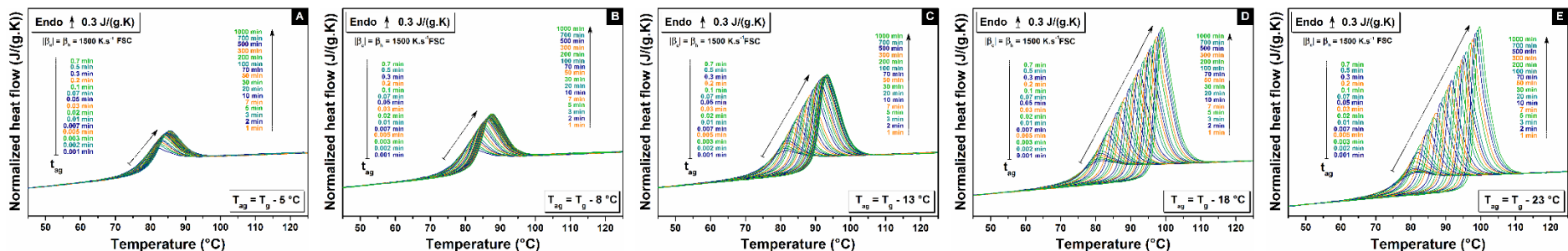


Figure III.5.3: Aged amorphous PLA investigations by standard DSC performed at a scanning rate of $|\beta_c| = \beta_h = 1500 \text{ K.s}^{-1}$ for aging times ranging from 0.001 min to 1000 min. (A) $T_{ag} = T_g - 5 \text{ }^\circ\text{C}$ (B) $T_{ag} = T_g - 8 \text{ }^\circ\text{C}$ (C) $T_{ag} = T_g - 13 \text{ }^\circ\text{C}$ (D) $T_{ag} = T_g - 18 \text{ }^\circ\text{C}$ (E) $T_{ag} = T_g - 23 \text{ }^\circ\text{C}$.

Then, in Figure III.5.4.B, the structural relaxation of PLA through FSC for $\beta_c = 1500 \text{ K}\cdot\text{s}^{-1}$ exhibits two main characteristics. At the closer temperatures to T_g , the enthalpy recovery shows a standard single step decay towards equilibrium. In the range of aging time investigated, the glass is allowed to completely relax its excess of energy. The enthalpy recovery measured does match with the total enthalpy loss extrapolated from the melt. This result contrasts with the ideas of J.L. Gomez Ribelles et al. [48][49] who consider that the thermodynamic equilibrium cannot be reached due to the steric hindrances and the cooperativity of the molecular mobility induced during the structural relaxation. It also contrasts with J.M. Hutchinson et al. [50] who consider that only a certain fraction of the glass-forming liquid is vitrified through the glass transition. Thus, the thermodynamic equilibrium cannot be reached due to two kinds of processes involved (slow for the vitrified fraction and fast for the non-vitrified one). FSC shows that high enthalpy glasses allow to reach the thermodynamic equilibrium. At the farther temperatures below T_g , the enthalpy recovery is also driven by a single step decay. The aging time investigated does not allow to reach the equilibrium. Besides, no induction time, as well as no plateau, are observed for the aging time investigated.

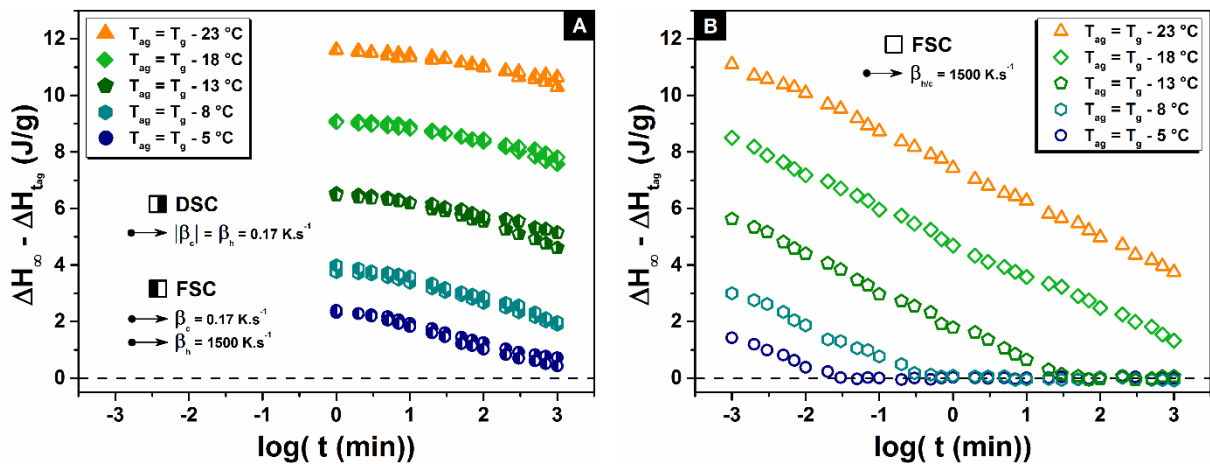


Figure III.5.4: Time evolution of the difference between the total enthalpy loss ΔH_{∞} and the enthalpy recovery $\Delta H_{t_{ag}}$ for the aged amorphous PLA at the five aging temperatures: $T_{ag} = T_g - 5 \text{ }^{\circ}\text{C}$ (blue circle), $T_{ag} = T_g - 8 \text{ }^{\circ}\text{C}$ (cyan hexagone), $T_{ag} = T_g - 13 \text{ }^{\circ}\text{C}$ (dark green pentagone), $T_{ag} = T_g - 18 \text{ }^{\circ}\text{C}$ (green square) and $T_{ag} = T_g - 23 \text{ }^{\circ}\text{C}$ (orange triangle). (A) Half-filled symbols: FSC and standard DSC experiments $\beta_c = 0.17 \text{ K}\cdot\text{s}^{-1}$. (B) Empty symbols: FSC experiments $\beta_c = 1500 \text{ K}\cdot\text{s}^{-1}$.

As mentioned above, the kinetics of the structural recovery are different from high to low enthalpy glasses. The comparison between both systems can be done by considering the same gap ΔT between the aging temperature T_{ag} and the fictive temperature T_f or the same

aging temperature T_{ag} , as depicted in Figure III.5.5. In the first case, as the step heat capacity is the same, the path to reach the equilibrium is the same in both systems independently of the cooling rate used, as observed in Figure III.5.5.A. In such configuration, it is clear that high cooling rate leads to more enthalpy, and more free volume in the glass, than low cooling rate. Thus, the diffusion related to the structural recovery is higher. As a consequence, the time needed to reach the equilibrium is shorter for high enthalpy glasses than low enthalpy glasses. In the second case, the step heat capacity is still the same, but the gap ΔT is higher for high enthalpy glasses due to the higher fictive temperatures, as presented in Figure III.5.5.B. Thus, higher the fictive temperature, higher the total enthalpy loss. Obviously, the low enthalpy glasses present a shorter path to reach the equilibrium than the high enthalpy glasses. However, the time needed to reach the equilibrium is shorter for the high enthalpy glasses. In literature [8][14], cooling rate β_c and relaxation rate τ are related by the Frenkel-Kobeko-Reiner relationship $\beta_c \cdot \tau = C$, where C is a constant. Thus, high cooling rates lead to short relaxation times. This might be explained by the fact that high enthalpy glasses do not present an induction time for structural relaxation, as observed in Figure III.5.4. The high fictive temperatures allow very short aging times for structural recovery. On the contrary, relative long induction times are needed for low enthalpy glasses. As a consequence, if only the aging temperature is considered, the acceleration of the structural relaxation might be related to the non-induction involved by the high fictive temperature.

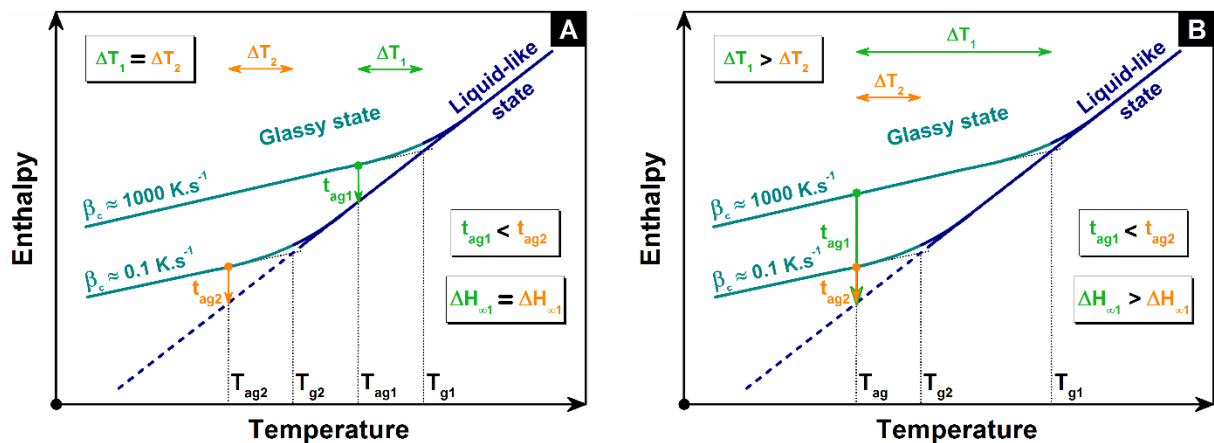


Figure III.5.5: Schematic illustration of the temperature dependence of the enthalpy in the liquid-like state and the glassy state, as well as its evolution during structural recovery at aging temperature T_{ag} . The comparison is made between high (FSC $\approx 1000 \text{ K.s}^{-1}$) and slow (FSC or DSC $\approx 0.1 \text{ K.s}^{-1}$) cooling rates for the glasses investigated in the cases where (A) the difference ΔT between the glass transition temperature T_g and the aging temperature T_{ag} are the same, and (B) the aging temperature T_{ag} is the same.

III.6 Conclusion

Glass transition temperature is a significant parameter for further physical aging investigations. In that purpose, the observation of a constant fictive temperature, after thermal lag corrections, for cooling rates ranging from 300 K.s⁻¹ to 4000 K.s⁻¹ led us to investigate the physical aging in PLA by means of FSC and standard DSC. Aging investigations, just below the glass transition, depicts a significant influence of the cooling rate used to vitrify the glass: a gap of 80 to 90 % has been observed between standard DSC and FSC and, when glasses are vitrified at $\beta_c = 0.17 \text{ K.s}^{-1}$ and $\beta_c = 1500 \text{ K.s}^{-1}$, respectively. Such behaviors have been explained by an acceleration of the structural recovery for high cooling rates. Besides, for short aging times, an influence of the sample SA:V value has been measured. The critical thickness involving an acceleration of the structural recovery seems to be cooling rate dependent. Aging investigations for glasses formed at the same cooling rate independently of the techniques show that the few ng of sample analyzed by FSC are well representative of the bulk sample analyzed by DSC. Furthermore, thanks to the high cooling rates accessible by means of FSC, thermodynamic equilibrium has been reached after few minutes to few hours, which is impossible by standard DSC in the laboratory time scale. Such experimental observations open new possibilities for physical aging on complex systems, as it will be discussed in the next chapter.

REFERENCES

- [1] C. T. Moynihan, P. B. Macedo, C. J. Montrose, P. K. Gupta, M. A. DeBolt, J. F. Dill, B. E. Dom, P. W. Drake, A. J. Easteal, P. B. Elterman, R. P. Moeller, H. Sasabe, and J. A. Wilder, *Ann. N. Y. Acad. Sci.* **279**, 15 (1976).
- [2] V. Mathot, M. Pyda, T. Pijpers, G. Vanden Poel, E. van de Kerkhof, S. van Herwaarden, F. van Herwaarden, and A. Leenaers, *Thermochim. Acta* **522**, 36 (2011).
- [3] E. Verdonck, K. Schaap, and L. C. Thomas, *Int. J. Pharm.* **192**, 3 (1999).
- [4] S. Gao and S. L. Simon, *Thermochim. Acta* **603**, 123 (2015).
- [5] G. Tammann and W. Hesse, *Z. Für Anorg. Allg. Chem.* **156**, 245 (1926).
- [6] G. S. Fulcher, *J. Am. Ceram. Soc.* **8**, 339 (1925).
- [7] *J. Chem. Phys.* **141**, 184905 (2014).
- [8] J. E. K. Schawe, *Thermochim. Acta* **603**, 128 (2015).
- [9] C. Schick and V. Mathot, editors, *Fast Scanning Calorimetry* (Springer International Publishing, Cham, 2016).
- [10] G. V. Poel, D. Istrate, A. Magon, and V. Mathot, *J. Therm. Anal. Calorim.* **110**, 1533 (2012).
- [11] J. E. K. Schawe, *J. Therm. Anal. Calorim.* **116**, 1165 (2013).
- [12] S. Gao, Y. P. Koh, and S. L. Simon, *Macromolecules* **46**, 562 (2013).
- [13] N. Shamim, Y. P. Koh, S. L. Simon, and G. B. McKenna, *J. Polym. Sci. Part B Polym. Phys.* **52**, 1462 (2014).
- [14] A. Dhotel, B. Rijal, L. Delbreilh, E. Dargent, and A. Saiter, *J. Therm. Anal. Calorim.* **121**, 453 (2015).
- [15] X. Cao, A. Mohamed, S. H. Gordon, J. L. Willett, and D. J. Sessa, *Thermochim. Acta* **406**, 115 (2003).
- [16] N. Delpouve, A. Saiter, and E. Dargent, *Eur. Polym. J.* **47**, 2414 (2011).
- [17] L. C. E. Struik, *Polym. Eng. Sci.* **17**, 165 (1977).
- [18] M. Arnoult, E. Dargent, and J. F. Mano, *Polymer* **48**, 1012 (2007).
- [19] J. F. Mano, J. L. Gómez Ribelles, N. M. Alves, and M. Salmerón Sanchez, *Polymer* **46**, 8258 (2005).
- [20] D. Cangialosi, M. Wübbenhorst, J. Groenewold, E. Mendes, H. Schut, A. van Veen, and S. J. Picken, *Phys. Rev. B* **70**, 224213 (2004).
- [21] D. Cangialosi, M. Wübbenhorst, J. Groenewold, E. Mendes, and S. J. Picken, *J. Non-Cryst. Solids* **351**, 2605 (2005).
- [22] L. Dobircau, N. Delpouve, R. Herbinet, S. Domenek, L. Le Pluart, L. Delbreilh, V. Ducruet, and E. Dargent, *Polym. Eng. Sci.* **55**, 858 (2015).
- [23] P. Pan, B. Zhu, and Y. Inoue, *Macromolecules* **40**, 9664 (2007).
- [24] H. C. Booij and J. H. M. Palmén, *Polym. Eng. Sci.* **18**, 781 (1978).
- [25] A. R. Berens and I. M. Hodge, *Macromolecules* **15**, 756 (1982).
- [26] C. M. Laot, E. Marand, B. Schmittmann, and R. K. P. Zia, *Macromolecules* **36**, 8673 (2003).
- [27] Y. Huang and D. R. Paul, *Macromolecules* **39**, 1554 (2006).
- [28] Y. Huang and D. R. Paul, *Polymer* **45**, 8377 (2004).
- [29] K. D. Dorkenoo and P. H. Pfromm, *J. Polym. Sci. Part B Polym. Phys.* **37**, 2239 (1999).
- [30] K. D. Dorkenoo and P. H. Pfromm, *Macromolecules* **33**, 3747 (2000).
- [31] M. S. McCaig and D. R. Paul, *Polymer* **41**, 629 (2000).
- [32] P. H. Pfromm and W. J. Koros, *Polymer* **36**, 2379 (1995).

- [33] V. M. Boucher, D. Cangialosi, A. Alegría, and J. Colmenero, *Macromolecules* **43**, 7594 (2010).
- [34] V. M. Boucher, D. Cangialosi, A. Alegría, J. Colmenero, I. Pastoriza-Santos, and L. M. Liz-Marzan, *Soft Matter* **7**, 3607 (2011).
- [35] D. Cangialosi, V. M. Boucher, A. Alegría, and J. Colmenero, *Polymer* **53**, 1362 (2012).
- [36] V. M. Boucher, D. Cangialosi, A. Alegría, and J. Colmenero, *Macromolecules* **45**, 5296 (2012).
- [37] L. C. E. Struik, *Polym. Eng. Sci.* **17**, 165 (1977).
- [38] Y. Furushima, M. Nakada, H. Takahashi, and K. Ishikiriyama, *Polymer* **55**, 3075 (2014).
- [39] R. Pilar, P. Honcová, G. Schulz, C. Schick, and J. Málek, *Thermochim. Acta* **603**, 142 (2015).
- [40] X. Monnier, N. Delpouve, N. Basson, A. Guinault, S. Domenek, A. Saiter, P. E. Mallon, and E. Dargent, *Polymer* **73**, 68 (2015).
- [41] H. Huth, A. A. Minakov, and C. Schick, *J. Polym. Sci. Part B Polym. Phys.* **44**, 2996 (2006).
- [42] A. Celli and M. Scandola, *Polymer* **33**, 2699 (1992).
- [43] K. Liao, D. Quan, and Z. Lu, *Eur. Polym. J.* **38**, 157 (2002).
- [44] J. M. Hutchinson, *Prog. Polym. Sci.* **20**, 703 (1995).
- [45] Y. P. Koh, L. Grassia, and S. L. Simon, *Thermochim. Acta* **603**, 135 (2015).
- [46] V. M. Boucher, D. Cangialosi, A. Alegría, and J. Colmenero, *Macromolecules* **44**, 8333 (2011).
- [47] Y. P. Koh and S. L. Simon, *Macromolecules* **46**, 5815 (2013).
- [48] J. L. Gomez Ribelles and M. Monleon Pradas, *Macromolecules* **28**, 5867 (1995).
- [49] M. S. Sánchez, Y. Touzé, A. Saiter, J. M. Saiter, and J. L. G. Ribelles, *Colloid Polym. Sci.* **283**, 711 (2004).
- [50] J. M. Hutchinson, S. Montserrat, Y. Calventus, and P. Cortés, *Macromolecules* **33**, 5252 (2000).

CHAPTER IV

Structural anisotropy investigations through PLA flow induced crystalline structures: molecular dynamics from local to segmental scales

Parts of this chapter are extracted from:

Local and segmental motions of the mobile amorphous fraction in semi-crystalline polylactide crystallized under quiescent and flow-induced conditions

*X. Monnier, L. Chevalier, A. Esposito, L. Fernandez-Ballester, A. Saiter, E. Dargent
Polymer 126 (2017) 141-151*

CONTENTS

IV.1 Conventional vs. unconventional crystallization	94
IV.2 Thermal and microstructural properties	98
IV.3 Characteristic length at the glass transition	100
IV.4 Structural relaxation below the glass transition	103
IV.5 From local to segmental molecular motions	109
IV.6 Conclusion	110
References.....	112

The fourth chapter of this work deals with the influence of the structural anisotropy induced during the processing on crystalline systems. In order to achieve such investigation, flow induced crystallization has been used. As explained in the chapter I, the goal was to observe the impact of the molecular orientation prior to crystallization and vitrification on the molecular dynamics of the amorphous phase. First, lifetime of the crystal nuclei precursors induced by shear has been investigated to achieve flow induced crystalline structures. Conventional crystallization has also been studied. Special attention has been done on the characterization of the crystalline morphology as well as the thermal and microstructural properties through Polarized Optical Microscope (POM), Scanning Electronic Microscope (SEM) and Fast Scanning Calorimetry (FSC). Molecular dynamics have been characterized at the glass transition through the approach of Donth as well as in the glassy state through the phenomenon of structural relaxation.

IV.1 Conventional vs. unconventional crystallization

IV.1.1 Impact of the crystal nuclei precursors

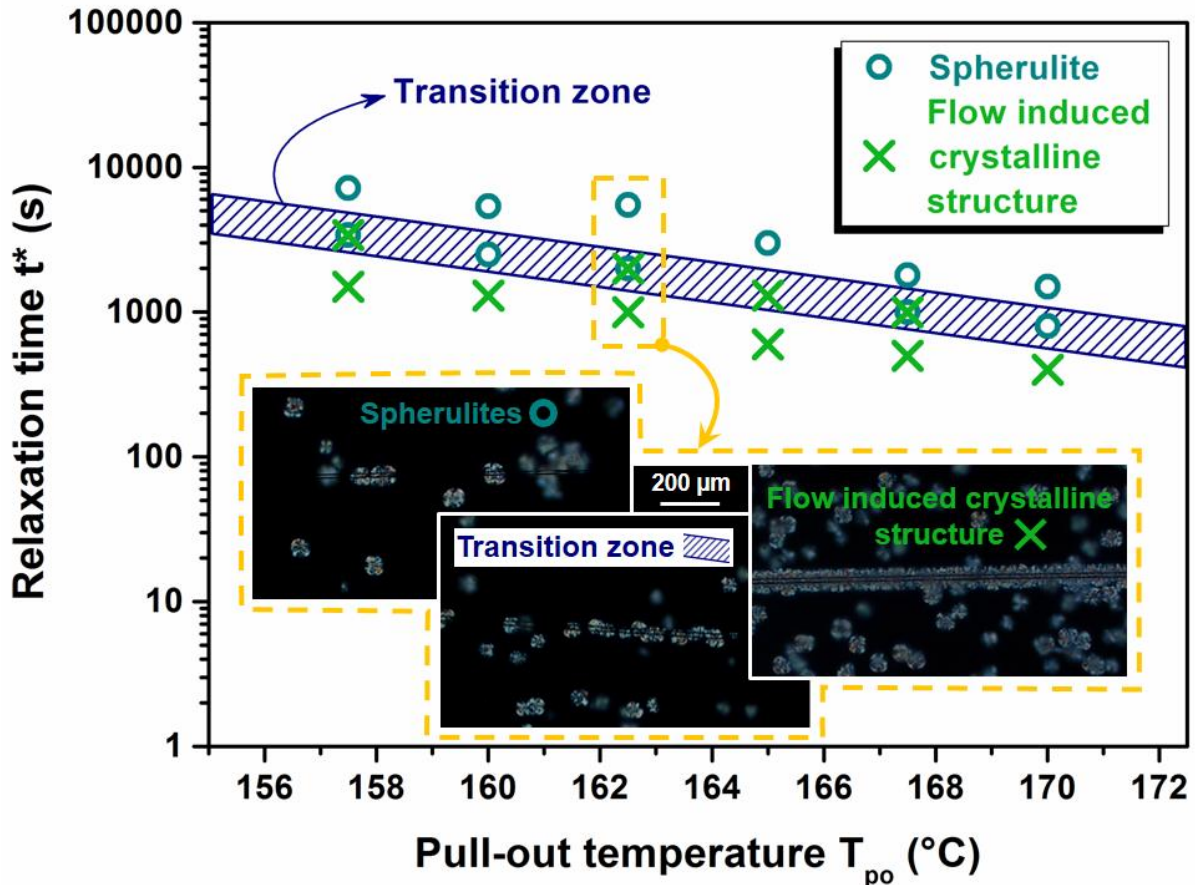


Figure IV.1.1: Relaxation time of the precursors (t^*) as a function of the pull-out temperature (T_{po}). For “long” relaxation time (cyan circle), the precursors relax and spherulites (SPE) are obtained. For “short” relaxation time, the precursors lead to flow-induced crystalline structures (FICS) (green crosses). For intermediate times, both SPE and FICS are observed and a transition zone can be defined (blue dashed area). The different behaviors are depicted for $T_{po} = 162.5$ °C by polarized optical microscopy.

As explained in the Chapter I, numerous investigations have been done on flow induced crystallization with PLA. By tailoring crystal morphology and lamellae orientation, physical properties of PLA, such as gas barrier properties or mechanical properties, have been improved. Flow induced crystallization in PLA has been reported in the presence of steady [1][2][3][4] or oscillating [5][6][7] shear conditions during injection molding, but also evidenced by pulling fibers [8][9]. The latter procedure is the easiest way to produce shear flows with significantly high shear rates up to ≈ 1500 s^{-1} [9]. However, to our knowledge, the lifetime of shear-induced crystal nucleation precursors in PLA has not been previously

investigated. Due to their metastability, the existence of shear-induced precursors is time and temperature dependent, as already observed for other polymers such as polypropylene, poly(1-butene), poly(ethylene oxide) or polystyrene [10]. In this work, the lifetime (i.e. the relaxation time) of PLA shear-induced precursors has been investigated in the temperature range where melting of semi-crystalline PLA is typically reported [11][12][13] in order to mimic the shear flow conditions typically applied during industrial processing prior to crystallization. The relaxation map in Figure IV.1.1 depicts the relaxation time of PLA shear-induced precursors (t^*) measured at different pull-out temperatures (T_{po}) and the type of morphology that develops after cooling to the crystallization temperature. Longer relaxation times above the “transition zone” in Figure IV.1.1 lead to only spherulites (SPE) because flow-induced precursors have completely relaxed, whereas for shorter relaxation times precursors are still present, which results in cylindrical flow-induced crystalline structures (FICS) near the fiber, i.e. in the region that was subjected to the highest shear stress. At intermediate times in the “transition zone”, there is much less enhanced nucleation near the fiber surface due to partial relaxation of flow-induced precursors, which results in a significant reduction of oriented structures. The different behaviors are depicted for $T_{po} = 162.5$ °C by polarized optical micrographs. It should also be noted that at higher pull-out and relaxation temperature, the critical relaxation time t_c^* for precursors decay becomes shorter, in agreement with relaxation studies performed on other polymers [10].

According to the relaxation map for PLA precursors in Figure IV.1.1, a pull-out temperature $T_{po} = 150$ °C is a judicious choice to obtain shear-induced precursors that do not significantly relax during cooling to the crystallization temperature $T_c = 130$ °C. Indeed, flow precursors would need at least a few hours to noticeably relax at 150°C. Therefore, fiber pull experiments for obtaining the maximum possible number density of shear-induced precursors are performed at $T_{po} = 150$ °C, with the purpose of examining the amorphous phase present within highly oriented structures and comparing its characteristics with the amorphous phase in conventional spherulites. This protocol also ensures that the cylindrical structure is not embedded within a “sea” of spherulites, facilitating its isolation for performing calorimetric experiments.

IV.1.2 From isotropic to anisotropic crystalline morphology

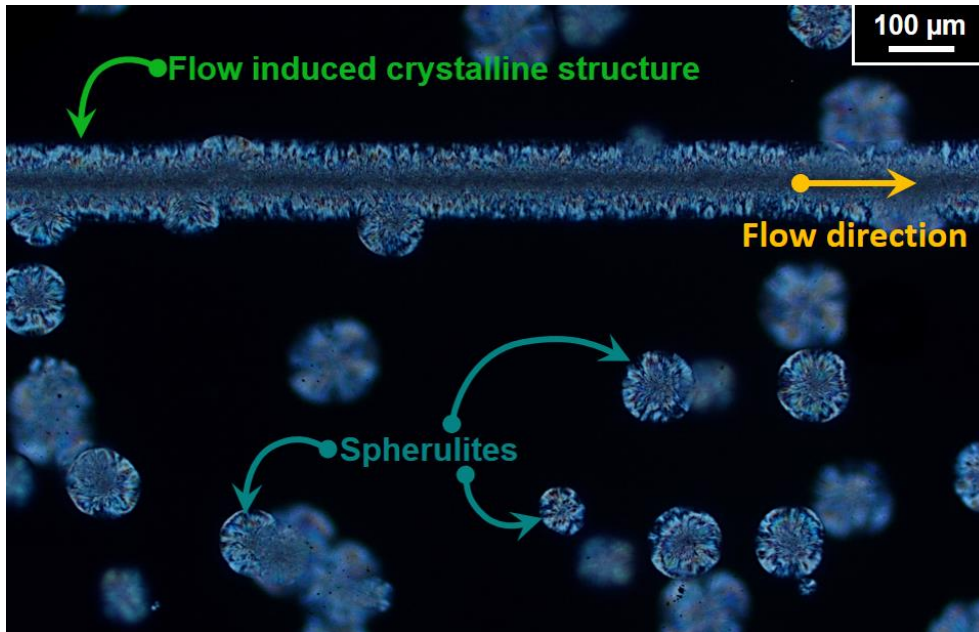


Figure IV.1.2: Polarized optical microscope picture of spherulites (SPE) and flow-induced crystalline structures (FICS) ($T_{po} = 150^{\circ}\text{C}$; $t^* \lll t_c^*$; $T_c = 130^{\circ}\text{C}$; $t_c = 90$ min). The glass fiber is completely pulled-out and the flow direction is symbolized by the yellow arrow.

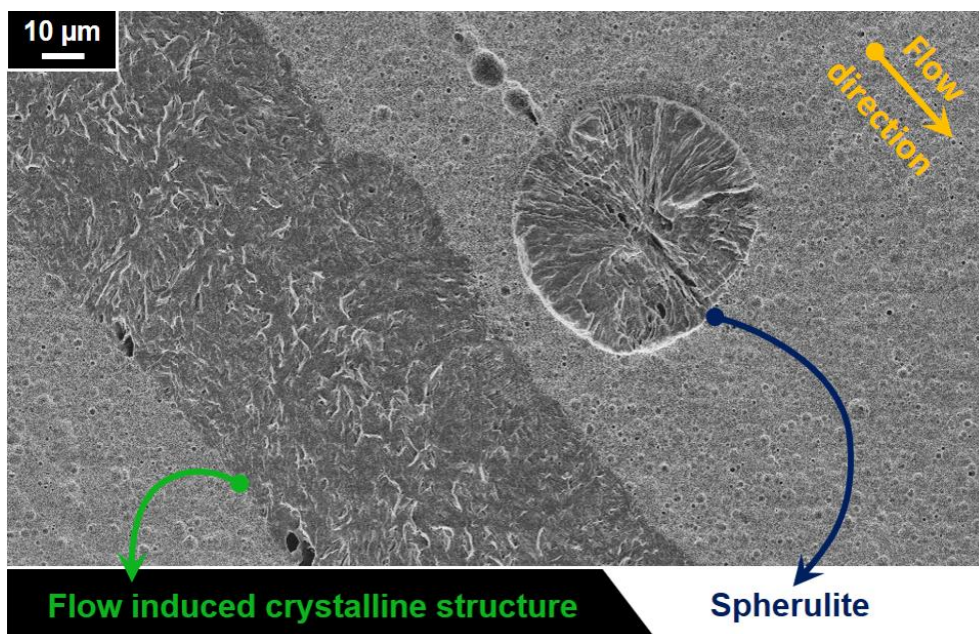


Figure IV.1.3: Scanning electron microscope picture of spherulites (SPE) and flow-induced crystalline structures (FICS) ($T_{po} = 150^{\circ}\text{C}$; $t^* \lll t_c^*$; $T_c = 130^{\circ}\text{C}$; $t_c = 90$ min). Prior to gold coating, the sample was trimmed by ultramicrotomy and chemically etched.

Figure IV.1.2 and Figure IV.1.3 show POM and SEM pictures of semi-crystalline PLA after being subjected to protocol 2, in which the fiber is fully pulled out of the polymer melt. Figure IV.1.2 shows that flow-induced precursors induced by pulling the glass fiber resulted in FICS, in the form of a cylindrical structure whose diameter reached approximately 100 μm after a crystallization time $t_c = 90$ min. The imposed shear rate strongly decreases with distance from the fiber, so no precursors are induced away from the pull-out region and only spherulites can be observed there. Note that the diameter of spherulites also reaches approximately 100 μm . Figure IV.1.3 showcases the differences between FICS and SPE through the contrast between amorphous and crystalline areas: lamellar growth in cylindrical FICS mostly occurred in the direction perpendicular to the flow—i.e. FICS are anisotropic—whereas SPE developed radially.

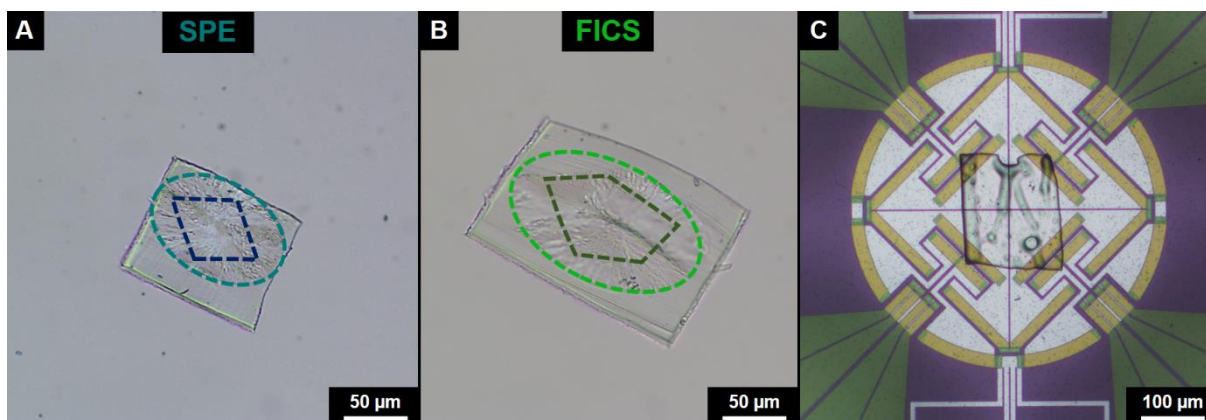


Figure IV.1.4: Optical microscope pictures of spherulite (SPE) and flow-induced crystalline structure (FICS) slices obtained by ultramicrotomy[‡] prior to FSC analysis (A-B), as well as an example of a slice of FICS placed on the FSC chip sensor after analysis (C). First, the sample within the ellipse plus the surrounding amorphous fraction were analyzed (“SCA” approach), then a fresh slice was used to further isolate the dashed polygon within the semi-crystalline structures (“SC” approach). The slices were 500 nm thick.

The differences between FICS and SPE, as well as their influence on the mobile amorphous fraction, have been investigated at the micro-scale, i.e. the typical length-scale of semi-crystalline structures, by FSC. Figure IV.1.4.A-B shows cross sectional slices of both FICS and SPE as obtained by ultramicrotomy prior to FSC analysis. In both slices, the semi-crystalline structure—indicated with a dashed ellipse—is surrounded by an amorphous matrix. Two approaches were used to investigate the amorphous fraction. First, in the so-called SCA approach, the whole sample (semi-crystalline structure along with surrounding amorphous

[‡] In order to perform analyses at the typical length-scale of the systems (SPE and FICS) by FSC, ultramicrotomy has been the only way to prepare the sample. Ultramicrotomy has been performed with the fruitful help of Laurence Chevalier (GPM).

matrix) was analyzed. Then, in the so-called SC approach, only a portion of the semi-crystalline structure was isolated and analyzed as indicated by the dashed polygon in Figure IV.1.4.A-B. Figure IV.1.4.C shows a slice of FICS after FSC analysis.

IV.2 Thermal and microstructural properties

Figure IV.2.1 reports FSC normalized heat flows recorded during the first and second heating ramps from 20 °C to 220 °C both for a slice of SPE and FICS. Figure IV.2.1.A shows the results of SCA investigations, whereas Figure IV.2.1.B shows the results of SC investigations. For all systems, the first heating ramp includes two thermal events: an endothermic step typical of the glass transition within the amorphous fraction, followed by an endothermic event related to the melting of the crystalline fraction. The second heating ramp reveals a system that is totally amorphous, as indicated by the increase in the magnitude of the heat flow step at the glass transition and the absence of the melting peak.

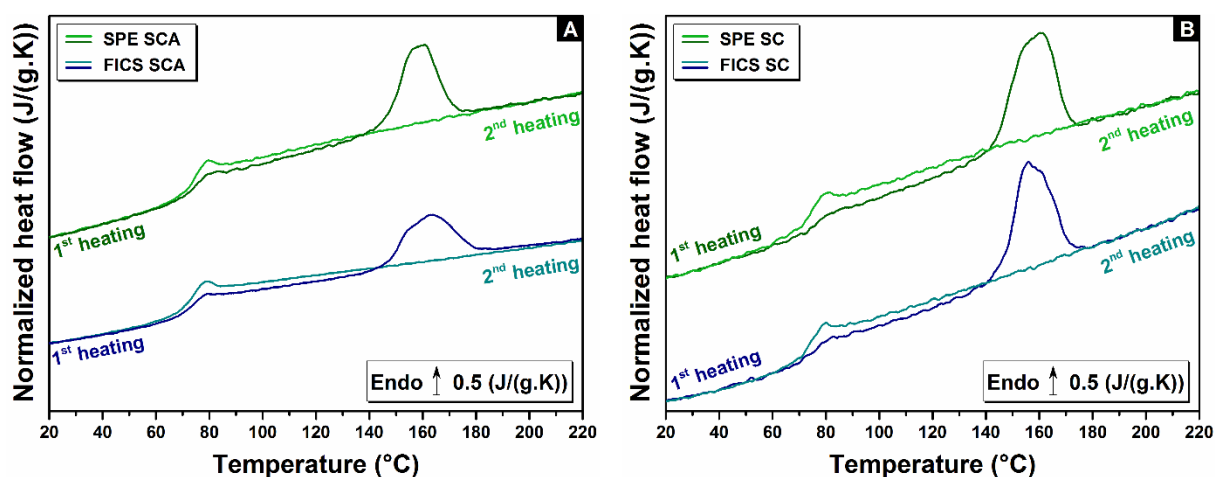


Figure IV.2.1: FSC normalized heat flows of the first and second heating ramps from 20 °C to 220 °C for spherulites (SPE) and flow-induced crystalline structures (FICS): (A) “SCA” approach vs. (B) “SC” approach.

Melting occurs as a very complex peak for both SPE and FICS, either within SCA or SC systems. When PLA is crystallized at 130 °C, only highly ordered α crystals are formed [14][15], as highlighted in the Chapter I. In addition, the use of high scanning rates ($1500 \text{ K}\cdot\text{s}^{-1}$) prevents any structural reorganization of the crystals, which means that the complexity of the melting peaks is only due to the complexity of the investigated semi-crystalline structures. Table IV.2.1 summarizes the values of enthalpy associated to the melting peaks observed during the first heating ramps in Figure IV.2.1, along with the physical properties measured at the glass

transition. The glass transition of wholly amorphous PLA was found to be 70.9 °C, with a step in heat capacity of 0.51 J/(g.K). This value was taken as a reference to estimate the mass of the sliced sample deposited onto the chip sensor, as described in the experimental section (section II.2.2.3). The mass of the sample was then used to correlate the step of heat capacity observed for the semi-crystalline systems with their respective degree of crystallinity. The glass transition temperature of the SCA systems reaches 72.7 °C and 72.9 °C respectively, with a step in heat capacity that drops to 0.35 J/(g.K) and 0.37 J/(g.K) for SPE and FICS respectively. The glass transition temperature of the SC systems reaches 74.2 °C and 74.1 °C respectively, with a step in heat capacity that drops to 0.32 J/(g.K) and 0.30 J/(g.K) for SPE and FICS respectively. Whatever the semi-crystalline morphology (SPE or FICS), the glass transition presents some similarities. The only parameter that differs is the amount of surrounding amorphous fraction, which explains the decrease in the step of heat capacity when comparing SCA and SC systems. The increase of the mid-point glass transition temperature of the SCA and SC systems with respect to wholly amorphous PLA (2 °C and 3 °C respectively) is due to the steric hindrances generated by the presence of the crystalline fraction.

From the enthalpy of melting reported in Table IV.2.1, the crystalline fraction X_c has been estimated according to the following equation:

$$X_c = \frac{\Delta H_m}{\Delta H_m^0} \quad (\text{IV.2.1})$$

in which ΔH_m and ΔH_m^0 are the enthalpy of melting and the enthalpy of a 100% crystallized PLA, respectively, determined from the recent formula proposed by Righetti et al. [16]. From the crystalline fraction X_c and the step of heat capacity at the glass transition ΔC_p , the mobile amorphous fraction X_{MAF} and the rigid amorphous fraction X_{RAF} have been estimated according to the following equations:

$$X_{MAF} = \frac{\Delta C_p}{\Delta C_p^0} \quad (\text{IV.2.2})$$

$$1 = X_{MAF} + X_{RAF} + X_c \quad (\text{IV.2.3})$$

in which $\Delta C_p^0 = 0.51 \text{ J.g}^{-1}.\text{K}^{-1}$ is the heat capacity step of wholly amorphous PLA.

Table IV.2.1: Thermal and microstructural properties measured while heating wholly amorphous, SPE and FICS systems, both with SCA and SC approaches: glass transition temperature T_{gmid} , heat capacity step ΔC_p , enthalpy of melting (ΔH_m), mobile amorphous fraction (X_{MAF}), crystalline fraction (X_c), and rigid amorphous fraction (X_{RAF}).

	T_{gmid} (°C ± 1)	ΔC_p (J/(g.K)) ± 0.05	ΔH_m (J/g ± 3)	X_{MAF} (% ± 5)	X_c (% ± 5)	X_{RAF} (% ± 10)
Amorphous	71	0.51	0	100	0	0
SPE SCA	73	0.35	24	69	18	13
FICS SCA	73	0.37	18	73	13	14
SPE SC	74	0.32	37	63	27	10
FICS SC	74	0.30	33	59	24	17

The values are summarized in Table IV.2.1. It is interesting to observe how the growth of either SPE or FICS has no influence on the apportionment of microstructural fractions. On average, SCA systems develop $X_{MAF} \approx 70\%$ and $X_c \approx 15\%$, whereas SC systems rather develop $X_{MAF} \approx 60\%$ and $X_c \approx 25\%$. Independently of the semi-crystalline morphology, and the approach used to investigate its microstructure, an average value of $X_{RAF} \approx 15\%$ is found. Apparently, the crystalline morphology plays no role during the competition between crystallization and vitrification. As observed by Righetti et al. [17][18], the establishment of the RAF depends on the crystallization temperature, i.e. on the molecular mobility of the polymer chains. These results show that the shear conditions imposed prior to crystallization only affected the kinetics and the morphology of the final crystalline structure, with no influence on the vitrification of the RAF (which appears to be influenced only by the temperature conditions).

IV.3 Characteristic length at the glass transition

Prior to FSC analysis, a visual estimation of the main microstructural areas developed in SCA systems has been performed by optical microscopy. The ratio of amorphous to semi-crystalline surface area was evaluated for both systems (SPE and FICS) from optical microscope pictures as displayed in Figure IV.1.4.A-B. Table IV.3.1 reports the fractions of surrounding amorphous matrix for SPE and FICS samples (35% and 50% respectively), namely the unconstrained mobile amorphous fraction X_{UCMAF} . However, mobile amorphous fractions X_{MAF} , measured by FSC, reach 69% and 73% for SPE and FICS, respectively. Thus, from optical microscopy and FSC analysis, a gap of 34% and 23% in the amorphous fractions, between SPE

and FICS respectively, is evidenced. This gap is related to constrained mobile amorphous fraction X_{CMAF} , within SPE and FICS, as depicted in Table IV.3.1.

Table IV.3.1: Visual estimation of amorphous and semi-crystalline areas on the slices of spherulite (SPE) and flow-induced crystalline structure (FICS) in Figure IV.1.4.A-B. Prior to thermal analysis, the total area A_{tot} , the semi-crystalline area A_{sc} , as well as the ratio of amorphous (A matrix) to semi-crystalline (SC structure) areas of the slice have been estimated by picture analysis. They highlight the unconstrained (X_{UCMAF}) and the constrained (X_{CMAF}) fractions representing the mobile amorphous fraction (X_{MAF}).

	$A_{\text{tot}} (\mu\text{m}^2)$	$A_{\text{sc}} (\mu\text{m}^2)$	A matrix (%)	SC structure (%)	$X_{\text{MAF}} = X_{\text{CMAF}} + X_{\text{UCMAF}} (\% \pm 5)$
SPE	10500 ± 300	6800 ± 100	35 ± 5	65 ± 5	$69 = 34 + 35$
FICS	21400 ± 700	10800 ± 200	50 ± 5	50 ± 5	$73 = 23 + 50$

Due to the competition between crystallization and vitrification, which defines the intrinsic properties of a spherulite, namely its semi-crystalline nature, constrained mobile amorphous regions prevail between crystalline lamellae. In the few past years, the existence of a so-called “intra-spherulitic mobile amorphous phase” has been shown for semi-crystalline polyesters such as PET and PLA [19][20][21], which behaves like a constrained amorphous fraction. Wang et al. [19] have shown for semi-crystalline PLA with several crystallinity degrees, different glass transition dynamics after structural relaxation. In particular, the process occurring at lower temperature was attributed to the bulk-like glass transition, whereas the process occurring at higher temperature was attributed to the glass transition of the amorphous fraction confined by the crystalline structures, i.e. the amorphous chains whose motions were hindered by the lamellar stacks. Later on, Delpouve et al. [20] investigated the relaxation dynamics of inter- and intra-spherulitic amorphous phases through the concept of Cooperative Rearranging Region (CRR) according to the thermodynamic approach proposed by Donth. The characteristic value of cooperativity length at the glass transition (3.0 nm for a wholly amorphous PLA) was found to decrease down to 2.0 nm when the maximum degree of crystallinity was reached. For intermediate degrees of crystallinity, the cooperativity length associated to the dynamics of both amorphous fractions was observed to decrease linearly from 3.0 nm down to 2.0 nm. It turned out that cooperativity could be correlated to the structural relaxation of the considered fractions [22]. By tracking the temperature evolution of the peak associated to the enthalpy recovery, they discussed the molecular dynamics of both inter- and intra-spherulitic amorphous phases and found it in agreement with the results previously published by Wang et al. [19]. In particular, the enthalpy recovery of the inter-spherulitic amorphous fraction was found to be similar to the one

observed for a wholly amorphous sample, whereas the enthalpy recovery of the intra-spherulitic amorphous fraction was found to depend on the degree of crystallinity. A system that is partially crystallized would show an enthalpy recovery whose maximum appears at lower temperatures with respect to the same system crystallized to the maximum extent. The temperature shift was attributed to differences induced by the crystallization process, that is to say secondary relaxation and development of the rigid amorphous fraction. In literature it has been shown that decreases in cooperativity can be associated to a decrease of the thickness of the mobile amorphous fraction confined within the crystal [23], as well as to isochoric [24] and multilayer [25] confinement. Thus, the molecular dynamics of the intra-spherulitic amorphous fraction depends on the lamellar thickness.

In addition to the aforementioned glass transition properties, the glass transition process has also been evaluated in terms of CRR. The experimental parameters necessary to estimate the cooperativity length at the glass transition have been extracted by following the “rule of thumb” [26], as explained in the experimental section (section II.3.1.1). The different values are summarized in Table IV.3.2. In order to assess the molecular dynamics of the constrained amorphous fraction, only the SC systems have been investigated. Such an approach cannot be used in the case of SCA systems because an average glass transition would be measured including both the constrained amorphous fraction and the surrounding amorphous matrix. With the values of glass transition temperature and heat capacity step reported above, similar values of mean fluctuation temperature, cooperativity length and volume were obtained for both SPE and FICS. However, the mean fluctuation temperatures at the glass transition for the constrained amorphous fractions in SPE and FICS are higher compared to the value obtained for a wholly amorphous PLA (5.4 °C vs. 3.8 °C). As a consequence, the cooperativity length and volume of the amorphous chains trapped within crystalline structures (SPE/FICS) are reduced to 1.9 nm and 7 nm³ respectively, as compared to the values of 2.6 nm and 18 nm³ that are classically observed for a wholly amorphous PLA [13][22]. These results are consistent with the reduction of mobility induced by the presence of lamellar stacks already reported by Wang et al. [19] and Delpouve et al. [20]. Whatever the SC system, the cooperative rearranging regions are 30 % smaller with respect to wholly amorphous PLA. This result suggests that the constrained amorphous fractions behave the same independently of the type of semi-crystalline morphology. Once again, the molecular

dynamics of the constrained amorphous fractions seems to be driven by the crystallization temperature, namely the nature of the competition between crystallization and vitrification, rather than by the crystalline morphology. The structural anisotropy induced prior the crystallization does not impact the molecular dynamics. However, another parameter should be taken into account: the degree of connection of the crystalline fraction to the surrounding amorphous fraction, i.e. the decoupling of fractions and the development of the RAF.

Table IV.3.2: Parameters obtained by FSC and used to calculate the Cooperative Rearranging Regions (CRR) for wholly amorphous and semi-crystalline PLA, in the case of SC systems only, for both spherulite (SPE) and flow-induced crystalline structures (FICS): mean temperature fluctuation δT , cooperativity length $\xi_{T\alpha}$ and cooperativity volume $\xi_{T\alpha}^3$.

	δT (°C)	$\xi_{T\alpha}$ (nm)	$\xi_{T\alpha}^3$ (nm ³)
Amorphous	3.8 ± 0.3	2.6 ± 0.3	18 ± 2
SPE SC	5.4 ± 0.5	1.9 ± 0.2	7 ± 1
FICS SC	5.3 ± 0.5	1.9 ± 0.2	7 ± 1

This hypothesis was confirmed by investigating the molecular mobility of the amorphous fraction through the well-known phenomenon of structural relaxation and physical aging, as introduced in the Chapter I. Using physical aging to reveal differences in molecular dynamics by thermal analysis is a common procedure, as pointed out by Wang et al. [19] and Delpouve et al. [20]. In addition, the high scanning rates attainable by FSC allow accelerating the kinetics of physical aging, because glassy states with higher level of enthalpy can be formed [27], as explained in the previous chapter. FSC allowed performing physical aging on a wider range of time (from milliseconds to days), reaching the thermodynamic equilibrium [27][28].

IV.4 Structural relaxation below the glass transition

Figure IV.4.1 shows FSC normalized heat flows for aged PLA. Figure IV.4.1.A focuses on wholly amorphous PLA. As aging progresses, a sequence of endothermic peaks is classically observed indicating the structural relaxation process superimposed to the glass transition. Besides, the endothermic peaks increase and shift towards high temperature as the aging time increases.

Physical aging of SCA systems is more complex, as shown in Figure IV.4.1.B-C. The peaks of enthalpy recovery for both SPE and FICS systems are clearly divided into two

contributions that become more and more visible as the aging time increases, indicating that a different behavior is observed for a crystalline environment. A similar behavior has already been reported in the literature for PLA [21][22], explained by the existence of two amorphous fractions having their own response to structural relaxation due to their respective environment. It has also been suggested that the high-temperature contribution could be related to the enthalpy recovery of the constrained mobile amorphous fraction (CMAF), whereas the low-temperature contribution would be associated to the relaxation of unconstrained mobile amorphous fraction (UNMAF), i.e. the surrounding amorphous matrix.

When the SC systems are considered, both SPE and FICS behave similarly to a wholly amorphous PLA. The only difference is that the enthalpy recovery peaks are broadened and shifted towards higher temperatures within a larger range of temperature in comparison with wholly amorphous PLA, as shown in Figure IV.4.1.D-E. This result could be due to the strong influence of the semi-crystalline environment on the molecular dynamics of the confined amorphous fraction, suggesting a stronger degree of confinement induced by tighter inter-lamellar stacks [22].

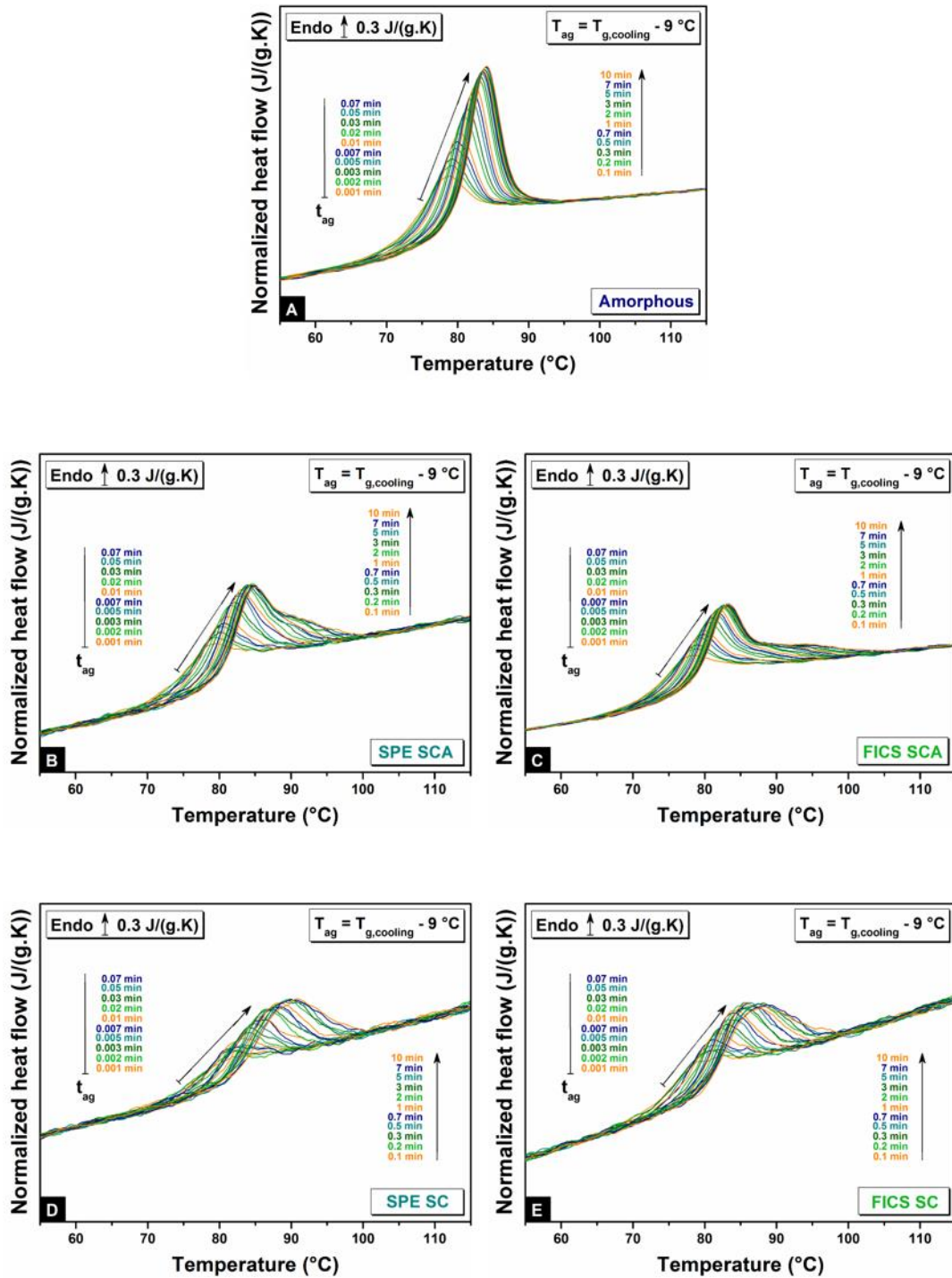


Figure IV.4.1: Normalized heat flows recorded after physical aging of wholly amorphous PLA (A), SPE SCA (B), FICS SCA (C), SPE SC (D) and FICS SC (E). Aging was performed *in situ* by FSC at a scanning rate of $|\beta_c| = \beta_h = 1500\text{ K.s}^{-1}$ at $T_{ag} = T_{g,cooling} - 9\text{ }^{\circ}\text{C}$ for aging times ranging from 0.001 min to 10 min.

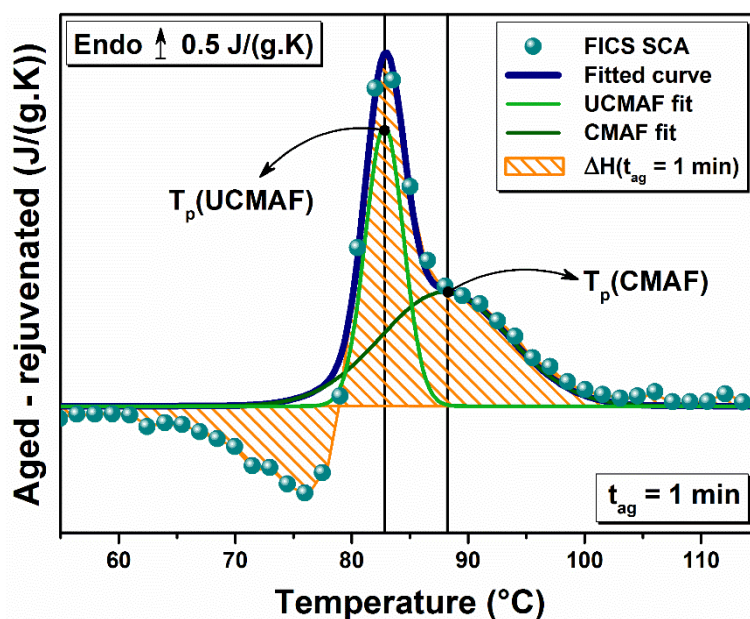


Figure IV.4.2: Normalized heat flow subtraction (aged – rejuvenated) of FICS SCA aged 1 min 9 °C below $T_{g, \text{cooling}}$. The curve illustrates how the enthalpy recovery $\Delta H(t_{\text{ag}} = 1 \text{ min})$ has been calculated, as well as the fitting procedure for the maximum T_p of the enthalpy recovery peaks.

Figure IV.4.2 shows the fitting procedure used to track the maximum T_p of the enthalpy recovery peak for all the contributions observed in Figure IV.4.1. The Gaussian fit has been performed on the normalized heat flow subtraction (aged - rejuvenated), as shown through the example of FICS SCA aged 1 min. Figure IV.4.3 reports the temperature evolution of the maximum of the enthalpy recovery peak as a function of aging time. Regarding the SCA systems, the first contribution of both SPE and FICS behaves as the unconstrained amorphous matrix, i.e. a linear increase is observed until a plateau is reached at about 84 °C after the same aging duration. This means that the first contribution recorded for both SPE and FICS is actually related to the surrounding amorphous matrix. As for the second contribution, SCA and SC systems show no differences: the trend is the same independently of the type of semi-crystalline morphology, and is shifted to higher temperatures as compared to the unconstrained mobile amorphous matrix. Thus, in both systems, the second contribution seems to be related to the amorphous fraction constrained within the lamellar stacks, with the same molecular dynamics.

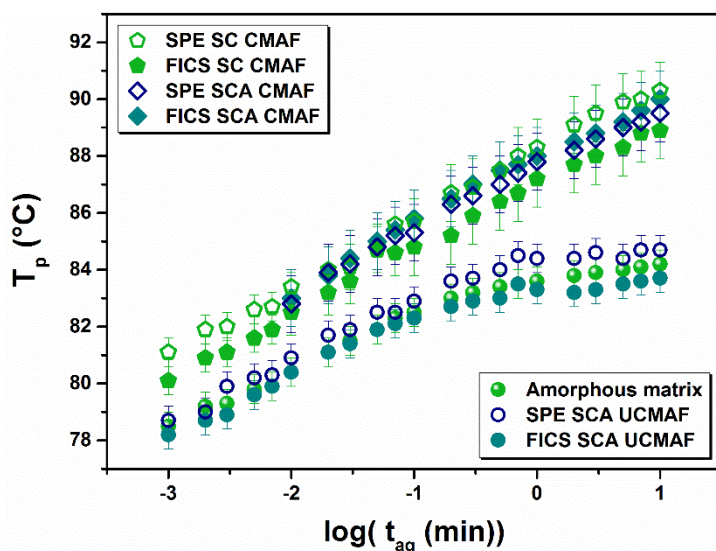


Figure IV.4.3: Evolution of the maximum T_p of the enthalpy recovery peak as a function of the aging time. Spheres: wholly amorphous PLA. Discs: unconstrained mobile amorphous fraction (UCMAF) within the SCA systems (FICS: filled discs, SPE: empty discs). Diamonds: constrained mobile amorphous fraction (CMAF) within the SCA systems (SPE: empty diamonds, FICS: filled diamonds). Pentagons: constrained mobile amorphous fraction (CMAF) within the SC systems (SPE: empty pentagons, FICS: filled pentagons).

Figure IV.4.4 shows the evolution of the difference between the enthalpy recovery ΔH_{tag} and the total enthalpy loss ΔH_{∞} as a function of aging time t_{ag} for a wholly amorphous PLA, as well as for the semi-crystalline samples (SCA and SC, SPE vs. FICS). When the crystallinity degree increases, the amorphous response decreases (see Table IV.2.1). Therefore the enthalpy recovery and the total enthalpy loss values are smaller for the semi-crystalline systems with respect to the wholly amorphous sample.

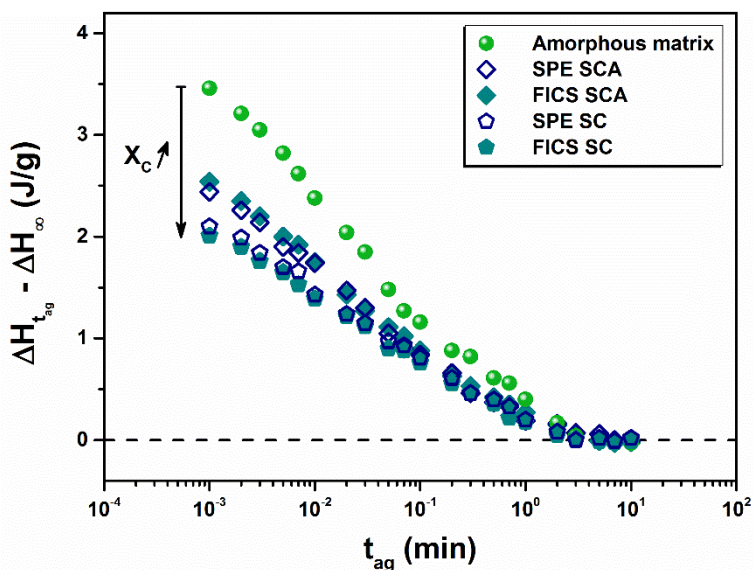


Figure IV.4.4: Time evolution of the difference between the enthalpy recovery ΔH_{tag} and the total enthalpy loss ΔH_{∞} . Spheres: wholly amorphous PLA. Diamonds: SCA systems. Pentagons: SC systems. Empty symbols: SPE. Filled symbols: FICS.

To compare the kinetics and the dynamics, the structural relaxation function ϕ has been plotted as a function of the aging time. The structural relaxation function is defined as:

$$\phi(t_{ag}) = \frac{\Delta H_{t_{ag}} - \Delta H_{\infty}}{\Delta H_{\infty}} \quad (IV.4.1)$$

in which $\Delta H_{t_{ag}}$ and ΔH_{∞} are the enthalpy recovery after an aging time t_{ag} and the total enthalpy loss after an infinite aging time, respectively. This function allows normalizing the enthalpy recovery to the same amount of mobile amorphous fraction. Figure IV.4.5 shows that the evolution of enthalpy recovery is the same independently of the environment of the mobile amorphous fraction (both type of morphology and degree of crystallinity). Besides, the whole structural relaxation process has been accelerated by the high scanning rates available in FSC [27]: all the samples reached the thermodynamic equilibrium after the same aging duration. It is worth mentioning that the Tool-Narayanaswamy-Moynihan model fits all the systems with the same parameters, meaning that the structural relaxation of the amorphous fraction does not depend on the microstructure and, more specifically, does not depend on the coupling between fractions, nor on the confinement by the crystals, nor on the orientation of macromolecules prior to crystallization.

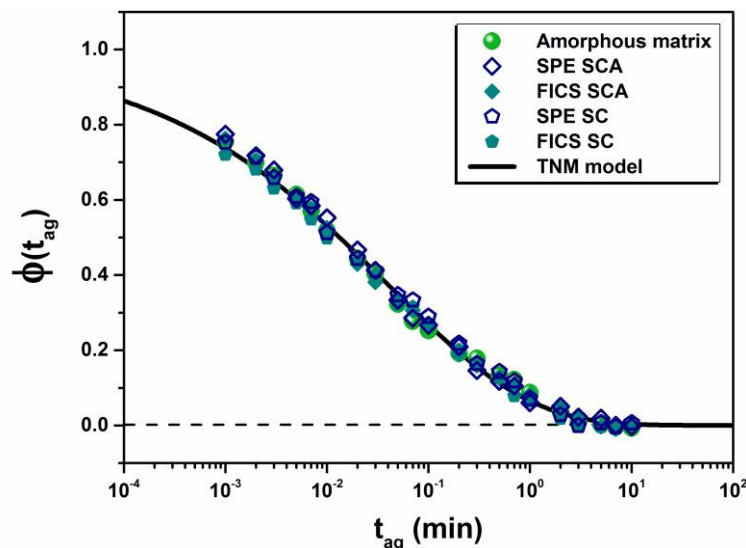


Figure IV.4.5: Time evolution of the structural relaxation function ϕ . Spheres: wholly amorphous PLA. Diamonds: SCA systems. Pentagons: SC systems. Empty symbols: SPE. Filled symbols: FISC.

IV.5 From local to segmental molecular motions

When comparing SPE and FICS SC systems, it is not surprising to observe similar dynamics and kinetics for the structural relaxation, because similar values of cooperativity length were observed. However, when comparing the systems in terms of crystallinity degree (i.e., wholly amorphous vs. SC), the fact that structural relaxation follows similar kinetics and dynamics is quite intriguing. Is this behavior consistent with the assumption that the confinement by the crystals and the coupling between fractions influence molecular dynamics? Structural relaxation is due to the expression of molecular mobility at temperatures below the glass transition: how is it possible to observe a difference in molecular mobility from the concepts of CRR and physical aging?

Cooperativity is evaluated by DSC, MT-DSC or FSC measurements of the glass transition, i.e. of α -relaxation. Physical aging is performed at a given temperature below the glass transition. During sub- T_g structural relaxation, only local molecular motions, such as the rotation of sub-segmental flexible groups along the polymer backbone [29], are possible. For example, Priestley et al. [30] have shown by dielectric studies a significant decrease in the strength of the β -relaxation dynamics when silica nanospheres are dispersed in a poly (methyl methacrylate) (PMMA) matrix. Such a decrease has been attributed to the hydrogen bonds between the flexible ester side-groups on PMMA and the hydroxyl groups on silica. Due to presence of the silica, the hydrogen bonds inhibit the motions of the ester side-group. Therefore, by assuming that the motions of the side-groups are the driving forces for PMMA structural relaxation, the reduction of physical aging rates in silica-PMMA nanocomposites have been explained and associated to a reduction of the β process. More recently, Cangialosi et al. [31] have observed two equilibration mechanisms during physical aging of polystyrene (PP) and poly(bisphenol-A-carbonate) (PBAC). They reported either a single or a double decay in the enthalpy recovery, when physical aging is performed close to or far below the glass transition, respectively. The first (faster) decay has been assigned to secondary relaxations, whereas the second (slower) decay has been attributed to the α process. In the literature it is well established that structural relaxation is related to a free volume hole diffusion towards the surfaces of the sample [29][32]. This means that the mechanism of free volume hole diffusion leading to structural relaxation is mainly done through local motions or secondary

relaxations close to the glass transition. However, in this study, differences in the structural relaxation were observed by heating the samples through the glass transition, i.e. by measuring the results of cooperative motions. This suggests that, in addition to the local motions happening during physical aging, cooperative motions through α -relaxation are also required to fully understand the phenomenon of structural relaxation.

An influence of the crystalline environment, both in terms of confinement and coupling between fractions, has been observed on the macromolecular scale, but no influence has been highlighted on the structural relaxation at the atomic/molecular scale, because only a single decay has been observed. Following the assumption that physical aging is driven by local motions, this result suggests that, contrarily to α -relaxation, secondary relaxations are not influenced by the crystalline environment. The length-scale matters. It is worth mentioning that Schick et al. [33] have observed just a slight influence of the crystals on the local movements of mobile amorphous fraction in the case of semi-crystalline PET by dielectric measurements. Later on, Kattan et al. showed no-dependency of the β relaxations with the degree of crystallinity on various amorphous and semi-crystalline polyesters, by thermally stimulated depolarization current experiments [34]. In this work, similar values of enthalpy recovery normalized to the mobile amorphous fraction have been obtained for all the systems; however, the shape of the enthalpy recovery peaks was not the same. Wholly amorphous PLA has a cooperativity length of 2.6 nm and sharper enthalpy recovery peaks because of the relatively large cooperativity domains, which make easier the recovery to the equilibrium upon heating. Consistently, SC PLA (both FICS and SPE) have a reduced cooperativity length (1.9 nm) and broader enthalpy recovery peaks because the relatively small cooperativity domains delay the recovery to the equilibrium upon heating. Consequently, qualitative information on the cooperativity length characteristics are then observed through the enthalpy recovery peaks.

IV.6 Conclusion

The relaxation of shear-induced precursors has been investigated at high temperature to mimic the industrial injecting process of PLA. Below 160 °C, the critical relaxation time is much larger than the time required to quench the sample to a suitable crystallization temperature, resulting in the formation of highly oriented cylindrical structures which are

embedded in an amorphous PLA matrix. This observation allowed investigating the influence of the crystalline environment generated either by flow-induced crystallization (FIC) or quiescent crystallization (SPE) on the amorphous phase after a thermal treatment performed in optimized conditions. Slices of the semi-crystalline samples have been analyzed by FSC to investigate the behavior of the amorphous phase at the same scale of the semi-crystalline structure. Thanks to the high scanning rates accessible via FSC, physical aging has been accelerated, which allowed scanning up to four decades of aging time. Segmental and local relaxations have been investigated through the concept of cooperativity and physical aging, respectively. A decrease of the cooperativity length in the semi-crystalline systems has been observed in comparison to wholly amorphous PLA, essentially due to the coupling between phases and the confinement effect of the crystals. No differences were observed in the crystalline morphology. The structural anisotropy induced prior to the crystallization has no impact. The molecular dynamics were found to depend on the crystallinity degree at the macromolecular scale. However, the same enthalpy recovery was measured for all the systems, meaning that the structural relaxation is not influenced by the crystallinity degree. This result is consistent with the fact that physical aging is due to local motions, and local motions are not affected by the crystalline environment (different length-scale). The only influence that could be observed is the one measured during the subsequent heating ramp through the α -relaxation, i.e. the glass transition.

REFERENCES

- [1] S. Yamazaki, M. Itoh, T. Oka, and K. Kimura, *Eur. Polym. J.* **46**, 58 (2010).
- [2] S. Huang, H. Li, S. Jiang, X. Chen, and L. An, *Polymer* **52**, 3478 (2011).
- [3] J. Bojda and E. Piorkowska, *Polym. Test.* **50**, 172 (2016).
- [4] X.-L. Xie, Z.-H. Sang, J.-Z. Xu, G.-J. Zhong, Z.-M. Li, X. Ji, R. Wang, and L. Xu, *Polymer* **110**, 196 (2017).
- [5] H. Tang, J.-B. Chen, Y. Wang, J.-Z. Xu, B. S. Hsiao, G.-J. Zhong, and Z.-M. Li, *Biomacromolecules* **13**, 3858 (2012).
- [6] H. Xu, G.-J. Zhong, Q. Fu, J. Lei, W. Jiang, B. S. Hsiao, and Z.-M. Li, *ACS Appl. Mater. Interfaces* **4**, 6774 (2012).
- [7] N. Najafi, M.-C. Heuzey, P. Carreau, and D. Therriault, *Rheol. Acta* **54**, 831 (2015).
- [8] H. Xu, L. Xie, and M. Hakkarainen, *ACS Sustain. Chem. Eng.* **3**, 1443 (2015).
- [9] H. Xu, L. Xie, X. Jiang, M. Hakkarainen, J.-B. Chen, G.-J. Zhong, and Z.-M. Li, *Biomacromolecules* **15**, 1676 (2014).
- [10] F. Azzurri and G. C. Alfonso, *Macromolecules* **41**, 1377 (2008).
- [11] J. Zhang, Y. Duan, H. Sato, H. Tsuji, I. Noda, S. Yan, and Y. Ozaki, *Macromolecules* **38**, 8012 (2005).
- [12] J. Zhang, K. Tashiro, H. Tsuji, and A. J. Domb, *Macromolecules* **41**, 1352 (2008).
- [13] X. Monnier, N. Delpouve, N. Basson, A. Guinault, S. Domenek, A. Saiter, P. E. Mallon, and E. Dargent, *Polymer* **73**, 68 (2015).
- [14] K. Wasanasuk and K. Tashiro, *Polymer* **52**, 6097 (2011).
- [15] M. Cocca, M. L. D. Lorenzo, M. Malinconico, and V. Frezza, *Eur. Polym. J.* **47**, 1073 (2011).
- [16] M. C. Righetti, M. Gazzano, M. L. Di Lorenzo, and R. Androsch, *Eur. Polym. J.* **70**, 215 (2015).
- [17] M. C. Righetti and E. Tombari, *Thermochim. Acta* **522**, 118 (2011).
- [18] M. C. Righetti, D. Prevosto, and E. Tombari, *Macromol. Chem. Phys.* **217**, 2013 (2016).
- [19] Y. Wang and J. F. Mano, *J. Appl. Polym. Sci.* **100**, 2628 (2006).
- [20] N. Delpouve, A. Saiter, J. F. Mano, and E. Dargent, *Polymer* **49**, 3130 (2008).
- [21] Y. Wang, J. L. Gómez Ribelles, M. Salmerón Sánchez, and J. F. Mano, *Macromolecules* **38**, 4712 (2005).
- [22] N. Delpouve, M. Arnoult, A. Saiter, E. Dargent, and J.-M. Saiter, *Polym. Eng. Sci.* **54**, 1144 (2014).
- [23] N. Delpouve, A. Saiter, and E. Dargent, *Eur. Polym. J.* **47**, 2414 (2011).
- [24] C. Zhang, Y. Guo, and R. D. Priestley, *ACS Macro Lett.* **3**, 501 (2014).
- [25] K. Arabeche, L. Delbreilh, R. Adhikari, G. H. Michler, A. Hiltner, E. Baer, and J.-M. Saiter, *Polymer* **53**, 1355 (2012).
- [26] E. Hempel, G. Hempel, A. Hensel, C. Schick, and E. Donth, *J. Phys. Chem. B* **104**, 2460 (2000).
- [27] X. Monnier, A. Saiter, and E. Dargent, *Thermochim. Acta* **648**, 13 (2017).
- [28] Y. P. Koh, S. Gao, and S. L. Simon, *Polymer* **96**, 182 (2016).
- [29] L. C. E. Struik, *Polym. Eng. Sci.* **17**, 165 (1977).
- [30] R. D. Priestley, P. Rittigstein, L. J. Broadbelt, K. Fukao, and J. M. Torkelson, *J. Phys. Condens. Matter* **19**, 205120 (2007).
- [31] D. Cangialosi, V. M. Boucher, A. Alegría, and J. Colmenero, *Phys. Rev. Lett.* **111**, 095701 (2013).

- [32] D. Cangialosi, V. M. Boucher, A. Alegría, and J. Colmenero, *Polymer* **53**, 1362 (2012).
- [33] C. Schick, J. Dobbertin, M. Pötter, H. Dehne, A. Hensel, A. Wurm, A. Ghoneim, and S. Weyer, *J. Therm. Anal. Calorim.* **49**, 499 (1997).
- [34] M. Kattan, E. Dargent, J. Grenet, *J. Therm. Anal. Calorim.* **76**, 379 (2004).

CHAPTER V

Structural anisotropy investigations through electrospun amorphous plasticized PLA fibers

Parts of this chapter are extracted from:

Molecular dynamics in electrospun amorphous plasticized polylactide fibers

*X. Monnier, N. Delpouve, N. Basson, A. Guinault, S. Domenek, A. Saiter, P.E. Mallon, E. Dargent
Polymer 73 (2015) 68-78*

CONTENTS

V.1 As-spun fibers: Morphological aspects	118
V.2 Macromolecular organizations	118
V.3 Molecular Dynamics.....	135
V.4 Conclusions.....	140
References.....	141

This last chapter approaches the influence of the structural anisotropy induced during the processing on non-crystalline systems. In order to achieve such investigation, electrospinning process has been used. As explained in the chapter I, the goal has been to observe the impact alone of the so-called mesophase, as well as the molecular orientation, on the molecular dynamics of the amorphous phase. Thus, as-pun plasticized polylactide fibers and plasticized polylactide quenched films have been characterized and compared to observe any influence related to the structural anisotropy. Special attention have been done on the characterization of the macromolecular organization through Wide Angle X-ray Scattering (WAXS) and Modulated Temperature Differential Scanning Calorimetry (MT-DSC). The concept of Cooperative Rearranging Region (CRR) has been used to characterize the molecular dynamics. An interpretation is given to highlight the role of the weak intermolecular interactions in the amorphous phase during the α -relaxation.

V.1 As-spun fibers: Morphological aspects

In Figure V.1.1, scanning electronic microscopy (SEM) images of as-spun fibers are presented. It is evidenced that the process of electrospinning produces PLA fibers with diameters and distributions that are largely independent of the composition. No visible morphological defects such as beads are evident. Neat PLA fibers (Figure V.1.1.A) exhibit an average fiber diameter of $0.80 \mu\text{m}$ with a standard deviation of $0.18 \mu\text{m}$, when plasticized PLA fibers (5 %, 10 % and 15 %) display an average fiber diameter and a standard deviation of $0.78 \pm 0.18 \mu\text{m}$, $0.69 \pm 0.17 \mu\text{m}$ and $0.81 \pm 0.18 \mu\text{m}$, respectively (Figure V.1.1.B-D). No visible morphological defects such as beads are evident, and no significant change is observed on the addition of plasticizer. This indicates that the plasticizer has no influence on the fiber diameter during the processing, and that no fiber size variations will interfere in the subsequent analyses of the fibers.

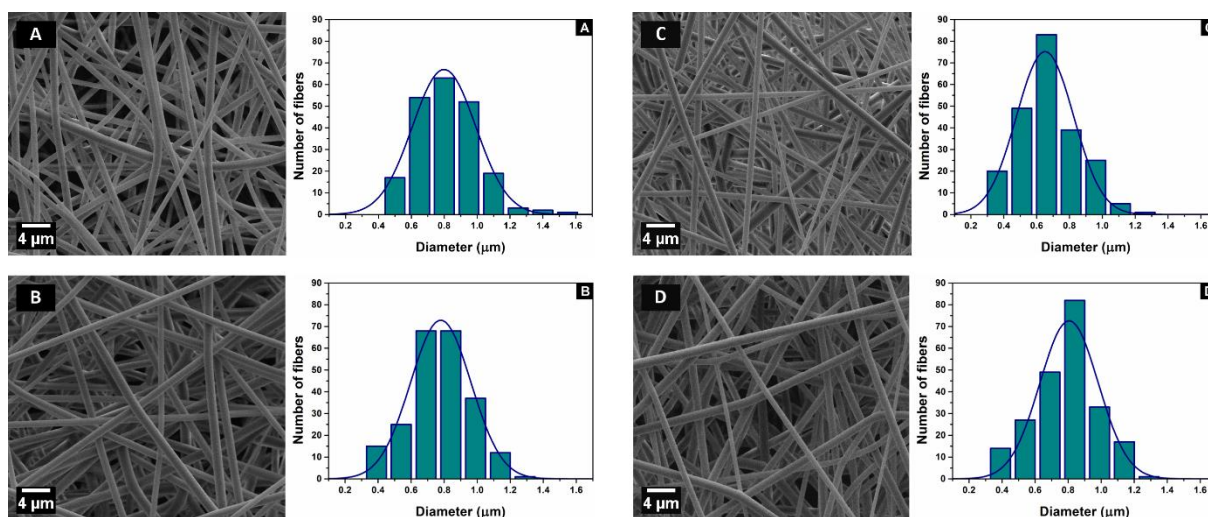


Figure V.1.1: SEM pictures along with the fiber diameter distribution of as-spun neat and plasticized PLA fibers. (A) Neat PLA. (B) PLA + 5 % ATBC. (C) PLA + 10 % ATBC. (D) PLA + 15 % ATBC.

V.2 Macromolecular organizations

V.2.1 Wide Angle X-ray Scattering (WAXS)

V.2.1.1 Neat PLA

Figure V.2.1 shows the WAXS analysis for the neat PLA, of the quenched films as well as the as-spun fibers. For the quenched film of neat PLA (Figure V.2.1.A), the experimental

spectrum displays the usual pattern of a non-crystalline PLA. The fit of the WAXS intensity profile displays three peaks with maxima located at $2\theta = 15.5^\circ$, $2\theta = 21.3^\circ$, and $2\theta = 30.9^\circ$. Stoclet et al. [1] have reported three peaks located at $2\theta = 15.0^\circ$, $2\theta = 21.2^\circ$, and $2\theta = 31.0^\circ$ for wholly amorphous films, which is in close agreement with our results. The three peaks are characteristics of the chain spacing in amorphous PLA. The components at $2\theta = 15.0^\circ$ and $2\theta = 21.2^\circ$ arise from two characteristic inter-chain spacing. The third component at $2\theta = 31.0^\circ$ is associated to the intra-chain spacing along the chains which refers to the distance of 0.29 nm between the methyl groups in the 3-fold helices [1]. As shown in Figure V.2.1.B, the fit of the WAXS intensity profile for the as-spun fibers of neat PLA also exhibits three peaks as defined above, but in addition there is a fourth Gaussian peak with a maximum located at 16.0° (see Table V.2.1).

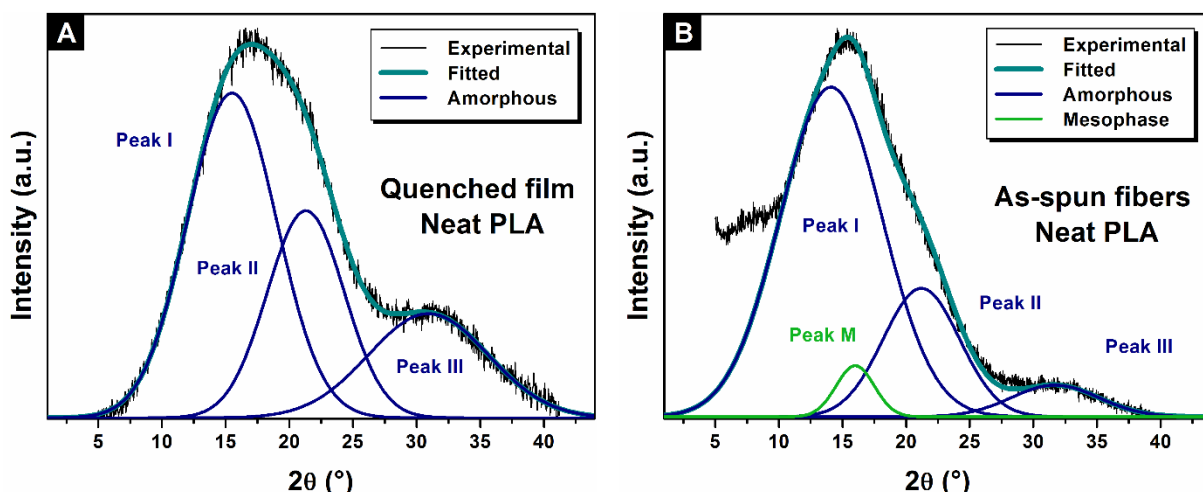


Figure V.2.1: WAXS intensity profiles and the associated fits of the experimental spectra for: (A) quenched film of neat PLA, (B) as-spun fibers of neat PLA.

Table V.2.1: Position 2θ ; Full width at mid-height FWHM; and relative area A of the characteristic peaks of the amorphous phase (I; II; III) and the mesophase (M) obtained from the fitting of the WAXS experimental spectra for the quenched films and the as-spun fibers of neat PLA.

NEAT PLA	Peak I			Peak II			Peak III			Peak M		
	2θ (°)	FWHM (°)	A (%)	2θ (°)	FWHM (°)	A (%)	2θ (°)	FWHM (°)	A (%)	2θ (°)	FWHM (°)	A (%)
Quenched films	15.5	7.0	51	21.3	6.1	28	30.9	9.4	21	/	/	/
As-spun fibers	14.1	8.0	70	21.2	6.0	20	31.7	6.9	6	16.0	3.0	4

The relative area of this fourth peak is only 4 %, but as shown in Figure V.2.2, its introduction increases the fit correlation. In Figure V.2.2.A, when assuming the mesophase response the correlation coefficient goes up to 0.9977, whereas in Figure V.2.2.B, the correlation coefficient reaches 0.9945 when ignoring the mesophase response. Moreover, Ma et al. [2] have recently reported the need for the introduction of this fourth peak for non-crystalline electrospun fibers. This fourth peak exhibits a low FWHM equal to 3.0° . That is characteristic of a microstructural organization with an order that is intermediate between the amorphous phase and the crystals. For this reason it has been attributed to the response of the mesophase. The presence of mesophase in electrospun fibers is concordant with the assumption made by Zong et al. [3] that the electrospinning of polylactide can lead to highly oriented chains that do not have enough time to organize into crystals before solidification. It is also worth mentioning that this WAXS profile has also been reported by Stoclet et al. [1] when drawing PLA only 10°C above its glass transition.

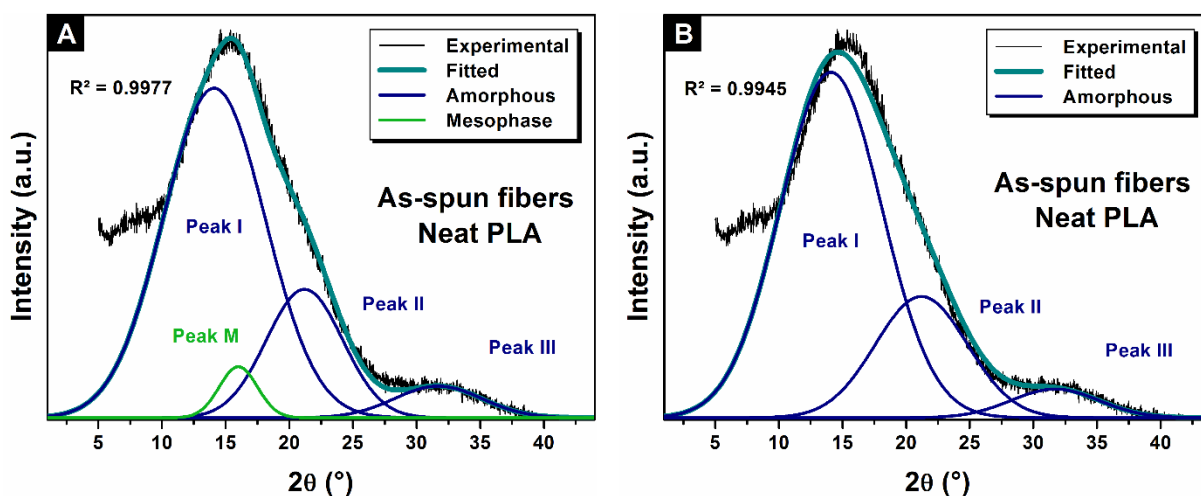


Figure V.2.2: WAXS intensity profiles and the associated fit of the experimental spectra for as-spun fibers of neat PLA, (A) by using the mesophase response (B) by ignoring the mesophase response.

V.2.1.2 Plasticized PLA

Figure V.2.3 displays the WAXS intensity profiles of the quenched films that are plasticized with 5 %, 10 % and 15 % ATBC respectively. For the quenched films, the WAXS intensity profiles of neat and plasticized PLA are superimposed in the value domain of 2θ ranging from about 20° to 40° . From this observation, we can deduce that the addition of the

plasticizer does not affect the characteristic intra-chain distances. On the other hand, in the value domain of 2θ ranging from about 10 to 20°, the WAXS intensity profiles are slightly differentiated.

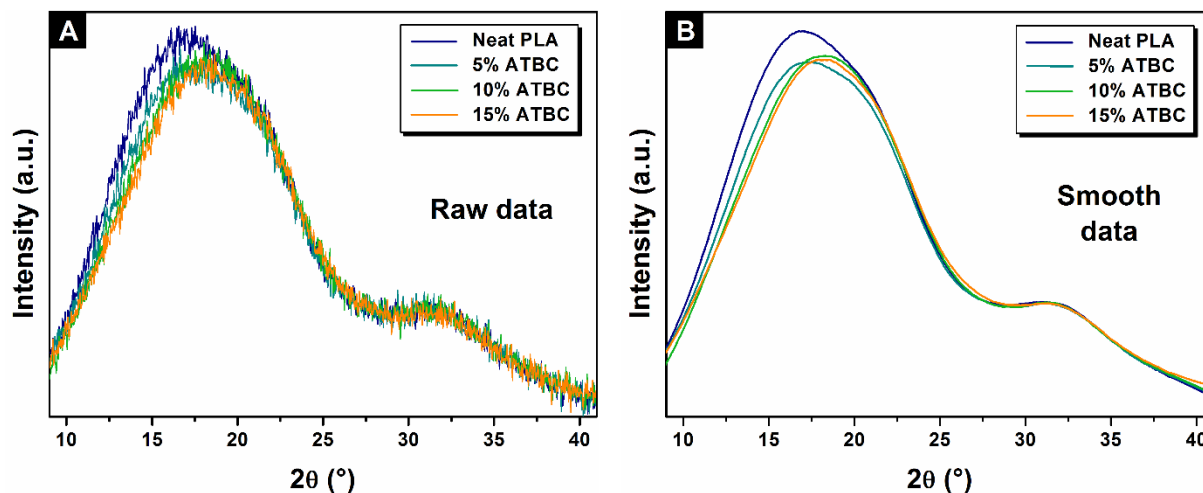


Figure V.2.3: WAXS intensity profiles of the experimental spectra for plasticized quenched films. **(A)** Raw data. **(B)** Smooth data for more clarity.

Because of the lack of evidence in literature about the fitting procedure for the analysis of plasticized PLA, many fits have been tested. As sum up in Figure V.2.4, the possibilities to fit the domain related to the inter-chain characteristic spacing by one or two contributions have been particularly detailed. For the lowest content of ATBC, it is clear that the best fitting procedure is the one with three contributions. However, it was impossible to clearly establish the best fitting procedure due to the high similarity of the correlation coefficients when the ATBC content reaches 10 % or 15 % ATBC. As a consequence, the same fitting procedure was used than for the quenched film of neat PLA. In this way, only peak I corresponding to the highest inter chain spacing is modified by the addition of plasticizer, as reported in Table V.2.2. This variation may suggest that the addition of plasticizer involves a redistribution of the inter-chain spacing in the amorphous phase.

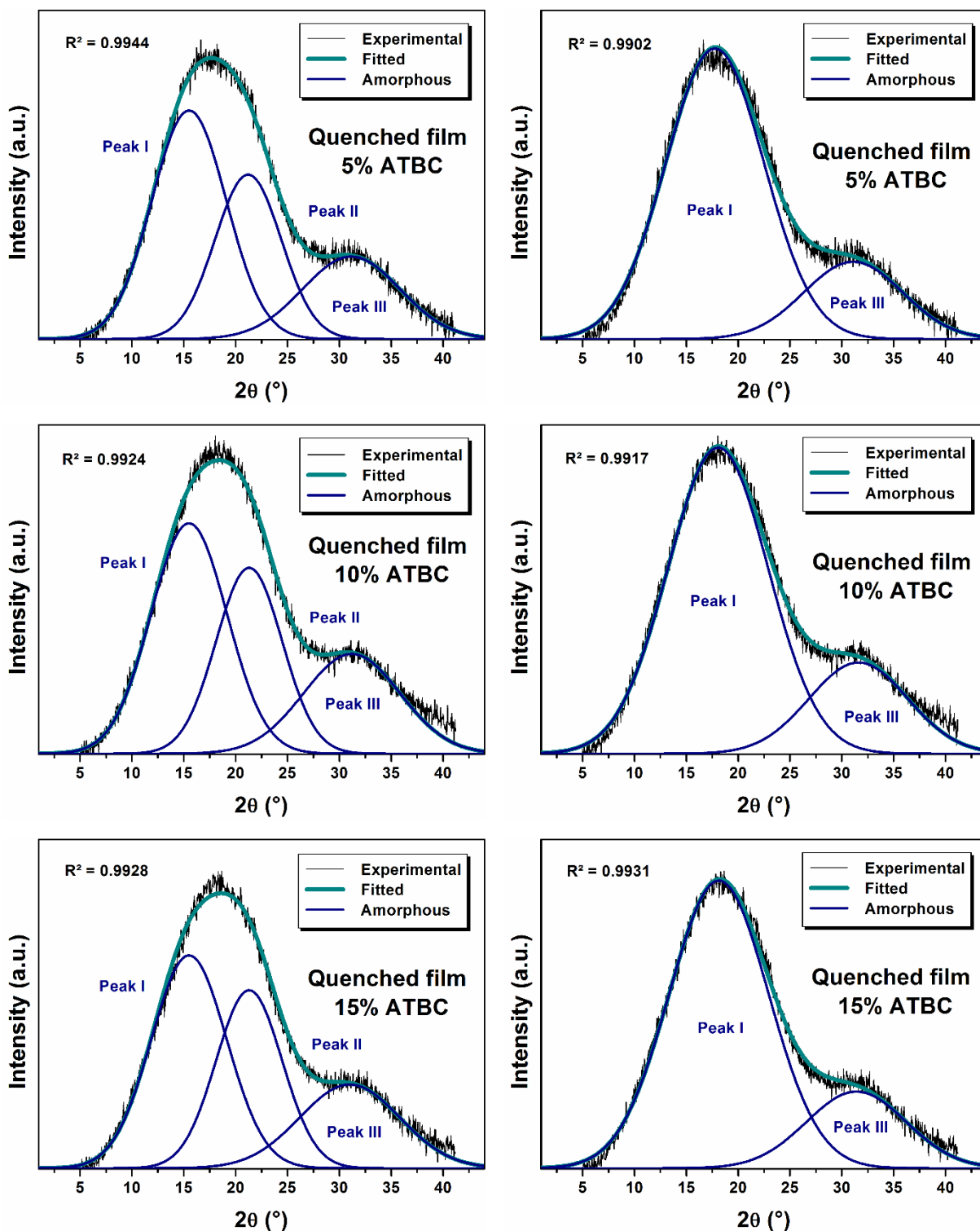


Figure V.2.4: Comparison of the different contributions to find out the best fitting procedure associated to the WAXS intensity profiles of the experimental spectra for plasticized quenched films. **(Top)** PLA + 5 % ATBC. **(Middle)** PLA + 10 % ATBC. **(Bottom)** PLA + 15 % ATBC. **(Left)** Three contributions. **(Right)** Two contributions.

Table V.2.2: Position 2θ ; Full width at mid-height FWHM; and relative area A of the characteristic peaks of the amorphous phase (I; II; III) obtained from the fitting of the WAXS experimental spectra for the neat and plasticized PLA quenched films.

QUENCHED FILMS ATBC (%)	Peak I			Peak II			Peak III		
	2θ (°)	FWHM (°)	A (%)	2θ (°)	FWHM (°)	A (%)	2θ (°)	FWHM (°)	A (%)
0	15.5	7.0	51	21.3	6.1	28	30.9	9.4	21
5	15.5	7.1	48	21.3	6.3	30	31.2	9.1	22
10	15.5	7.3	45	21.3	6.4	31	31.2	9.3	24
15	15.5	7.3	44	21.3	6.4	32	31.0	9.6	23

Figure V.2.5 displays the WAXS intensity profiles of the as-spun fibers that are plasticized with 5 %, 10 % and 15 % ATBC respectively. For as-spun fibers, the 2θ value domain that is characteristic of the intra-chain distances has WAXS intensity profiles that are the same for neat and plasticized PLA. This observation confirms the assumption made for the quenched films. On the other hand, significant modifications related to the inter-chain distances domain occur when fibers are plasticized.

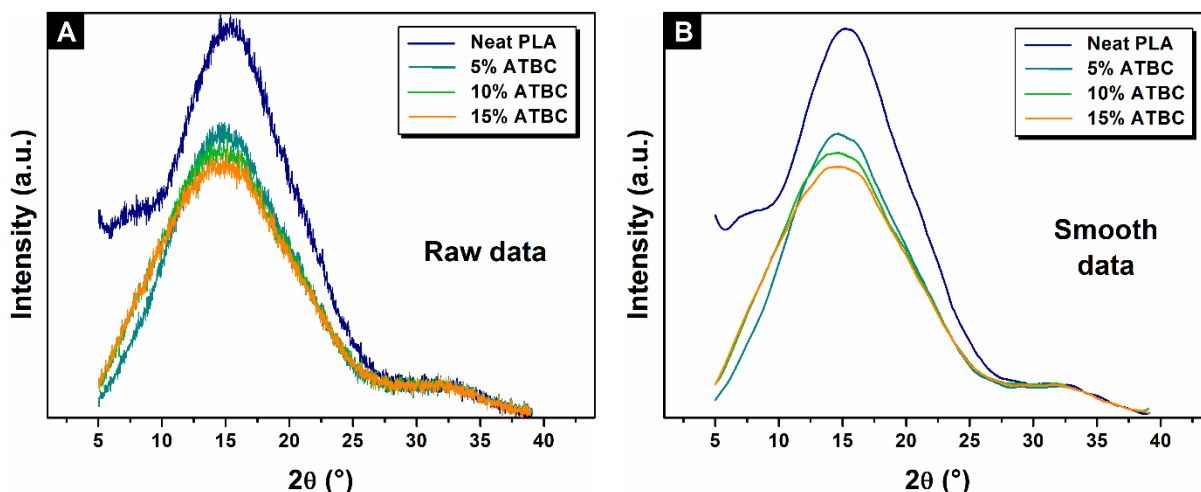


Figure V.2.5: WAXS intensity profiles of the experimental spectra for plasticized as-spun fibers. (A) Raw data. (B) Smooth data for more clarity.

Like plasticized quenched films, different possibilities to fit the domain related to the inter-chain characteristic spacing have been done. Especially, the possibilities to fit with the mesophase response or only with two contributions, as sum up in Figure V.2.6. It is worth mentioning that the fitting procedure using the mesophase response is the same than this for the as-spun fibers of neat PLA. For the lowest content of ATBC, it is unclear to define a best

procedure given that both correlation coefficients are close from each other. Besides, by fitting with the mesophase response and letting the FWHM free same results are observed than for as-spun fibers of neat PLA.

The answer is given for the highest content of ATBC, namely 10% and 15% ATBC. In both cases, it is clear from figure V.2.6 and the correlation coefficients that none mesophase response might be observed in such systems. Besides, by fitting with the mesophase response and letting the FWHM free, the mesophase contribution is not detected and the domain related to the inter-chain characteristic spacing displays only two contributions. This may be due to the broadening of the signals. As a consequence, due to the significant increase of the correlation coefficient when fitting with only three peaks, i.e., by removing the contribution associated to the presence of the mesophase when the content of ATBC increases, it has been postulated that the best fitting procedure is the one with three contributions for the plasticized as-spun fibers. Moreover, the position and shape of the two contributions linked to the inter-chain spacing in the amorphous phase of the plasticized as-spun fibers are modified compared to neat PLA (see Table V.2.3). This variation does suggest that the addition of plasticizer involves a redistribution of the inter-chain spacing in the amorphous phase.

From the WAXS investigations, it is clear that the electrospinning of neat PLA induces the creation of a highly ordered non-crystalline microstructure with the presence of mesophase. In the case of plasticized electrospun PLA fibers, the mesophase is no detected. In a general way, the addition of plasticizer changes the environment in the amorphous phase. It does not affect the intra-chain characteristic spacing but induces a strong redistribution of the inter-chain characteristic spacing.

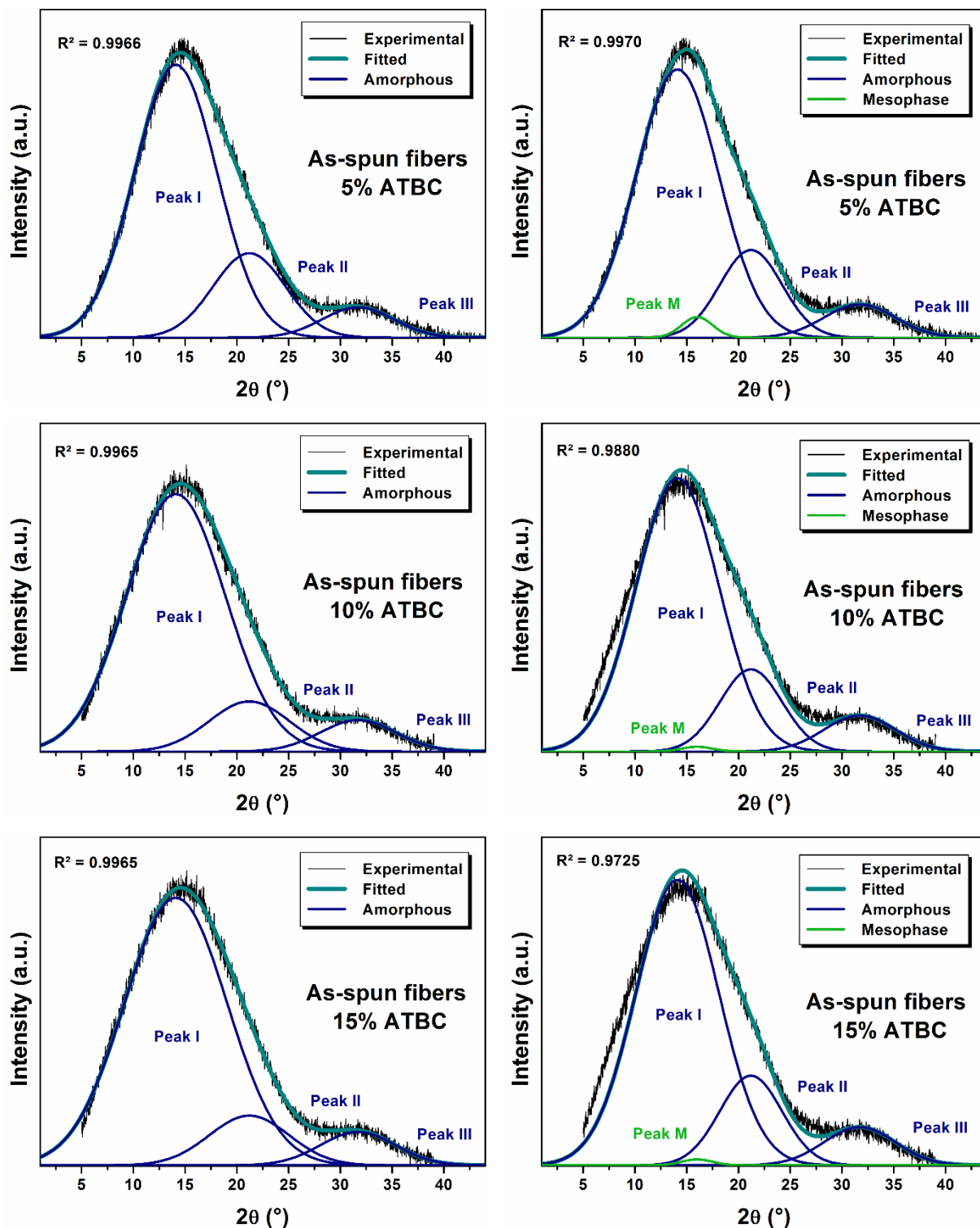


Figure V.2.6: Comparison of the different contributions to find out the best fitting procedure associated to the WAXS intensity profiles of the experimental spectra for plasticized as-spun fibers. **(Top)** PLA + 5 % ATBC. **(Middle)** PLA + 10 % ATBC. **(Bottom)** PLA + 15 % ATBC. **(Left)** Three contributions. **(Right)** Three contributions as well as the mesophase response.

Table V.2.3: Position 2θ ; Full width at mid-height FWHM; and relative area A of the characteristic peaks of the amorphous phase (I; II; III) and the mesophase (M) obtained from the fitting of the WAXS experimental spectra for the neat and plasticized PLA as-spun fibers.

AS-SPUN FIBERS ATBC (%)	Peak I			Peak II			Peak III			Peak M		
	2θ (°)	FWHM (°)	A (%)	2θ (°)	FWHM (°)	A (%)	2θ (°)	FWHM (°)	A (%)	2θ (°)	FWHM (°)	A (%)
0	14.1	8.0	70	21.2	6.0	20	31.7	6.9	6	16.0	3.0	4
5	14.1	8.0	73	21.2	7.0	20	31.7	6.9	7	/	/	/
10	14.1	9.5	80	21.2	7.8	13	31.7	7.3	7	/	/	/
15	14.1	9.9	81	21.2	7.7	12	31.7	7.2	7	/	/	/

V.2.2 Modulated Temperature Differential Scanning Calorimetry (MT-DSC)

V.2.2.1 Non-crystalline nature

Figure V.2.7 shows the average heat flow versus temperature obtained from MT-DSC analysis for all the materials. In all cases, three thermal events are clearly observed: an endothermic heat flow step characteristic of the glass transition, an exothermic peak due to the cold-crystallization of a part of the amorphous phase and an endothermic event related to the melting of the crystalline phase.

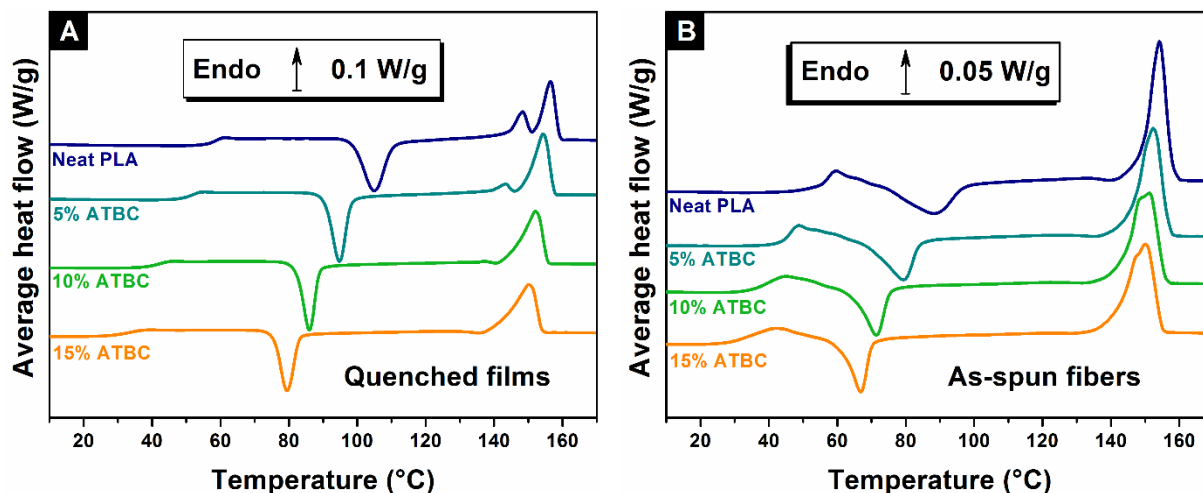


Figure V.2.7: Average heat flow vs. temperature from MT-DSC. (A) Quenched films. (B) As-spun fibers. The curves are shifted for more clarity.

As explained in the chapter I, the major issue in this chapter lies in the creation of non-crystalline samples. It has been verified by the equality between the enthalpy of cold-

crystallization and the enthalpy of melting that no crystals are present prior to the MT-DSC analysis. However, one could immediately see for the as-spun fiber series that the cold-crystallization encroaches on the temperature range of the glass transition. For this reason, the quantitative analysis of both thermal events has been made by separating the events related to the variations of the heat capacity which appear in the reversing heat flow, from the kinetic events which appear in the non-reversing heat flow. At the same time, the equality between the enthalpy of cold-crystallization and the enthalpy of melting has been double checked using the average heat flow signal on one hand as usually performed from classical DSC, and both the reversing and the non-reversing heat flow signals from MT-DSC on the other hand, as shown in figure V.2.8 and V.2.9 for quenched films and as-spun fibers respectively. It is worth mentioning that cold-crystallization induces negligible noises for enthalpy calculations on the reversing heat flow for all samples. The enthalpies of cold-crystallization and melting are shown in Table V.2.4. These are independently equal which proves that the samples are non-crystalline prior to the analysis. This result confirms the previous observations made from WAXS.

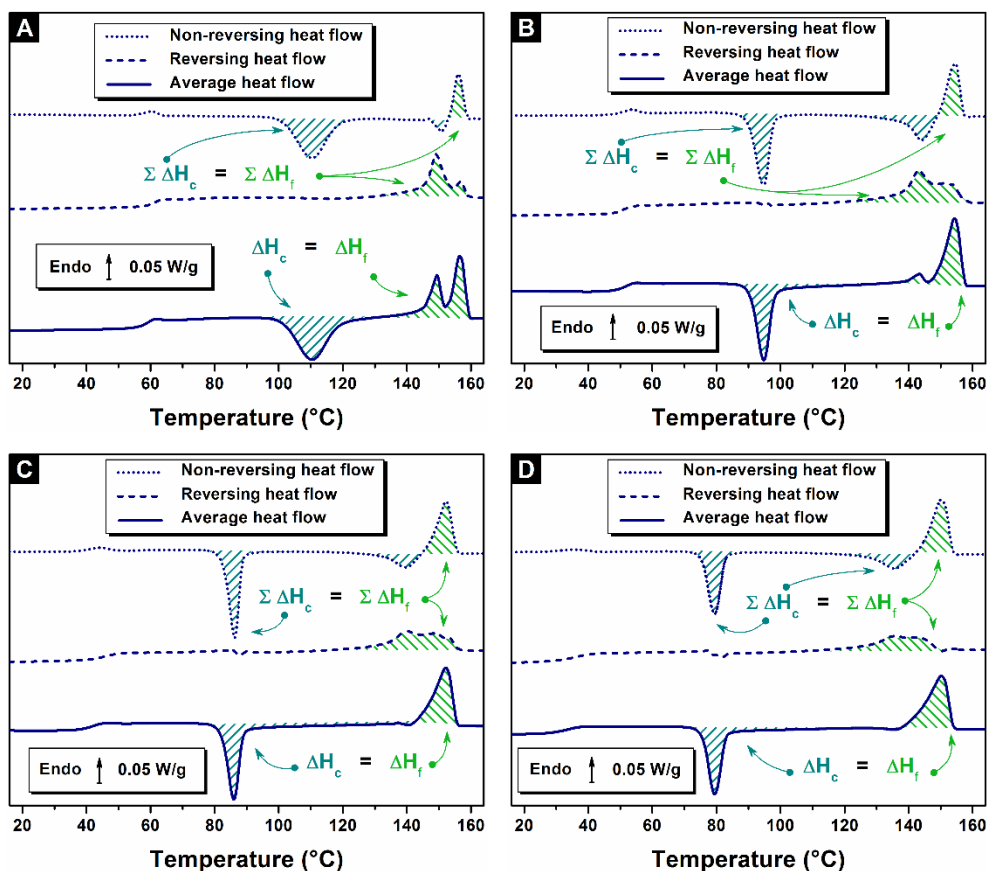


Figure V.2.8: Determination of the degree of crystallinity from MT-DSC curves for the quenched films: Average heat flow (solid line); reversing heat flow (dashed line); and non-reversing heat flow (dotted line) vs. temperature: **(A)** Neat PLA; **(B)** PLA + 5 % ATBC; **(C)** PLA + 10 % ATBC; **(D)** PLA + 15 % ATBC.

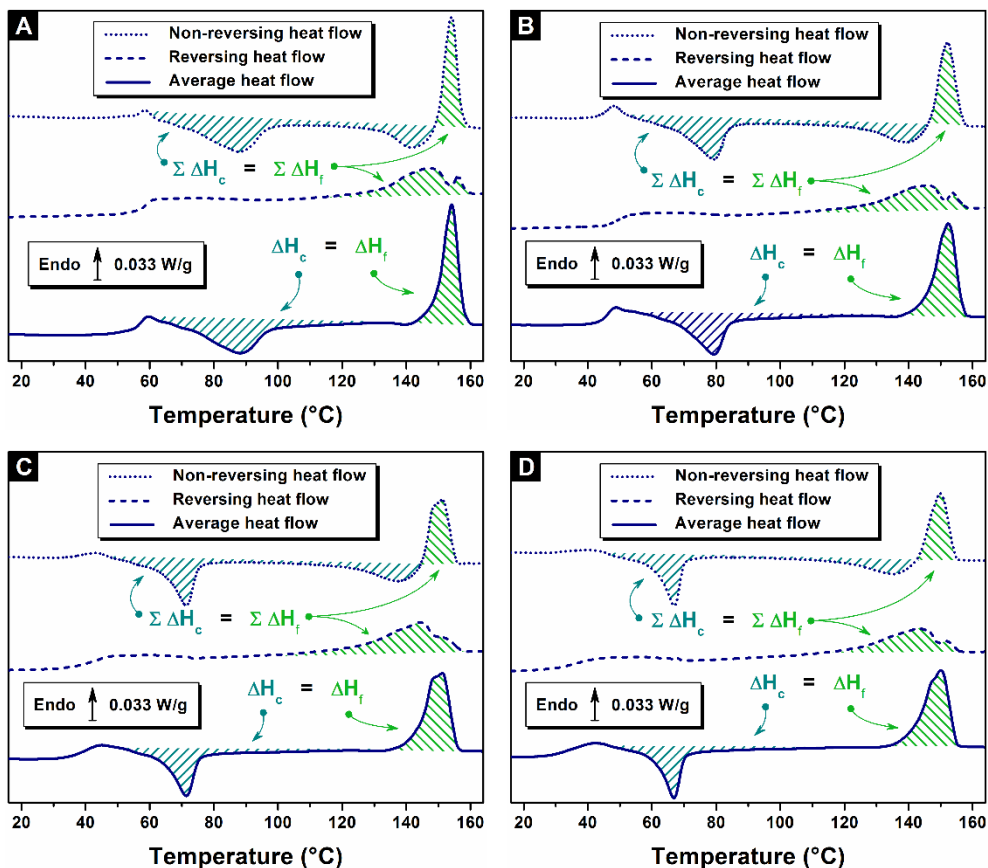


Figure V.2.9: Determination of the degree of crystallinity from MT-DSC curves for the as-spun fibers: Average heat flow (solid line); reversing heat flow (dashed line); and non-reversing heat flow (dotted line) vs. temperature: **(A)** Neat PLA; **(B)** PLA + 5 % ATBC; **(C)** PLA + 10 % ATBC; **(D)** PLA + 15 % ATBC.

Table V.2.4: ΔH_c enthalpy of crystallization and ΔH_m enthalpy of melting for the quenched films and the as-spun fibers. The values of the enthalpies are given with an accuracy of 2 J/g.

QUENCHED FILMS ATBC (%)	ΔH_c (J/g)	ΔH_m (J/g)	AS-SPUN FIBERS ATBC (%)	ΔH_c (J/g)	ΔH_m (J/g)
0	27	27	0	27	28
5	26	26	5	26	27
10	23	24	10	24	27
15	24	24	15	24	27

V.2.2.2 Thermal properties & thermal behaviors

As highlighted above, the cold-crystallization for the as-spun fibers series encroaches on the temperature range of the glass transition. As a consequence, the glass transition temperature has systematically been determined from the reversing heat flow. An example of this protocol is given in Figure V.2.10 in the case of as-spun fibers of neat PLA. The

characteristic temperatures (glass transition, crystallization temperature and melting temperature) are whole summarized in Table V.2.5.

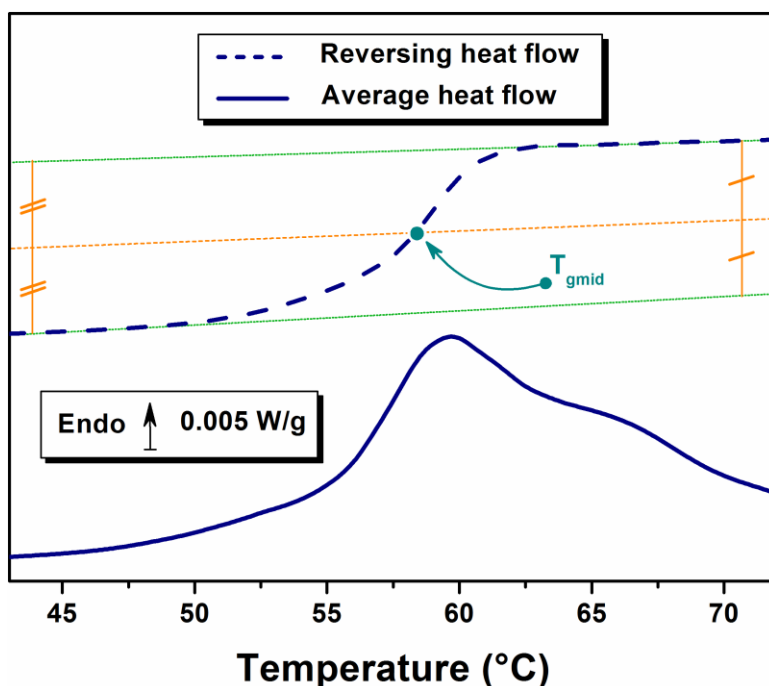


Figure V.2.10: Determination of the glass transition temperature from MT-DSC curves obtained for the as-spun fibers of neat PLA: Average heat flow (solid line); reversing heat flow (dashed line).

Table V.2.5: Characteristic temperatures from MT-DSC curves obtained for the quenched films and the as-spun fibers: $T_{g\ mid}$ glass transition temperature at the transition mid-point; $T_{c\ max}$ temperature at the maximum of the peak of crystallization; $T_{m\ max}$ temperature at the maximum of the peak of melting. The values of the temperatures are given with an accuracy of 1°C.

QUENCHED FILMS ATBC (%)	$T_{g\ mid}$ (°C)	$T_{c\ max}$ (°C)	$T_{c\ max} - T_{g\ mid}$ (°C)	$T_{m\ max}$ (°C)
0	61	105	44	156
5	52	95	43	154
10	45	86	41	152
15	36	79	43	150
AS-SPUN FIBERS ATBC (%)	$T_{g\ mid}$ (°C)	$T_{c\ max}$ (°C)	$T_{c\ max} - T_{g\ mid}$ (°C)	$T_{m\ max}$ (°C)
0	57	88	31	154
5	50	79	29	152
10	41	71	30	151
15	36	67	31	150

From the average heat flow curves for quenched neat and plasticized films (Figure V.2.7.A), we observe that when ATBC is introduced in the quenched film of PLA, both the glass transition and the cold crystallization are shifted to lower temperatures, due to the plasticization. This shift is constant for both thermal events leading to $T_{c\ max} - T_{g\ mid} = 43\ ^\circ\text{C}$ independently of the ATBC content. By contrast, the peak of melting changes from a double peak to a single one which is preceded by an exothermal event. According to many authors [4][5][6], the double peak is characteristic of the concomitant formation of both highly ordered α crystals and less ordered δ crystals [7][8]. On the other hand, the exothermal event is typically observed when only δ crystals form during the cold-crystallization [9] and is characteristic of their reorganization in α crystals just prior the melting [9][10]. As a consequence the nature of the crystalline form which is generated during the cold-crystallization changes when the PLA is plasticized. One can also note that the temperature of melting $T_{m\ max}$ decreases slightly with an increase of the ATBC content. This is likely due to the creation of crystals with a lower degree of perfection.

The electrospinning of PLA (Figure V.2.7.B) induces a decrease of the glass transition temperature from 61 to 57 $^\circ\text{C}$. A previous study by Zong et al. attributed this behavior to an increase of the surface to volume ratio in electrospun materials having air as a plasticizer. Obviously $T_{c\ max} - T_{g\ mid}$ also decreases from 43 $^\circ\text{C}$ to 30 $^\circ\text{C}$. This observation is usual in electrospun fibers [2][3][11] as the orientation of the macromolecules enhances the cold-crystallization which therefore occurs at a lower temperature. In the case of electrospun fibers, Tsuji et al. [11] conclude that the crystallization has been frozen by the fast removal of the solvent from the electrospun fibers. Edwards et al. [12] and Ma et al. [2] even consider that extended polymer chains in electrospun fibers can act as row nuclei during heating just above glass transition. When electrospinning is carried on plasticized PLA, $T_{g\ mid}$ decreases from 57 $^\circ\text{C}$ to 36 $^\circ\text{C}$ as the content of ATBC increasing from 0% to 15% evidencing the plasticizing effect of ATBC. The decrease of both $T_{c\ max}$ and $T_{m\ max}$ previously reported for quenched films is also recorded. Eventually, $T_{c\ max} - T_{g\ mid}$ remains equal to 30 $^\circ\text{C}$ which means that in spite of the plasticizer addition, the macromolecules are oriented during the electrospinning. As we discussed before, the plasticizing effect of ATBC is evidenced in both quenched films and electrospun fibers. However one can rightfully question the solubility of ATBC in PLA when the blend is dissolved in a mix of chloroform and acetone. From the Hildebrand solubility theory

[13][14], the small molecules in the electrospinning solution (chloroform, acetone and ATBC) have closely matching parameters; [18.4 (MJ m⁻³)^{1/2}] for ATBC, [19.0 (MJ m⁻³)^{1/2}] for chloroform, [20.0 (MJ m⁻³)^{1/2}] for acetone. On the other hand, the Hildebrand solubility parameter of PLA is equal to [21.9 (MJ m⁻³)^{1/2}]. Consequently there is a chance that the ATBC will be partially carried along by the solvent during the evaporation. In Figure V.2.11, the $T_{g, mid}$ is given as a function of the ATBC weight content for both quenched films and as-spun fibers. Clearly the trend is independent on the process, as the $T_{g, mid}$ decreases similarly with an increasing content of ATBC. The expected variations of the $T_{g, mid}$ with the content of ATBC according to Fox law have also been included in the figure. To do this, it has been foreseen that the tendency will shift whether we consider $T_{g, mid}$ of quenched films or as-spun fibers as the reference $T_{g, mid}$ for neat PLA. In both cases the variations of the glass transition temperature roughly follow Fox's law. This proves that the ATBC remains trapped in PLA during the evaporation of the solvent, likely because of its lower vapor pressure at ambient temperature, its higher molecular weight and its higher boiling point compared to chloroform and acetone. Consequently, the electrospinning of plasticized PLA is successful.

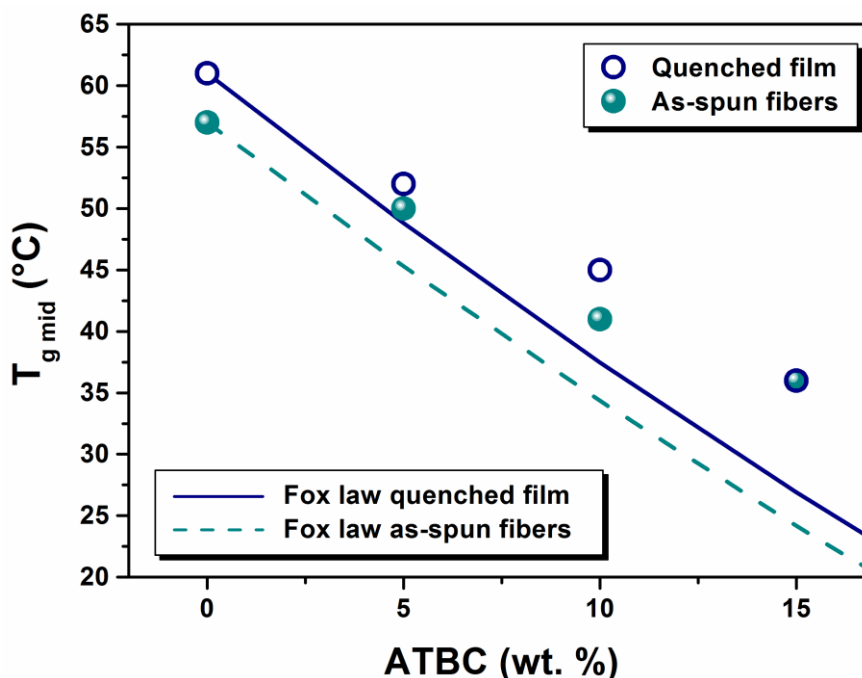


Figure V.2.11: $T_{g, mid}$ vs. ATBC weight content for all materials. The solid curve corresponds to the Fox law by considering the $T_{g, mid}$ value of the quenched film of neat PLA. The dashed curve corresponds to the Fox law by considering the $T_{g, mid}$ of the as-spun fibers of neat PLA.

V.2.2.3 Parallel with WAXS investigations

To confirm the structural modifications revealed by WAXS, it is interesting to investigate whether plasticization and electrospinning cause changes affecting the glass transition profile. Figure V.2.12 shows the average heat flow and the non-reversing heat flow for the quenched films in the glass transition domain. The interest in using the non-reversing heat flow in this case is to highlight the possible kinetic events occurring simultaneously with the glass transition. For example, in Figure V.2.12.A, a peak is recorded on the non-reversing heat flow signal, which is related to the existence of an endothermic event. Classically, due to the glassy character of PLA at ambient temperature, this peak might be attributed to physical aging. For the plasticized PLA, the profiles presented in Figure V.2.12.B-C-D are similar but the glass transition as well as the peak in the non-reversing heat flow signal are significantly broadened as the content of ATBC increases. Those observations are consistent with previous observations on plasticized polylactide [15][16] and are related to an increase of the relaxation temperature distribution induced by the plasticizer addition. We cannot be definitive concerning the nature of this peak. Nevertheless, its enlargement with plasticization coincides with the increase of the dynamic heterogeneity in the amorphous phase [15]. Typically this heterogeneity reflects in the structural relaxation [15][17], so the initial hypothesis of physical aging is reinforced.

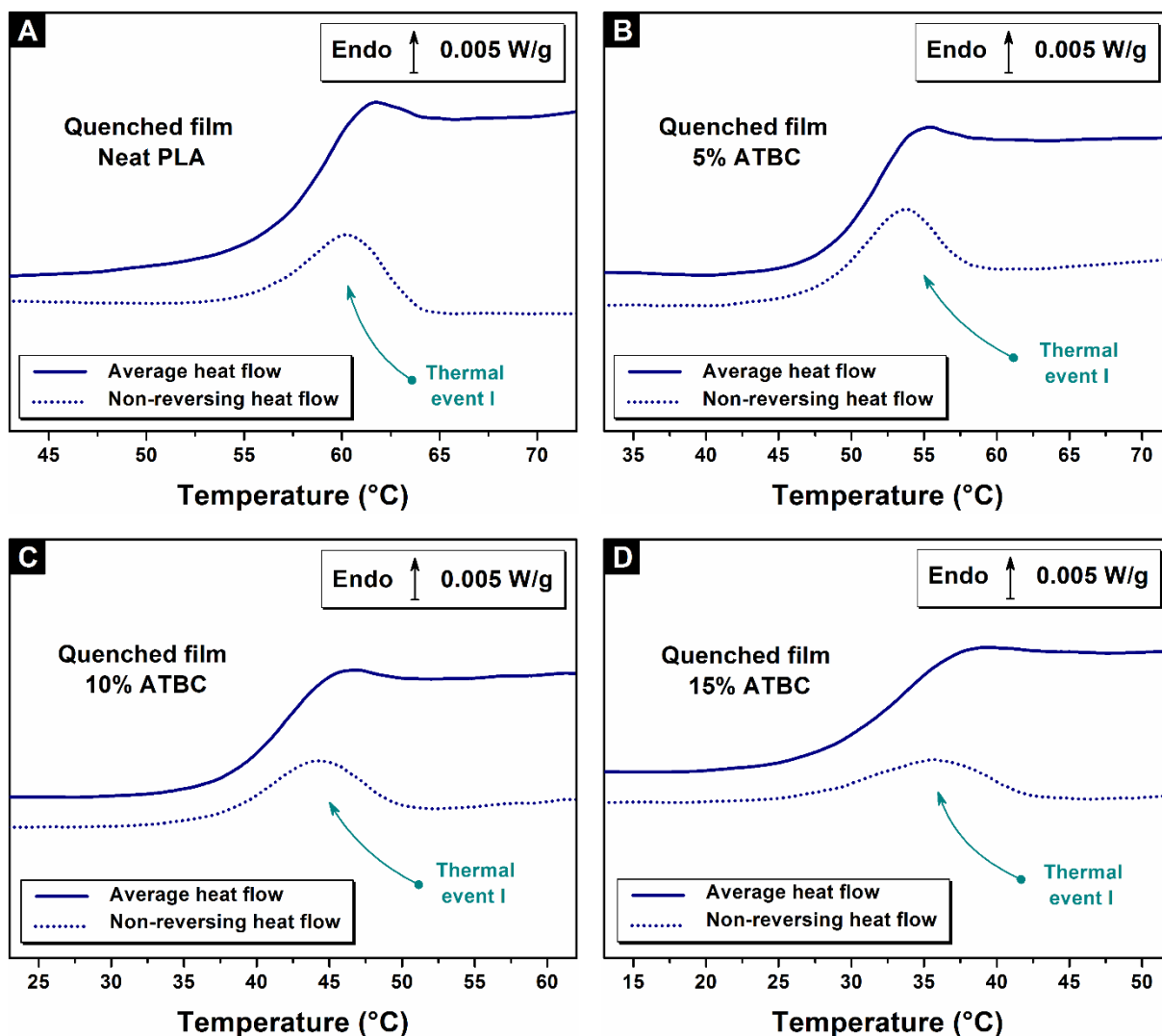


Figure V.2.12: Average heat flow (solid line) and non-reversing heat flow (dotted line) vs. temperature from MT-DSC for quenched films. **(A)** Neat PLA. **(B)** PLA + 5 % ATBC. **(C)** PLA + 10 % ATBC. **(D)** PLA + 15 % ATBC.

Figure V.2.13 shows the average heat flow and the non-reversing heat flow regarding the as-spun fibers in the glass transition domain. In Figure V.2.13.A, two thermal events can be distinguished. The first appears at the beginning of the glass transition, similar to the peaks observed in the cases of the quenched films. It is reasonable to consider that it is related to the same thermal event, most likely the recovery of structural relaxation. The second peak occurs just at the junction between the glass transition and the cold-crystallization. Ma et al. [2] in their DSC analyses on free-end fibers, also observed a shouldering between the glass transition and the cold-crystallization but they did not ascribed it to any given thermal event. In our study, this behavior is only clearly observed for the as-spun fibers of neat PLA, so the existence of the second peak could be related to the presence of mesophase previously

revealed by WAXS. Indeed it has been reported that the “melting” of the mesophase in oriented PLA often occurs in the glass transition temperature range when its thermal stability is low [18][19]. According to Lv et al. [19], when the formation of the mesophase is not followed by a subsequent crystallization (which provides a good representation of the microstructure of as-spun fibers), the molecular ordering induced by the process is completely destroyed above T_g due to the conformational rearrangements of the macromolecules that become possible with the sudden gain of molecular mobility.

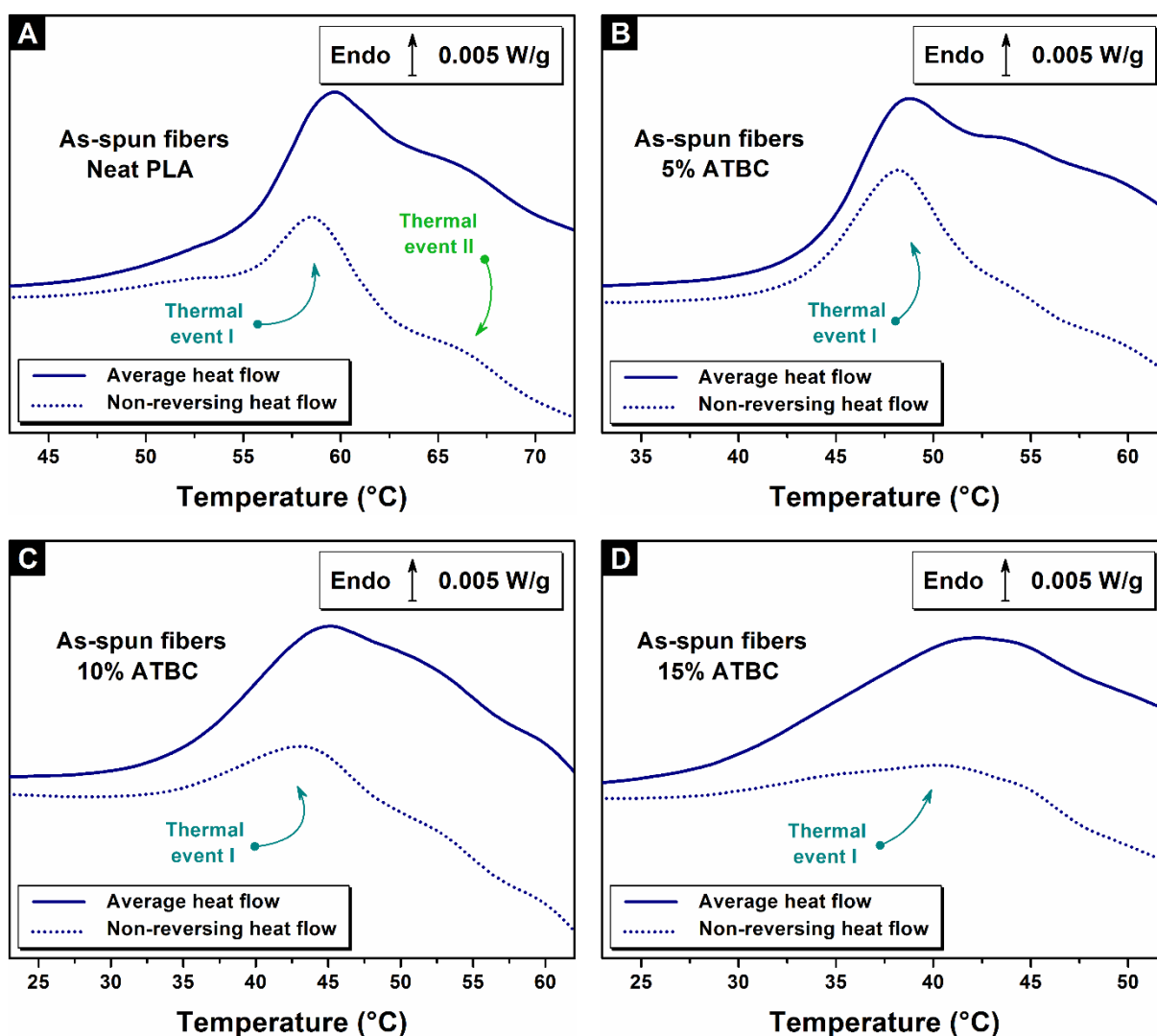


Figure V.2.13: Average heat flow (solid line) and non-reversing heat flow (dotted line) vs. temperature from MT-DSC for as-spun fibers. (A) Neat PLA. (B) PLA + 5 % ATBC. (C) PLA + 10 % ATBC. (D) PLA + 15 % ATBC.

When electrospinning is carried on plasticized PLA, as shown in Figure V.2.13.B-C-D, the two separated thermal events observed for as-spun fibers of neat PLA are less evident to distinguish. The thermal event related to the structural relaxation is easily perceptible in all

cases. On the other hand, especially for the 5% and 10% ATBC, the fluctuations do not allow to clearly establish the lack of mesophase. Independently, in the case of the 15% ATBC a broad peak covering the entire temperature range is visible and related to the structural relaxation. In these conditions, it is impossible to definitively assert whether or not this peak constitutes the signature of only one thermal event. It is clear, however, that the ATBC strongly impacts the organization of the macromolecules.

V.3 Molecular Dynamics

Figure V.3.1 shows the C' and C'' signals for the quenched films. From these two components, as explained in the chapter I, it is possible to extract the dynamic glass transition temperature T_α that corresponds to the maximum of the C'' peak, the heat capacity at constant pressure extrapolated to T_α in the glassy $C_{p, \text{glass}}$ and liquid $C_{p, \text{liquid}}$ states, as well as the mean temperature fluctuation associated with the glass transition δT that allows the calculation of the cooperativity length ξ_{T_α} . The density of the amorphous phase is also needed for the calculation of the ξ_{T_α} and has been approximated as being equal to the density of the material, i.e., equal to 1.25 due to the obvious majority of the amorphous phase in all the samples. All these relaxation parameter values are presented in Table V.3.1, for the quenched films as well as for the as-spun fibers. As expected, the plasticizer addition in quenched films of PLA from 0 % to 15 % ATBC content induces a decrease of T_α from 62 °C to 36 °C. It also increases δT from 3.1 °C to 5.5 °C without clear modification of the heat capacity step $\Delta C'$ which leads ξ_{T_α} to decrease from 2.8 nm down to 2.0 nm. The values of cooperativity lengths agree with those reported by Dobircau et al. [15] on PLA plasticized with ATBC, as well as those reported by Delpouve et al. regarding neat PLA bulk [20].

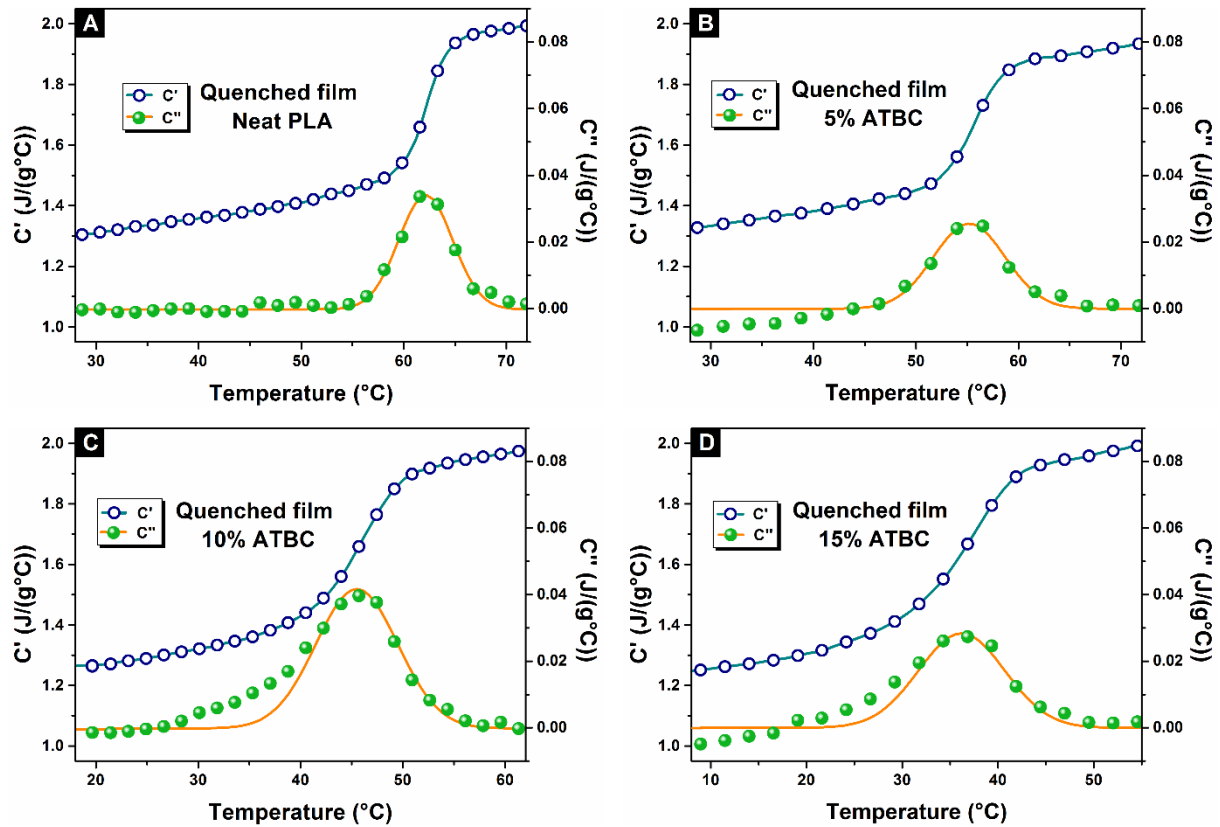


Figure V.3.1: MT-DSC in-phase component C' and out-of-phase C'' of the complex heat capacity C^* for the quenched films. (A) Neat PLA. (B) PLA + 5 % ATBC. (C) PLA + 10 % ATBC. (D) PLA + 15 % ATBC.

Table V.3.1: MT-DSC parameters for the quenched films and the as-spun fibers: T_α dynamic glass transition temperature; $\Delta C'$ heat capacity step from the in-phase component; δT mean temperature fluctuation related to the glass transition; ξ_{T_α} cooperativity length at the dynamic glass transition temperature. MT-DSC signals are normalized to the mass of PLA.

QUENCHED FILMS ATBC (%)	$\Delta C'$ ($\text{J}\cdot\text{g}^{-1}\cdot\text{K}^{-1}$)	T_α ($^\circ\text{C}$)	δT ($^\circ\text{C}$)	ξ_{T_α} (nm)
0	0.49 ± 0.05	62 ± 1	3.1 ± 0.2	2.8 ± 0.3
5	0.44 ± 0.05	55 ± 1	4.1 ± 0.2	2.5 ± 0.2
10	0.49 ± 0.05	46 ± 1	4.7 ± 0.3	2.1 ± 0.3
15	0.51 ± 0.05	36 ± 1	5.3 ± 0.3	2.0 ± 0.3
AS-SPUN FIBERS ATBC (%)	$\Delta C'$ ($\text{J}\cdot\text{g}^{-1}\cdot\text{K}^{-1}$)	T_α ($^\circ\text{C}$)	δT ($^\circ\text{C}$)	ξ_{T_α} (nm)
0	0.57 ± 0.05	59 ± 1	2.4 ± 0.1	3.6 ± 0.3
5	0.50 ± 0.05	51 ± 1	4.0 ± 0.2	2.6 ± 0.2
10	0.51 ± 0.05	42 ± 1	4.7 ± 0.3	2.2 ± 0.2
15	0.45 ± 0.05	35 ± 1	5.4 ± 0.3	2.0 ± 0.2

Figure V.3.2 shows the C' and C'' signals for the as-spun fibers. When the neat PLA undergoes electrospinning (see Table V.3.1), T_α decreases similarly to $T_{g\text{ mid}}$ from 62 °C to 59 °C. An increase of $\Delta C'$ from 0.49 to 0.57 J.g⁻¹.K⁻¹ is also recorded. However, the usually high uncertainty around the values of the heat capacity step does not allow for the distinguishing of whether this variation is significant or not. On the other hand, the C'' peak is obviously narrower for the as-spun fibers than the quenched film. Consequently, the as-spun fibers present an average fluctuation temperature of 2.4 °C against 3.1 °C for the quenched film and the cooperativity length in the as-spun fibers reaches 3.6 nm against 2.8 nm in the quenched film, which corresponds approximately to an increase of the cooperativity length of around 30%. Such an increase of cooperativity induced by the process is unusual and rarely mentioned in literature, so it will get further consideration in the following paragraphs. Finally one can observe that the plasticized materials exhibit similar values of relaxation parameters whether they are electrospun or not, as observed in Figure V.3.3. In other words, the electrospinning has no effect on the α -relaxation of plasticized polylactide.

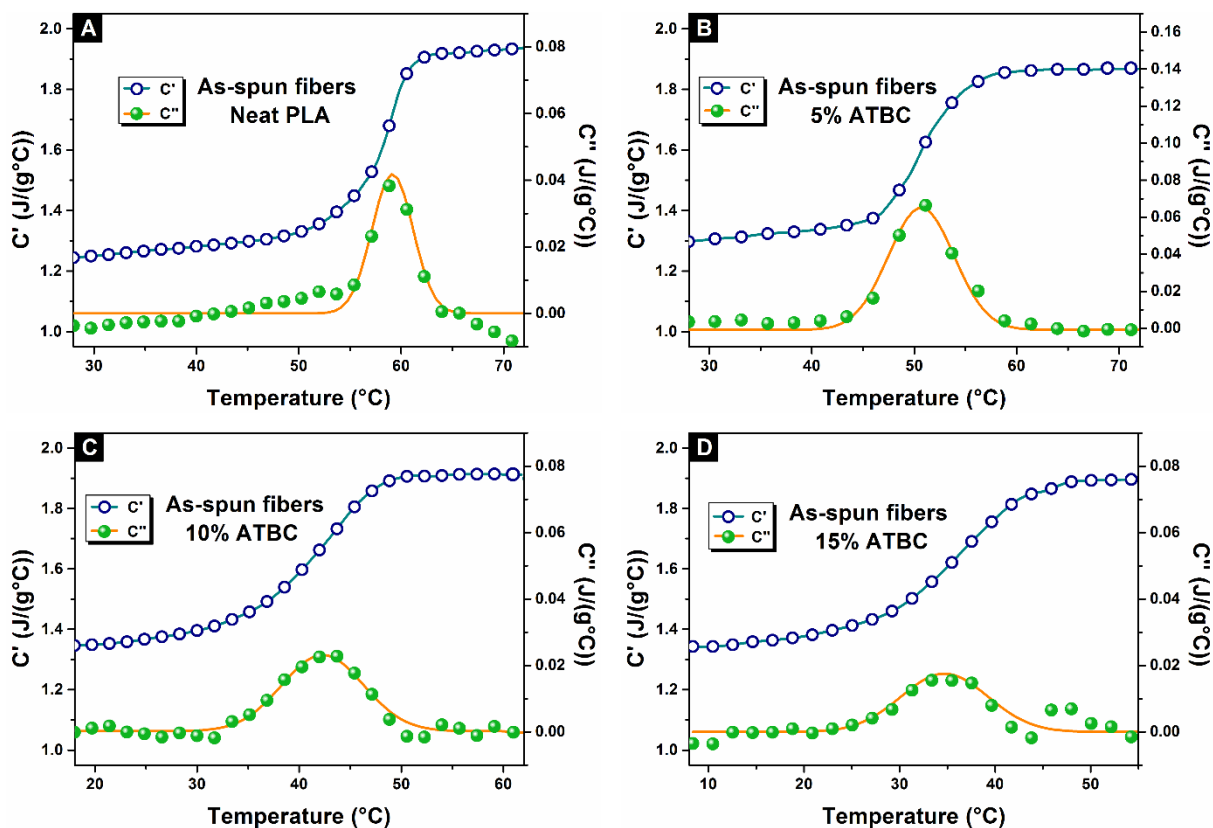


Figure V.3.2: MT-DSC in-phase component C' and out-of-phase C'' of the complex heat capacity C^* for the as-spun fibers. (A) Neat PLA. (B) PLA + 5 % ATBC. (C) PLA + 10 % ATBC. (D) PLA + 15 % ATBC.

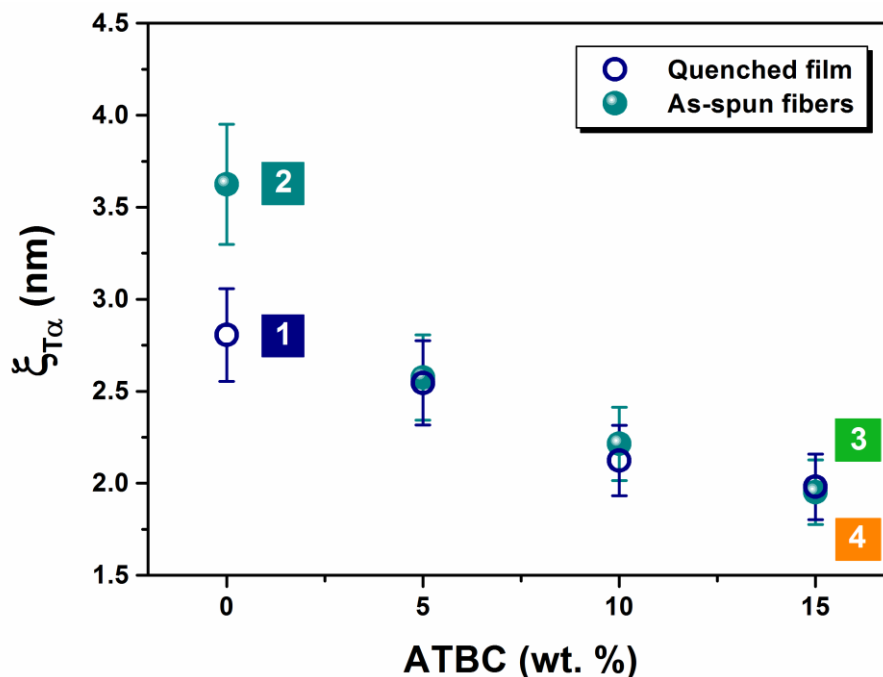


Figure V.3.3: Cooperativity length vs. ATBC content in quenched films as well as as-spun fibers. (1), (2), (3) and (4) are related to the schematic view of the macromolecules organization for representative systems depicted in Figure V.3.4.

As mentioned in the chapter I, the cooperativity length is dependent on both the temperature and the structural organization into the material. In the present study, the cooperativity length has been calculated for each material at the dynamic glass transition temperature in order to limit the observed variations to structural causes. Figure V.3.4 aims at picturing the structural dependence of the cooperativity resulting from the external and internal hindrances imposed on the material by focusing on four representative systems. In the quenched film amorphous PLA (system 1), the macromolecules arrange themselves into random coil, leading to a cooperativity length close to 3 nm which is in accordance with reported values of dynamic heterogeneities [21][22][23]. It is often reported in the literature that the relaxation time distribution broadens when the amorphous phase becomes constrained [17][20]. Since the electrospinning induces the orientation of the macromolecules of PLA in the amorphous phase (system 2), one might have expected that the cooperativity at the glass transition will decrease. On the contrary the molecular motions at the glass transition are more cooperative. To explain this result, we should first consider that despite the orientation of the macromolecules, the material is non-crystalline which means that the amorphous phase is not confined in any way. That makes a big difference compared to semi-crystalline drawn materials that typically exhibit lower cooperativity motions at the glass

transition [24][25]. In this latter case, the decrease of cooperativity induced by the drawing should not be attributed to the induced orientation of the macromolecules but to the presence of crystallites confining the amorphous phase, as observed in the previous chapter with regard to flow induced crystalline structure. It is also interesting to notice that the cooperativity increase in an initially quenched film amorphous material is often related to the same cause, i.e. the creation of nano-domains playing the role of anchoring points between the macromolecules [26][27]. In our case, we can reasonably assume that the highly cohesive mesophase plays this role by increasing the level of inter-molecular interactions, thus leading to the global increase of the cooperativity length. The opposite effect occurs when adding ATBC to the quenched film of PLA (system 3). Although the action of the plasticizer still deserves more investigations, it is revealed from our WAXS measurements that the increase of the dynamic heterogeneities which leads to the decrease of the average cooperativity length is associated to a redistribution of the inter-chain distances. This is consistent with the assumption that the cooperativity length is correlated with the nature and the number of inter-chain interactions [28]. In regard to this hypothesis, the decrease of the cooperativity length could be interpreted as the consequence of inter-chain bond breaking. Finally, although MT-DSC results suggest that the macromolecules are oriented in the electrospun plasticized materials (system 4), the cooperativity at the glass transition remains unchanged before and after electrospinning. We assume that the changes in molecular dynamics induced by the plasticizer addition are prevalent over the structural reorganization induced by electrospinning, and that the plasticization is not favorable to the formation of the mesophase.

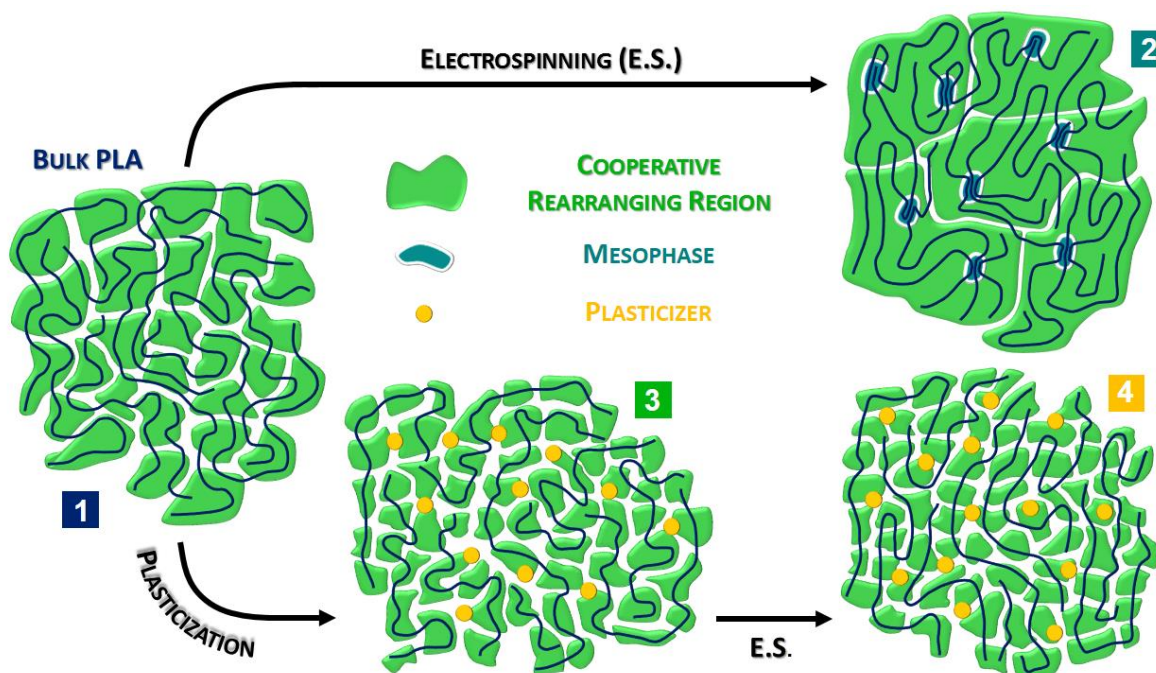


Figure V.3.4: Structural dependence of the cooperativity at the glass transition: Schematic view of the macromolecules organization for representative systems.

V.4 Conclusions

The microstructure induced by the electrospinning of polylactide depends both on the level of orientation of the macromolecules and on the necessary time for the macromolecules to reorganize in crystals. In our case, the structural anisotropy has been investigated through the formation of a highly ordered but non-crystalline microstructure, exhibiting about 4% of mesophase. In comparison to quenched film of polylactide, the α -relaxation of electrospun PLA is more cooperative. Since the cooperative motions at the glass transition are often related to the aptitude of the polymeric chains to connect by physical bonds, it is assumed that the mesophase plays the role of anchoring points between macromolecules due to its high cohesiveness. The plasticization of polylactide cancels any difference of cooperativity length between quenched films and as-spun fibers. Both exhibit a cooperativity decrease with the content of plasticizer. We assume that the plasticization induces strong modifications in the inter-chain characteristic spacing, and frustrates the creation of physical interactions between macromolecules. This effect prevails over the changes in the macromolecule organization that are induced by electrospinning.

REFERENCES

- [1] G. Stoclet, R. Seguela, J. M. Lefebvre, S. Elkoun, and C. Vanmansart, *Macromolecules* **43**, 1488 (2010).
- [2] Q. Ma, M. Pyda, B. Mao, and P. Cebe, *Polymer* **54**, 2544 (2013).
- [3] X. Zong, K. Kim, D. Fang, S. Ran, B. S. Hsiao, and B. Chu, *Polymer* **43**, 4403 (2002).
- [4] M. Yasuniwa, S. Tsubakihara, K. Iura, Y. Ono, Y. Dan, and K. Takahashi, *Polymer* **47**, 7554 (2006).
- [5] P. Pan, W. Kai, B. Zhu, T. Dong, and Y. Inoue, *Macromolecules* **40**, 6898 (2007).
- [6] M. L. Di Lorenzo, *J. Appl. Polym. Sci.* **100**, 3145 (2006).
- [7] K. Wasanasuk and K. Tashiro, *Polymer* **52**, 6097 (2011).
- [8] C.-Y. Chen, C.-F. Yang, U.-S. Jeng, and A.-C. Su, *Macromolecules* **47**, 5144 (2014).
- [9] J. Zhang, K. Tashiro, H. Tsuji, and A. J. Domb, *Macromolecules* **41**, 1352 (2008).
- [10] T. Kawai, N. Rahman, G. Matsuba, K. Nishida, T. Kanaya, M. Nakano, H. Okamoto, J. Kawada, A. Usuki, N. Honma, K. Nakajima, and M. Matsuda, *Macromolecules* **40**, 9463 (2007).
- [11] H. Tsuji, M. Nakano, M. Hashimoto, K. Takashima, S. Katsura, and A. Mizuno, *Biomacromolecules* **7**, 3316 (2006).
- [12] M. D. Edwards, G. R. Mitchell, S. D. Mohan, and R. H. Olley, *Eur. Polym. J.* **46**, 1175 (2010).
- [13] A. Ruellan, V. Ducruet, S. Domenek, CHAPTER 5 Plasticization Polylactide, 2014 (Chapter 5).
- [14] R.S. Ruoff, D.S. Tse, R. Malhotra, D.C. Lorents, *J. Phys. Chem.* **97** (1993) 3379-3383.
- [15] L. Dobircau, N. Delpouve, R. Herbinet, S. Domenek, L. Le Pluart, L. Delbreilh, V. Ducruet, and E. Dargent, *Polym. Eng. Sci.* **55**, 858 (2015).
- [16] C. Courgneau, S. Domenek, A. Guinault, L. Avérous, and V. Ducruet, *J. Polym. Environ.* **19**, 362 (2011).
- [17] N. M. Alves, J. F. Mano, E. Balaguer, J. M. Meseguer Dueñas, and J. L. Gómez Ribelles, *Polymer* **43**, 4111 (2002).
- [18] G. Stoclet, R. Seguela, J.-M. Lefebvre, and C. Rochas, *Macromolecules* **43**, 7228 (2010).
- [19] R. Lv, B. Na, N. Tian, S. Zou, Z. Li, and S. Jiang, *Polymer* **52**, 4979 (2011).
- [20] N. Delpouve, A. Saiter, J. F. Mano, and E. Dargent, *Polymer* **49**, 3130 (2008).
- [21] E. Hempel, G. Hempel, A. Hensel, C. Schick, and E. Donth, *J. Phys. Chem. B* **104**, 2460 (2000).
- [22] D. Fragiadakis, P. Pissis, and L. Bokobza, *Polymer* **46**, 6001 (2005).
- [23] J. Koppensteiner, W. Schranz, and M. A. Carpenter, *Phys. Rev. B* **81**, 024202 (2010).
- [24] F. Hamonic, D. Prevosto, E. Dargent, and A. Saiter, *Polymer* **55**, 2882 (2014).
- [25] Y. Furushima, K. Ishikiriya, and T. Higashioji, *Polymer* **54**, 4078 (2013).
- [26] A. Saiter, D. Prevosto, E. Passaglia, H. Couderc, L. Delbreilh, and J. M. Saiter, *Phys. Rev. E* **88**, 042605 (2013).
- [27] C. E. Corcione and A. Maffezzoli, *Thermochim. Acta* **485**, 43 (2009).
- [28] M. Nakanishi and R. Nozaki, *Phys. Rev. E* **84**, 011503 (2011).

CONCLUSION AND PROSPECTS

In the past few years, influence of the structural environment on the molecular dynamics of the amorphous phase in various polymer systems have been widely investigated. In that purpose, this research work was conducted in order to investigate the influence of the structural anisotropy on the molecular dynamics with regard to crystalline (flow induced crystalline structure) and non-crystalline (electrospun fibers) complex PLA systems prior to crystallization and vitrification. For crystalline structures, due to their micro- to nano-scale, an advanced technique in thermal analysis - FSC - have been mainly used in this work to characterize the microstructure as well as the molecular dynamics.

First, by working on wholly amorphous PLA, parameters influencing the structural relaxation by FSC have been investigated. Investigations have concluded that high cooling rates accelerate the structural relaxation due to the higher level of enthalpy induced in the glass, and the high fictive temperature formed. Besides, for short aging times, an influence of the sample geometry has been measured. The critical thickness involving an acceleration of the structural relaxation seems to be cooling rate dependent. Indeed, aging investigations for glasses formed at the same cooling rate, from DSC or FSC, show that the few mg of sample analyzed by FSC are well representative of the bulk sample analyzed by DSC.

Then, from this first part of the study, structural anisotropy induced prior to the crystallization have been investigated by FSC. From the cooperativity concept, the molecular dynamics at the glass transition were found to depend on the crystallinity degree at the macromolecular scale rather than on the crystalline morphology. The same enthalpy recovery was measured for all the systems (amorphous and crystallized ones), meaning that the structural relaxation is not influenced by the crystallinity degree. This result is consistent with the fact that physical aging is due to secondary relaxations and local motions, which are not affected by the crystalline environment (different length-scale) as well as the crystalline morphology. The only influence that could be observed is the one measured during the subsequent heating ramp through the α -relaxation, i.e. the glass transition, where segmental motions come back.

Finally, structural anisotropy generated on the amorphous phase by the electrospinning has been investigated through the formation of a highly ordered but non-crystalline microstructure, exhibiting about 4 % of mesophase. In comparison to wholly

amorphous PLA, the α -relaxation of electrospun PLA is more cooperative. Since the cooperative motions at the glass transition are often related to the aptitude of the macromolecular chains to connect by physical bonds, it is assumed that the mesophase plays the role of anchoring points between macromolecules due to its high cohesiveness. The plasticization of PLA cancels any difference of cooperativity length between amorphous samples and electrospun fibers. Both exhibit a decrease of cooperativity with increasing the content of plasticizer. It is assumed that the plasticization induces strong modifications in the inter-chain characteristic spacing and frustrates the creation of physical interactions between macromolecules. This effect prevails over the changes in the macromolecule organization that are induced by electrospinning.

This research work shows the difficulty and the complexity related to the understanding of the glass transition phenomenon, according to the nature of the structural anisotropy applied, either from glassy or liquid state. To extend to previous works, strain induced (Florian Hamonic Thesis) and flow induced crystallizations tend to display a similar impact on the molecular dynamics. Therefore in those specific cases, structural anisotropy is not the main parameter influencing the molecular dynamics, but the crystallization itself, namely the confinement effect of the crystals on the amorphous phase and the resulting strong coupling between both phases. For non-crystalline systems, structural anisotropy nature plays a significant role on the molecular dynamics. Strained PET_g, in the glassy state, depicts oriented and constrained structure where chain packing constrain their conformations (Florian Hamonic Thesis). On the contrary, non-crystalline PLA electrospun fibers depict oriented and unconstrained structure where chains display high cohesiveness. That is why, in addition to the present work, it could be interesting to examine the molecular dynamics of various polyester, such as PET, PET_g or polyethylene furanoate (PEF) subjected to the three different kinds of structural anisotropy mentioned above. Nature of molecular interactions seems to be the key to understand the molecular dynamics.

Besides, the most significant and intriguing prospects of this research work are the new possibilities opened by FSC for physical aging, as it has been discussed through wholly amorphous PLA and flow induced crystalline PLA structure. To go further, thanks to the acceleration of the structural relaxation kinetics, a temperature-time map of the fictive temperature, or the enthalpy recovery, can be investigated. Similar to a relaxation map, more

information on the molecular dynamics could be achieved for a wide range of aging temperatures and aging times. FSC can provide larger opportunities for future works. Finally, structural relaxation is now possible, and can be considered on other complex polymer systems such as multilayer polymers, semi-crystalline polymers or polymers with additives, among others. Especially, structural relaxation on electrospun fibers have to be performed to characterize their molecular dynamics in the glassy state to complete the work realized so far.

SCIENTIFIC COMMUNICATIONS

PUBLICATIONS: (*displayed in the following pages*)

1. X. Monnier, N. Delpouve, N. Basson, A. Guinault, S. Domenek, A. Saiter, P.E. Mallon, E. Dargent - "*Molecular dynamics in electrospun amorphous plasticized polylactide fibers*". **Polymer 73 (2015) 68-78**
2. X. Monnier, A. Saiter, E. Dargent - "*Physical aging in PLA through standard DSC and fast scanning calorimetry investigations*". **Thermochimica Acta 648 (2017) 13-22**
3. B. Schammé, X. Monnier, N. Couvrat, L. Delbreilh, V. Dupray, E. Dargent, G. Coquerel - "*Insights on the physical state reached by an active pharmaceutical ingredient upon high-energy milling*". **The Journal of Physical Chemistry B 121 (2017) 5142-5150**
4. X. Monnier, J-E. Maigret, D. Lourdin, A. Saiter - "*Glass transition of anhydrous starch by fast scanning calorimetry*". **Carbohydrate Polymers 173 (2017) 77-83**
5. X. Monnier, L. Chevalier, A. Esposito, L. Fernandez-Ballester, A. Saiter, E. Dargent - "*Local and segmental motions of the mobile amorphous fraction in semi-crystalline polylactide crystallized under quiescent and flow-induced conditions*". **Polymer 126 (2017) 141-151**

ORAL COMMUNICATIONS:

1. X. Monnier, N. Delpouve, N. Basson, A. Guinault, S. Domenek, A. Saiter, P.E. Mallon, E. Dargent - "*Anisotropie structurale dans des fibres électrofilées de polylactide plastifiées: Etude de la phase amorphe*". **37^{ème} Journées du Groupe Français des Polymères, section Grand Ouest - Alençon, France, 2016**
2. X. Monnier, N. Delpouve, N. Basson, A. Guinault, S. Domenek, A. Saiter, P.E. Mallon, E. Dargent - "*Investigations of the amorphous phase in electrospun PLA fibers*". **8^{ème} Journées Des Doctorants de l'école doctorale n°591 SPMII (JDD) - Le Havre, France, 2016**

3. X. Monnier, D. Lourdin, A. Saiter - "*Interest of the fast scanning calorimetry: from polylactide to anhydrous starch*". **Séminaire invité, INRA, UR1268 Biopolymères Interactions Assemblages, Nantes, France, 2016**
4. X. Monnier, A. Saiter, E. Dargent - "*Structural relaxation of amorphous Polylactide : Parallel between DSC and FSC*". **48^{ème} Journées de Calorimétrie et d'Analyse Thermique (JCAT 48) - Reuil-Malmaison, France, 2017**
5. X. Monnier - "*Fast scanning calorimetry: thermal analysis from micro- to nano-scale*". **1^{ère} Journée scientifique du département Systèmes Désordonnés et Polymères - Saint-Etienne du Rouvray, France, 2017**
6. X. Monnier, A. Saiter, E. Dargent - "*Glass transition and glassy state of a wholly amorphous Polylactide from standard differential and fast scanning calorimetry*". **4th Central and Eastern European Conference on Thermal Analysis and Calorimetry (CEEC-TAC4) - Chisinau, Moldova, 2017**

POSTER COMMUNICATIONS: (*displayed in the following pages*)

1. X. Monnier, N. Delpouve, N. Basson, A. Guinault, S. Domenek, A. Saiter, P.E. Mallon, E. Dargent - "*Molecular dynamics in electrospun fibers of plasticized polylactide*". **Polychar 23 World Forum on Advanced Materials - Lincoln, USA, 2015**
2. X. Monnier, A. Saiter, E. Dargent - "*Structural anisotropy: Microstructure and molecular dynamic investigations*". **7^{ème} Journées Des Doctorants de l'école doctoral n°591 SPMII (JDD) - Rouen, France, 2015**
3. X. Monnier, L. Chevalier, L. Delbreilh, A. Saiter, E. Dargent - "*Thermal analysis at the micro-scale of semi-crystalline polymers through fast scanning calorimetry - Skin/Core layers investigations*". **47^{ème} Journées de Calorimétrie et d'Analyse Thermique (JCAT 47) - Angelet, France, 2016**
4. X. Monnier, A. Saiter, E. Dargent - "*Insight and understanding of physical aging through DSC and FSC from Polylactic acid*". **14th Laehnwitzseminar on Calorimetry - "Interplay between nucleation, crystallization and the glass transition" - Rostock, Germany, 2016**

5. X. Monnier, A. Saiter, E. Dargent - "*Investigations of Polylactide subjected to anisotropic and confinement effects by fast and modulated temperature differential scanning calorimetry (FSC and MT-DSC)*". **6th International Conference on Biobased and Biodegradable Polymers (BIOPOL) - Mons, Belgium, 2017**



Molecular dynamics in electrospun amorphous plasticized polylactide fibers



X. Monnier^{a, d}, N. Delpouve^{a, *}, N. Basson^d, A. Guinault^b, S. Domenek^c, A. Saiter^a, P.E. Mallon^d, E. Dargent^a

^a AMME-LECAP EA 4528 International Lab, Av. de l'Université, BP12, Normandie Univ. France, Université and INSA Rouen, 76801 St Etienne de Rouvray, France

^b CNAM, Laboratoire PIMM, UMR 8006, 151 Boulevard de l'Hôpital, 75013 Paris, France

^c AgroParisTech, UMR1145 Ingénierie Procédés Aliments, 1 Avenue des Olympiades, 91300 Massy, France

^d Department of Chemistry and Polymer Science, University of Stellenbosch, Private Bag X1, 7602 Matieland, South Africa

ARTICLE INFO

Article history:

Received 10 April 2015

Received in revised form

21 July 2015

Accepted 24 July 2015

Available online 26 July 2015

Keywords:

Nanofibers

PLA

Amorphous phase

ABSTRACT

The molecular dynamics in the amorphous phase of electrospun fibers of polylactide (PLA) has been investigated using the cooperative rearranging region concept. An unusual and significant increase of the cooperativity length at the glass transition induced by the electrospinning has been observed. This behavior is attributed to the singularity of the amorphous phase organization. Electrospun PLA fibers rearrange in a pre-ordered metastable state which is characterized by highly oriented but non-crystalline polymer chains, and the presence of highly cohesive mesophase which plays the role of an anchoring point in the amorphous phase. The successful processing of electrospun fibers of plasticized polylactide is also demonstrated. It is shown that the plasticizer remains in the polymer matrix of the nanofiber after electrospinning. When PLA is plasticized, the loosening of the macromolecules prevails over the preferential orientation of the chains; therefore no mesophase is formed during the electrospinning and the cooperativity length remains the same. When the content of plasticizer increases, the inter-chain characteristic distances estimated from wide angle X-ray scattering (WAXS) are redistributed, suggesting a change in the level of interactions between macromolecules. It is assumed that the resulting decrease of the cooperativity length is driven by the progressive reduction of the number of inter-chain weak bonds. It is shown that in a non-confined environment, the number of structural entities involved in the alpha relaxation is strongly dependent on the level of physical interactions in the amorphous phase.

© 2015 Elsevier Ltd. All rights reserved.

1. Introduction

In the theory of Adam and Gibbs [1], the relaxation process related to the glass transition is cooperative, and the motion of a structural unit is only possible if a given number of neighboring units are also in motion. Among the different models used to estimate the size of the Cooperative Rearranging Region (CRR) or cooperativity length, is the thermodynamic approach proposed by Donth [2] which relates the CRR to the dynamic heterogeneity deduced from the temperature fluctuation associated with the glass transition. This approach provides a picture of the relaxation

time at the glass transition which is directly observable through calorimetric measurements [3]. According to this approach [2], the cooperativity volume $\xi_{T\alpha}^3$ at the dynamic glass transition temperature T_α can be estimated from the following equation:

$$\xi_{T\alpha}^3 = \frac{(1/C_p)_{Glass} - (1/C_p)_{Liquid}}{\rho(\delta T)^2} k_B T_\alpha^2 \quad (1)$$

With k_B the Boltzmann constant, δT the average temperature fluctuation related to the dynamic glass transition of a CRR, ρ the density, and C_p the heat capacity at constant pressure. Two causes for cooperativity changes have been observed so far. The first relates to changes in thermodynamic variables such as temperature, and the second to structural modifications of the material. In the first case, it is well known that the cooperativity length increases

* Corresponding author.

E-mail address: nicolas.delpouve1@univ-rouen.fr (N. Delpouve).

when the temperature decreases from the crossover temperature for which the cooperativity arises to the glass transition temperature [4–6]. In the second case, the approach of Donth has widely been used to investigate the decrease of cooperativity for two kinds of structural hindrances namely external and internal hindrances. External hindrances are related to geometrical restrictions like the confinement between nanolayers [7,8] or the addition of additives such as fillers [9,10] or plasticizer [11]. On the other hand, internal hindrances are related to the materials itself, in other words its microstructural modifications such as spherulitic crystallization [12,13] or orientation/crystallization of the amorphous phase induced by drawing [5,14].

In the last decade, the growing interest for polylactide (PLA) as a promising substitute to petroleum issued polymers has led researchers to investigate how its macroscopic properties could be tailored by controlling its microstructure. Because of the strong dependence of PLA macroscopic properties on its microstructure [15] and molecular dynamics [16], the cooperativity of the alpha relaxation process has been particularly investigated when the relaxation dynamics of the amorphous phase are modified by orientation [17], crystallization [13], or even plasticization [11]. However, the impact of several microstructural modifications on the amorphous phase dynamics remains unknown. For example, as illustrated by several authors [18–20], given conditions for drawing or thermal crystallization may induce the development of an intermediate ordering structure called a mesophase which prefigures the crystallization. The observation of the mesophase is generally reported for semi-crystalline materials [18–22] for which crystals strongly impact the investigation of the molecular mobility. Consequently, no study deals with the impact alone of the mesophase on the molecular dynamics of the amorphous phase. One of the challenges to carry out such a study lies in obtaining a unique microstructure where the mesophase is only dispersed in the oriented amorphous phase, without the presence of crystals. In the current study, we propose to electrospin polylactide (PLA) fibers to create this specific microstructure. Electrospinning is a simple technique to implement in order to produce polymer fibers with diameters ranging from the micro- to the nanoscale [23–25]. The technique has emerged as a useful technique to produce micro- and nano-fibers that have found wide applications in fields such as tissue engineering [26], biomedical [27], filtration [28], or electronic [29]. Despite the simplicity of the technique, many factors influence the fiber morphology including the solution flow rate, the distance between the syringe and the collector, solution concentration and the spinning voltage among others. In addition, very complex processes are involved that influences the fiber structure including the very rapid solvent evaporation as well as the mechanical and electrical forces which induce an orientation of the macromolecular chains along the fiber axis [24]. For these reasons, electrospinning can lead to complicated internal microstructures and high contents of mesophase [30]. Zong et al. [31] initially reported that electrospun fibers of polylactide (PLA) exhibit highly oriented chains although they are non-crystalline. Recently Ma et al. [32] confirmed this result by showing that the electrospinning carried on free-end fibers of PLA leads to the formation of an original microstructure where the amorphous phase is oriented with evidence of a mesophase but without the formation of any crystals. In the current study, we report for the first time on the cooperativity lengths obtained for as-spun fibers of polylactide using Donth's approach. We use the electrospinning technique in order to avoid the effects related to the confinement of the amorphous phase by crystals, similar to what is observed during drawing. The process has been designed to prevent any formation of the crystalline phase during the fiber formation.

As is well known, the applications for neat PLA are usually

compromised due to its inherent brittleness [33]. Thus, plasticizers are often added to PLA in order to improve its mechanical properties. Acetyl Tributyl Citrate (ATBC) considered here, is among the most widely used plasticizers [33,34]. In this study, we report for the first time the electrospinning of plasticized PLA. Here, the goal is to observe if the internal modifications related to the mesophase still exist when ATBC is added as a plasticizer. It will allow another aspect of the impact of microstructural modifications on the amorphous phase dynamics to be depicted from the combination of both internal/external hindrances. Two series of samples have been analyzed: as-spun plasticized fibers and bulk plasticized PLA. Finally it is of interest to determine if the plasticizer remains inside the fibers after the electrospinning process and thus still acts as a plasticizer for the polymer nanofibers.

2. Experimental

2.1. Materials

Semi-crystalline PLA pellets (grade 4042D) were provided by Natureworks. The content of *l*-lactide and *d*-lactide were about 96% and 4% respectively. The number-average and weight-average molecular weights were $M_n = 116$ kDa and $M_w = 188$ kDa respectively, as measured by Gel Permeation Chromatography. Acetyl tributyl citrate (ATBC, CAS Number 77-90-7) was purchased from sigma Aldrich (France). PLA and ATBC were dried at 80 °C under vacuum for 12 h. Blending was performed with an internal mixer (Haake Rhecord 9000) at 160 °C and 60 rpm for 15 min. After a subsequent drying step (4 h at 80 °C under vacuum) bulk samples were obtained. In order to perform WAXS, bulk samples were thermo-molded in films of 1 mm thickness. For each system, neat PLA were heated during 5 min between two hot plates, and then the obtained films were quickly quenched in cold water. The measure of density leads to a constant value equal to 1.25 g/mol independent of the plasticizer content.

2.2. Electrospinning set-up

The polymer solutions were prepared in mix solvent of chloroform and acetone (chloroform:acetone = 2:1 in volume), both purchased from sigma Aldrich (South Africa). Plasticized and non-plasticized PLA were dissolved in the mix solvent and stirred using a magnetic stir bar at room temperature until homogenization of the solution. The required amounts of polymer were figured out to give a concentration solution of 8 wt% in PLA. Then, the polymer solution was placed in a horizontally glass pipette with a capillary around 1 mm diameter. At 5 cm from the needle, a petri-dish covered by an aluminum foil took place as a collector. The needle and the collector were connected to a high-voltage power supply which can generate a voltage up to 50 kV. The electric field applied was 1 kV cm^{-1} . The flow rate was controlled by a pump at 0.04 mL min^{-1} . The electrospinning process took place under controlled atmospheric conditions at 25 ± 2 °C and $35 \pm 4\%$ relative humidity. The thickness of the final as-spun fibers mat was less than 1 mm.

2.3. Scanning electronic microscopy (SEM)

The morphology of as-spun PLA fibers was investigated by scanning electronic microscopy (LEO 1430VP) after being gold coated during 3 min. The diameter of as-spun fibers was measured with an image analyzer (AxioVision 40LE). For each sample, average fiber diameter and standard deviation were determined from more than 200 measurements of the random fibers.

2.4. Wide angle X-ray scattering (WAXS)

WAXS measurements were performed on a PANalytical X'Pert Pro diffractometer in Bragg–Brentano mode with X'Celerator detector. The generator was set up at 45 kV and 40 mA and the copper Cu K α radiation ($\lambda = 1.54 \text{ \AA}$) was selected. The system was equipped with a silicon-made sample holder on a spinner stage PW3064, and a goniometer PW3050/60 system. The silicon holder used is neutral (no diffraction peak) in order to avoid a baseline subtraction step. The distance from the sample to the detector was fixed at 14 cm. The measurements were run at room temperature from 5° to 45° at 0.04 °/s and with a rotational speed equal to one revolution per second. Quenched films and as-spun fibers mats were directly placed on the silicon holder without any preparation. The peak fitting was then performed using the Graftylabs software after background subtraction to determine the different amorphous contributions by following the method outlined by Stoclet et al. [21].

2.5. Modulated temperature differential scanning calorimetry (MT-DSC)

Modulated temperature differential scanning calorimetry (MT-DSC) experiments were performed in a DSC Q100 from Thermal Analysis instruments under nitrogen atmosphere (50 mL min⁻¹). The calibration in temperature and energy was done using standard of indium, while the calibration of the heat capacity was carried out using sapphire as reference. The MT-DSC experiments were performed in heating from 0 to 200 °C, in "Heat-Only" mode ($\pm 0.318 \text{ K}$ for the oscillation amplitude, 60 s for the oscillation period and 2 K min⁻¹ regarding the heating rate). This mode is recommended to investigate the coupling of different thermal events such as glass transition and cold crystallization without any disturbance caused by instantaneous cooling. The as-spun fibers and bulk samples mass were kept around 5 mg. The Al reference and sample couples, pan and lid, were identical to within $\pm 0.01 \text{ mg}$. By MT-DSC, in addition of the modulated heat flow, the apparent specific complex heat capacity C^* can be obtained by following the complete deconvolution procedure proposed by Reading and co-authors [35]. Its in-phase component versus temperature C' appears as a step, when its out-of-phase component C'' draws a peak in the glass transition region.

3. Results and discussion

From the SEM images shown in Fig. 1, it is evidenced that the process of electrospinning produces PLA fibers with diameters and distributions that are largely independent of the composition. No visible morphological defects such as beads are evident. Neat PLA fibers (Fig. 1A) exhibit an average fiber diameter of 0.80 μm with a standard deviation of 0.18 μm , when plasticized PLA fibers (5%, 10% and 15%) display an average fiber diameter and a standard deviation of $0.78 \pm 0.18 \mu\text{m}$, $0.69 \pm 0.17 \mu\text{m}$ and $0.81 \pm 0.18 \mu\text{m}$, respectively (Fig. 1(B)–(D)). No visible morphological defects such as beads are evident, and no significant change is observed on the addition of plasticizer. This indicates that the plasticizer has no influence on the fiber diameter during the processing, and that no fiber size variations will interfere in the subsequent analyses of the fibers.

Fig. 2 shows the WAXS analysis for the neat PLA of the quenched films as well as the as-spun fibers. For the quenched film of neat PLA (Fig. 2A), the experimental spectrum displays the usual pattern of a non-crystalline PLA. The fit of the WAXS intensity profile displays three peaks with maxima located at $2\theta = 15.5^\circ$, $2\theta = 21.3^\circ$, and $2\theta = 30.9^\circ$. Stoclet et al. [21] have reported three peaks located

at $2\theta = 15.0^\circ$, $2\theta = 21.2^\circ$ and $2\theta = 31.0^\circ$ for wholly amorphous films, which is in close agreement with our results. The three peaks are characteristics of the chain spacings in amorphous PLA. The components at $2\theta = 15.0^\circ$ and $2\theta = 21.2^\circ$ arise from two characteristic inter-chain spacings. The third component at $2\theta = 31.0^\circ$ is associated to the intra-chain spacing along the chains which refers to the distance of 0.29 nm between the methyl groups in the 3-fold helices [21]. As shown in Fig. 2B, the fit of the WAXS intensity profile for the as-spun fibers of neat PLA also exhibits three peaks as defined above, but in addition there is a fourth Gaussian peak with a maximum located at 16.0° (see Table 1). The relative area of this fourth peak is only 4% but its introduction increases the fit correlation (shown in Supplementary information). Moreover, Ma et al. [32] have recently reported the need for the introduction of this fourth peak for non-crystalline electrospun fibers. This fourth peak exhibits a low FWHM equal to 3.0° . That is characteristic of a microstructural organization with an order that is intermediate between the amorphous phase and the crystals. For this reason it has been attributed to the response of the mesophase. The presence of mesophase in electrospun fibers is concordant with the assumption made by Zong et al. [31] that the electrospinning of polylactide can lead to highly oriented chains that do not have enough time to organize into crystals before solidification. It is also worth mentioning that this WAXS profile has also been reported by Stoclet et al. [21] when drawing PLA only 10 °C above its glass transition.

Fig. 3 displays the WAXS intensity profiles of the quenched films (Fig. 3A) and as-spun fibers (Fig. 3B) that are plasticized with 15% ATBC. For the quenched films, the WAXS intensity profiles of neat and plasticized PLA are superimposed in the value domain of 2θ ranging from about 20 to 40°. From this observation, we can deduce that the addition of the plasticizer does not affect the characteristic intra-chain distances. On the other hand, in the value domain of 2θ ranging from about 10 to 20°, the WAXS intensity profiles are slightly differentiated. Because of the lack of evidence in literature about the fitting procedure for the analysis of plasticized PLA, many fits have been tested, particularly the possibility to fit the domain related to the inter-chain characteristic spacings by one or two contributions. It was, however, impossible to clearly establish the best fit due to the high similarity of the correlation coefficients. As a consequence, the same fitting procedure was used for the quenched film of neat PLA. In this way, only peak I corresponding to the highest inter chain spacing is modified by the addition of plasticizer. This variation may suggest that the addition of plasticizer involves a redistribution of the inter-chain spacing in the amorphous phase.

Fig. 3B shows that, for as-spun fibers, the 2θ value domain that is characteristic of the intra-chain distances has WAXS intensity profiles that are the same for neat and plasticized PLA. This observation confirms the assumption made for the quenched films. On the other hand, the fitting procedure reveals a significant increase of the correlation coefficient when fitting with only three peaks, i.e., by removing the contribution associated to the presence of the mesophase. Moreover, the position and shape of the two contributions linked to the inter-chain spacing in the amorphous phase are modified compared to neat PLA. The results confirm that the electrospinning of neat PLA induces the creation of a highly ordered non-crystalline microstructure with the presence of mesophase. In the case of plasticized electrospun PLA fibers, the mesophase is no detected. In a general way, the addition of plasticizer changes the environment in the amorphous phase. It does not affect the intra-chain characteristic spacings but induces a strong redistribution of the inter-chain characteristic spacings.

Fig. 4 shows the average heat flow versus temperature obtained from MT-DSC analysis for all the materials. In all cases, three

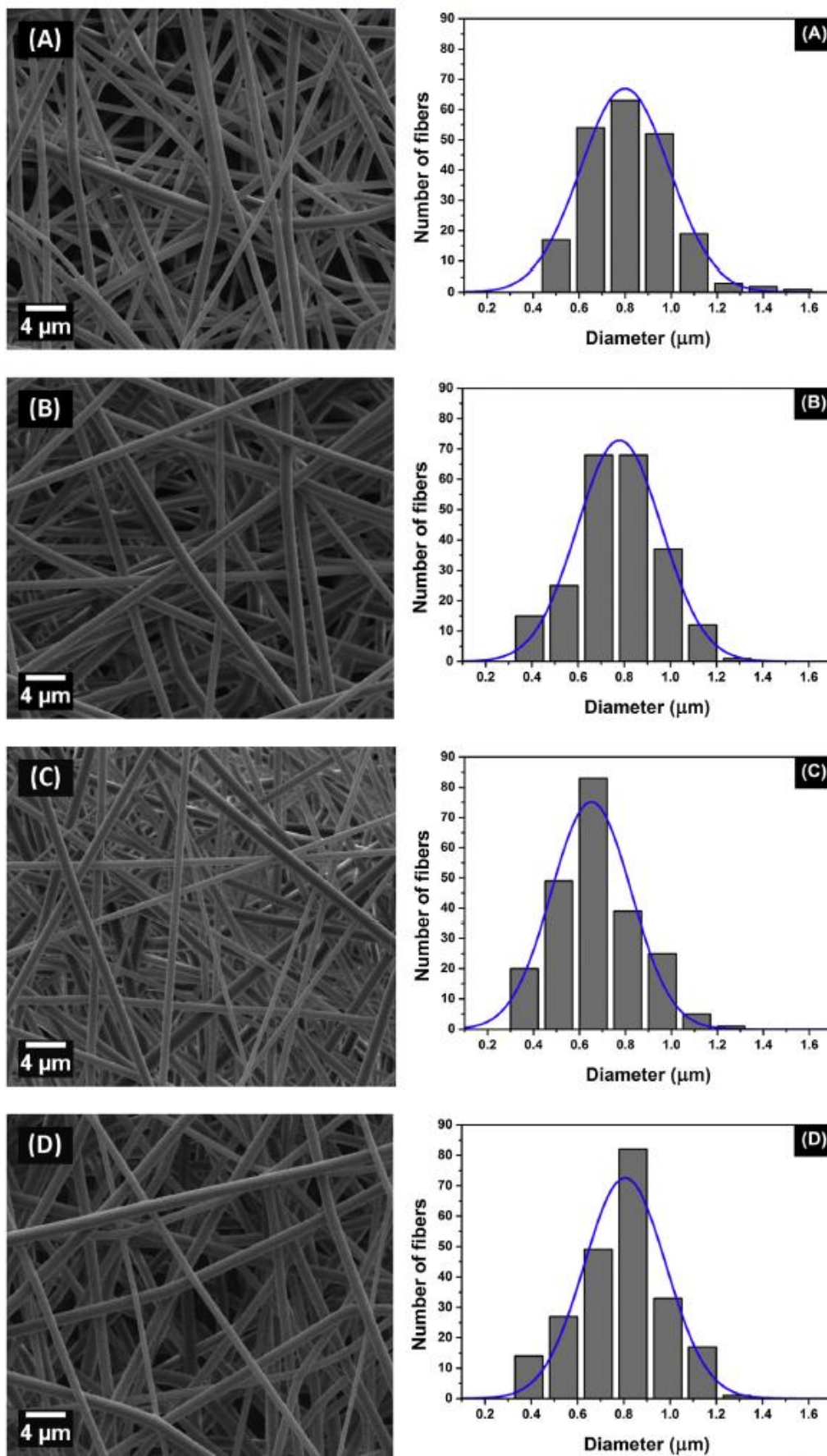


Fig. 1. SEM pictures along with the fiber diameter distribution of as-spun neat and plasticized PLA fibers. (A) Neat PLA. (B) PLA + 5% ATBC. (C) PLA + 10% ATBC. (D) PLA + 15% ATBC.

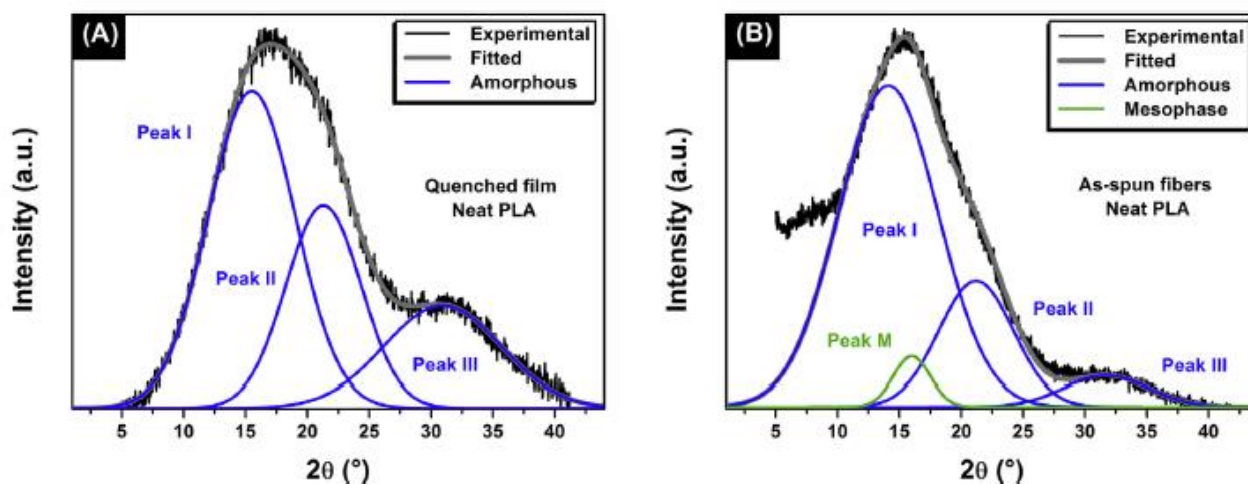


Fig. 2. WAXS intensity profiles and the associated fit of the experimental spectra for: (A) quenched film of neat PLA, (B) as-spun fibers of neat PLA.

Table 1

Position 2θ ; Full width at mid-height FWHM; and relative area A of the characteristic peaks of the amorphous phase (I; II; III) and the mesophase (M) obtained from the fitting of the WAXS experimental spectra for the as-spun fibers and the quenched films of neat PLA.

Neat PLA	Peak I			Peak II			Peak III			Peak M		
	2θ ($^\circ$)	FWHM ($^\circ$)	A (%)	2θ ($^\circ$)	FWHM ($^\circ$)	A (%)	2θ ($^\circ$)	FWHM ($^\circ$)	A (%)	2θ ($^\circ$)	FWHM ($^\circ$)	A (%)
Quenched films	15.5	7.0	51	21.3	6.1	28	30.9	9.4	21	/	/	/
As-spun fibers	14.1	8.0	70	21.2	6.0	20	31.7	6.9	6	16.0	3.0	4

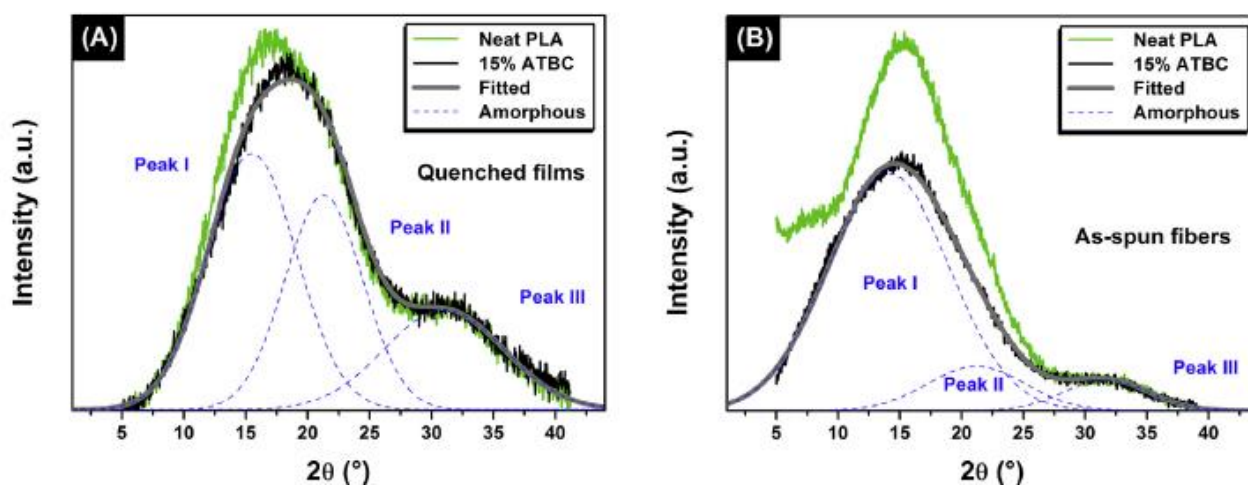


Fig. 3. WAXS intensity profiles for: (A) quenched film of neat PLA (green line) and quenched film of PLA + 15% ATBC (black line), (B) as-spun fibers of neat PLA (green line) and as-spun fibers of PLA + 15% ATBC (black line). The supposed fits of the experimental spectra for the plasticized materials are displayed in solid gray lines with the individual contributions in dashed blue lines. (For interpretation of the references to color in this figure legend, the reader is referred to the web version of this article.)

thermal events are clearly observed: an endothermic heat flow step characteristic of the glass transition, an exothermic peak due to the cold-crystallization of a part of the amorphous phase and an endothermic event related to the fusion of the crystalline phase. As explained in the introduction, one of the major concerns of the study lies in the creation of non-crystalline samples. It has been verified by the equality between the enthalpy of cold-crystallization and the enthalpy of fusion that no crystals are present prior to the MT-DSC analysis. However, one could immediately see for the as-spun fibers series that the cold-crystallization encroaches on the temperature range of the glass transition. For this reason, the quantitative analysis of both thermal events has been

made by separating the events related to the variations of the heat capacity which appear in the reversing heat flow, from the kinetic events which appear in the non-reversing heat flow. An example of this protocol is given in Fig. 5.

In practice, the glass transition temperature has systematically been determined from the reversing heat flow. At the same time, the equality between the enthalpy of cold-crystallization and the enthalpy of fusion has been double checked using the average heat flow signal on the one hand as usually performed from classical DSC, and both the reversing and the non-reversing heat flow signals from MT-DSC on the other hand. The enthalpies of cold-crystallization and fusion are shown in Table 2. These are

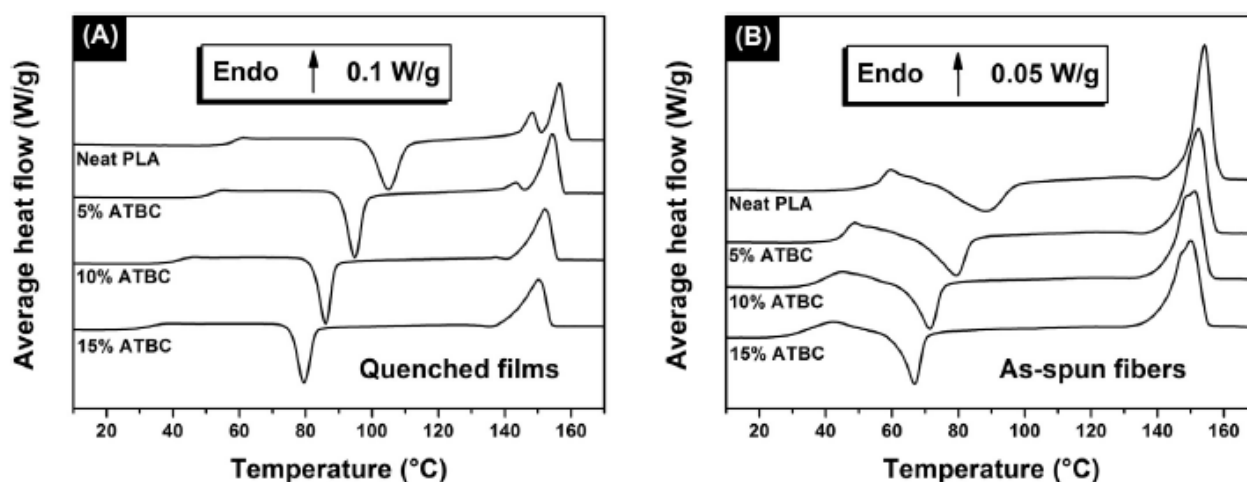


Fig. 4. Average heat flow versus temperature from MT-DSC for: (A) quenched films, (B) as-spun fibers. The curves are shifted for the sake of clarity.

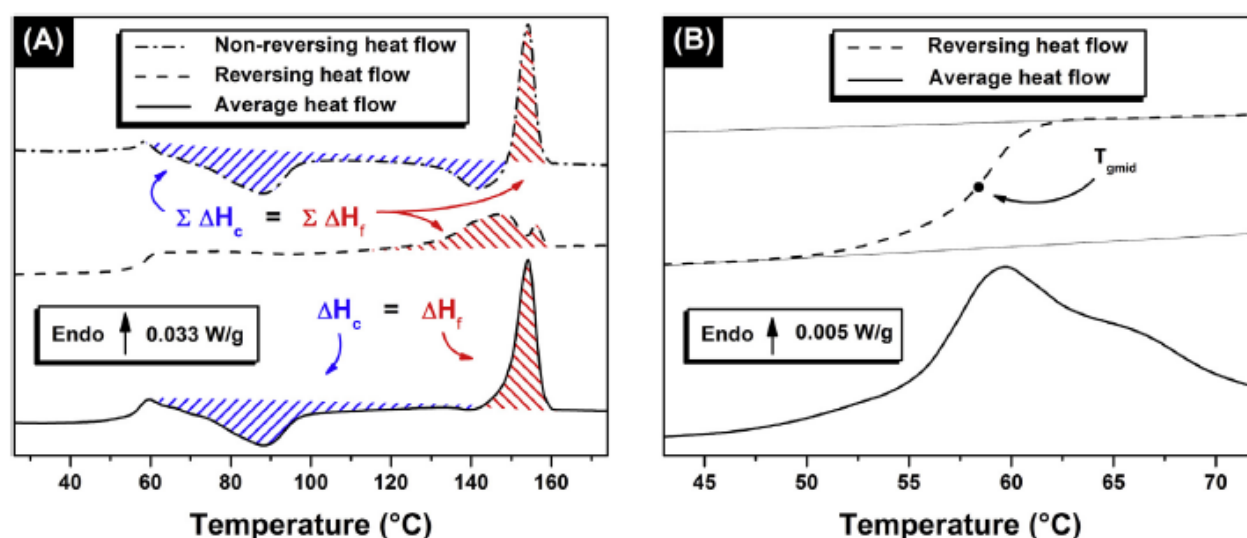


Fig. 5. Protocol for the determination of the degree of crystallinity and the glass transition temperature from MT-DSC curves obtained for the as-spun fibers of neat PLA: Average heat flow (solid line); reversing heat flow (dashed line); and non-reversing heat flow (dashed dotted line) versus temperature: (A) full DSC scan temperature range; (B) glass transition domain.

independently equal which proves that the samples are non-crystalline prior to the analysis. This result confirms the previous observations made from WAXS. From the average heat flow curves for quenched neat and plasticized films (Fig. 4A), we observe that when ATBC is introduced in the bulk PLA, both the glass transition

and the cold crystallization are shifted to lower temperatures, due to the plasticization. This shift is constant for both thermal events leading to $T_{c \max} - T_{g \text{ mid}} = 43 \text{ }^\circ\text{C}$ independent of the content of ATBC. By contrast, the peak of fusion changes from a double peak to a single peak which is preceded by an exothermal event. According

Table 2

Classical DSC parameters for the quenched films and the as-spun fibers: $T_{g \text{ mid}}$ glass transition temperature at the transition mid-point; $T_{c \max}$ temperature at the maximum of the peak of crystallization; ΔH_c enthalpy of crystallization; $T_{f \max}$ temperature at the maximum of the peak of fusion; ΔH_f enthalpy of fusion. In the case of double fusion peaks, $T_{f \max}$ corresponds to the maximum of the peak with the highest surface. The values of the temperatures are given with an accuracy of 1 °C when the values of the enthalpies are given with an accuracy of 2 J/g.

	ATBC (%)	$T_{g \text{ mid}}$ (°C)	$T_{c \max}$ (°C)	$T_{c \max} - T_{g \text{ mid}}$ (°C)	ΔH_c (J/g)	$T_{f \max}$ (°C)	ΔH_f (J/g)
Quenched films	0	61	105	44	27	156	27
	5	52	95	43	26	154	26
	10	45	86	41	23	152	24
	15	36	79	43	24	150	24
As-spun fibers	0	57	88	31	27	154	28
	5	50	79	29	26	152	27
	10	41	71	30	24	151	27
	15	36	67	31	24	150	27

to many authors [36–38], the double peak is characteristic of the concomitant formation of both highly ordered α crystals and less ordered δ crystals [39] (also called α' crystals [40]). On the other hand, the exothermal event is typically observed when only δ crystals form during the cold-crystallization [41] and is characteristic of their reorganization in α crystals just prior the fusion [41,42]. As a consequence the nature of the crystalline form which is generated during the cold-crystallization changes when the PLA is plasticized. One can also note that the temperature of fusion $T_{f \max}$ decreases slightly with an increase of the ATBC content. This is likely due to the creation of crystals with a lower degree of perfection. The electrospinning of PLA (Fig. 4B) induces a decrease of the glass transition temperature from 61 to 57 °C. A previous study by Zong et al. attributed this behavior to an increase of the surface to volume ratio in electrospun materials having air as a plasticizer. Obviously $T_{c \max} - T_{g \text{ mid}}$ also decreases from 43 °C to 30 °C. This observation is usual in electrospun fibers [31,32,43] as the orientation of the macromolecules enhances the cold-crystallization which therefore occurs at a lower temperature. In the case of electrospun fibers, Tsuji et al. [43] conclude that the crystallization has been frozen by the fast removal of the solvent from the electrospun fibers. Edwards et al. [44] and Ma et al. [32] even consider that extended polymer chains in electrospun fibers can act as row nuclei during heating just above glass transition. When electrospinning is carried on plasticized PLA, $T_{g \text{ mid}}$ decreases from 57 °C to 36 °C as the content of ATBC increasing from 0% to 15% evidencing the plasticizing effect of the ATBC. The decrease of both $T_{c \max}$ and $T_{f \max}$ previously reported for quenched films is also recorded. Eventually, $T_{c \max} - T_{g \text{ mid}}$ remains equal to 30 °C which means that in spite of the plasticizer addition, the macromolecules are oriented during the electrospinning. As we discussed before, the plasticizing effect of ATBC is evidenced in both quenched films and electrospun fibers. However one can rightfully question the solubility of ATBC in PLA when the blend is dissolved in a mix of chloroform and acetone. From the Hildebrand solubility theory [45,46], the small molecules in the electrospinning solution (chloroform, acetone and ATBC) have closely matching parameters; [18.4 (MJ m⁻³)^{0.5}] for ATBC, [19.0 (MJ m⁻³)^{0.5}] for chloroform, [20.0 (MJ m⁻³)^{0.5}] for acetone. On the other hand, the Hildebrand solubility parameter of PLA is equal to [21.9 (MJ m⁻³)^{0.5}]. Consequently there is a chance that the ATBC will be partially carried along by the solvent during the evaporation. In Fig. 6, the $T_{g \text{ mid}}$ is given as a function of the ATBC weight content for both quenched films and electrospun fibers. Clearly the trend is independent on the process, as the $T_{g \text{ mid}}$ decreases similarly with an increasing content of ATBC. The expected variations of the $T_{g \text{ mid}}$ with the content of ATBC according to Fox law have also been included in the figure. To do this, it has been foreseen that the tendency will shift whether we consider $T_{g \text{ mid}}$ of quenched films or as-spun fibers as the reference $T_{g \text{ mid}}$ for neat PLA. In both cases the variations of the glass transition temperature roughly follow Fox's law. This proves that the ATBC remains trapped in PLA during the evaporation of the solvent, likely because of its lower vapor pressure at ambient temperature, its higher molecular weight and its higher boiling point compare to chloroform and acetone.

To confirm the structural modifications revealed by WAXS, it is interesting to investigate whether plasticization and electrospinning cause changes affecting the glass transition profile. Fig. 7A shows the average heat flow and the non-reversing heat flow for the quenched film of neat PLA in the glass transition domain. The interest in using the non-reversing heat flow in this case is to highlight the possible kinetic events occurring simultaneously with the glass transition. For example, in Fig. 7A, a peak is recorded on the non-reversing heat flow signal, which is related to the existence of an endothermic event. Classically, due to the glassy character of

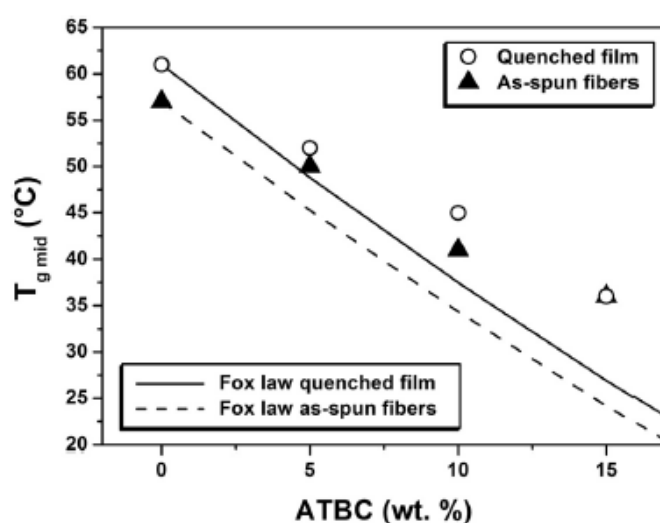


Fig. 6. $T_{g \text{ mid}}$ versus ATBC weight content for all materials. The solid curve corresponds to the Fox law by considering the T_g value of the quenched film of neat PLA. The dashed curve corresponds to the Fox law by considering the T_g value of the as-spun fibers of neat PLA.

PLA at ambient temperature, this peak might be attributed to physical aging. For the PLA plasticized with 15% ATBC, the profile presented in Fig. 7B is similar but the glass transition as well as the peak in the non-reversing heat flow signal are significantly broadened. This observation is consistent with previous observations on plasticized polylactide [11,33] and is related to an increase of the relaxation temperature distribution induced by the plasticizer addition. We cannot be definitive concerning the nature of this peak. Nevertheless, its enlargement with plasticization coincides with the increase of the dynamic heterogeneity in the amorphous phase [11]. Typically this heterogeneity reflects in the structural relaxation [11,47] so the initial hypothesis of physical aging is reinforced. In Fig. 7C, two thermal events can be distinguished. The first appears at the beginning of the glass transition, similar to the peaks observed in Fig. 7A and B. It is reasonable to consider that it is related to the same thermal event, most likely the recovery of structural relaxation. The second peak occurs just at the junction between the glass transition and the cold-crystallization. Ma et al. [32] in their DSC analyses on free-end fibers, also observed a shouldering between the glass transition and the cold-crystallization but they did not ascribe it to any given thermal event. In our study, this behavior is only observed for the as-spun fibers of neat PLA so the existence of the second peak could be related to the presence of mesophase previously revealed by WAXS. Indeed it has been reported that the "melting" of the mesophase in oriented PLA often occurs in the glass transition temperature range when its thermal stability is low [18,48]. According to Lv et al. [48], when the formation of the mesophase is not followed by a subsequent crystallization (which provides a good representation of the microstructure of as-spun fibers), the molecular ordering induced by the process is completely destroyed above T_g due to the conformational rearrangements of the macromolecules that become possible with the sudden gain of molecular mobility. When electrospinning is carried on plasticized PLA, as shown in Fig. 7D, the two separated thermal events observed for as-spun fibers of neat PLA are replaced by a broad peak covering the entire temperature range. In these conditions, it is impossible to definitively assert whether or not this peak constitutes the signature of only one thermal event. It is clear, however, that the ATBC strongly impacts the organization of the macromolecules.

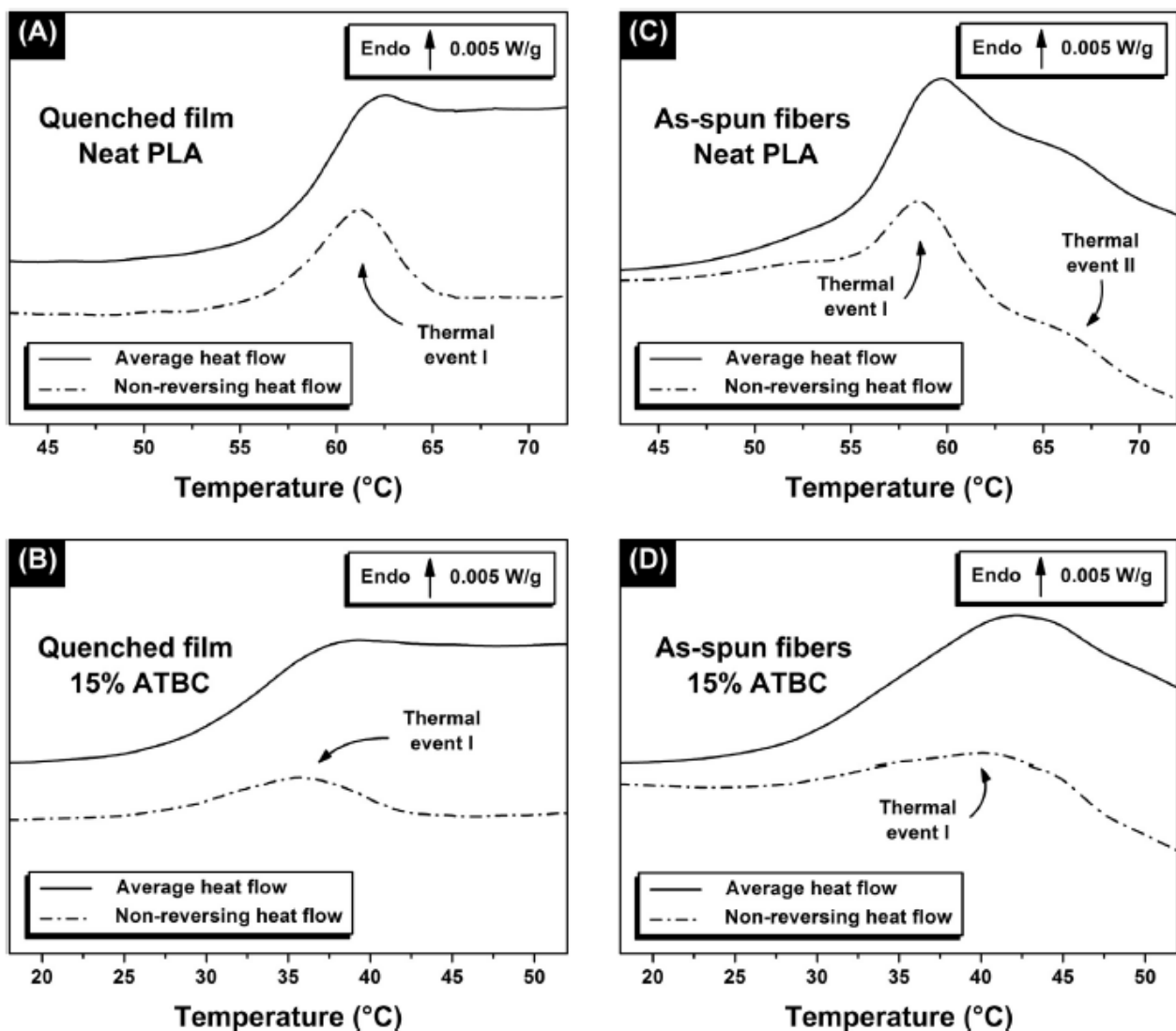


Fig. 7. Average heat flow (solid lines) and non-reversing heat flow (dashed dotted lines) versus temperature from MT-DSC for: (A) quenched films of neat PLA, (B) quenched films of PLA + 15% ATBC, (C) as-spun fibers of neat PLA, (D) as-spun fibers of PLA + 15% ATBC.

Fig. 8 shows the C' and C'' signals for neat PLA and blends with 15% ATBC for the as-spun fibers and the bulk samples. From these two components, as explained elsewhere [13], it is possible to extract the dynamic glass transition temperature T_{α} that corresponds to the maximum of the C'' peak, the heat capacity at constant pressure extrapolated to T_{α} in the glassy $C_{p, \text{glass}}$ and liquid $C_{p, \text{liquid}}$ states, as well as the mean temperature fluctuation associated with the glass transition δT that allow the calculation of the cooperativity length $\xi_{T_{\alpha}}$. The density of the amorphous phase is also needed for the calculation of the $\xi_{T_{\alpha}}$ and has been approximated as being equal to the density of the material, i.e., equal to 1.25 g/mol due to the obvious majority of the amorphous phase in all the samples. All these relaxation parameter values are presented in Table 3.

As expected, the plasticizer addition in bulk PLA from 0% to 15% weight content induces a decrease of T_{α} from 62 °C to 36 °C. It also increases δT from 3.1 °C to 5.5 °C without clear modification of the heat capacity step $\Delta C'$ which leads $\xi_{T_{\alpha}}$ to decrease from 2.8 nm down to 2.0 nm. The values of cooperativity lengths agree with those reported by Dobircan et al. [11] on PLA plasticized with ATBC, as well as those reported by Delpouve et al. regarding neat PLA bulk

[13]. When the neat PLA undergoes electrospinning, T_{α} decreases similarly to T_g from 62 °C to 59 °C. An increase of $\Delta C'$ from 0.49 to 0.57 J g⁻¹ K⁻¹ is also recorded. However, the usually high uncertainty around the values of the heat capacity step does not allow for the distinguishing of whether this variation is significant or not. On the other hand, the C'' peak is obviously narrower for the as-spun fibers than the bulk. Consequently, the as-spun fibers present an average fluctuation temperature of 2.4 °C against 3.1 °C for the bulk and the cooperativity length in the as-spun fibers reaches 3.6 nm against 2.8 nm in the bulk, which corresponds approximately to an increase of the cooperativity length of around 30%. Such an increase of cooperativity induced by the process is not usual and rarely mentioned in literature, so it will get further consideration in the following paragraphs. Finally one can observe that the plasticized materials exhibit similar values of relaxation parameters whether they are electrospun or not. In other words, the electrospinning has no effect on the alpha relaxation of plasticized polylactide.

As mentioned in the introduction, the cooperativity length is dependent on both the temperature and the structural organization into the material. In the present study, the cooperativity length has

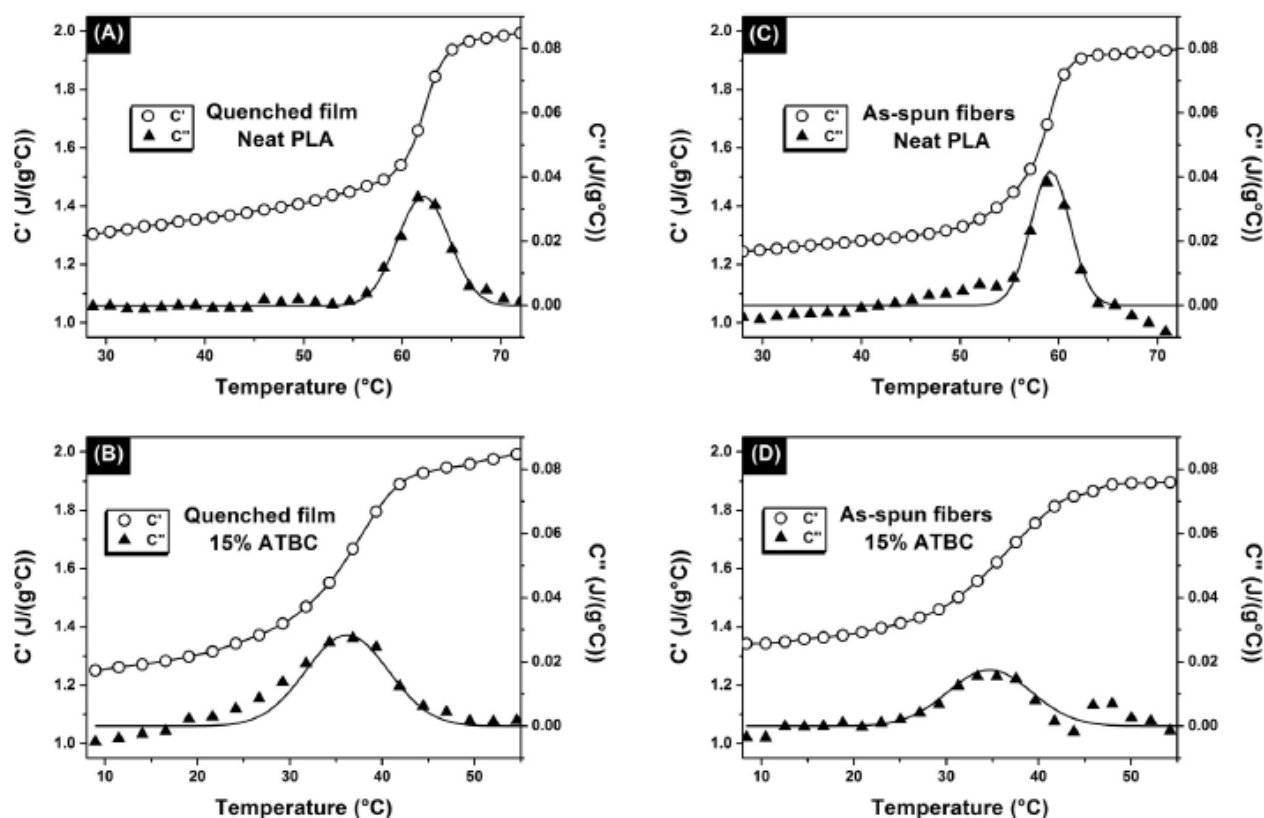


Fig. 8. MT-DSC in-phase component C' and out-of-phase component C'' of the complex heat capacity C^* : (A) quenched films of neat PLA, (B) quenched films of PLA + 15% ATBC, (C) as-spun fibers of neat PLA, (D) as-spun fibers of PLA + 15% ATBC.

been calculated for each material at the dynamic glass transition temperature in order to limit the observed variations to structural causes. Fig. 9 aims at picturing the structural dependence of the cooperativity resulting from the external and internal hindrances imposed on the material by focusing on four representative systems. In the bulk amorphous PLA (system 1), the macromolecules arrange themselves into random coil, leading to a cooperativity length close to 3 nm which is in accordance with reported values for the characteristic length of the glass transition related to dynamic heterogeneity [3,49,50]. It is often reported in the literature that the relaxation time distribution broadens when the amorphous phase becomes constrained [13,47]. Since the electrospinning induces the orientation of the macromolecules of PLA in the amorphous phase (system 2), one might have expected that the cooperativity at the glass transition will decrease. On the contrary the molecular motions at the glass transition are more cooperative. To explain this result, we should first consider that despite the

orientation of the macromolecules, the material is non-crystalline which means that the amorphous phase is not confined in any way. That makes a big difference compare to semi-crystalline drawn materials that typically exhibit lower cooperativity motions at the glass transition [5,14]. In this latter case, the decrease of cooperativity induced by the drawing should not be attributed to the induced orientation of the macromolecules but to the presence of crystallites confining the amorphous phase. It is also interesting to notice that the increase of cooperativity in an initially bulk amorphous material is often related to the same cause, i.e. the creation of nano-domains playing the role of anchoring points between the macromolecules [10,51]. In our case, we can reasonably assume that the highly cohesive mesophase plays this role by increasing the level of inter-molecular interactions, thus leading to the global increase of the cooperativity length. The opposite effect occurs when adding ATBC to the bulk PLA (system 3). Although the action of the plasticizer still deserves more investigations, it is revealed from our WAXS measurements that the increase of the dynamic heterogeneities which leads to the decrease of the average cooperativity length is associated to a redistribution of the inter-chain distances. This is consistent with the assumption that the cooperativity length is correlated with the nature and the number of inter-chain interactions [52]. In regard to this hypothesis, the decrease of the cooperativity length could be interpreted as the consequence of inter-chain bond breaking. Finally, although MT-DSC results suggest that the macromolecules are oriented in the electrospun plasticized materials (system 4), the cooperativity at the glass transition remains unchanged before and after electrospinning. We assume that the changes in molecular dynamics induced by the plasticizer addition are prevalent over the structural reorganization induced by electrospinning, and that the plasticization is not favorable to the formation of the mesophase.

Table 3

Modulated Temperature DSC parameters for the quenched films and the as-spun fibers: T_g dynamic glass transition temperature, $\Delta C'$ heat capacity step from the in-phase component; δT mean temperature fluctuation related to the glass transition, ξ_{Tg} cooperativity length at the dynamic glass transition temperature.

	ATBC (%)	$\Delta C'$ ($J g^{-1} K^{-1}$)	T_g ($^{\circ}C$)	δT ($^{\circ}C$)	ξ_{Tg} (nm)
Quenched films	0	0.49 ± 0.05	62 ± 1	3.1 ± 0.2	2.8 ± 0.3
	5	0.44 ± 0.05	55 ± 1	4.1 ± 0.2	2.5 ± 0.2
	10	0.49 ± 0.05	46 ± 1	4.7 ± 0.3	2.1 ± 0.3
	15	0.51 ± 0.05	36 ± 1	5.3 ± 0.3	2.0 ± 0.3
As-spun fibers	0	0.57 ± 0.05	59 ± 1	2.4 ± 0.1	3.6 ± 0.3
	5	0.50 ± 0.05	51 ± 1	4.0 ± 0.2	2.6 ± 0.2
	10	0.51 ± 0.05	42 ± 1	4.7 ± 0.3	2.2 ± 0.2
	15	0.45 ± 0.05	35 ± 1	5.4 ± 0.3	2.0 ± 0.2

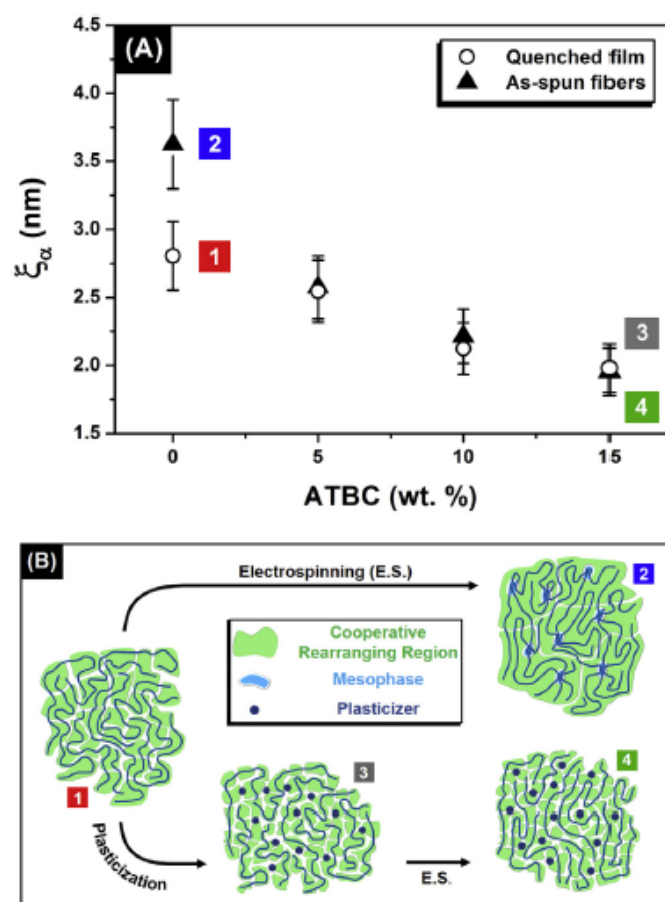


Fig. 9. Structural dependence of the cooperativity at the glass transition: (A) Cooperativity length versus ATBC content in quenched films and as-spun fibers, (B) schematic view of the macromolecule organization for representative systems.

4. Conclusion

The microstructure induced by the electrospinning of polylactide depends both on the level of orientation of the macromolecules and on the necessary time for the macromolecules to reorganize in crystals. In this study, a highly ordered but non-crystalline microstructure has been generated, exhibiting about 4% of mesophase. In comparison to bulk polylactide, the alpha relaxation of electrospun PLA is more cooperative. Since the cooperative motions at the glass transition are often related to the aptitude of the polymeric chains to connect by physical bonds, it is assumed that the mesophase plays the role of anchoring points between macromolecules due to its high cohesiveness. The plasticization of polylactide cancels any difference of cooperativity length between bulk and as-spun fibers. Both exhibit a decrease of cooperativity with the content of plasticizer. We assume that the plasticization induces strong modifications in the inter-chain characteristic spacing and frustrates the creation of physical interactions between macromolecules. This effect prevails over the changes in the macromolecule organization that are induced by electrospinning. It is also worth mentioning that the electrospinning of plasticized PLA is successful.

Acknowledgments

The authors would like to gratefully thank the University of Rouen for the financial support for Xavier Monnier: "International Mobility Help".

Appendix A. Supplementary information

Supplementary data related to this article can be found at <http://dx.doi.org/10.1016/j.polymer.2015.07.047>.

References

- [1] G. Adam, J.H. Gibbs, On the temperature dependence of cooperative relaxation properties in glass-forming liquids, *J. Chem. Phys.* 43 (2004) 139–146, <http://dx.doi.org/10.1063/1.1696442>.
- [2] E. Donth, The size of cooperatively rearranging regions at the glass transition, *J. Non-Cryst. Solids* 53 (1982) 325–330, [http://dx.doi.org/10.1016/0022-3093\(82\)90089-8](http://dx.doi.org/10.1016/0022-3093(82)90089-8).
- [3] E. Hempel, G. Hempel, A. Hense, C. Schick, E. Donth, Characteristic length of dynamic glass transition near T_g for a wide assortment of glass-forming substances, *J. Phys. Chem. B* 104 (2000) 2460–2466, <http://dx.doi.org/10.1021/jp991153f>.
- [4] Y.Z. Chua, G. Schulz, E. Shoifet, H. Huth, R. Zorn, J.W.P. Scmelzer, et al., Glass transition cooperativity from broad band heat capacity spectroscopy, *Colloid Polym. Sci.* 292 (2014) 1893–1904, <http://dx.doi.org/10.1007/s00396-014-3280-2>.
- [5] F. Hamonic, D. Prevosto, E. Dargent, A. Saiter, Contribution of chain alignment and crystallization in the evolution of cooperativity in drawn polymers, *Polymer* 55 (2014) 2882–2889, <http://dx.doi.org/10.1016/j.polymer.2014.04.030>.
- [6] R. Casalini, D. Fragiadakis, C.M. Roland, Dynamic correlation length scales under isochronal conditions, *J. Chem. Phys.* 142 (2015) 064504, <http://dx.doi.org/10.1063/1.4907371>.
- [7] T.A. Tran, S. Saïd, Y. Grohens, Nanoscale characteristic length at the glass transition in confined syndiotactic poly(methyl methacrylate), *Macromolecules* 38 (2005) 3867–3871, <http://dx.doi.org/10.1021/ma0487296>.
- [8] K. Arabeche, L. Delbreilh, R. Adhikari, G.H. Michler, A. Hiltner, E. Baer, et al., Study of the cooperativity at the glass transition temperature in PC/PMMA multilayered films: influence of thickness reduction from macro- to nanoscale, *Polymer* 53 (2012) 1355–1361, <http://dx.doi.org/10.1016/j.polymer.2012.01.045>.
- [9] G.P. Kar, P. Xavier, S. Bose, Polymer-grafted multiwall carbon nanotubes functionalized by nitrene chemistry: effect on cooperativity and phase miscibility, *Phys. Chem. Chem. Phys.* PCCP 16 (2014) 17811–17821, <http://dx.doi.org/10.1039/c4cp01594k>.
- [10] A. Saiter, D. Prevosto, E. Passaglia, H. Couderc, L. Delbreilh, J.M. Saiter, Cooperativity length scale in nanocomposites: interfacial and confinement effects, *Phys. Rev. E* 88 (2013) 042605, <http://dx.doi.org/10.1103/PhysRevE.88.042605>.
- [11] L. Dobircan, N. Delpouve, R. Herbinet, S. Domenek, L. Le Pluart, L. Delbreilh, et al., Molecular mobility and physical ageing of plasticized poly(lactide), *Polym. Eng. Sci.* 55 (2015) 858–865, <http://dx.doi.org/10.1002/pen.23952>.
- [12] J. Dobbertin, A. Hense, C. Schick, Dielectric spectroscopy and calorimetry in the glass transition region of semi-crystalline poly(ethylene terephthalate), *J. Therm. Anal.* 47 (1996) 1027–1040, <http://dx.doi.org/10.1007/BF01979446>.
- [13] N. Delpouve, A. Saiter, J.F. Mano, E. Dargent, Cooperative rearranging region size in semi-crystalline poly(L-lactic acid), *Polymer* 49 (2008) 3130–3135, <http://dx.doi.org/10.1016/j.polymer.2008.04.045>.
- [14] Y. Furushima, K. Ishikiriya, T. Higashioji, The characteristic length of cooperative rearranging region for uniaxial drawn poly(ethylene terephthalate) films, *Polymer* 54 (2013) 4078–4084, <http://dx.doi.org/10.1016/j.polymer.2013.06.030>.
- [15] H. Bai, C. Huang, H. Xiu, Q. Zhang, Q. Fu, Enhancing mechanical performance of polylactide by tailoring crystal morphology and lamellae orientation with the aid of nucleating agent, *Polymer* 55 (2014) 6924–6934, <http://dx.doi.org/10.1016/j.polymer.2014.10.059>.
- [16] W. Chen, D. Reichert, T. Miyoshi, Helical jump motions of poly(L-lactic acid) chains in the α phase as revealed by solid-state NMR, *J. Phys. Chem. B* 119 (2015) 4552–4563, <http://dx.doi.org/10.1021/acs.jpcc.5b00694>.
- [17] N. Delpouve, L. Delbreilh, G. Stoclet, A. Saiter, E. Dargent, Structural dependence of the molecular mobility in the amorphous fractions of polylactide, *Macromolecules* 47 (2014) 5186–5197, <http://dx.doi.org/10.1021/ma500839p>.
- [18] G. Stoclet, R. Seguela, J.-M. Lefebvre, C. Rochas, New insights on the strain-induced mesophase of poly(D,L-lactide): in situ WAXS and DSC study of the thermo-mechanical stability, *Macromolecules* 43 (2010) 7228–7237, <http://dx.doi.org/10.1021/ma101430c>.
- [19] K. Wasanasuk, K. Tashiro, Structural regularization in the crystallization process from the glass or melt of poly(L-lactic acid) viewed from the temperature-dependent and time-resolved measurements of FTIR and wide-angle/small-angle X-ray scatterings, *Macromolecules* 44 (2011) 9650–9660, <http://dx.doi.org/10.1021/ma2017666>.
- [20] Y. Wang, H. Zhang, M. Li, W. Cao, C. Liu, C. Shen, Orientation and structural development of semicrystalline poly(lactic acid) under uniaxial drawing assessed by infrared spectroscopy and X-ray diffraction, *Polym. Test.* 41 (2015) 163–171, <http://dx.doi.org/10.1016/j.polymertesting.2014.11.010>.
- [21] G. Stodet, R. Seguela, J.M. Lefebvre, S. Elkoun, C. Vanmansart, Strain-induced molecular ordering in polylactide upon uniaxial stretching, *Macromolecules*

- 43 (2010) 1488–1498, <http://dx.doi.org/10.1021/ma9024366>.
- [22] L. Liu, Y. Ren, Y. Li, Y. Liang, Effects of hard and soft components on the structure formation, crystallization behavior and mechanical properties of electrospun poly(L-lactic acid) nanofibers, *Polymer* 54 (2013) 5250–5256, <http://dx.doi.org/10.1016/j.polymer.2013.07.046>.
- [23] G.M. Bayley, P.E. Mallon, Porous microfibers by the electrospinning of amphiphilic graft copolymer solutions with multi-walled carbon nanotubes, *Polymer* 53 (2012) 5523–5539, <http://dx.doi.org/10.1016/j.polymer.2012.08.058>.
- [24] N. Bhardwaj, S.C. Kundu, Electrospinning: a fascinating fiber fabrication technique, *Biotechnol. Adv.* 28 (2010) 325–347, <http://dx.doi.org/10.1016/j.biotechadv.2010.01.004>.
- [25] R. Neppalli, V. Causin, E.M. Benetti, S.S. Ray, A. Esposito, S. Wanjale, et al., Polystyrene/TiO₂ composite electrospun fibers as fillers for poly(butylene succinate-co-adipate): structure, morphology and properties, *Eur. Polym. J.* 50 (2014) 78–86, <http://dx.doi.org/10.1016/j.eurpolymj.2013.11.002>.
- [26] G. Liao, S. Jiang, X. Xu, Y. Ke, Electrospun aligned PLLA/PCL/HA composite fibrous membranes and their in vitro degradation behaviors, *Mater. Lett.* 82 (2012) 159–162, <http://dx.doi.org/10.1016/j.matlet.2012.05.085>.
- [27] I. Keun Kwon, S. Kidoaki, T. Matsuda, Electrospun nano- to microfiber fabrics made of biodegradable copolyesters: structural characteristics, mechanical properties and cell adhesion potential, *Biomaterials* 26 (2005) 3929–3939, <http://dx.doi.org/10.1016/j.biomaterials.2004.10.007>.
- [28] K. Yoon, K. Kim, X. Wang, D. Fang, B.S. Hsiao, B. Chu, High flux ultrafiltration membranes based on electrospun nanofibrous PAN scaffolds and chitosan coating, *Polymer* 47 (2006) 2434–2441, <http://dx.doi.org/10.1016/j.polymer.2006.01.042>.
- [29] W. Serrano, A. Meléndez, I. Ramos, N.J. Pinto, Electrospun composite poly(L-lactic acid)/polyaniline nanofibers from low concentrations in CHCl₃: making a biocompatible polyester electro-active, *Polymer* 55 (2014) 5727–5733, <http://dx.doi.org/10.1016/j.polymer.2014.09.015>.
- [30] B. Na, P. Zhang, R. Lv, R. Tian, Y. Ju, Q. Liu, Effect of ionic liquids on the morphology and mesophase formation of electrospun polylactide nanofibers, *Polymer* 65 (2015) 55–62, <http://dx.doi.org/10.1016/j.polymer.2015.03.077>.
- [31] X. Zong, K. Kim, D. Fang, S. Ran, B.S. Hsiao, B. Chu, Structure and process relationship of electrospun bioabsorbable nanofiber membranes, *Polymer* 43 (2002) 4403–4412, [http://dx.doi.org/10.1016/S0032-3861\(02\)00275-6](http://dx.doi.org/10.1016/S0032-3861(02)00275-6).
- [32] Q. Ma, M. Pyda, B. Mao, P. Cebe, Relationship between the rigid amorphous phase and mesophase in electrospun fibers, *Polymer* 54 (2013) 2544–2554, <http://dx.doi.org/10.1016/j.polymer.2013.03.019>.
- [33] C. Courgneau, S. Domenek, A. Guinault, L. Avérous, V. Ducruet, Analysis of the structure-properties relationships of different multiphase systems based on plasticized poly(lactic acid), *J. Polym. Environ.* 19 (2011) 362–371, <http://dx.doi.org/10.1007/s10924-011-0285-5>.
- [34] F. Hassouna, J.-M. Raquez, F. Addiego, V. Toniazzo, P. Dubois, D. Ruch, New development on plasticized poly(lactide): chemical grafting of citrate on PLA by reactive extrusion, *Eur. Polym. J.* 48 (2012) 404–415, <http://dx.doi.org/10.1016/j.eurpolymj.2011.12.001>.
- [35] A.A. Lacey, D.M. Price, M. Reading, Theory and practice of modulated temperature differential scanning calorimetry, *Modul. Temp. Differ. Scanning Calorim.*, Springer (2006) 1–81.
- [36] M. Yasuniwa, S. Tsubakihara, K. Iura, Y. Ono, Y. Dan, K. Takahashi, Crystallization behavior of poly(L-lactic acid), *Polymer* 47 (2006) 7554–7563, <http://dx.doi.org/10.1016/j.polymer.2006.08.054>.
- [37] P. Pan, W. Kai, B. Zhu, T. Dong, Y. Inoue, Polymorphous crystallization and multiple melting behavior of poly(L-lactide): molecular weight dependence, *Macromolecules* 40 (2007) 6898–6905, <http://dx.doi.org/10.1021/ma071258d>.
- [38] M.L. Di Lorenzo, Calorimetric analysis of the multiple melting behavior of poly(L-lactic acid), *J. Appl. Polym. Sci.* 100 (2006) 3145–3151, <http://dx.doi.org/10.1002/app.23136>.
- [39] K. Wasanasuk, K. Tashiro, Crystal structure and disorder in poly(L-lactic acid) δ form (α' form) and the phase transition mechanism to the ordered α form, *Polymer* 52 (2011) 6097–6109, <http://dx.doi.org/10.1016/j.polymer.2011.10.046>.
- [40] C.-Y. Chen, C.-F. Yang, U.-S. Jeng, A.-C. Su, Intrinsic metastability of the α' phase and its partial transformation into α crystals during isothermal cold-crystallization of poly(L-lactide), *Macromolecules* 47 (2014) 5144–5151, <http://dx.doi.org/10.1021/ma501167e>.
- [41] J. Zhang, K. Tashiro, H. Tsuji, A.J. Domb, Disorder-to-order phase transition and multiple melting behavior of poly(L-lactide) investigated by simultaneous measurements of WAXD and DSC, *Macromolecules* 41 (2008) 1352–1357.
- [42] T. Kawai, N. Rahman, G. Matsuba, K. Nishida, T. Kanaya, M. Nakano, et al., Crystallization and melting behavior of poly(L-lactic acid), *Macromolecules* 40 (2007) 9463–9469, <http://dx.doi.org/10.1021/ma070082c>.
- [43] H. Tsuji, M. Nakano, M. Hashimoto, K. Takashima, S. Katsura, A. Mizuno, Electrospinning of poly(lactic acid) stereocomplex nanofibers, *Biomacromolecules* 7 (2006) 3316–3320, <http://dx.doi.org/10.1021/bm060786e>.
- [44] M.D. Edwards, G.R. Mitchell, S.D. Mohan, R.H. Olley, Development of orientation during electrospinning of fibres of poly(ϵ -caprolactone), *Eur. Polym. J.* 46 (2010) 1175–1183, <http://dx.doi.org/10.1016/j.eurpolymj.2010.03.017>.
- [45] A. Ruellan, V. Ducruet, S. Domenek, CHAPTER 5 Plasticization Poly(lactide), 2014 (Chapter 5).
- [46] R.S. Ruoff, D.S. Tse, R. Malhotra, D.C. Lorents, Solubility of fullerene (C₆₀) in a variety of solvents, *J. Phys. Chem.* 97 (1993) 3379–3383, <http://dx.doi.org/10.1021/j100115a049>.
- [47] N.M. Alves, J.F. Mano, E. Balaguer, J.M. Meseguer Dueñas, J.L. Gómez Ribelles, Glass transition and structural relaxation in semi-crystalline poly(ethylene terephthalate): a DSC study, *Polymer* 43 (2002) 4111–4122, [http://dx.doi.org/10.1016/S0032-3861\(02\)00236-7](http://dx.doi.org/10.1016/S0032-3861(02)00236-7).
- [48] R. Lv, B. Na, N. Tian, S. Zou, Z. Li, S. Jiang, Mesophase formation and its thermal transition in the stretched glassy polylactide revealed by infrared spectroscopy, *Polymer* 52 (2011) 4979–4984, <http://dx.doi.org/10.1016/j.polymer.2011.08.023>.
- [49] D. Fragiadakis, P. Pissis, L. Bokobza, Glass transition and molecular dynamics in poly(dimethylsiloxane)/silica nanocomposites, *Polymer* 46 (2005) 6001–6008, <http://dx.doi.org/10.1016/j.polymer.2005.05.080>.
- [50] J. Koppensteiner, W. Schranz, M.A. Carpenter, Revealing the pure confinement effect in glass-forming liquids by dynamic mechanical analysis, *Phys. Rev. B* 81 (2010) 024202, <http://dx.doi.org/10.1103/PhysRevB.81.024202>.
- [51] C.E. Corcione, A. Maffezzoli, Glass transition in thermosetting day-nanocomposite polyurethanes, *Thermochim. Acta* 485 (2009) 43–48, <http://dx.doi.org/10.1016/j.tca.2008.12.009>.
- [52] M. Nakanishi, R. Nozaki, Model of the cooperative rearranging region for polyhydric alcohols, *Phys. Rev. E* 84 (2011), <http://dx.doi.org/10.1103/PhysRevE.84.011503>.



Contents lists available at ScienceDirect

Thermochimica Acta

journal homepage: www.elsevier.com/locate/tca

Physical aging in PLA through standard DSC and fast scanning calorimetry investigations



Xavier Monnier, Allisson Saiter*, Eric Dargent

Normandy University, UNIROUEN, LECAP, 76000 Rouen, France

ARTICLE INFO

Article history:

Received 13 October 2016

Received in revised form

28 November 2016

Accepted 10 December 2016

Available online 14 December 2016

Keywords:

Fast scanning calorimetry

Differential scanning calorimetry

Polylactide

Accelerating physical aging

Thermodynamic equilibrium

ABSTRACT

Physical aging on wholly amorphous polylactide (PLA) has been performed by means of standard differential scanning calorimetry (DSC) and fast scanning calorimetry (FSC) just below its glass transition. Compared to the in-situ aging study through the standard DSC, an increase of 80–90% has been observed in the enthalpy recovery by FSC investigations. Such increase has been related to the high cooling rates used by FSC. Besides, an influence of the sample geometry has been measured when glasses are vitrified by high cooling rates. This implies that the critical thickness involved in the physical aging acceleration is cooling rate dependent. High cooling rates allow to reach the thermodynamic equilibrium, as observed from physical aging investigations by FSC. In addition, few mg of material analyzed by FSC are representative of the bulk one analyzed by standard DSC, when the glass is formed in the same conditions.

© 2016 Elsevier B.V. All rights reserved.

1. Introduction

When a glass-forming liquid is cooled down, its viscosity increases and reaches a value close to 10^{12} Pa s at a temperature which defines the well-known glass transition temperature [1]. The formation of the glassy state is the resulting effect of the impossibility of the liquid to equilibrate in the available time imposed by the cooling rate [1]. As a consequence, going through the glass transition, the thermodynamic properties (volume, enthalpy, entropy...) of the glass formed go out of equilibrium [1,2]. Even if the glass formed looks “frozen” on the laboratory time scale, below the glass transition a molecular mobility exists [1,3]. Thus, if glass forming liquids are held below their respective glass transition temperature, the structural relaxation occurs. Also called physical aging, the structural relaxation is the slow evolution of the thermodynamic properties towards equilibrium [3].

The concept of fictive temperature T_f introduced by Tool in 1931 allows characterizing the non-equilibrium state and the glass to liquid-like transition, as shown in Fig. 1. Tool defines T_f as the temperature at which any properties, related to the structural relaxation, are at the equilibrium state [4]. Moreover, the kinetics of structural recovery have been well formulated by stretched exponential decays through the Tool-Narayanaswamy-Moynihan [5]

or Kovacs-Aklonis-Hutchinson-Ramos [6] models, and even more recently through the Lunkenheimer-Wehn-Schneider-Loidl model [7].

In the recent years, understanding of the glassy state nature, and its physical aging, still supports the focus of many researchers on a variety of glass forming liquids such as metallic glasses [8], small organic glasses [9], chalcogenide glasses [10], colloidal glasses [11,12] or polymer glasses [13,14]. Regarding polymer science, polymer glasses are used in a wide range of applications such as food packaging [15], electronics [16] or membrane separation process [17] for examples. Investigations of physical aging is a major issue in order to understand the structural relaxation process on the physical property evolution [18]. It has been proposed, from various investigations [19–21], that the driving forces of the physical aging, leading to the decrease of the thermodynamic properties towards equilibrium, are related to a free volume hole diffusion [3].

In the same time, the recent development of fast scanning calorimeters [22–24] has received a significant interest regarding the study of polymer crystallization [25], polymer melting [22] or amorphous polymer properties [26]. Such technique allows to heat up and cool down polymers as fast as thousand Kelvin per second. As a consequence, the sample masses are drastically reduced from few mg by standard DSC to tens ng by FSC, in order to minimize the thermal lag. The thermal lag is due to the smearing effects induced by the technique and the scanning rates employed [27]. In the purpose of glass transition properties and physical aging investigations, the recent works of Simon and coworkers [28–31]

* Corresponding author.

E-mail address: allisson.saiter@univ-rouen.fr (A. Saiter).

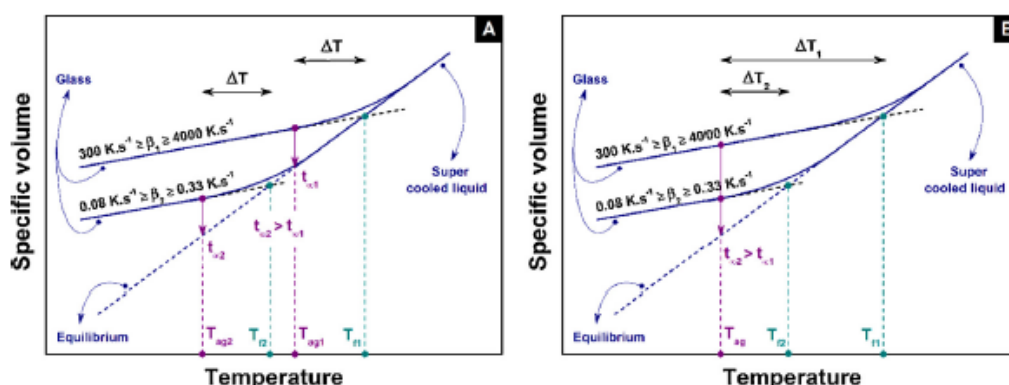


Fig. 1. Schematic illustration of the temperature dependence of the specific volume in the liquid like state and the glassy state, as well as its evolution during structural recovery at aging temperature T_{ag} . The comparison is made between high (FSC) and slow (FSC or DSC) cooling rates for the glasses investigated in the cases where (A) the difference ΔT between the fictive temperature T_f and the aging temperature T_{ag} are the same, and (B) the aging temperature T_{ag} is the same.

on polystyrene have shown new possibilities by the FSC compared to standard DSC. By standard DSC, the understanding of the structural relaxation remains disputed. When some authors claim that thermodynamic equilibrium can be reached [29,32], others claim the contrary [33–36]. Besides, some works have observed plateau and different time scale in the change of properties towards equilibrium [37,38]. In that purpose, we have investigated physical aging of polylactide through FSC by comparing it with aging through standard DSC. The investigations have been done through the measurement of the enthalpy recovery. As a consequence, the determination of the glass transition temperature for both techniques is significant for comparison. Besides, drawing a parallel from both techniques, with different scanning rates leads to bring new insights and new understanding in the mechanism involved in the physical aging.

2. Methodology

2.1. Materials

Semi-crystalline PLA pellets (grade 4042D) were provided by Natureworks. The content of L-lactide and D-lactide were about 96% and 4% respectively. The number-average and weight-average molecular weights were $M_n = 116$ kDa and $M_w = 188$ kDa respectively, as measured by Gel Permeation Chromatography.

2.2. Differential scanning calorimetry measurements

DSC analyses were performed under a 50 mL min^{-1} nitrogen gas flow using a DSC Q100 from Thermal Analysis instruments (with scanning rates ranging from 0.08 K s^{-1} to 0.33 K s^{-1}). The calibration in energy was done using a standard of indium, while the calibration in temperature was done using a standard of indium as well as a standard of benzophenone. PLA masses were ranging from 2 mg up to 8 mg. The aluminum reference and sample couples, pan and lid, were identical to within ± 0.01 mg.

Physical aging were carried in-situ with the following procedure: PLA was heated up to 180°C and held 2 min to erase any previous thermal history. Then, PLA was cooled down to the aging temperature T_{ag} at a given cooling rate β_c , aged isothermally for aging times t_{ag} , and finally cooled down to 0°C at β_c . The enthalpy recovery was observed during a heating scan with a rate $|\beta_c| = \beta_h$. Five different aging temperatures T_{ag} , with $5^\circ\text{C} \leq T_f - T_{ag} \leq 23^\circ\text{C}$, were used.

2.3. Fast scanning calorimetry measurements

FSC analyses were performed using a power compensation twin-type chip based fast scanning calorimeter Flash 1 DSC from Mettler Toledo. Samples were placed on the sensitive area of a MultiSTAR UFS 1 MEMS chip sensors. To do so, PLA were previously thermo-molded in films of tens microns thick, at a pressure of 1 bar and a temperature of 180°C between two hot plates, then quickly quenched in cold water and finally cut in small pieces. A Huber TC100 intra cooler was used to cool samples down to -90°C and operate high cooling rates. PLA was continuously flushed with a 20 mL min^{-1} nitrogen flow gas to avoid water condensation from the environment and to optimize the program temperature applied [22]. The thermal contact between the sample and the chip was improved by using a thin layer of silicone oil. PLA mass was estimated from the step change in heat flow at the glass transition, by comparing the value of the heat capacity step ΔC_p from the one obtained through FSC at $|\beta_c| = \beta_h = 1500 \text{ K s}^{-1}$ and the one obtained through standard DSC at $|\beta_c| = \beta_h = 0.17 \text{ K s}^{-1}$ equal to 0.51 J/(g K) for a wholly amorphous PLA according to the literature [40,41].

The thermal lag has been estimated from the method proposed by Schawe [27]. The symmetric correction, namely the dynamic correction, has been made for each sample, when the static correction through the melting of an indium has been done by an independent measurement on a different chip.

The sample shape was observed with a universal EPI-illuminator optical microscope and a digital sight camera system from Nikon Corporation in reflection mode. Perimeter and surface area evolution were measured with ImageJ software.

The properties of the amorphous PLA glass transition, and the mechanisms involved during the aging process were investigated through different scanning rates, different masses as well as different aging temperatures and aging times. For the lowest cooling rate, we have checked that no crystallization has occurred.

3. Results and discussions

As we have compared two thermal analysis techniques, standard DSC and FSC, we have first focused on the glass transition properties, and more exactly how to figure out properly a glass transition temperature by FSC, in order to be able to compare aging between both techniques. Fig. 2 displays the normalized heat flows as a function of temperature of a 40 ng fully amorphous PLA sample, measured upon heating and cooling, by FSC experiments. The heat capacity step at the glass transition is clearly observed independently of the scanning rate. By FSC experiments [22], as well as by standard or modulated temperature DSC experiments, the

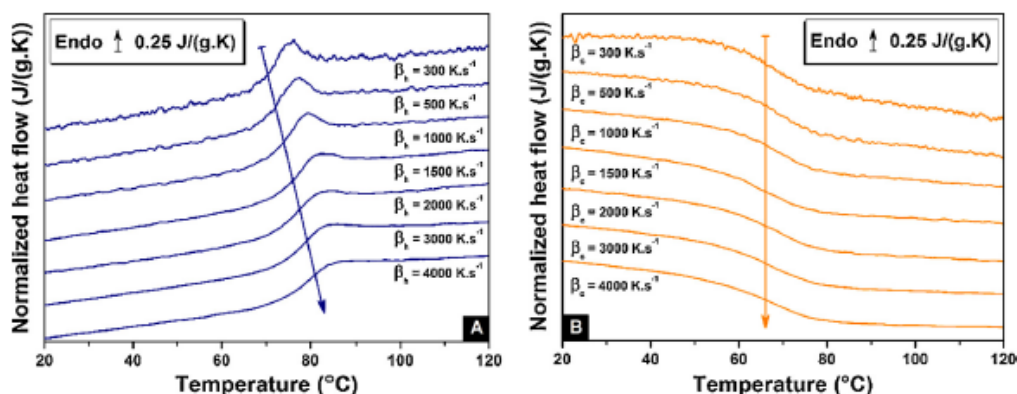


Fig. 2. FSC normalized heat flow of 40 ng fully amorphous PLA glass transition, upon heating (A) and cooling (B), for scanning rates $|\beta_c| = \beta_h$ ranging from 300 K.s^{-1} to 4000 K.s^{-1} .

sensitivity (i.e. signal-to-noise ratio) of the heat flow is drastically dependent of the sample mass and the scanning rate [42]. Consequently, below 300 K.s^{-1} the sensitivity being too low, none heat flow has been properly measured. On the contrary, the sensitivity becomes higher when the scanning rate increases, providing smoother heat flow signals as clearly shown in Fig. 2.

As depicted in Fig. 2(A), endothermic peaks related to the enthalpy relaxation, and shifts of the glass transition temperature related to the thermal lag, are observed upon heating. On the contrary, neither enthalpy relaxation nor thermal lag are observed upon cooling as shown in Fig. 2(B).

For FSC experiments, the thermal lags related to the sample mass/dimension ratio and the scanning rate have been widely discussed [43,44], and corrected from the melting of an indium piece placed on the top of the sample [45,46]. Recently, Schawe has proposed two thermal lag corrections (dynamic and static) in order to accurately measure the glass transition temperature by FSC experiments [27].

The different thermal lag values are summarized in Table 1. At $|\beta_c| = \beta_h = 300 \text{ K.s}^{-1}$, no dynamic thermal lag has been observed, while it reaches practically 5°C at $|\beta_c| = \beta_h = 4000 \text{ K.s}^{-1}$. Due to the sample thickness, a static thermal lag exists even at the lower scanning rate, and reaches practically 6°C at $|\beta_c| = \beta_h = 4000 \text{ K.s}^{-1}$. The values measured are consistent with the low mass and the scanning rates employed [28,45,47]. As observed, the measured fictive temperature increases when the scanning rate increases. From the lowest to the highest scanning rate used, the fictive temperature increases of 10°C , from 65.9°C up to 76.3°C . Usually, by standard DSC experiments performed at 0.17 K.s^{-1} , the fictive temperature of PLA is equal to 57°C (not shown here) [48,49]. Due to the smearing effects, gaps of 9°C for $|\beta_c| = \beta_h = 300 \text{ K.s}^{-1}$, up to 19°C for $|\beta_c| = \beta_h = 4000 \text{ K.s}^{-1}$, are measured between standard DSC and FSC experiments. Thanks to the dynamic and static thermal lag estimations, the raw fictive temperatures measured upon heating are corrected, depending on the scanning rate (see Table 1). The fictive temperatures corrected do not depend in the scanning rate, and

are close to an average value of 66°C . Table 1 also depicts the fictive temperatures measured upon cooling, and as already noticed in Fig. 2(B), do not depend on the cooling rate. Thus, an average value of $T_{f1} = 66^\circ\text{C}$ is obtained upon cooling, matching with the average value of the corrected fictive temperatures measured upon heating. Consequently, from the corrected fictive temperatures, it seems that the same PLA glass is formed from the different cooling rates used. However, we may note the lack of dependence of the fictive temperature on the applied cooling rate is atypical. Indeed, as observed for PS or PET_g, the fictive temperature depends on the applied cooling rate [28,47]. Such result seems to be specific to PLA. To schematize, Fig. 1 shows that with low cooling rates included between 0.08 K.s^{-1} and 0.33 K.s^{-1} , a $T_{f2} = 57^\circ\text{C}$ is obtained. Such a range of low cooling rates does not provide an observable variation of the fictive temperatures (not shown here). For high cooling rates (FSC) included between 300 K.s^{-1} and 4000 K.s^{-1} , a constant value of $T_{f1} = 66^\circ\text{C}$ is determined. These results also correlate with the work of Cangialosi et al. [50,51] by means of dielectric experiments: by cooling down polycarbonate films at 60 and 100 K.s^{-1} , they observed similar relaxation patterns.

To validate the assumption of a single PLA glass formed independently of the scanning rate used, physical aging were performed at $T_{\text{ag}} = T_g - 18^\circ\text{C}$ (with $T_g = T_f = 66^\circ\text{C}$ taking into account the thermal lag correction) for different aging times t_{ag} by FSC.

For each scanning rate investigated $\beta_{h/c}$, Fig. 3(A) displays the normalized heat flow subtraction (aged – rejuvenated) for PLA with $t_{\text{ag}} = 100 \text{ min}$, and Fig. 3(B) presents the enthalpy recovery as a function of $\beta_{h/c}$ obtained for different t_{ag} . Due to the smearing effects, the peaks are shifted at higher temperatures when the scanning rates increase (Fig. 3(A)). This is also observed for the other aging times investigated (not shown here). As shown in Fig. 3(B), the enthalpy recoveries measured do not depend on the scanning rate, and average values of 4.7 , 5.2 and 6.1 J/g were measured for the three different aging times, respectively. As depicted above and highlighted in the case of polycarbonate cooled down at few tens degree per seconds [50,51], the enthalpy recoveries measured from

Table 1

Dynamic, static and thermal lag values, as well as the fictive temperatures measured and corrected from heating, and measured from cooling for the different scanning rates investigated.

$ \beta_c = \beta_h (\text{K.s}^{-1})$	$\Delta T_D (\text{K})$	$\Delta T_S (\text{K})$	$\Delta T = \Delta T_D + \Delta T_S (\text{K})$	T_f from heating ($^\circ\text{C}$)	T_f corrected from heating ($^\circ\text{C}$)	T_f from cooling ($^\circ\text{C}$)
300	0.0	0.7	0.7	65.9	65.2	65.9
500	0.7	1.1	1.8	67.8	66.0	66.5
1000	1.7	1.9	3.6	69.7	66.1	66.3
1500	2.7	2.7	5.4	71.3	65.9	66.5
2000	3.3	3.6	6.9	73.1	66.2	66.7
3000	4.4	4.7	9.1	75.3	66.2	66.0
4000	4.8	5.9	10.7	76.6	65.6	66.5

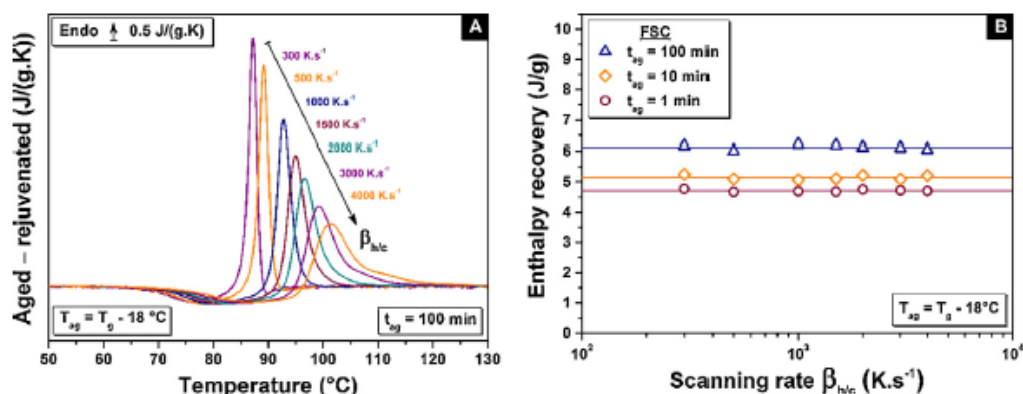


Fig. 3. Aging of PLA glasses at $T_{ag} = T_g - 18^\circ\text{C}$ studied by FSC. (A) Normalized heat flow subtraction (aged – rejuvenated) for $t_{ag} = 100$ min. (B) Enthalpy recovery as a function of β_{hlc} for $t_{ag} = 100$ min (blue triangle), $t_{ag} = 10$ min (orange square) and $t_{ag} = 1$ min (wine circle). (For interpretation of the references to colour in this figure legend, the reader is referred to the web version of this article.)

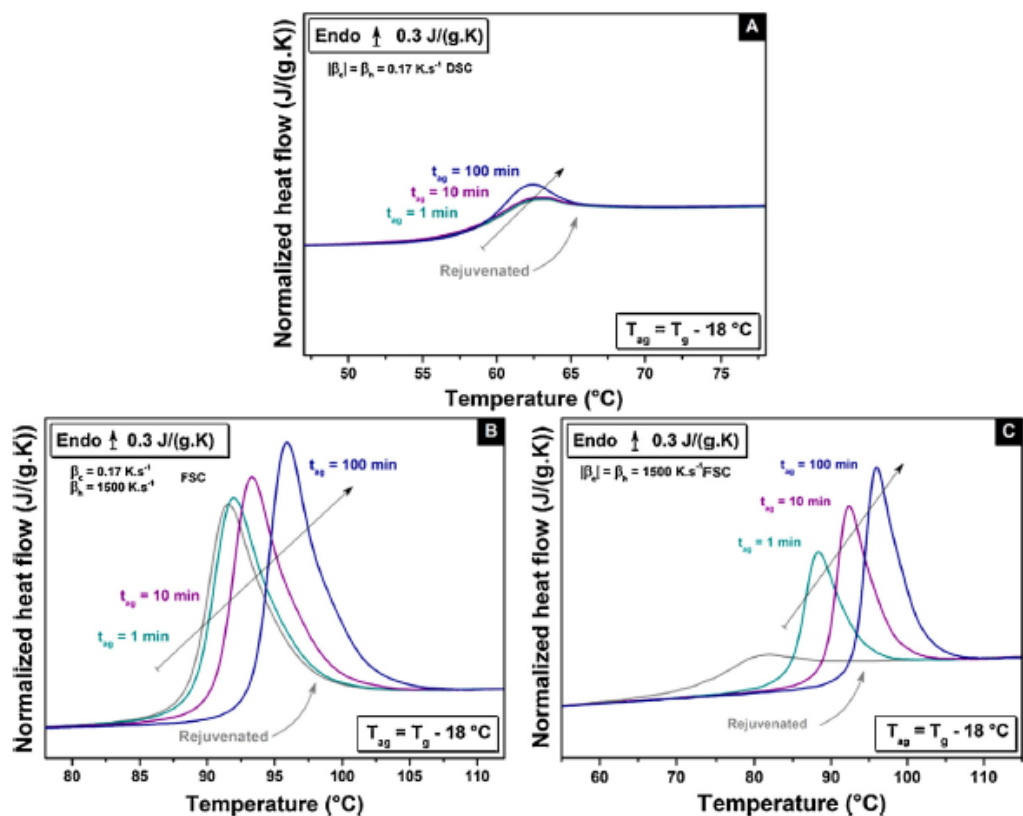


Fig. 4. FSC and standard DSC normalized heat flows of amorphous PLA aged at $T_{ag} = T_g - 18^\circ\text{C}$ for three aging times $t_{ag} = [1; 10; 100]$ min. (A) Standard DSC experiments were performed at a scanning rate of $|\beta_c| = \beta_h = 0.17 \text{ K.s}^{-1}$. (B) FSC experiments were performed at a scanning rate of $\beta_c = 0.17 \text{ K.s}^{-1}$ and $\beta_h = 1500 \text{ K.s}^{-1}$. $|\beta_c| \neq \beta_h$ explains the overshoot for the rejuvenated curve. (C) FSC experiments were performed at a scanning rate of $|\beta_c| = \beta_h = 1500 \text{ K.s}^{-1}$.

the physical aging in PLA glasses are the same independently of the scanning rate used to form the glass. Only the molecular dynamics involved are different, mainly due to the smearing effects of the technique itself [27]. To sum up, not only the same fictive temperature, but also the same enthalpy recovery, are measured from the glasses formed with the different scanning rates investigated. From two different approaches, it is clear that only one glass is formed.

One can notice that the three aging times (i.e. 1, 10 and 100 min), investigated by FSC 18°C below the glass transition T_g , depict higher values of the enthalpy recovery (4.7, 5.2 and 6.1 J/g respectively) compared to those measured by standard DSC [49,52]: in the same conditions (not shown here), enthalpy recoveries depict 0.1, 0.4 and 1.0 J/g respectively. Thus, an enthalpy recovery increase of

80–90% is observed between FSC and standard DSC. How to explain this gap? Why the physical aging seems to be accelerated by FSC?

In literature, accelerated physical aging are reported either for polymers subjected to quenching or medium cooling rates up to 100 K.s^{-1} [50,51,53–55] as well as for polymers with specific geometries, such as polymer thin films [19–21,51,56,57,58] or polymer nanocomposites [59–61]. In all cases, the mechanism of structural relaxation involved during the physical aging is correlated to a free volume hole diffusion towards surfaces. Those surfaces may be the external ones of the bulk, the internal ones tied to the creation of low density regions induced by a high cooling rate, or the interfaces between polymer and fillers. Consequently, in a first approach, it is obvious to correlate the gap in enthalpy recov-

Table 2

Enthalpy recovery values recorded from the amorphous PLA aged at $T_{ag} = T_g - 18^\circ\text{C}$ for three aging times $t_{ag} = [1; 10; 100\text{ min}]$ by standard DSC at a cooling rate of $\beta_c = 0.17\text{ K s}^{-1}$ as well as by FSC at cooling rates of $\beta_c = 0.17\text{ K s}^{-1}$ and $\beta_c = 1500\text{ K s}^{-1}$. Values are recorded from the aging curves in Fig. 4.

$t_{ag}(\text{min})$	Standard DSC($\beta_c = 0.17\text{ K s}^{-1}$)	FSC($\beta_c = 0.17\text{ K s}^{-1}$)	FSC($\beta_c = 1500\text{ K s}^{-1}$)
1	0.1 ± 0.1	0.2 ± 0.2	4.4 ± 0.3
10	0.3 ± 0.2	0.5 ± 0.3	5.0 ± 0.5
100	0.8 ± 0.2	0.7 ± 0.3	6.2 ± 0.5

ery recorded in this work between FSC and standard DSC from the difference of the scanning rates used: up to six decades [27]. Such differences in cooling rate might induce low density regions, and so more free volume or enthalpy, in rapidly quenched samples as illustrated in Fig. 1.

The FSC and standard DSC normalized heat flows of aged PLA during 1, 10 and 100 min 18°C below their respective T_g are shown in Fig. 4. First, Fig. 4(A) depicts aged curves from standard DSC. PLA sample was cooled down and heated up at $|\beta_c| = \beta_h = 0.17\text{ K s}^{-1}$. To erase influence of high cooling rates, FSC experiments with $\beta_c = 0.17\text{ K s}^{-1}$ and $\beta_h = 1500\text{ K s}^{-1}$ have been performed. The resulting curves are shown in Fig. 4(B). Finally, Fig. 4(C) depicts aged curves from FSC when PLA sample was cooled down and heated up at $|\beta_c| = \beta_h = 1500\text{ K s}^{-1}$. A classical behavior is observed when $|\beta_c| = \beta_h$: endothermic peaks related to the structural relaxation process superimpose to the glass transition. When $|\beta_c| \neq \beta_h$, endothermic peaks related to the structural relaxation process also superimpose to the glass transition, but in addition an overshoot due to the difference between β_c and β_h is observed.

From standard DSC and FSC, the different enthalpy recoveries are determined and reported in Table 2. By FSC or standard DSC, the same enthalpy recovery is measured when the samples are cooled down at 0.17 K s^{-1} , but for $\beta_c = 1500\text{ K s}^{-1}$ a significant increase is observed. The idea that high cooling rates accelerate the aging process by FSC is evidenced. In a second approach, the gap of enthalpy recovery observed initially between FSC and standard DSC might also be explained by the sample geometry, i.e. the ratio between the surface area and the volume noted SA:V. As the relaxation process involved during the physical aging is believed to be driven by a free volume hole diffusion towards surfaces, if the sample geometry is only considered, namely the external surfaces, accelerated aging process might be expected by FSC, as observed for polymer thin films [19–21,51,53,55–57,58] or polymer nanocomposites [59–61], due to the few ng of sample analyzed, in other words due to an increase of SA:V value. Fig. 5 presents the enthalpy recoveries measured by FSC and standard DSC as a function of SA:V values related to different samples with different masses. As highlighted above in Table 2, the same enthalpy recovery is measured from FSC and standard DSC when $\beta_c = 0.17\text{ K s}^{-1}$, independently of the SA:V values. In the same way, an increase of the enthalpy recovery is recorded for $\beta_c = 1500\text{ K s}^{-1}$. For examples, the enthalpy recovery measured is around 1 J/g for a glass formed at $\beta_c = 0.17\text{ K s}^{-1}$ and aged 100 min, when it goes up to around 6 J/g for a glass formed at $\beta_c = 1500\text{ K s}^{-1}$ and aged 100 min. However, as pointed out by Cangialosi et al., the thickness influencing the physical aging of polystyrene films is only measured from few microns down to nanometers ($2\text{ }\mu\text{m}$ – 29 nm), in other words below a critical thickness L_c [62]. As the sample thickness analyzed by our FSC experiments are ranging from $19\text{ }\mu\text{m}$ down to $2\text{ }\mu\text{m}$, the same enthalpy recovery measured from standard DSC and FSC correlate with the idea that none influence of the SA:V (namely the thickness) is observed on the structural relaxation when the same cooling rate is used between both techniques. It attests that acceleration of the aging process observed by FSC is related to the high level of enthalpy, or free volume, induced by the high cooling rate available [3,53].

Even if the acceleration of the physical aging is now confirm by FSC thanks to the high cooling rate used, we want to pay attention

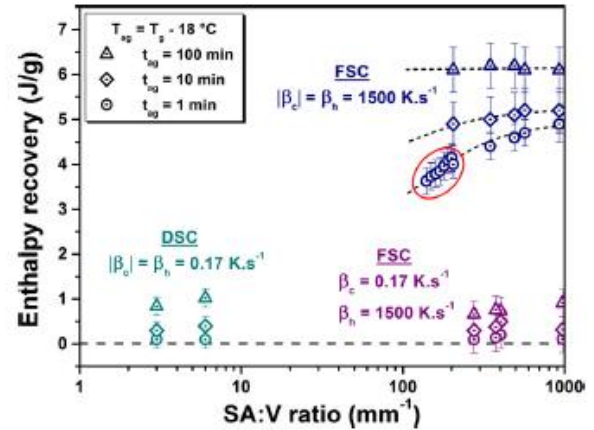


Fig. 5. Enthalpy recovery measured by FSC and standard DSC as a function of the SA:V ratio. By DSC, the glasses investigated were formed at $\beta_c = 0.17\text{ K s}^{-1}$. By FSC, the glasses were formed at $\beta_c = 1500\text{ K s}^{-1}$, as well as $\beta_c = 0.17\text{ K s}^{-1}$ to investigate the cooling rate influence.

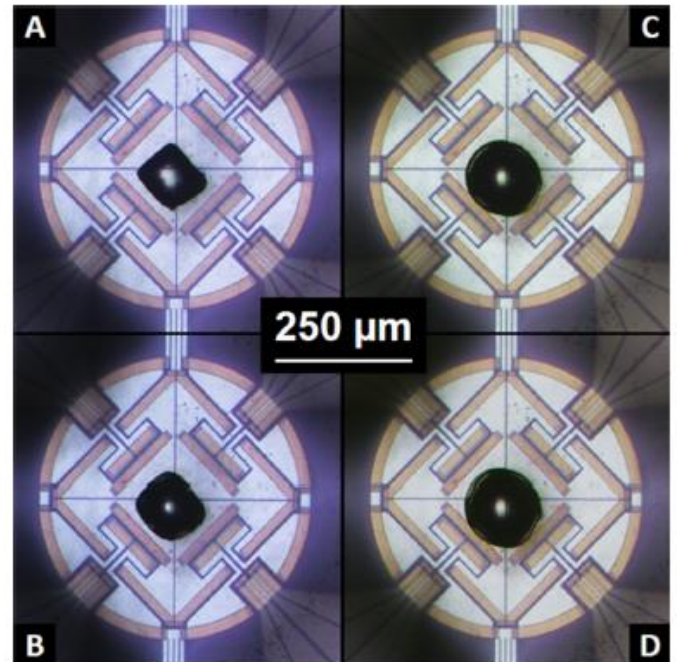


Fig. 6. Wetting evolution of 260 ng PLA sample. (A) After first heating at $\beta_h = 1500\text{ K s}^{-1}$ from -50°C to 230°C . (B) After 1 cycle. (C) After 7 cycles. (D) Chip stored overnight at room temperature and after 3 cycles (10 cycles in total).

on the enthalpy recovery measured after an aging duration of 1 min with the 260 ng sample (series of points in the red ellipse in Fig. 5).

Premelting by FSC experiments are usually done to improve the thermal contact between the sensor and the sample [27]. However, the sample changes from an uneven to an even shape, after pre-heating and melting, to reach a fine and stable geometry [63,64]. Such behaviors are depicted in Fig. 6. The sample shape evolves from a parallelepiped to a fine and stable disc after 10 cycles (1

Table 3
Evolution of the characteristic sizes of the sample shape for the different temperature cycles applied.

Number of cycles	Surface on the sensor ($\times 10^2 \mu\text{m}^2$)	Perimeter (μm)	Thickness (μm)	Surface area to volume ratio (SA:V) (μm^{-1})
1	105	395	19	0.14
2	123	406	17	0.15
3	133	416	15	0.16
4	143	431	14	0.17
5	157	450	13	0.18
6	168	463	12	0.19
7	175	471	12	0.20
8	176	473	12	0.20
9	176	475	12	0.20
10	176	478	12	0.20

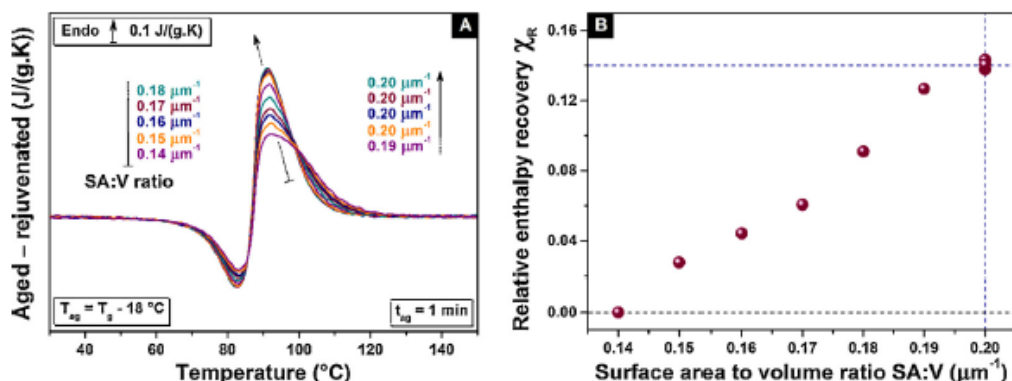


Fig. 7. FSC investigations of enthalpy recovery evolution as a function of SA:V for a 260 ng PLA sample aged at $T_{ag} = T_g - 18^\circ\text{C}$ with $t_{ag} = 1$ min. (A) Normalized heat flow subtraction (aged – rejuvenated) after different cycles at $\beta_{c1} = \beta_h = 1500 \text{ K s}^{-1}$ involving an evolution of SA:V (B) Evolution of the relative enthalpy recovery χ_R as a function of SA:V.

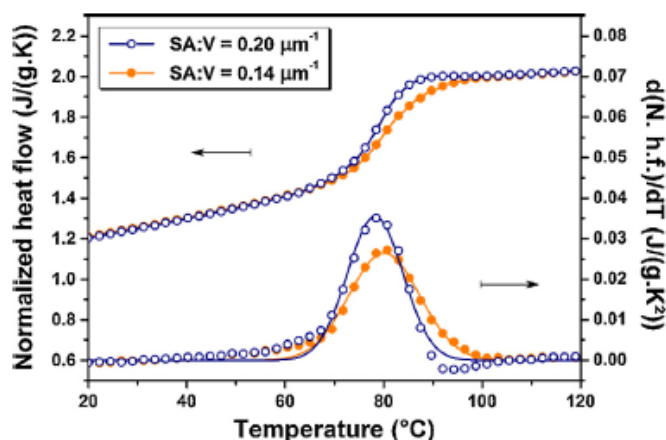


Fig. 8. Molecular dynamic investigations by FSC, as a function of SA:V value for a 260ng fully amorphous PLA. Normalized heat flows and their derivatives of unaged sample at a scanning rate $\beta_{c1} = \beta_h = 1500 \text{ K s}^{-1}$ with SA:V = $0.14 \mu\text{m}^{-1}$ (orange disc) and SA:V = $0.20 \mu\text{m}^{-1}$ (blue circles). (For interpretation of the references to colour in this figure legend, the reader is referred to the web version of this article.)

cycle corresponds to two heat/cool ramps from -50°C to 230°C , as well as one physical aging step of 1 min 18°C below T_g). By assuming a constant density, knowing the mass from calculation, and measuring the perimeter, we were able to figure out the thickness evolution induced from the different cycles, as well as the SA:V values. Table 3 summarizes the different characteristic sizes after each cycle applied.

Fig. 7(A) shows FSC investigations of enthalpy recovery evolution as a function of SA:V for the 260 ng PLA sample aged at $T_{ag} = T_g - 18^\circ\text{C}$ with $t_{ag} = 1$ min. An increase of the amplitude of the endothermic peaks related to the physical aging is observed when the SA:V increases, even if the aging time remains constant. In order to quan-

tify the SA:V influence on the aging process, we define a relative enthalpy recovery χ_R by the Eq. (1):

$$\chi_R = (\Delta H_{SA:V} - \Delta H_{0.14}) / \Delta H_{0.14} \quad (1)$$

where $\Delta H_{SA:V}$ and $\Delta H_{0.14}$ are the enthalpy recovery for a given SA:V value and the enthalpy recovery measured for SA:V equal to $0.14 \mu\text{m}^{-1}$ (cycle 1), respectively. Fig. 7(B) depicts the χ_R values as a function of SA:V. An improvement close to 14% of χ_R is observed when SA:V increases from $0.14 \mu\text{m}^{-1}$ to $0.20 \mu\text{m}^{-1}$. This χ_R increase does correlate with the hypothesis that the diffusion of free volume holes to the surface is the driving forces of the physical aging [19,61]. As the final thickness dropped from $19 \mu\text{m}$ to $12 \mu\text{m}$ after 10 cycles, it is clear that the critical thickness L_c influencing the acceleration of the physical aging is cooling rate dependent. Indeed, thanks to the high cooling rate used by FSC, the thickness influencing the physical aging is superior to the critical one L_c observed by standard DSC in the case of polystyrene films [62]. This is an important result and we show here that the acceleration of physical aging could be observed for thicker sample presenting a high level of enthalpy. Moreover, one can notice that the endothermic peaks become less broadened when SA:V value increases (Fig. 7). Indeed, as shown in Fig. 8, a decrease of the width at the middle height observed on the derivative normalized heat flow curves for SA:V = $0.20 \mu\text{m}^{-1}$, in comparison to a SA:V = $0.14 \mu\text{m}^{-1}$, could be related to a decrease of the heterogeneity in terms of molecular mobility at the glass transition [41]. However, as shown in literature by means of AC-chip calorimeter for thin polystyrene films [65], the dynamic glass transition is thickness independent down to 10 nm. As presented above, the recovery of equilibrium is driven by a free hole diffusion from the external interfaces toward the core. Consequently, samples with high SA:V values ($0.20 \mu\text{m}^{-1}$) will present more homogeneous recovery of equilibrium when heated up because the equilibration of the core will not be significantly delayed in comparison to the external interfaces. On the contrary, samples with small SA:V values ($0.14 \mu\text{m}^{-1}$) will present

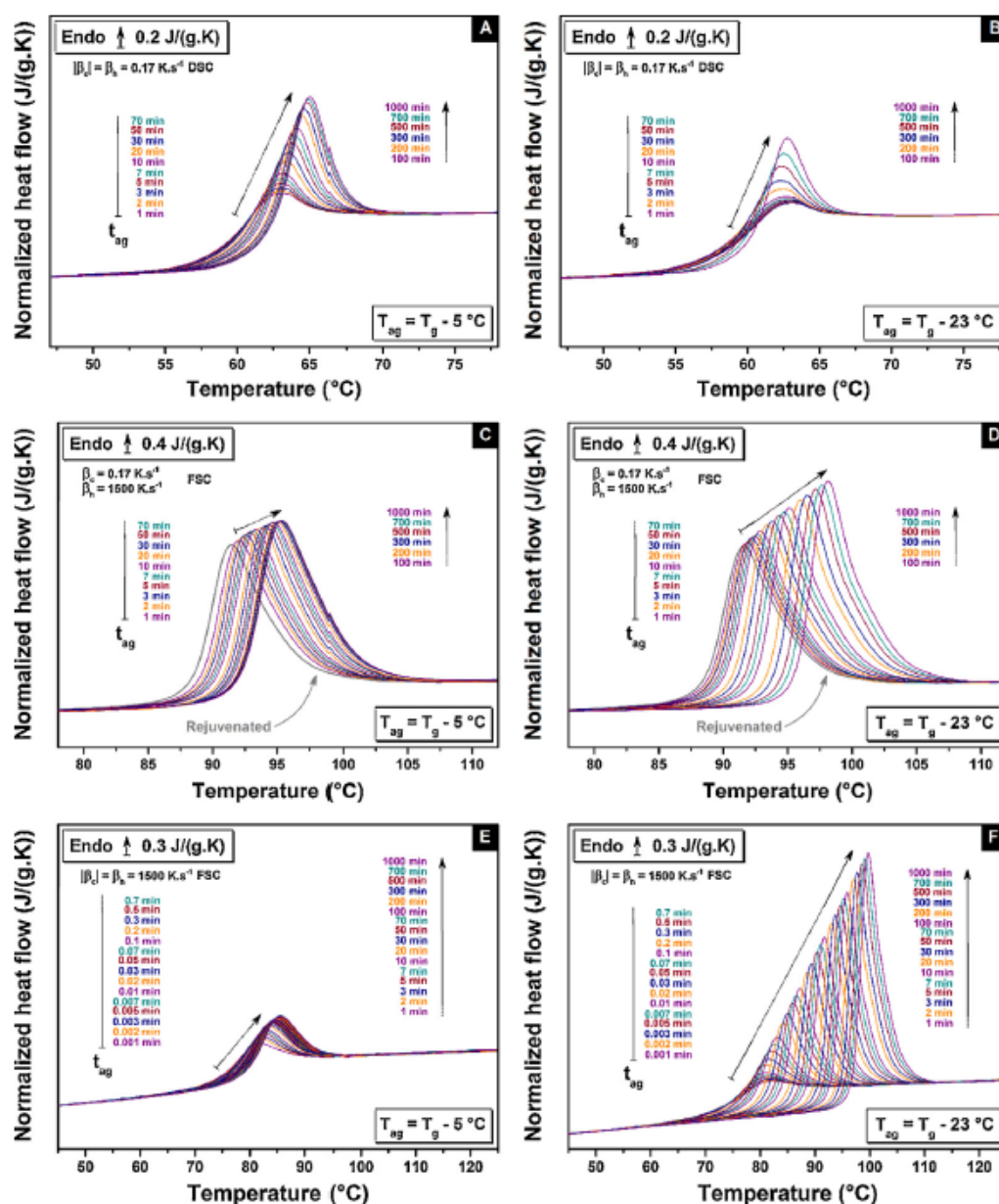


Fig. 9. Aged amorphous PLA investigations by standard DSC and FSC experiments (left) $T_{ag} = T_g - 5^\circ\text{C}$ (right) $T_{ag} = T_g - 23^\circ\text{C}$. (A and B) Standard DSC experiments were performed at a scanning rate of $|\beta_c| = \beta_h = 0.17\text{ K s}^{-1}$ for aging times ranging from 1 min to 1000 min. (C and D) FSC experiments were performed at a scanning rate of $\beta_c = 0.17\text{ K s}^{-1}$ and $\beta_h = 1500\text{ K s}^{-1}$ for aging times ranging from 1 min to 1000 min. $|\beta_c| \neq \beta_h$ explains the overshoot for the rejuvenated curve (grey curve). (E and F) FSC experiments were performed at a scanning rate of $|\beta_c| = \beta_h = 1500\text{ K s}^{-1}$ for aging times ranging from 0.001 min to 1000 min.

a delay, and thus will exhibit a more heterogeneous recovery of equilibrium as observed in Fig. 8. These observations evidence that the acceleration of physical aging observed is not related to the modification of the molecular mobility.

In addition, that series of points recorded from the 260 ng sample match with the trend of enthalpy recovery measured from the other samples presenting higher SA:V values (see \odot symbols in Fig. 5). An increase of 15% is observed when the SA:V value increases from 200 mm^{-1} up to 1000 mm^{-1} . Such behavior is still depicted by aging time of 10 min, with an increase of 10% in the enthalpy recovery. However, for longer aging times, namely $t_{ag} = 100\text{ min}$, the enthalpy recoveries reached do not seem to be affected by the SA:V values. A constant value of enthalpy recovery close to 6 J/g is measured, independently of the SA:V values.

Up to this point, the accelerated physical aging has been observed only in the case of glasses presenting a high level of

enthalpy induced by the quenching. As highlighted above, a difference of 80–90% in the enthalpy recovery is recorded between standard DSC and FSC, respectively between a cooling at 0.17 K s^{-1} and 1500 K s^{-1} . Consequently, are the accelerated kinetics, related to high cooling rates by FSC experiment, provide access to the whole structural relaxation?

Fig. 9 displays FSC and standard DSC normalized heat flows of aged PLA up to 1000 min, 5°C and 23°C below the respective T_g . Three other temperatures have been investigated (see Supplementary material). The same endothermic relaxation peak evolutions, than those described in Fig. 3 are observed from FSC and standard DSC. In these three cases, endothermic relaxation peaks increase and shift towards high temperatures when the aging times increase, as classically observed for PLA [48,49,52,66] and other systems [67]. Besides, no variation of the glass transition, as well as of

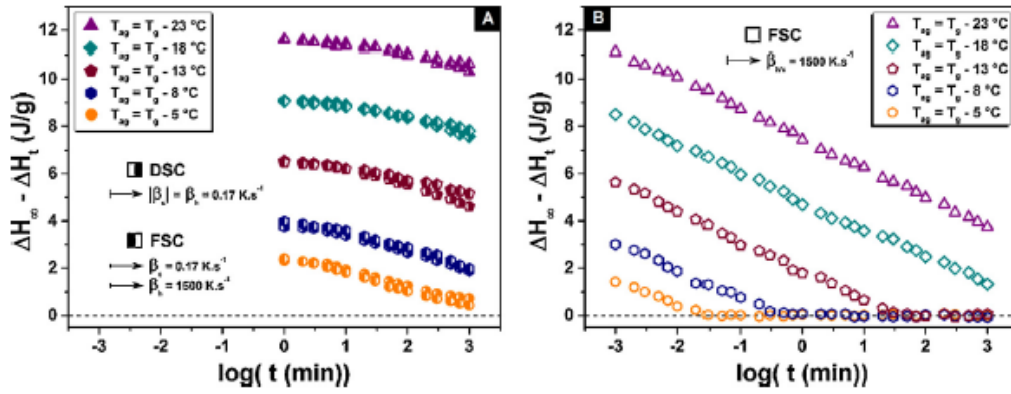


Fig. 10. Time evolution of the difference between the total enthalpy loss ΔH_{∞} and the enthalpy recovery ΔH_t for the aged amorphous PLA at the five aging temperatures: $T_{ag} = T_g - 5^\circ\text{C}$ (orange circle), $T_{ag} = T_g - 8^\circ\text{C}$ (blue hexagone), $T_{ag} = T_g - 13^\circ\text{C}$ (wine pentagone), $T_{ag} = T_g - 18^\circ\text{C}$ (cyansquare) and $T_{ag} = T_g - 23^\circ\text{C}$ (purple triangle). (A) Half-filled symbols: FSC and standard DSC experiments $\beta_c = 0.17\text{ K s}^{-1}$. (B) Empty symbols: FSC experiments $\beta_c = 1500\text{ K s}^{-1}$. (For interpretation of the references to colour in this figure legend, the reader is referred to the web version of this article.)

the heat capacity step, are detected from rejuvenated scans, either by FSC or standard DSC.

In the case of $|\beta_c| = \beta_1$, endothermic peaks are more intense and broadened by FSC than those observed by standard DSC for a same aging duration. Besides, two opposite behaviors are observed when the aging temperature decreases. By standard DSC, the highest enthalpy recovery reached during the physical aging goes through a given temperature. Thus, 23°C below the glass transition, namely below that given temperature, the enthalpy recovery measured in standard DSC drops due to a lack of mobility. On the contrary, by FSC the smaller the aging temperature, the higher the enthalpy recovery. By FSC, when $\beta_c = 0.17\text{ K s}^{-1}$, the endothermic peaks are more intense and broadened due to the addition of the overshoot. However, the same phenomenon than the one observed in standard DSC is observed, namely a drop of the enthalpy recovery below a given temperature (see Supplementary material). Thus, the cooling rate does play a role on the structural relaxation process.

Usually, enthalpy recovery of a glass, aged at a temperature T_{ag} during a time t_{ag} , is calculated by integrating the difference between the scans of aged and rejuvenated sample, according to the following equation:

$$\Delta H(T_{ag}, t_{ag}) = \int_{T_1}^{T_2} [C_p^a(T) - C_p^r(T)] \cdot dT \quad (2)$$

in which $C_p^a(T)$ and $C_p^r(T)$ are the normalized heat flows of the aged and rejuvenated sample, respectively, and T_1 and T_2 are temperatures below and above the glass transition temperature T_g , respectively [68]. Enthalpy recovery represents the energy needed by the glass to reach the thermodynamic equilibrium. For an infinite time, it is believed that equilibrium is reached. The expected total enthalpy loss ΔH_{∞} extrapolated from the equilibrium melt depends on the aging temperature T_{ag} , as well as the glass transition temperature T_g and the heat capacity step ΔC_p of the sample, as depicted from the following relation:

$$\Delta H_{\infty} = \Delta C_p \cdot (T_g - T_{ag}) \quad (3)$$

For FSC and standard DSC, Fig. 10 depicts the drops of the enthalpy during physical aging for the five aging temperatures investigated. The difference between the total enthalpy loss ΔH_{∞} and the enthalpy recovery ΔH_t at a given aging time displays different behaviors. Despite the different techniques used, similarities are also observed when the cooling rate is the same, as shown in Fig. 10(A). Indeed, by standard DSC and FSC, for $\beta_c = 0.17\text{ K s}^{-1}$, the decays of the enthalpy during the physical aging are exactly the

same in kinetics. It is worth mentioning that the few ng analyzed by FSC are totally representative of the bulk sample analyzed by DSC. Furthermore, we observe slower kinetics compared to glasses formed at $\beta_c = 1500\text{ K s}^{-1}$. Thus, for given aging time and temperature, the enthalpy recovery reached is much lower. As an example, the total enthalpy loss is reached after 1 min 5°C below T_g for a cooling rate of $\beta_c = 1500\text{ K s}^{-1}$, when almost none structural relaxation is observed after 1 min 5°C below T_g in the case of $\beta_c = 0.17\text{ K s}^{-1}$. Besides, the enthalpy recovery measurement is only possible for aging times down to 1 min, whereas with a glass cooled down at $\beta_c = 1500\text{ K s}^{-1}$ the measurement of enthalpy recovery for shorter aging times down to 0.001 min is possible, due to the formation of a high fictive temperature glass having very short relaxation time [29]. The enthalpy recovery is driven by a single step decay. However, the decays follow a well-known stretched tendency. Such physical aging processes are classically observed for glassy polymers [59,69,70].

Then, in Fig. 10(B), the structural relaxation of PLA through FSC for $\beta_c = 1500\text{ K s}^{-1}$ exhibits two main characteristics. At the closest temperatures to T_g , the enthalpy recovery shows a standard single step decay towards equilibrium. In the range of aging time investigated, the glass is allowed to completely relax its excess of energy. The enthalpy recovery measured does match with the total enthalpy loss extrapolated from the melt. This result contrasts with the ideas of J.L. Gomez Ribelles et al. [33,34] who consider that the thermodynamic equilibrium cannot be reached due to the steric hindrances and the cooperativity of the molecular mobility induced during the structural relaxation. It also contrasts with J.M. Hutchinson et al. [36] who consider that only a certain fraction of the glass-forming liquid is vitrified through the glass transition. Thus, the thermodynamic equilibrium cannot be reached due to two kinds of processes involved (slow for the vitrified fraction and fast for the non-vitrified one). FSC shows that high enthalpy glasses allow to reach the thermodynamic equilibrium. At farthest temperatures below T_g , the enthalpy recovery is also driven by a single step decay. The aging time investigated do not allow to reach the equilibrium. Besides, no induction time, as well as no plateau, are observed for the aging time investigated.

As mentioned above, the kinetics of the structural recovery are different from high to low enthalpy glasses. The comparison between both systems can be done by considering the same gap ΔT between the aging temperature T_{ag} and the fictive temperature T_f or the same aging temperature T_{ag} , as depicted in Fig. 1. In the first case, as the step heat capacity is also the same, the path to reach the equilibrium is the same in both systems independently of the cooling rate used, as observed in Fig. 1(A). In such config-

uration, it is clear that high cooling rate leads to more enthalpy, and more free volume in the glass, than low cooling rate. Thus, the diffusion related to the structural recovery is higher. As a consequence, the time needed to reach the equilibrium is shorter for high enthalpy glasses than low enthalpy glasses. In the second case, the step heat capacity is still the same, but the gap ΔT is higher for high enthalpy glasses due to the higher fictive temperature, as presented in Fig. 1(B). Thus, higher the fictive temperature, higher the total enthalpy loss. Obviously, the low enthalpy glasses present a shorter path to reach the equilibrium than the high enthalpy glasses. However, the time needed to reach the equilibrium is shorter for the high enthalpy glasses. In literature [27,47], cooling rate β_c and relaxation rate τ are related by the Frenkel-Kobeko-Reiner relationship $\beta_c \times \tau = C$, where C is a constant. Thus, high cooling rates lead to short relaxation time. This might be explained by the fact that high enthalpy glasses do not present an induction time, as observed in Fig. 10. The high fictive temperatures allow very short aging time for structural recovery. On the contrary, a relative long induction time is needed for low enthalpy glasses. As a consequence, if only the aging temperature is considered, the acceleration of the structural relaxation might be related to the non-induction involved by the high fictive temperature.

4. Conclusion

Thermal lag correction is a significant parameter for further physical aging. In that purpose, the observation of a constant fictive temperature, after corrections, for cooling rates ranging from 300Ks^{-1} to 4000Ks^{-1} led us to investigate the physical aging in PLA by means of FSC and standard DSC. Aging investigations, just below the glass transition, depicts a significant influence of the cooling rate used to vitrify the glass: a gap of 80–90% has been observed between FSC and standard DSC, when glasses are vitrified at $\beta_c = 0.17\text{Ks}^{-1}$ and $\beta_c = 1500\text{Ks}^{-1}$, respectively. Such behaviors have been explained by an acceleration of the structural recovery for high cooling rates. Besides, for short aging time, an influence of the sample SA:V value has been measured. The critical thickness involving an acceleration of the structural recovery seems to be cooling rate dependent. Aging investigations for glasses formed at the same cooling rate independently of the techniques show that the few mg of sample analyzed by FSC are well representative of the bulk sample analyzed by DSC. Furthermore, thanks to the high cooling rates accessible by means of FSC, thermodynamic equilibrium has been reached after few minutes to few hours, which is impossible by standard DSC in the laboratory time scale. Such experimental observations open new possibilities for physical aging on complex systems.

Acknowledgments

The authors are grateful to the Normandy Region, France, for the financial support for PhD thesis and FSC equipment. The authors gratefully acknowledge discussions with Dr. D Cangialosi, Pr. R Richert and Pr. C Schick.

Appendix A. Supplementary data

Supplementary data associated with this article can be found, in the online version, at <http://dx.doi.org/10.1016/j.tca.2016.12.006>.

References

[1] P.G. Debenedetti, T.M. Truskett, C.P., Lewis, F.H. Stillinger, The ory of supercooled liquids and glasses: Energy landscape and statistical geometry perspectives, in: B.-A. in C. Engineering (Ed.), Academic Press, 2001: pp. 21–79. <http://www.sciencedirect.com/science/article/pii/S006523770128003X> (accessed May 27, 2016).

[2] A.J. Kovacs, Transition vitre use dans les polymères amorphes. Etude phénoménologique, in: Fortschritt Hochpolym.-Forsch., Springer Berlin Heidelberg, 1964: pp. 394–507. DOI: 10.1007/BFb0050366 (accessed May 27, 2016).

[3] L.C.E. Struik, Physical aging in plastics and other glassy materials, *Polym. Eng. Sci.* 17 (1977) 165–173, <http://dx.doi.org/10.1002/pen.760170305>.

[4] I.M. Hodge, Adams-Gibbs Formulation of Enthalpy Relaxation Near the Glass Transition, in: 1996: p. 195. <http://adsabs.harvard.edu/abs/1996APS.MAR.13003H> (accessed April 26, 2016).

[5] C.T. Moynihan, P.B. Macedo, C.J. Montrose, C.J. Montrose, P.K. Gupta, M.A. DeBolt, J.F. Dill, B.E. Dom, P.W. Drake, A.J. Eastale, P.B. Elterman, R.P. Moeller, H. Saabe, J.A. Wilder, Structural relaxation in vitreous materials, *Ann. N. Y. Acad. Sci.* 279 (1976) 15–35, <http://dx.doi.org/10.1111/j.1749-6632.1976.tb39688.x>.

[6] A.J. Kovacs, J.J. Aklonis, J.M. Hutchinson, A.R. Ramos, Isobaric volume and enthalpy recovery of glasses II. A transparent multiparameter theory, *J. Polym. Sci. Polym. Phys. Ed.* 17 (1979) 1097–1162, <http://dx.doi.org/10.1002/pol.1979.180170701>.

[7] P. Lunkenheimer, R. Wehn, U. Schneider, A. Loidl, Glassy aging dynamics, *Phys. Rev. Lett.* 95 (2005) 055702, <http://dx.doi.org/10.1103/PhysRevLett.95.055702>.

[8] Z. Evenson, T. Koschine, S. Wei, O. Gross, J. Bednarik, I. Gallina, J.J. Krucz, K. Rätzke, F. Faupel, R. Busch, The effect of low-temperature structural relaxation on free volume and chemical short-range ordering in a Au49Cu26.9Si16.3Ag5.5Pd2.3 bulk metallic glass, *Scr. Mater.* 103 (2015) 14–17, <http://dx.doi.org/10.1016/j.scriptamat.2015.02.026>.

[9] B. Schammé, M. Mignot, N. Couvrat, V. Tognetti, L. Joubert, V. Dupray, L. Delbreilh, E. Dargent, G. Coquerel, Molecular relaxations in supercooled liquid and glassy states of a morphous quinidine: dielectric spectroscopy and density functional theory approaches, *J. Phys. Chem. B* 120 (2016) 7579–7592, <http://dx.doi.org/10.1021/jacs.jpcc.6b04242>.

[10] R. Golovchak, A. Ingram, S. Kozyukhin, O. Shpotyuk, Free volume fragmentation in glassy chalcogenides during natural physical ageing as probed by PAL spectroscopy, *J. Non-Cryst. Solids* 377 (2013) 49–53, <http://dx.doi.org/10.1016/j.jnoncrysol.2013.01.039>.

[11] R. Golovchak, J. Oelgoetz, M. Vlcek, A. Esposito, A. Saiter, J.-M. Saiter, H. Jain, Complex structural rearrangements in As-Se glasses, *J. Chem. Phys.* 140 (2014) 054505, <http://dx.doi.org/10.1063/1.4863561>.

[12] X. Peng, G.B. McKenna, Physical aging and structural recovery in a colloidal glass subjected to volume-fraction jump conditions, *Phys. Rev. E* 93 (2016) 042603, <http://dx.doi.org/10.1103/PhysRevE.93.042603>.

[13] C. Lixon Buquet, F. Harmonic, A. Saiter, E. Dargent, D. Langevin, Q.T. Nguyen, Physical aging and molecular mobilities of sulfonated polysulfone for proton exchange membranes, *Thermochim. Acta* 509 (2010) 18–23, <http://dx.doi.org/10.1016/j.tca.2010.05.015>.

[14] D. Cangialosi, A. Alegria, J. Colmenero, Effect of nanostructure on the thermal glass transition and physical aging in polymer materials, *Prog. Polym. Sci.* 54–55 (2016) 128–147, <http://dx.doi.org/10.1016/j.progpolymsci.2015.10.005>.

[15] R. Avolio, R. Castaldo, G. Gentile, V. Ambrogio, S. Fiori, M. Avella, M. Cocca, M.E. Errico, Plasticization of poly(lactic acid) through blending with oligomers of lactic acid: effect of the physical aging on properties, *Eur. Polym. J.* 66 (2015) 533–542, <http://dx.doi.org/10.1016/j.eurpolymj.2015.02.040>.

[16] Y.-Y. Noh, N. Zhao, M. Caironi, H. Sirringhaus, Downscaling of self-aligned, all-printed polymer thin-film transistors, *Nat. Nanotechnol.* 2 (2007) 784–789, <http://dx.doi.org/10.1038/nnano.2007.365>.

[17] M. Takht Ravanchi, T. Kaghazchi, A. Kargari, Application of membrane separation processes in petrochemical industry: a review, *Desalination* 235 (2009) 199–244, <http://dx.doi.org/10.1016/j.desal.2007.10.042>.

[18] H. Wang, X. Sun, P. Seib, Properties of poly(lactic acid) blends with various starches as affected by physical aging, *J. Appl. Polym. Sci.* 90 (2003) 3683–3689, <http://dx.doi.org/10.1002/app.13001>.

[19] Y. Huang, D.R. Paul, Physical aging of thin glassy polymer films monitored by optical properties, *Macromolecules* 39 (2006) 1554–1559, <http://dx.doi.org/10.1021/ma050533y>.

[20] Y. Huang, D.R. Paul, Physical aging of thin glassy polymer films monitored by gas permeability, *Polymer* 45 (2004) 8377–8393, <http://dx.doi.org/10.1016/j.polymer.2004.10.019>.

[21] K.D. Dorkenoo, P.H. Pfromm, Experimental evidence and theoretical analysis of physical aging in thin and thick amorphous glassy polymer films, *J. Polym. Sci. B* 37 (1999) 2239–2251, [http://dx.doi.org/10.1002/\(SICI\)1099-0488\(19990815\)37:16<2239:AI D-POLB26>3.0.CO;2-8](http://dx.doi.org/10.1002/(SICI)1099-0488(19990815)37:16<2239:AI D-POLB26>3.0.CO;2-8).

[22] V. Mathot, M. Pyda, T. Pijpers, G. Vanden Poel, E. van de Kerkhof, S. van Herwaarden, F. van Herwaarden, A. Leenaers, The flash DSC 1, a power compensation twin-type, chip-based fast scanning calorimeter (FSC): First findings on polymers, *Thermochim. Acta* 522 (2011) 36–45.


[23] E. Zhuravlev, C. Schick, Fast scanning power compensated differential scanning nano-calorimeter: 1. The device, *Thermochim. Acta* 505 (2010) 1–13, <http://dx.doi.org/10.1016/j.tca.2010.03.019>.

[24] C. Schick, V. Mathot, Fast Scanning Calorimetry, Springer International Publishing, Cham, 2016. DOI: 10.1007/978-3-319-3129-0 (accessed September 16, 2016).

[25] M. van Drongelen, T. Meijer-Vissers, D. Cavallo, G. Portale, G.V. Poel, R. Andrioch, Microfocus wide-angle X-ray scattering of polymers crystallized in

- a fast scanning chip calorimeter, *Thermochim. Acta* 563 (2013) 33–37, <http://dx.doi.org/10.1016/j.tca.2013.04.007>.
- [26] P. Cebe, B.P. Partlow, D.L. Kaplan, A. Wurm, E. Zhuravlev, C. Schick, Using flash DSC for determining the liquid state heat capacity of silk fibrin, *Thermochim. Acta* 615 (2015) 8–14, <http://dx.doi.org/10.1016/j.tca.2015.07.009>.
- [27] J.E.K. Schawe, Measurement of the thermal glass transition of polystyrene in a cooling rate range of more than six decades, *Thermochim. Acta* 603 (2015) 128–134, <http://dx.doi.org/10.1016/j.tca.2014.05.025>.
- [28] S. Gao, S.L. Simon, Measurement of the limiting fictive temperature over five decades of cooling and heating rates, *Thermochim. Acta* 603 (2015) 123–127, <http://dx.doi.org/10.1016/j.tca.2014.08.019>.
- [29] Y.P. Koh, L. Grassia, S.L. Simon, Structural recovery of a single polystyrene thin film using nanocalorimetry to extend the aging time and temperature range, *Thermochim. Acta* 603 (2015) 135–141, <http://dx.doi.org/10.1016/j.tca.2014.08.025>.
- [30] Y.P. Koh, S. Gao, S.L. Simon, Structural recovery of a single polystyrene thin film using flash DSC at low aging temperatures, *Polymer* 96 (2016) 182–187, <http://dx.doi.org/10.1016/j.polymer.2016.04.047>.
- [31] E. Lopez, S.L. Simon, Signatures of structural recovery in polystyrene by nanocalorimetry, *Macromolecules* 49 (2016) 2365–2374, <http://dx.doi.org/10.1021/acs.macromol.5b02112>.
- [32] S.E.B. Petrie, Thermal behavior of annealed organic glasses, *J. Polym. Sci.* 2 10 (1972) 1255–1272, <http://dx.doi.org/10.1002/pol.1972.160100706>.
- [33] J.L. Gomez Ribelles, M. Monleon Pradas, Structural relaxation of glass-forming polymers based on an equation for configurational entropy. 1. DSC experiments on polycarbonate, *Macromolecules* 28 (1995) 5867–5877, <http://dx.doi.org/10.1021/ma00121a025>.
- [34] M.S. Sánchez, Y. Touzé, A. Saiter, J.M. Saiter, J.L.G. Ribelles, Influence of the chemical structure on the kinetics of the structural relaxation process of acrylate and methacrylate polymer networks, *Colloid Polym. Sci.* 283 (2004) 711–720, <http://dx.doi.org/10.1007/s00396-004-1207-z>.
- [35] J.M.G. Cowie, R. Ferguson, Physical ageing of poly(methyl methacrylate) from enthalpy relaxation measurements, *Polymer* 34 (1993) 2135–2141, [http://dx.doi.org/10.1016/0032-3861\(93\)90741-R](http://dx.doi.org/10.1016/0032-3861(93)90741-R).
- [36] J.M. Hutchinson, S. Montserrat, Y. Calventus, P. Cortés, Application of the Adam-Gibbs equation to the non-equilibrium glassy state, *Macromolecules* 33 (2000) 5252–5262, <http://dx.doi.org/10.1021/ma992015r>.
- [37] D. Cangialosi, V.M. Boucher, A. Alegría, J. Colmenero, Direct evidence of two equilibrium mechanisms in glassy polymers, *Phys. Rev. Lett.* 111 (2013) 095701, <http://dx.doi.org/10.1103/PhysRevLett.111.095701>.
- [38] R. Golovchak, A. Kozdras, V. Balitska, O. Shpotyuk, Step-wise kinetics of natural physical ageing in arsenic selenide glasses, *J. Phys. Condens. Matter* 24 (2012) 505106, <http://dx.doi.org/10.1088/0953-8984/24/50/505106>.
- [40] X. Cao, A. Mohamed, S.H. Gordon, J.L. Willett, D.J. Sessa, DSC study of biodegradable poly(lactic acid) and poly(hydroxy ester ether) blends, *Thermochim. Acta* 406 (2003) 115–127, [http://dx.doi.org/10.1016/S0040-6031\(03\)00252-1](http://dx.doi.org/10.1016/S0040-6031(03)00252-1).
- [41] X. Monnier, N. Delpouve, N. Basson, A. Guinault, S. Domenek, A. Saiter, P.E. Mallon, E. Dargent, Molecular dynamics in electrospon amorphous plasticized polylactide fibers, *Polymer* 73 (2015) 68–78, <http://dx.doi.org/10.1016/j.polymer.2015.07.047>.
- [42] E. Verdonck, K. Schaap, L.C. Thomas, A discussion of the principles and applications of modulated temperature DSC (MTDSC), *Int. J. Pharm.* 192 (1999) 3–20, [http://dx.doi.org/10.1016/S0378-5173\(99\)00267-7](http://dx.doi.org/10.1016/S0378-5173(99)00267-7).
- [43] G.V. Poel, D. Istrate, A. Magon, V. Mathot, Performance and calibration of the Flash DSC 1, a new, MEMS-based fast scanning calorimeter, *J. Therm. Anal. Calorim.* 110 (2012) 1533–1546, <http://dx.doi.org/10.1007/s10973-012-2722-7>.
- [44] J.E.K. Schawe, Influence of processing conditions on polymer crystallization measured by fast scanning DSC, *J. Therm. Anal. Calorim.* 116 (2013) 1165–1173, <http://dx.doi.org/10.1007/s10973-013-3563-8>.
- [45] S. Gao, Y.P. Koh, S.L. Simon, Calorimetric glass transition of single polystyrene ultrathin films, *Macromolecules* 46 (2013) 562–570, <http://dx.doi.org/10.1021/ma3020036>.
- [46] N. Shamim, Y.P. Koh, S.L. Simon, G.B. McKenna, Glass transition temperature of thin polycarbonate films measured by flash differential scanning calorimetry, *J. Polym. Sci. B* 52 (2014) 1462–1468, <http://dx.doi.org/10.1002/polb.23583>.
- [47] A. Dhôtel, B. Rijal, L. Delbreil, E. Dargent, A. Saiter, Combining Flash DSC, DSC and broadband dielectric spectroscopy to determine fragility, *J. Therm. Anal. Calorim.* 121 (2015) 453–461, <http://dx.doi.org/10.1007/s10973-015-4650-9>.
- [48] A. Celli, M. Scandola, Thermal properties and physical ageing of poly(l-lactic acid), *Polymer* 33 (1992) 2699–2703, [http://dx.doi.org/10.1016/0032-3861\(92\)90440-8](http://dx.doi.org/10.1016/0032-3861(92)90440-8).
- [49] L. Dobircau, N. Delpouve, R. Herbinet, S. Domenek, L. Le Pluart, L. Delbreil, V. Ducruet, E. Dargent, Molecular mobility and physical ageing of plasticized poly(lactide), *Polym. Eng. Sci.* 55 (2015) 858–865, <http://dx.doi.org/10.1002/pen.23952>.
- [50] D. Cangialosi, M. Wübbenhorst, J. Groenewold, E. Mendes, H. Schut, A. van Vee, S.J. Picken, Physical aging of polycarbonate far below the glass transition temperature: evidence for the diffusion mechanism, *Phys. Rev. B* 70 (2004) 224213, <http://dx.doi.org/10.1103/PhysRevB.70.224213>.
- [51] D. Cangialosi, M. Wübbenhorst, J. Groenewold, E. Mendes, S.J. Picken, Diffusion mechanism for physical aging of polycarbonate far below the glass transition temperature studied by means of dielectric spectroscopy, *J. Non-Cryst. Solids* 351 (2005) 2605–2610, <http://dx.doi.org/10.1016/j.jnoncrysol.2005.03.070>.
- [52] P. Pan, B. Zhu, Y. Inoue, Enthalpy relaxation and embrittlement of poly(l-lactide) during physical aging, *Macromolecules* 40 (2007) 9664–9671, <http://dx.doi.org/10.1021/ma071737c>.
- [53] H.C. Booij, J.H.M. Palmen, Viscoelasticity of ABS samples differing in thermal history, *Polym. Eng. Sci.* 18 (1978) 781–787, <http://dx.doi.org/10.1002/pen.760181008>.
- [54] A.R. Berens, I.M. Hodge, Effects of annealing and prior history on enthalpy relaxation in glassy polymers. 1. Experimental study on poly(vinyl chloride), *Macromolecules* 15 (1982) 756–761, <http://dx.doi.org/10.1021/ma00231a015>.
- [55] C.M. Laot, E. Marand, B. Schmittmann, R.K.P. Zia, Effects of cooling rate and physical aging on the gas transport properties in polycarbonate, *Macromolecules* 36 (2003) 8673–8684, <http://dx.doi.org/10.1021/ma021720a>.
- [56] K.D. Dorkenoo, P.H. Pfromm, Accelerated physical aging of thin poly[1-(trimethylsilyl)-1-propyne] films, *Macromolecules* 33 (2000) 3747–3751, <http://dx.doi.org/10.1021/ma9921145>.
- [57] M.S. McCaig, D.R. Paul, Effect of film thickness on the changes in gas permeability of a glassy polyarylate due to physical aging Part I. Experimental observations, *Polymer* 41 (2000) 629–637, [http://dx.doi.org/10.1016/S0032-3861\(99\)00172-X](http://dx.doi.org/10.1016/S0032-3861(99)00172-X).
- [58] P.H. Pfromm, W.J. Koros, Accelerated physical ageing of thin glassy polymer films: evidence from gas transport measurements, *Polymer* 36 (1995) 2379–2387, [http://dx.doi.org/10.1016/0032-3861\(95\)97336-E](http://dx.doi.org/10.1016/0032-3861(95)97336-E).
- [59] V.M. Boucher, D. Cangialosi, A. Alegría, J. Colmenero, Enthalpy recovery of PMMA/silica nanocomposites, *Macromolecules* 43 (2010) 7594–7603, <http://dx.doi.org/10.1021/ma101217y>.
- [60] V.M. Boucher, D. Cangialosi, A. Alegría, J. Colmenero, I. Pastoriza-Santos, L.M. Liz-Marzan, Physical aging of polystyrene/gold nanocomposites and its relation to the calorimetric Tg depression, *Soft Matter* 7 (2011) 3607–3620, <http://dx.doi.org/10.1039/C0SM01326A>.
- [61] D. Cangialosi, V.M. Boucher, A. Alegría, J. Colmenero, Enhanced physical aging of polymer nanocomposites: the key role of the area to volume ratio, *Polymer* 53 (2012) 1362–1372, <http://dx.doi.org/10.1016/j.polymer.2012.01.033>.
- [62] V.M. Boucher, D. Cangialosi, A. Alegría, J. Colmenero, Enthalpy recovery in nanometer to micrometer thick polystyrene films, *Macromolecules* 45 (2012) 5296–5306, <http://dx.doi.org/10.1021/ma300622k>.
- [63] Y. Furushima, M. Nakada, H. Takahashi, K. Ishikiryama, Study of melting and crystallization behavior of polyacrylonitrile using ultrafast differential scanning calorimetry, *Polymer* 55 (2014) 3075–3081, <http://dx.doi.org/10.1016/j.polymer.2014.05.015>.
- [64] R. Hilar, P. Honcová, G. Schulz, C. Schick, J. Málek, Enthalpy relaxation of selenium observed by fast scanning calorimetry, *Thermochim. Acta* 603 (2015) 142–148, <http://dx.doi.org/10.1016/j.tca.2014.09.026>.
- [65] H. Huth, A.A. Minakov, C. Schick, Differential AC-chip calorimeter for glass transition measurements in ultrathin films, *J. Polym. Sci. Part B* 44 (2006) 2996–3005, <http://dx.doi.org/10.1002/polb.20921>.
- [66] K. Liao, D. Quan, Z. Lu, Effects of physical aging on glass transition behavior of poly(dl-lactide), *Eur. Polym. J.* 38 (2002) 157–162, [http://dx.doi.org/10.1016/S0014-3057\(01\)00166-5](http://dx.doi.org/10.1016/S0014-3057(01)00166-5).
- [67] J.M. Hutchinson, Physical aging of polymers, *Prog. Polym. Sci.* 20 (1995) 703–760, [http://dx.doi.org/10.1016/0079-6700\(94\)00001-1](http://dx.doi.org/10.1016/0079-6700(94)00001-1).
- [68] I.M. Hodge, Enthalpy relaxation and recovery in amorphous materials, *J. Non-Cryst. Solids* 169 (1994) 211–266, [http://dx.doi.org/10.1016/0022-3093\(94\)90321-2](http://dx.doi.org/10.1016/0022-3093(94)90321-2).
- [69] V.M. Boucher, D. Cangialosi, A. Alegría, J. Colmenero, Enthalpy recovery of glassy polymers: dramatic deviations from the extrapolated liquidlike behavior, *Macromolecules* 44 (2011) 8333–8342, <http://dx.doi.org/10.1021/ma2018233>.
- [70] Y.P. Koh, S.L. Simon, Enthalpy recovery of polystyrene: does a long-term aging plateau exist? *Macromolecules* 46 (2013) 5815–5821, <http://dx.doi.org/10.1021/ma4011236>.

Insights on the Physical State Reached by an Active Pharmaceutical Ingredient upon High-Energy Milling

Benjamin Schammé,^{†,‡} Xavier Monnier,[‡] Nicolas Couvrat,[†] Laurent Delbreilh,^{*,‡} Valérie Dupray,^{*,†}  ^{ib}
Éric Dargent,[‡] and Gérard Coquerel[†]

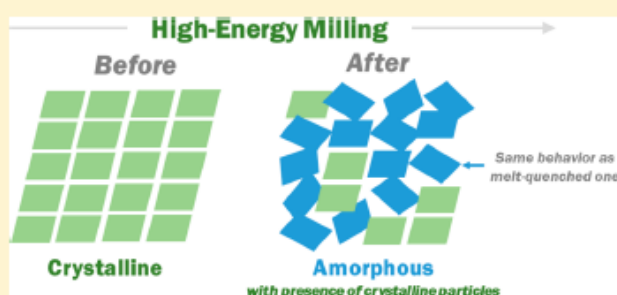
[†]Normandie Univ, UNIROUEN, Sciences et Méthodes Séparatives, 76000, Rouen, France

[‡]Normandie Univ, UNIROUEN, INSA Rouen, CNRS, Groupe de Physique des Matériaux, 76000 Rouen, France

Supporting Information

ABSTRACT: We study the physicochemical transformations of crystalline quinidine upon high-energy milling. The investigations have been achieved by classical, high performance, and fast scanning calorimetry combined with broadband dielectric spectroscopy and X-ray powder diffraction. As evolution of crystalline quinidine with time of milling revealed a prominent sub- T_g cold-crystallization phenomenon, independent and complementary analytical techniques were implemented. Fast scanning calorimetry was performed for the first time on a milled pharmaceutical compound to postpone the crystallization event to higher temperatures.

These fast thermal analyses allowed one to spotlight a genuine glass transition event. In addition, an aging experiment on the milled powder revealed a clear structural relaxation testifying to the presence of a glassy fraction in the milled sample. Last, dielectric analysis of milled quinidine disclosed the presence of localized and delocalized molecular mobility characteristics of glasses. Results for samples obtained by two distinct amorphization routes, vitrification and high-energy milling, indicate that amorphous fraction in milled quinidine behaves the same way as melt-quenched quinidine. These above-mentioned techniques proved their relevancy and efficiency to characterize milled quinidine, and fast scanning calorimetry in particular appears a promising screening tool for disordered systems.



■ INTRODUCTION

Among all accessible preparation pathways, amorphous solids are conventionally obtained by melt-quenching.^{1–6} For organic compounds, elevated temperatures often lead to chemical degradations, unacceptable for the preparation of chemically pure amorphous materials.⁷ In the pharmaceutical industry, several alternative processes such as spray-drying⁸ or lyophilization⁹ operating at low temperatures can lead to amorphous solids. However, these processes require an initial dissolution stage, and sometimes the obtained amorphous compounds are not completely dry. Consequently, further subsequent heating steps are necessary but likely to chemically affect the materials. High-energy milling, for all those reasons, is a valuable candidate to become an efficient manufacturing method of amorphous substances, preserving the chemical completeness when it is not accompanied by excessive heating.^{10–14} Although observed in numerous compounds of pharmaceutical interest, phase transformations upon milling have still not been investigated thoroughly to rationalize experimentally encountered situations.^{15–18} Yet, understanding these transformations is of practical value for the pharmaceutical industry. Controlling the milling process would prevent the formation of undesired physical states¹⁹ (poorly soluble crystalline forms, unstable amorphous substances, etc.) and establish innovative and suitable formulations enabling

pharmaceutical ingredients to be placed into therapeutically efficient states.²⁰ Furthermore, all these formulations involve transformations which fall into complex and fundamental problems within the sphere of condensed matter: non-equilibrium systems and glassy states.

A literature survey of recent research devoted to preparation pathways indicates that characteristic properties of glassy pharmaceuticals depend heavily on the treatment undergone by the material.^{1,21–24} Each of the various pathways to the amorphous state gives rise to a glassy state with its specific thermodynamic properties. Within the framework of molecular dynamics of amorphous trehalose, it has been demonstrated that mobility below T_g may depend on how the glassy state has been achieved.²⁵ Surana et al. concluded that amorphous compounds may exist in several potential relaxation states, each one with its own kinetic properties. In the case of ursodeoxycholic acid, a significant discrepancy in the recrystallization phenomenon was pointed out: milled material showed recrystallization within 2 days while the vitrified material did not display crystallization after a month's time.^{26,27} Graeser et al.²⁸ followed the same approach while analyzing

Received: March 9, 2017

Revised: April 14, 2017

Published: April 21, 2017

amorphous simvastatin prepared by cryomilling and melt-quenching. It has been established that cryomilled sample possesses a lower physical stability than melt-quenched material. These comparative studies have been successfully developed for other amorphous compounds as griseofulvin,²⁹ indomethacin,³⁰ and carbamazepine.²⁴ Attested by distinct thermal and structural properties of amorphous materials prepared by various methods, suggestions were made that molecular mobility may be different for the same drugs using different preparation techniques.³¹ Besides influencing the thermodynamic properties of the generated amorphous state, preparation method may lead to an altered surface area impacting, therefore, crystallization tendencies.³² Small particles will tend to crystallize more readily than larger particles.^{33,34} Another tendency that emerges from a literature overview is the complex and challenging discrimination between amorphization or a mere particle size reduction free of structural changes.^{35,36} This lies in the fact that usual structural investigation analyses give similar signatures for an amorphous state and a nanocrystalline powder.³⁵

To date, a streamlining of transformations for a wider range of APIs (Active Pharmaceutical Ingredients)/excipients reached by various preparation methods has not been attained even if some concluding remarks are emerging from the above current investigations. In this context we have used quinidine, prescribed for its antiarrhythmic activity, as a model compound for the purpose of ensuring whether or not dynamical properties of amorphous substances depend on the amorphization method. Our recent investigation has highlighted the various molecular relaxations in the supercooled liquid and glassy states of melt-quenched quinidine.³⁷ Our aim in the present study is to provide a clear picture of relevant information from structural, spectroscopic, and thermal independent strategies to characterize the nature of the physical state of quinidine reached upon milling. First, transformations of crystalline quinidine upon milling have been recorded by X-ray powder diffraction (XRPD) and standard differential scanning calorimetry (DSC), with benchmarks of comparison with the amorphous state obtained by melt-quenching. Along with these analyses, high-performance DSC (hyper DSC) was employed to discern traces of glass transition incorporated in the cold-recrystallization event in milled quinidine. In addition, fast scanning calorimetry (FSC) measurements, allowing to heat up and cool down materials as fast as 1000 K/s, were performed for the first time on a milled pharmaceutical compound to spotlight a genuine glass transition event. Last, broadband dielectric spectroscopy (BDS) was implemented to seek the presence of localized (secondary relaxations) and delocalized (primary relaxation) molecular mobility in the generated amorphous state.

■ EXPERIMENTAL METHODS

Quinidine ($C_{20}H_{24}N_2O_2$, $M_w = 324.43$ g/mol) received as a crystalline white powder was purchased from Sigma-Aldrich (purity $\geq 98\%$). No impurity was detected via high performance liquid chromatography. The compound was consequently used without prepurification. An X-ray diffractogram of commercial quinidine was recorded and revealed a completely anhydrous crystalline form, in agreement with Kashino and Haisa (Cambridge Structural Database (CSD-BOMDUC)).³⁸ This API only consists, so far, of the stable commercial form.

Milling experiments were performed in a high energy planetary mill "Pulverisette 7" (Fritsch). Room temperature

milling experiments were conducted at 25 °C ($T_g - 35$ °C) with two milling jars of 80 mL made of zirconium oxide containing three balls ($\phi = 20$ mm) of the same material. Each milling operation was conducted with one gram of crystalline quinidine powder, corresponding to a ball/sample weight ratio of 72:1. Vial rotation speed ω was set up to 400 rpm. The rotation of the solar disk, Ω , was performed in the opposite direction compared to the vials. One milling program of milling periods of 5 min and pauses of 5 min was used. These milling conditions have been chosen to limit the mechanical heating of the sample. Each experiment was conducted on a fresh crystalline sample.

X-ray powder diffraction (XRPD) analyses were recorded using a D8 diffractometer (Bruker) equipped with a LynxEye detector. Cu $K\alpha$ radiation ($\lambda = 1.541$ Å) with a tube voltage and amperage set at 40 kV and 40 mA respectively was used as reference configuration. Powder samples were placed onto a flat-frosted glass and analyzed at room temperature with a step of 0.04° (2θ) and a dwell time of 0.5 s from 3 to 50° (2θ). XRPD analysis time was of 10 min performed promptly after sample production.

Classical differential scanning calorimetry (DSC) experiments were performed with a DSC 204 F1 (Netzsch) apparatus equipped with an intracooler. Sample masses of 5 ± 0.5 mg were enclosed into 25 μ L aluminum pans with closed lids. Temperature and enthalpy calibrations were performed using five distinct standards (adamantane, indium, bismuth, tin, and zinc) at the same scanning rate (5 K/min) and with the same pans used in the experiments. The atmosphere of the analyses was regulated by a nitrogen flow (40 mL/min).

High performance scanning calorimetry (hyper DSC) experiments were performed using a PerkinElmer 8500 apparatus equipped with a refrigerated cooling system. Sample masses of 5 ± 0.5 mg were enclosed into sealed standard aluminum pans to improve thermal conductivity and ensure that powder will follow the imposed thermal variations. Baseline was calibrated from -70 to 260 °C with the scanning rate of 200 K/min used in the experiments. Prior to measurement, two standards, benzophenone and indium, were used for temperature and enthalpy calibrations. The atmosphere of the analyses was regulated by a nitrogen flow (20 mL/min).

Fast scanning calorimetry (FSC) measurements were performed using a power compensation twin-type chip based fast scanning calorimeter Flash 1 DSC from Mettler Toledo. Samples were placed on the sensitive area of MultiSTAR UFS 1 MEMS chip sensors. A Huber TC 100 intracooler was used to cool samples down to -90 °C and operate at high cooling rates. The measuring cell was continuously flushed with a 20 mL/min nitrogen gas flow. All analyses were made with the heating rate β_h equal to the cooling one β_c ($\beta_h = |\beta_c|$). Sample masses were estimated from the step change in heat flow at the glass transition. Masses ranged from 10 to 15 ng. Value of the heat capacity step (ΔC_p) was compared between the one obtained through FSC at $\beta_h = 1000$ K/s and the one obtained through modulated standard DSC at $\beta_h = 0.017$ K/s (1 K/min), equal to 0.44 J/(g K) for melt-quenched quinidine.³⁷

Broadband dielectric spectroscopy (BDS) measurements were performed using the Novocontrol Alpha-A dielectric spectrometer over the frequency range from 10^{-2} to 2×10^6 Hz. Non-isothermal dielectric spectra were collected over a wide temperature range from -140 to 100 °C with appropriate successive steps. Accurate temperature control was achieved

using the Quatro system coupled with a nitrogen gas cryostat, allowing a temperature stability of ± 0.2 °C. Melt-quenched quinidine was analyzed using high-quality interdigitated electrodes from Novocontrol Technologies (sensor diameter 20 mm, gold-plated copper combs) as recently described by Schammé et al.³⁷ For milled quinidine, powdered sample was placed between two parallel electrodes, using two stainless steel flat polished electrodes (thickness, 2 mm; diameter, 30 mm). During the whole period of measurement, the sample was kept in a pure nitrogen atmosphere.

RESULTS AND DISCUSSION

Crystalline Quinidine Milled at 25 °C ($T_g - 35$ °C).

Figure 1 shows the XRPD patterns of crystalline quinidine milled from 5 min to 47 h at room temperature. A diffractogram of unmilled crystalline quinidine is shown for comparison.

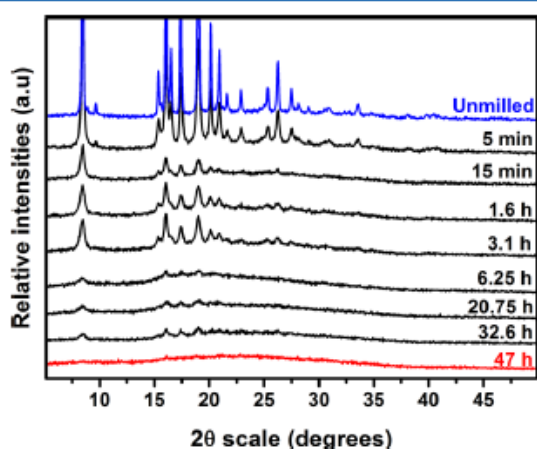


Figure 1. XRPD patterns recorded at room temperature from crystalline quinidine samples subjected to various high-energy milling times ranging from 5 min to 47 h. Unmilled crystalline quinidine is shown as a benchmark of comparison.

A significant decrease of the intensity of Bragg peaks is noticed as milling time increases, demonstrating that high-energy milling progressively reduces the crystallinity. Moreover, a broadening of the Bragg peaks (increased FWHM) is observed, which indicates that milling under these conditions has also an effect on the size of the resulting crystallites. Only from at least 47 h of milling, Bragg peaks have vanished, suggesting that milled quinidine can be considered as X-ray amorphous.

Figure 2 shows the DSC thermograms of crystalline quinidine milled from 5 min to 47 h, for a heating rate of 5 K/min. DSC scans of unmilled crystalline quinidine and melt-quenched quinidine are also presented for comparison.

The thermogram of unmilled crystalline quinidine shows a sharp endothermic event related to the melting process of the commercial stable form. The heating scan corresponding to the quenched liquid reveals a C_p jump ($T_g = 60$ °C) and a cold-crystallization process consistent with the literature. DSC analyses of milled compounds were performed immediately after milling to prevent any possible subsequent evolution. The significant impact of high-energy milling on crystalline quinidine becomes detectable after 15 min of milling. With regard to the DSC up scan, an emerging exothermic event

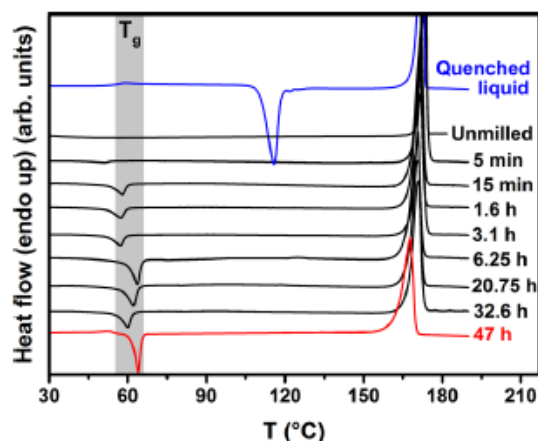


Figure 2. Thermograms obtained upon heating at 5 K/min quinidine samples subjected to various high-energy milling times at room temperature ranging from 5 min to 47 h. Solid blue line corresponds to melt-quenched quinidine.

associated with the cold crystallization of milled quinidine can be ascertained. This exothermic contribution is an indirect signature that a fraction of the sample underwent amorphization during the milling procedure.

It must be noted that quinidine obtained by milling lacks a stationary crystallization temperature. Indeed, the temperature of the crystallization exotherm was found to shift on either side of the glass transition temperature of melt-quenched quinidine, namely, from 55 to 65 °C. This fluctuation may be explained by the fact that milled quinidine seems to be constituted of a wide array of more or less disordered states, ranging from crystalline to amorphous ones. Thus, throughout the milling process, the specific amount of each state may slightly vary, giving rise to a discrepancy of the recrystallization phenomenon.^{39,40} Interestingly, this recrystallization process occurs at ca. 60 °C below the cold-recrystallization process of vitrified quinidine. This difference in crystallization temperature value between vitrified and milled substances has been emphasized for other compounds such as mannitol⁴¹ or etravirine.¹⁰

Additionally, this demonstrates that milled quinidine recrystallizes above and below its T_g . This feature suggests that, in the course of a conventional DSC scan, the broad exotherm associated with the recrystallization tends to overlap the small C_p jump related to the glass transition, which becomes likely difficult to detect (or even nondetectable). Factors that could cause sub- T_g recrystallization have already been assessed, and the main trend that emerges is as follows: molecular mobility of the molecules on the surface area of amorphous grains appears to be strengthened with respect to the ones of the bulk. Consequently, this may trigger a discernible increase of growth rate kinetics leading to a more efficient crystallization of those particles. Fast surface crystallization of amorphous API in the glass transition zone has been successfully reported for griseofulvin.^{42–45} In our situation, we can also consider the role of self-seeding process during milling experiments. To take this phenomenon into account, the amorphous fraction present in the milled samples was determined by XRPD (according to the Saleki-Gerhardt et al. method⁴⁶) and DSC (according to the Lefort et al. method⁴⁷) (Figure 3).

We can note that the results obtained from both techniques differ on the determination of amorphization kinetics. This was already highlighted in the α -lactose case by Caron and co-

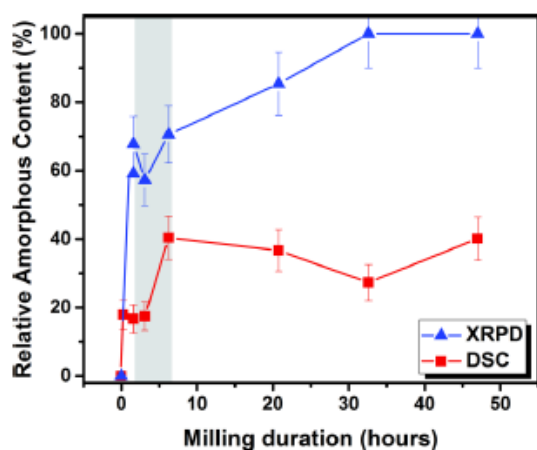


Figure 3. Evolution of the amorphous content of crystalline quinidine upon milling derived from XRPD (blue curve) and DSC (red curve) results. Solid lines are guides for eyes.

workers.³⁹ It is worthwhile to recall that quantitative determination of amorphous fraction depends on the evaluated properties; thus, various techniques could yield to disparate values of amorphous fraction,^{46,48,49} and analytical analyses should be combined toward a more comprehensive description.⁵⁰ This finding is in line with a recent study on glibenclamide where three complementary approaches (XRPD, DSC, and Raman spectroscopy) were employed. Strachan and co-workers established that, depending on the applied analytical method, different milling duration was required to reach an “apparent” fully amorphous state.⁵¹

These above-mentioned results indicate that (i) the two techniques do not lead to the same values of amorphous content alongside milling process.³⁹ This is going along with the fact stating that samples of quinidine should not be considered as a mixture of perfect crystalline matter and amorphous fraction (along with the detection threshold of the considered techniques). (ii) A self-seeding phenomenon seems to occur in the course of milling process. Therefore, the remaining crystals act as seeds in the milled material and tend to promote the crystallization: indeed, if crystalline seeds are still present in the material after milling operations, the time interval between the end of the milling process and the analysis can be sufficient to initiate crystallization. This could explain the early recrystallization mechanism of milled quinidine, in the course of the glass transition zone, along with the relatively low amorphous content detected by DSC (ca. 40%).

The existence of an X-ray amorphous halo combined with thermograms revealing cold-crystallization suggests that an amorphous solid has been generated. However, no apparent glass transition (or C_p jump) which characterizes the quenched liquid could be detected. As a matter of fact, the high-energy milling process of quinidine discloses the complexity to discriminate its final physical state. Therefore, by combining fast scanning calorimetry and dielectric spectroscopy approaches, the following experimental sections will help to clarify the nature of the physical state reached by crystalline quinidine upon milling.

Difference between Milled and Melt-Quenched Quinidine by Means of Hyper DSC. Crystallization, as a kinetic process, results from the complex interplay of nucleation and growth processes.⁵² We therefore applied high scanning

rates to shift the process of recrystallization toward higher temperatures, well above T_g .^{53,10} Figure 4 shows the hyper DSC scans of melt-quenched quinidine (top blue curve) and crystalline quinidine milled for 48 h (bottom red curve), recorded at a 200 K/min scanning rate.

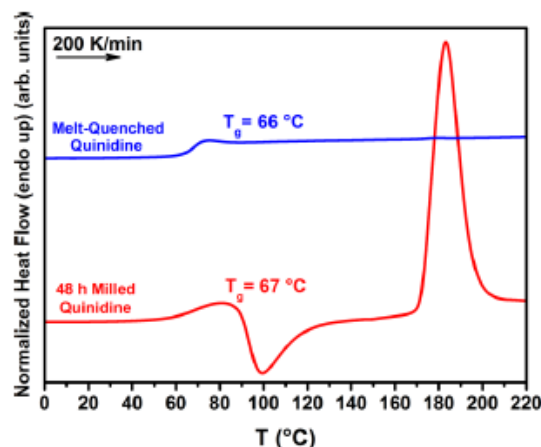


Figure 4. DSC scans obtained upon heating at 200 K/min quinidine samples. Solid blue line corresponds to melt-quenched quinidine while solid red line corresponds to crystalline quinidine milled at room temperature for 48 h.

By comparing the scans of melt-quenched quinidine analyzed at 5 K/min (Figure 2) and 200 K/min, one notes two distinct behaviors. The thermogram of the quenched liquid of quinidine at fast heating rate demonstrates only the C_p jump specific to the glass transition, with a slight common shift in temperature to $T_g = 66$ °C. Thus, it appears that at 200 K/min, recrystallization could be totally prevented. On the other hand, the hyper DSC scan of milled crystalline quinidine still displays a cold-crystallization as well as a melting event. However, it should be noted that recrystallization is mildly shifted toward high temperatures compared to the one occurring during slow heating scan. A close inspection of the glass transition range reveals the beginning of a C_p jump which is not entirely hidden anymore by the crystallization onset. Moreover, no mass loss or physical changes were detected. In this sense, hyper DSC scans indicate that the dynamical state reached by crystalline quinidine under high-energy milling is partially in a glassy amorphous state. The lack of glass transition upon heating milled quinidine at a conventional rate (5 K/min) arises thus from a prompt recrystallization phenomenon occurring in the temperature range of the glass transition and appear to be promoted by a remaining crystalline fraction. Moreover, within the framework decision of the physical state reached under milling, thermal events detected under modulated DSC also support the presence of an amorphous fraction in milled quinidine (Figure S1).

Milled Crystalline Quinidine upon Fast Scanning Calorimetry Experiments. Even though high-performance DSC uses scan rates significantly faster than conventional DSC, the recent work of Corvis and co-workers evidenced the potential application of flash DSC (FSC) to low molecular mass organic compounds, highlighting either new melting data,⁵⁴ pathway to a vitreous state,⁵⁵ or identification of new polymorphs.⁵⁶ Yet, despite the recent development of fast scanning calorimetry,^{57–59} this one was not implemented for

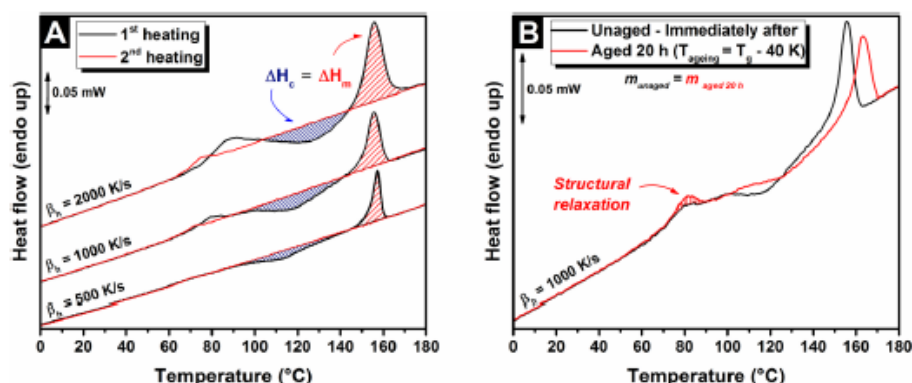


Figure 5. (A) FSC curves obtained for quinidine milled 48 h for scanning rates β_h ranging from 500 to 2000 K/s. Solid black lines correspond to the first heating scans while solid red lines represent second heating ones. (B) FSC curves obtained for unaged (solid black line) and aged milled 48 h quinidine at $T_{\text{aging}} = T_g - 40$ K (solid red line) with a scanning rate of $\beta_h = 1000$ K/s.

milled pharmaceuticals. Hence, in the following section, quinidine milled during 48 h was investigated upon heating through a range of increasing scanning rates to correctly visualize its glass transition while preventing crystallization disturbances.

Figure 5A displays the FSC curves of 48 h milled quinidine samples heated at 500, 1000, and 2000 K/s (evolution of the shape of milled quinidine samples after a scanning rate of $\beta_h = 1000$ K/s and $\beta_h = 2000$ K/s can be seen in Figure S2). Upon heating milled quinidine with a $\beta_h = 500$ K/s scan rate, a cold-crystallization followed by a melting process can be noticed, by contrast to the vitrified one (Figure S3). Interestingly, higher scanning rates (i.e., $\beta_h = 1000$ K/s and $\beta_h = 2000$ K/s) are not sufficient to inhibit the crystallization mechanism. A scanning rate of 1000 K/s definitely outlines a clear heat capacity step at the glass transition of milled quinidine. This process is distinctly and entirely separated from the cold-crystallization, which was previously not possible by hyper DSC scans. Besides, values of crystallization and melting enthalpies were found to be the same (considering the error range), indicating that all quinidine sample that has crystallized subsequently melts. Reheating curves of milled quinidine, irrespective of the scan rate, do not show any presence of cold-crystallization and melting. It is therefore intuitive that all thermal history of milled crystalline quinidine could be erased by overcoming the melting temperature, displaying thus a similar behavior as melt-quenched quinidine. Besides, as recently reported for amorphous polylactide,⁵⁹ the few nanograms analyzed by FSC are representative of the bulk sample investigated by DSC.

Consequently, by applying very high scanning rates, we have shown that milled quinidine shows characteristic features of a genuine amorphous state. It also validates that the thermodynamic signature of the C_p jump was hidden in our previous analyses by a proper crystallization close to T_g . To support this statement and disclose the intrinsic properties of milled quinidine, an aging experiment was implemented. After milling operation, quinidine samples were stored for 20 h in a temperature-controlled chamber with an aging temperature fixed at 40 K below the respective glass transition temperature of quinidine. Figure 5B displays the unaged and aged FSC curves of two milled samples with identical respective masses at a heating rate of $\beta_h = 1000$ K/s. It becomes obvious that milled quinidine is indeed in a partial glassy amorphous state as an endothermic peak related to the structural relaxation process superimposes to the glass transition phenomenon. Only one

small grain is analyzed during FSC experiments. As regards to the representivity of this grain as compared with the whole sample, it can be mentioned that a different amorphous fraction in the chosen grain would only impact the amplitude of the structural relaxation peak. Hence, this enthalpic recovery marks the slow evolution of the thermodynamic properties toward equilibrium, as effectively demonstrated for trehalose.⁶⁰

Relaxation Process in Milled Crystalline Quinidine below T_g . An inherent property of the amorphous state involves the presence of molecular mobility referred to as secondary relaxations.^{61–63} Entirely lacking in the crystalline state, the presence of secondary motions detected by dielectric spectroscopy is another more valuable tool to reveal the physicochemical properties of milled quinidine. Figure 6 shows the frequency evolution of the imaginary part ϵ'' of the complex permittivity for melt-quenched liquid and milled quinidine. Measurements displayed were taken at the same temperature condition, at $T = -55$ °C, i.e., far below the glass transition temperature of quinidine. As can be seen, quinidine milled 48 h exhibits a broad and quasi-symmetrical shape of the dielectric permittivity, which clearly reveals the presence of a relaxation process at -55 °C ($T_g - 115$ °C).

Quenched liquid sample behaves similarly to the milled one, except for the existence of an additional shoulder at the high frequency side as displayed in Figure 6B. The position of the secondary relaxation of milled quinidine is identical with the spectrum gathered at exactly the same temperature as quenched liquid sample. The occurrence of such additional contribution has been already monitored for other pharmaceutical compounds including griseofulvin⁴⁴ and glibenclamide.⁶⁴ The amorphous fraction in quinidine milled 48 h (analyzed by BDS) may be obtained through the ratio of the dielectric strength between milled ($\Delta\epsilon_{\text{milled}}$) and vitrified quinidine ($\Delta\epsilon_{\text{vitrified}}$), bringing a value of ca. 20%. This value, somewhat lower than the ones obtained by DSC and XRPD, falls in line with the recent investigation of Kothari et al.⁶⁵ Upon a panel of model pharmaceutical glass-formers, their dielectric behaviors obtained using powder and film samples were compared. It has been demonstrated that the measured value of $\Delta\epsilon$ is dependent on the sample density and, thus, on the entrapped air of the powdered sample. Therefore, it is clear from Figure 6 that the dielectric strength obtained with melt-quenched quinidine was higher than with milled quinidine.

The secondary relaxation peak in milled quinidine was found to move toward the high frequencies with increasing temper-

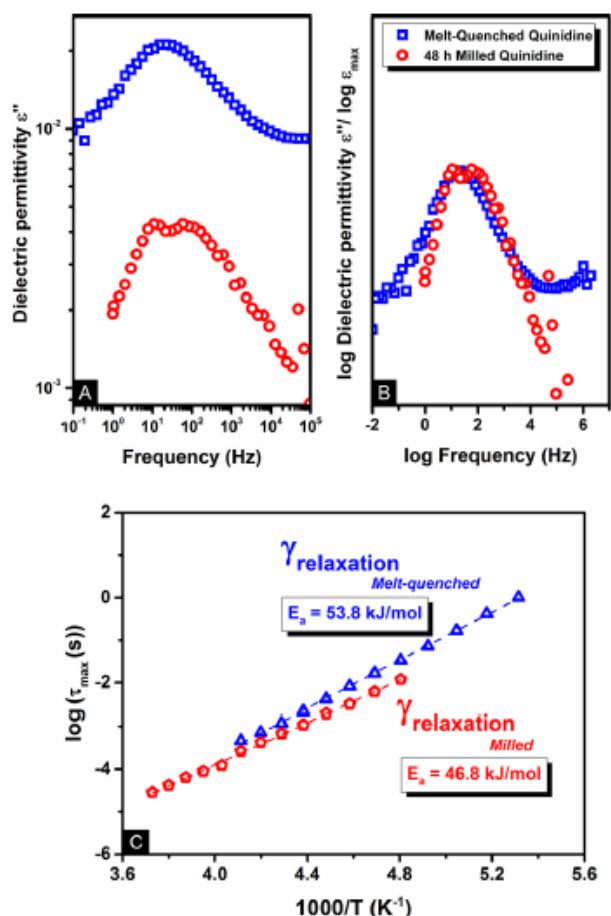


Figure 6. (A) Imaginary part of the dielectric permittivity of melt-quenched quinidine (open blue squares) and 48 h milled quinidine (open red circles) taken at $T = -55$ °C. (B) Master curve constructed from loss spectra of left panel in double logarithmic scale. (C) Temperature dependence of the secondary relaxations of melt-quenched (open blue triangles) and milled quinidine (open red pentagons) fitted by an Arrhenius equation.

ature (Figure S4). The dependence of relaxation times of milled quinidine satisfies the Arrhenius law and reveals an activation energy of 46.8 kJ/mol (Figure 6C). The obtained energy of activation corresponds to the value reported in the literature of 53.8 kJ/mol from melt-quenched quinidine.³⁷ The same value

of the activation barrier for the secondary relaxation in quenched-liquid and milled quinidine indicates that, regardless of the method of amorphization selected, this mode exhibits the same behavior. On behalf of the prompt recrystallization of milled quinidine, the analyzed sample surely contains a percentage of crystals. According to BDS results, apart from intensities, the shape and position of secondary relaxations seem not impacted by crystalline regions, indicating that the state created upon milling possesses the same features as amorphous melt-quenched quinidine. However, local fluctuations of dipoles connected to the secondary relaxation can occur.

Relaxation Process in Milled Crystalline Quinidine above T_g . BDS experiments also enable investigation of the dielectric relaxation process associated with the dynamic glass transition. Herein, Figure 7 presents the comparison of dielectric permittivity ϵ'' for quenched liquid and milled quinidine in the supercooled liquid state at $T = 65$ °C. As can be seen, the position of structural relaxation peaks and the distribution of relaxation times were found to be quite similar, despite different intensities. This is coherent with the work of Kothari et al.⁶⁵ Despite that the magnitude of dielectric properties was found to be lower with powdered samples, they outlined that relaxation times were not impacted by the sample configuration.

The ratio of the dielectric strength between milled ($\Delta\epsilon_{\text{milled}}$) and vitrified quinidine ($\Delta\epsilon_{\text{vitrified}}$) brings an amorphous fraction value of ca. 3%. This would seem coherent as dielectric permittivity ϵ'' was taken at 65 °C; for that temperature, crystallization was already initiated, giving rise to almost no amorphous content in the investigated sample. Moreover, the above finding indicates that, irrespectively of the preparation method, once the material enters the supercooled liquid state, differences in dynamical properties should be erased. In addition to this, dielectric loss spectra drop drastically upon further heating; it was impossible to follow α -relaxation dynamics in such a wide range of temperatures as it happens in the case of vitrified sample (Figure S5). Thus, it is worth noting that the ease of recrystallization upon heating of milled quinidine confirms that milled pharmaceuticals are physically less stable than quenched ones.^{14,66,67} The results of the stability analysis point in the same direction: milled quinidine shows a tendency to crystallization in solely 1 week, in contrast to more than 1 year for quenched liquid (at room temperature, under standard conditions).³⁷

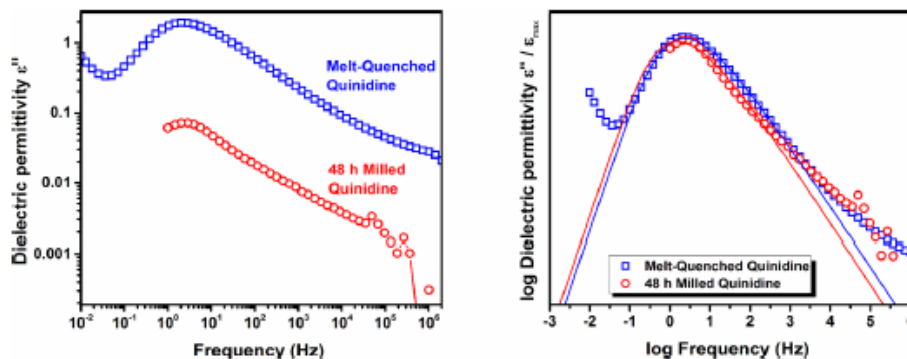


Figure 7. Plots of the dielectric loss spectra for melt-quenched quinidine and 48 h milled quinidine at 65 °C (left) and in double logarithmic scale (right).

CONCLUSIONS

In this paper, process-induced disorder in milled samples of quinidine has been studied. Milled crystalline quinidine appeared to undergo a sub- T_g cold-crystallization phenomenon. This indicates that the physical state reached by milled crystalline quinidine is different from the quenched liquid one. To separate the crystallization process from the glass transition domain, fast scanning calorimetry was proven to be a valuable tool. With a 1000 K/s scan, at T_g , the heat capacity jump could be entirely observed, providing the information that milled quinidine contains a genuine amorphous state. It is a confirmation that the thermodynamic signature of the C_p jump was therefore hidden by a proper crystallization below T_g . Moreover, with broadband dielectric spectroscopy experiments, we successfully identified a secondary relaxation in milled quinidine, characteristic of glassy substances. Consequently, this provides the dynamical evidence that a solid-state amorphization process has occurred upon milling. Besides, according to dielectric experiments, as the glass transition region is reached, the material continues in the supercooled liquid area, and all the differences among dynamical properties are erased. It has been shown through FSC scans that cooling milled quinidine for the purpose of its reamorphization leads to the relaxation times and dynamics of quenched quinidine. Moreover, the FSC investigation highlighted that milled quinidine has undergone an aging process and thus disclosed the intrinsic properties of a glassy system. We therefore pointed out that the amorphous fraction within milled quinidine samples acts the same way with the quenched-liquid one. This only distinct difference lies in the easiest tendency toward crystallization of milled quinidine.

More widely, description of a material in the course of milling operations (composed of structural states more or less disordered) and ranging from the crystalline to the amorphous states seems to be more relevant as opposed to considering systems as being completely amorphous or completely crystalline. Due to this complexity, defining a clear boundary between crystalline and amorphous states is highly sensitive. Therefore, the delicate threshold among these two states gives rise for quinidine to display complex recrystallization properties. Our conducted research here tends to reveal that the presence of crystalline nuclei upon milling operations yields to the early observed recrystallization (below and inside the glass transition area) with respect to the vitrified ones. In light of the above outcomes, our analytical approach developed herein provides a multiscale assessment enabling an accurate picture of amorphous systems. This approach could be of particular interest especially when identification of the reached physical states becomes a challenging issue.

ASSOCIATED CONTENT

Supporting Information

The Supporting Information is available free of charge on the ACS Publications website at DOI: 10.1021/acs.jpcc.7b02247.

DSC scans, wetting evolution of milled samples, FSC curves, dielectric loss spectra, and crystallization process (PDF)

AUTHOR INFORMATION

Corresponding Authors

*E-mail: valerie.dupray@univ-rouen.fr. Tel: +33 2 32 39 90 82.

*E-mail: laurent.delbreilh@univ-rouen.fr. Tel: +33 2 32 95 50 84.

ORCID

Valérie Dupray: 0000-0001-6188-0943

Notes

The authors declare no competing financial interest.

ACKNOWLEDGMENTS

The Region Normandie is acknowledged for financial support to B.S. and X.M. via the E.D. No. 591 (PSIME) as well as for FSC equipment.

REFERENCES

- (1) Yu, L. Amorphous Pharmaceutical Solids: Preparation, Characterization and Stabilization. *Adv. Drug Delivery Rev.* **2001**, *48*, 27–42.
- (2) Adrjanowicz, K.; Kaminski, K.; Paluch, M.; Włodarczyk, P.; Grzybowska, K.; Wojnarowska, Z.; Hawelek, L.; Sawicki, W.; Lepek, P.; Lunio, R. Dielectric Relaxation Studies and Dissolution Behavior of Amorphous Verapamil Hydrochloride. *J. Pharm. Sci.* **2010**, *99*, 828–839.
- (3) Grzybowska, K.; Paluch, M.; Grzybowski, A.; Wojnarowska, Z.; Hawelek, L.; Kolodziejczyk, K.; Ngai, K. L. Molecular Dynamics and Physical Stability of Amorphous Anti-Inflammatory Drug: Celecoxib. *J. Phys. Chem. B* **2010**, *114*, 12792–12801.
- (4) Schammé, B.; Couvrat, N.; Malpeli, P.; Delbreilh, L.; Dupray, V.; Dargent, É.; Coquerel, G. Crystallization Kinetics and Molecular Mobility of an Amorphous Active Pharmaceutical Ingredient: A Case Study with Biclotymol. *Int. J. Pharm.* **2015**, *490* (1–2), 248–257.
- (5) Viel, Q.; Brandel, C.; Cartigny, Y.; Eusébio, M. E. S.; Canotilho, J.; Dupray, V.; Dargent, E.; Coquerel, G.; Petit, S. Crystallization from the Amorphous State of a Pharmaceutical Compound: Impact of Chirality and Chemical Purity. *Cryst. Growth Des.* **2017**, *17*, 337–346.
- (6) Zograf, G.; Newman, A. Interrelationships Between Structure and the Properties of Amorphous Solids of Pharmaceutical Interest. *J. Pharm. Sci.* **2017**, *106*, 5–27.
- (7) Kaminski, K.; Adrjanowicz, K.; Wojnarowska, Z.; Grzybowska, K.; Hawelek, L.; Paluch, M.; Zakowiecki, D.; Mazgalski, J. Molecular Dynamics of the Cryomilled Base and Hydrochloride Ziprasidone by Means of Dielectric Spectroscopy. *J. Pharm. Sci.* **2011**, *100*, 2642–2657.
- (8) Grisedale, L. C.; Jamieson, M. J.; Belton, P. S.; Barker, S. A.; Craig, D. Q. M. Characterization and Quantification of Amorphous Material in Milled and Spray-Dried Salbutamol Sulfate: A Comparison of Thermal, Spectroscopic, and Water Vapor Sorption Approaches. *J. Pharm. Sci.* **2011**, *100*, 3114–3129.
- (9) Bhardwaj, S. P.; Suryanarayanan, R. Molecular Mobility as an Effective Predictor of the Physical Stability of Amorphous Trehalose. *Mol. Pharmaceutics* **2012**, *9*, 3209–3217.
- (10) Qi, S.; Weuts, I.; De Cort, S.; Stokbroekx, S.; Leemans, R.; Reading, M.; Belton, P.; Craig, D. Q. M. An Investigation into the Crystallisation Behaviour of an Amorphous Cryomilled Pharmaceutical Material above and below the Glass Transition Temperature. *J. Pharm. Sci.* **2010**, *99*, 196–208.
- (11) Caron, V.; Tajber, L.; Corrigan, O. I.; Healy, A. M. A Comparison of Spray Drying and Milling in the Production of Amorphous Dispersions of Sulfathiazole/Polyvinylpyrrolidone and Sulfadimidine/Polyvinylpyrrolidone. *Mol. Pharmaceutics* **2011**, *8*, 532–542.
- (12) Caron, V.; Hu, Y.; Tajber, L.; Erxleben, A.; Corrigan, O. I.; McArdle, P.; Healy, A. M. Amorphous Solid Dispersions of Sulfonamide/Soluplus® and Sulfonamide/PVP Prepared by Ball Milling. *AAPS PharmSciTech* **2013**, *14*, 464–474.
- (13) Curtin, V.; Amharar, Y.; Hu, Y.; Erxleben, A.; McArdle, P.; Caron, V.; Tajber, L.; Corrigan, O. I.; Healy, A. M. Investigation of the Capacity of Low Glass Transition Temperature Excipients to Minimize Amorphization of Sulfadimidine on Comilling. *Mol. Pharmaceutics* **2013**, *10*, 386–396.

- (14) Descamps, M.; Willart, J. F. Perspectives on the Amorphisation/milling Relationship in Pharmaceutical Materials. *Adv. Drug Delivery Rev.* **2016**, *100*, 51–66.
- (15) Willart, J. F.; Descamps, M. Solid State Amorphization of Pharmaceuticals. *Mol. Pharmaceutics* **2008**, *5*, 905–920.
- (16) Dujardin, N.; Dudoignon, E.; Willart, J.-F.; Hédoux, A.; Guinet, Y.; Paccou, L.; Descamps, M. Solid State Mutarotation of Glucose. *J. Phys. Chem. B* **2011**, *115*, 1698–1705.
- (17) Dujardin, N.; Willart, J. F.; Dudoignon, E.; Danède, F.; Descamps, M. Mechanism of Solid State Amorphization of Glucose upon Milling. *J. Phys. Chem. B* **2013**, *117*, 1437–1443.
- (18) Descamps, M. Amorphous Pharmaceutical Solids. *Adv. Drug Delivery Rev.* **2016**, *100*, 1–2.
- (19) Amharar, Y.; Curtin, V.; Gallagher, K. H.; O'Siochru, E.; O'Connell, P.; Healy, A.-M. Mitigating Unwanted Amorphisation: A Screening Method for the Selection of Suitable Excipients. *Eur. J. Pharm. Sci.* **2016**, *81*, 181–188.
- (20) Laitinen, R.; Löbmann, K.; Strachan, C. J.; Grohganz, H.; Rades, T. Emerging Trends in the Stabilization of Amorphous Drugs. *Int. J. Pharm.* **2013**, *453*, 65–79.
- (21) Patterson, J. E.; James, M. B.; Forster, A. H.; Lancaster, R. W.; Butler, J. M.; Rades, T. The Influence of Thermal and Mechanical Preparative Techniques on the Amorphous State of Four Poorly Soluble Compounds. *J. Pharm. Sci.* **2005**, *94*, 1998–2012.
- (22) Patterson, J. E.; James, M. B.; Forster, A. H.; Lancaster, R. W.; Butler, J. M.; Rades, T. Preparation of Glass Solutions of Three Poorly Water Soluble Drugs by Spray Drying, Melt Extrusion and Ball Milling. *Int. J. Pharm.* **2007**, *336*, 22–34.
- (23) Lim, A. W.; Löbmann, K.; Grohganz, H.; Rades, T.; Chieng, N. Investigation of Physical Properties and Stability of Indomethacin-cimetidine and Naproxen-cimetidine Co-Amorphous Systems Prepared by Quench Cooling, Coprecipitation and Ball Milling. *J. Pharm. Pharmacol.* **2016**, *68*, 36–45.
- (24) Guinet, Y.; Paccou, L.; Danède, F.; Willart, J.-F.; Derollez, P.; Hédoux, A. Comparison of Amorphous States Prepared by Melt-Quenching and Cryomilling Polymorphs of Carbamazepine. *Int. J. Pharm.* **2016**, *509* (1–2), 305–313.
- (25) Surana, R.; Pyne, A.; Suryanarayanan, R. Effect of Preparation Method on Physical Properties of Amorphous Trehalose. *Pharm. Res.* **2004**, *21*, 1167–1176.
- (26) Yonemochi, E.; Ueno, Y.; Ohmae, T.; Oguchi, T.; Nakajima, S.; Yamamoto, K. Evaluation of Amorphous Ursodeoxycholic Acid by Thermal Methods. *Pharm. Res.* **1997**, *14*, 798–803.
- (27) Yonemochi, E.; Inoue, Y.; Buckton, G.; Moffat, A.; Oguchi, T.; Yamamoto, K. Differences in Crystallization Behavior Between Quenched and Ground Amorphous Ursodeoxycholic Acid. *Pharm. Res.* **1999**, *16*, 835–840.
- (28) Graeser, K. A.; Strachan, C. J.; Patterson, J. E.; Gordon, K. C.; Rades, T. Physicochemical Properties and Stability of Two Differently Prepared Amorphous Forms of Simvastatin. *Cryst. Growth Des.* **2008**, *8*, 128–135.
- (29) Feng, T.; Pinal, R.; Carvajal, M. T. Process Induced Disorder in Crystalline Materials: Differentiating Defective Crystals from the Amorphous Form of Griseofulvin. *J. Pharm. Sci.* **2008**, *97*, 3207–3221.
- (30) Savolainen, M.; Heinz, A.; Strachan, C.; Gordon, K. C.; Yliruusi, J.; Rades, T.; Sandler, N. Screening for Differences in the Amorphous State of Indomethacin Using Multivariate Visualization. *Eur. J. Pharm. Sci.* **2007**, *30*, 113–123.
- (31) Graeser, K. A.; Patterson, J. E.; Zeitler, J. A.; Gordon, K. C.; Rades, T. Correlating Thermodynamic and Kinetic Parameters with Amorphous Stability. *Eur. J. Pharm. Sci.* **2009**, *37* (3–4), 492–498.
- (32) Kestur, U. S.; Ivanovic, I.; Alonzo, D. E.; Taylor, L. S. Influence of Particle Size on the Crystallization Kinetics of Amorphous Felodipine Powders. *Powder Technol.* **2013**, *236*, 197–204.
- (33) Crowley, K. J.; Zografi, G. The Effect of Low Concentrations of Molecularly Dispersed Poly(Vinylpyrrolidone) on Indomethacin Crystallization from the Amorphous State. *Pharm. Res.* **2003**, *20*, 1417–1422.
- (34) Yu, L. Surface Mobility of Molecular Glasses and Its Importance in Physical Stability. *Adv. Drug Delivery Rev.* **2016**, *100*, 3–9.
- (35) Bates, S.; Zografi, G.; Engers, D.; Morris, K.; Crowley, K.; Newman, A. Analysis of Amorphous and Nanocrystalline Solids from Their X-Ray Diffraction Patterns. *Pharm. Res.* **2006**, *23*, 2333–2349.
- (36) Newman, A.; Zografi, G. Critical Considerations for the Qualitative and Quantitative Determination of Process-Induced Disorder in Crystalline Solids. *J. Pharm. Sci.* **2014**, *103*, 2595–2604.
- (37) Schammé, B.; Mignot, M.; Couvrat, N.; Tognetti, V.; Joubert, L.; Dupray, V.; Delbreilh, L.; Dargent, E.; Coquerel, G. Molecular Relaxations in Supercooled Liquid and Glassy States of Amorphous Quinidine: Dielectric Spectroscopy and Density Functional Theory Approaches. *J. Phys. Chem. B* **2016**, *120*, 7579–7592.
- (38) Kashino, S.; Haisa, M. Structure of Quinidine, C₂₀H₂₄N₂O₂. *Acta Crystallogr., Sect. C: Cryst. Struct. Commun.* **1983**, *39*, 310–312.
- (39) Caron, V.; Willart, J.-F.; Lefort, R.; Derollez, P.; Danède, F.; Descamps, M. Solid State Amorphization Kinetic of Alpha Lactose upon Mechanical Milling. *Carbohydr. Res.* **2011**, *346*, 2622–2628.
- (40) Smith, G.; Hussain, A.; Bukhari, N. I.; Ermolina, I. Quantification of Residual Crystallinity of Ball-Milled, Commercially Available, Anhydrous β -Lactose by Differential Scanning Calorimetry and Terahertz Spectroscopy. *J. Therm. Anal. Calorim.* **2015**, *121*, 327–333.
- (41) Yu, L.; Mishra, D. S.; Rigsbee, D. R. Determination of the Glass Properties of D-Mannitol Using Sorbitol as an Impurity. *J. Pharm. Sci.* **1998**, *87*, 774–777.
- (42) Trasi, N. S.; Boerrigter, S. X. M.; Byrn, S. R. Investigation of the Milling-Induced Thermal Behavior of Crystalline and Amorphous Griseofulvin. *Pharm. Res.* **2010**, *27*, 1377–1389.
- (43) Zhu, L.; Jona, J.; Nagapudi, K.; Wu, T. Fast Surface Crystallization of Amorphous Griseofulvin Below T_g. *Pharm. Res.* **2010**, *27*, 1558–1567.
- (44) Willart, J.-F.; Carpentier, L.; Danède, F.; Descamps, M. Solid-State Vitrification of Crystalline Griseofulvin by Mechanical Milling. *J. Pharm. Sci.* **2012**, *101*, 1570–1577.
- (45) Shi, Q.; Cai, T. Fast Crystal Growth of Amorphous Griseofulvin: Relations between Bulk and Surface Growth Modes. *Cryst. Growth Des.* **2016**, *16*, 3279–3286.
- (46) Saleki-Gerhardt, A.; Ahlneck, C.; Zografi, G. Assessment of Disorder in Crystalline Solids. *Int. J. Pharm.* **1994**, *101*, 237–247.
- (47) Lefort, R.; De Gussemme, A.; Willart, J.-F.; Danède, F.; Descamps, M. Solid State NMR and DSC Methods for Quantifying the Amorphous Content in Solid Dosage Forms: An Application to Ball-Milling of Trehalose. *Int. J. Pharm.* **2004**, *280* (1–2), 209–219.
- (48) Shah, B.; Kakumanu, V. K.; Bansal, A. K. Analytical Techniques for Quantification of Amorphous/crystalline Phases in Pharmaceutical Solids. *J. Pharm. Sci.* **2006**, *95*, 1641–1665.
- (49) Hu, Y.; Macfhuionghaile, P.; Caron, V.; Tajber, L.; Healy, A. M.; Erxleben, A.; McArdle, P. Formation, Physical Stability, and Quantification of Process-Induced Disorder in Cryomilled Samples of a Model Polymorphic Drug. *J. Pharm. Sci.* **2013**, *102*, 93–103.
- (50) Heinz, A.; Strachan, C. J.; Atassi, F.; Gordon, K. C.; Rades, T. Characterizing an Amorphous System Exhibiting Trace Crystallinity: A Case Study with Saquinavir. *Cryst. Growth Des.* **2008**, *8*, 119–127.
- (51) Mah, P. T.; Laaksonen, T.; Rades, T.; Aaltonen, J.; Peltonen, L.; Strachan, C. J. Unravelling the Relationship between Degree of Disorder and the Dissolution Behavior of Milled Glibenclamide. *Mol. Pharmaceutics* **2014**, *11*, 234–242.
- (52) Descamps, M.; Dudoignon, E. Crystallization from the Amorphous State: Nucleation-Growth Decoupling, Polymorphism Interplay, and the Role of Interfaces. *J. Pharm. Sci.* **2014**, *103*, 2615–2628.
- (53) Saunders, M.; Podluis, K.; Shergill, S.; Buckton, G.; Royall, P. The Potential of High Speed DSC (Hyper-DSC) for the Detection and Quantification of Small Amounts of Amorphous Content in Predominantly Crystalline Samples. *Int. J. Pharm.* **2004**, *274* (1–2), 35–40.

(54) Corvis, Y.; Négrier, P.; Soulestin, J.; Espeau, P. New Melting Data of the Two Polymorphs of Prednisolone. *J. Phys. Chem. B* **2016**, *120*, 10839–10843.

(55) Corvis, Y.; Wurm, A.; Schick, C.; Espeau, P. Vitreous State Characterization of Pharmaceutical Compounds Degrading upon Melting by Using Fast Scanning Calorimetry. *J. Phys. Chem. B* **2015**, *119*, 6848–6851.

(56) Corvis, Y.; Wurm, A.; Schick, C.; Espeau, P. New Menthol Polymorphs Identified by Flash Scanning Calorimetry. *CrystEngComm* **2015**, *17*, 5357–5359.

(57) Mathot, V.; Pyda, M.; Pijpers, T.; Vanden Poel, G.; van de Kerkhof, E.; van Herwaarden, S.; van Herwaarden, F.; Leenaers, A. The Flash DSC 1, a Power Compensation Twin-Type, Chip-Based Fast Scanning Calorimeter (FSC): First Findings on Polymers. *Thermochim. Acta* **2011**, *522* (1–2), 36–45.

(58) Dhotel, A.; Rijal, B.; Delbreilh, L.; Dargent, E.; Saiter, A. Combining Flash DSC, DSC and Broadband Dielectric Spectroscopy to Determine Fragility. *J. Therm. Anal. Calorim.* **2015**, *121*, 453–461.

(59) Monnier, X.; Saiter, A.; Dargent, E. Physical Aging in PLA through Standard DSC and Fast Scanning Calorimetry Investigations. *Thermochim. Acta* **2017**, *648*, 13–22.

(60) Surana, R.; Pyne, A.; Suryanarayanan, R. Effect of Aging on the Physical Properties of Amorphous Trehalose. *Pharm. Res.* **2004**, *21*, 867–874.

(61) Wojnarowska, Z.; Adrjanowicz, K.; Włodarczyk, P.; Kaminska, E.; Kaminski, K.; Grzybowska, K.; Wrzalik, R.; Paluch, M.; Ngai, K. L. Broadband Dielectric Relaxation Study at Ambient and Elevated Pressure of Molecular Dynamics of Pharmaceutical: Indomethacin. *J. Phys. Chem. B* **2009**, *113*, 12536–12545.

(62) Adrjanowicz, K.; Kaminski, K.; Wojnarowska, Z.; Dulski, M.; Hawelek, L.; Pawlus, S.; Paluch, M.; Sawicki, W. Dielectric Relaxation and Crystallization Kinetics of Ibuprofen at Ambient and Elevated Pressure. *J. Phys. Chem. B* **2010**, *114*, 6579–6593.

(63) Szklarz, G.; Adrjanowicz, K.; Dulski, M.; Knapik, J.; Paluch, M. Dielectric Relaxation Study at Ambient and Elevated Pressure of the Modeled Lipophilic Drug Fenofibrate. *J. Phys. Chem. B* **2016**, *120*, 11298–11306.

(64) Wojnarowska, Z.; Grzybowska, K.; Adrjanowicz, K.; Kaminski, K.; Paluch, M.; Hawelek, L.; Wrzalik, R.; Dulski, M.; Sawicki, W.; Mazgalski, J.; et al. Study of the Amorphous Glibenclamide Drug: Analysis of the Molecular Dynamics of Quenched and Cryomilled Material. *Mol. Pharmaceutics* **2010**, *7*, 1692–1707.

(65) Kothari, K.; Ragoonanan, V.; Suryanarayanan, R. Dielectric Spectroscopy of Small Molecule Pharmaceuticals-Effect of Sample Configuration. *J. Pharm. Sci.* **2014**, *103*, 3190–3196.

(66) Chamarthy, S. P.; Pinal, R. The Nature of Crystal Disorder in Milled Pharmaceutical Materials. *Colloids Surf., A* **2008**, *331* (1–2), 68–75.

(67) Schammé, B.; Couvrat, N.; Malpeli, P.; Dudognon, E.; Delbreilh, L.; Dupray, V.; Dargent, É.; Coquerel, G. Transformation of an Active Pharmaceutical Ingredient upon High-Energy Milling: A Process-Induced Disorder in Biclodyl. *Int. J. Pharm.* **2016**, *499* (1–2), 67–73.



Contents lists available at ScienceDirect

Carbohydrate Polymers

journal homepage: www.elsevier.com/locate/carbpol

Glass transition of anhydrous starch by fast scanning calorimetry

Xavier Monnier^a, Jean-Eudes Maigret^b, Denis Lourdin^{b,*}, Allisson Saiter^a^a Normandie Univ, UNIROUEN Normandie, INSA Rouen, CNRS, Groupe de Physique des Matériaux, 76000 Rouen, France^b INRA, UR1268 BIA Biopolymers Interactions & Assemblies, 44300, Nantes, France

ARTICLE INFO

Article history:

Received 17 March 2017

Received in revised form 3 May 2017

Accepted 14 May 2017

Available online 23 May 2017

Keywords:

Anhydrous amorphous starch

Fast scanning calorimetry

Glass transition

Structural relaxation

ABSTRACT

By means of fast scanning calorimetry, the glass transition of anhydrous amorphous starch has been measured. With a scanning rate of 2000 Ks⁻¹, thermal degradation of starch prior to the glass transition has been inhibited. To certify the glass transition measurement, structural relaxation of the glassy state has been investigated through physical aging as well as the concept of limiting fictive temperature. In both cases, characteristic enthalpy recovery peaks related to the structural relaxation of the glass have been observed. Thermal lag corrections based on the comparison of glass transition temperatures measured by means of differential and fast scanning calorimetry have been proposed. The complementary investigations give an anhydrous amorphous starch glass transition temperature of 312 ± 7 °C. This estimation correlates with previous extrapolation performed on hydrated starches.

© 2017 Elsevier Ltd. All rights reserved.

1. Introduction

Starch, as a storage polysaccharide in plants, is one of the most abundant natural polymers found on a wide range of crops worldwide. Starch is a polyanhydroglucose that consists of two homologous polymers: the linear amylose and the hyper-branched amylopectin, whose molecular weights (M_w) range from 10⁴ to 10⁶ g mol⁻¹ and from 10⁷ to 10⁹ g mol⁻¹, respectively. Depending on its botanical origin, the amylose/amylopectin ratio can vary: 20/80 for potato starch, 25/75 for normal maize starch, 70/30 for amylo maize (high amylose maize). In its native form, starch is stored as granules and presents a semi-crystalline structure which is usually transformed in amorphous state for the most of applications. It is the major component of many foods, as cereal foods, and it is also widely utilized for the development of biodegradable materials for non-food uses. Starch presents a glass transition temperature which has a great impact on mechanical properties, i.e. the texture of food, and aging of products. The importance of the glass transition temperature, in understanding the physical state and physicochemical properties of food materials, has been extensively discussed at the end of the last century (Levine & Slade, 1988; Noel, Ring, & Whittam, 1991; Roos, 1995). The glass transition temperature of starch depends on water content, which has a very efficient plasticizing effect (Bizot et al., 1997). The modeling of glass transition temperature dependence of water concentration is very useful

in order to predict the behavior of starch materials and it has been the subject of numerous studies.

Couchman (Couchman, 1987) proposed a relation based on the thermodynamic, which describes the dependence of the glass transition of a mixture as a function of pure component properties:

$$T_{g(\text{mixture})} = \frac{w_1 \Delta C_{p1} T_{g1} + w_2 \Delta C_{p2} T_{g2}}{w_1 \Delta C_{p1} + w_2 \Delta C_{p2}} \quad (1)$$

where ΔC_{pi} is the heat capacity change of component i , w_i is the weight fraction of component i , and T_{gi} the glass transition of component i .

The Gordon Taylor formula (Gordon & Taylor, 1952) is often preferred. It is equivalent to the Couchman equation but uses the ratio of pure component heat capacity changes as an adjustable variable. Using the same notations as above, the equation becomes:

$$T_{g(\text{mixture})} = \frac{w_1 T_{g1} + k w_2 T_{g2}}{w_1 + k w_2} \quad \text{with } k = \frac{\Delta C_{p2}}{\Delta C_{p1}} \quad (2)$$

Because the degradation temperature is below the glass transition temperature of anhydrous starch, its glass transition temperature cannot be measured by « classic » thermal analysis method such as Differential Scanning Calorimetry (DSC). In fact, Orford et al. (Orford, Parker, Ring, & Smith, 1989) have shown that T_g of *gluco*-polymers increases from 29 °C for anhydrous glucose (DP1) to 167 °C for the anhydrous hexamer, maltohexaose (DP6), with a ΔC_p which decreases from 0.88 Jg⁻¹ K⁻¹ to 0.49 Jg⁻¹ K⁻¹, respectively. The measure for higher chain length is not possible because thermal degradation occurs at 177 °C. Until now, the glass transition temperature of anhydrous starch has only been

* Corresponding author.

E-mail address: denis.lourdin@inra.fr (D. Lourdin).

evaluated by using previous relations from the glass transition temperatures measured on hydrated starch (Bizot et al., 1997). The objective of this work is to study the feasibility of such a measure by fast scanning calorimetry (FSC).

The growing interest of the fast scanning calorimetry has opened new possibilities in the field of polymer science, either for crystallization (Furushima et al., 2017; Toda, Androsch, & Schick, 2016) or amorphous (Cebe et al., 2015; Koh, Gao, & Simon, 2016) properties. Such technique allows to heat up and cool down few nano-grams of sample through high scanning rates as fast as thousand Kelvin per second (Schawe, 2015). One of the interesting point of this technique is the possibility to inhibit and/or shift thermal events through the high scanning rates used. For example, inhibition of the nucleation or the crystallization have been reported for polymers such as poly(lactide) (Androsch, Iqbal, & Schick, 2015; Androsch, Di Lorenzo, & Schick, 2016) or poly(butylene terephthalate) (Androsch, Rhoades, Stolte, & Schick, 2015) by using high scanning rates. More specifically, Furushima et al. have succeeded to measure glass transition and melting for semi-crystalline poly(acrylonitrile) (PAN) (Furushima, Nakada, Takahashi, & Ishikiriyama, 2014). Through scanning rates above 250 K s^{-1} , exothermic reactions happening in the temperature range of the melting have been successfully inhibited. In addition, with regards to amorphous properties, FSC leads to shift in the glass transition (Schick & Mathot, 2016). Termed thermal lag, this shift is due to the heat transfer delay between the heater and the sample. It is caused by the high scanning rates used. Thus, the temperature gradient leads to smearing effect. The measured thermal events appear to occur at higher temperature. As FSC has reported inhibitions or shift of various thermal events, the thermal degradation of anhydrous amorphous starch happening below its glass transition might be successfully inhibited despite the shift of glass transition. However, the thermal lag induced by the technique has to be assessed in order to compare the values of glass transition temperature extrapolated by means of DSC from hydrated starches. Classic thermal lag corrections proposed by Schawe (Schawe, 2015), related to the static and the dynamic ones, cannot be performed due to the thermal degradation of anhydrous starch. Consequently, a novel thermal lag corrections is proposed by using two polymers, considered as standard in this work: poly(lactide) and poly(bisphenol A carbonate). Those polymers present different values of fragility index m . The fragility index m measures the rapidity with which glass-forming liquid properties change as the glassy state is approached (Angell, 1991). As heat transfer delay exists between the heater and the sample due to the high scanning rate, different shifts might be expected with regards to the fragility index. Consequently, the two polymers, which are well known glass-forming liquids, have been chosen in order to assess the differences of glass transition temperatures measured between FSC and standard DSC. By means of FSC, the aim is to figure out the correct glass transition temperature of the anhydrous amorphous starch that would be measured by DSC. Despite a large molar distribution due to its amylose and amylopectin composition, leading to a wide glass transition domain, potato starch exhibits a clear ΔC_p perfectly detectable and values available for hydrated system (Bizot et al., 1997). It is also the purest botanical origin. For these reasons potato starch has been chosen as a model for this study.

2. Materials and methods

2.1. Sample preparation

Potato starch was obtained from Roquette Frères (Lestrem, France). The amylose/amylopectine ratio was 22/78 and the molar weight M_w was $113.10^6 \text{ g mol}^{-1}$ (Rolland-Sabaté, Guilois, Jaillais, & Colonna, 2011). Starch films were obtained by the casting method.

Native granular starch was solubilized in a high-pressure reactor at 130°C for 20 min, using a 4% suspension in ultrapure water. The procedure was performed under a nitrogen atmosphere to avoid any risk of degradation. The solution was evenly spread on Teflon-coated hotplate maintained at 70°C to avoid starch recrystallization during drying. The transparent film obtained had a mean thickness of about $35 \mu\text{m}$ and contains about 10% water. The density of amorphous starch containing about 10% water was about 1.45 (Lourdin, Colonna, & Ring, 2003).

Semi-crystalline polylactide (PLA) pellets, grade 4042D, were provided by Natureworks. The content of L-lactide and D-lactide were about 96% and 4%, respectively. The number-average molecular weight was $M_w = 188.10^3 \text{ g mol}^{-1}$. The pellets were dried at 60°C overnight. Dried pellets were then thermo-molded in films of tens microns thick, at a pressure of 1 bar and a temperature of 180°C , in a manual hydraulic press (ATLASTM SPECAC). The density was $\rho = 1.25$.

Amorphous poly(bisphenol A carbonate) (PBAC) pellets, grade LEXANTM, were provided by General Electrics. The number-average molecular weight was $M_w = 47.10^3 \text{ g mol}^{-1}$. The pellets were dried at 120°C overnight. Dried pellets were then thermo-molded in films of tens microns thick, at a pressure of 1 bar and a temperature of 280°C , in a manual hydraulic press (ATLASTM SPECAC). The density was $\rho = 1.20$.

2.2. Thermogravimetric analysis

Thermogravimetric analysis was performed under a nitrogen atmosphere using a TA instruments TGA2050. Around 4 mg of sample is heated from room temperature to 130°C at 10 K min^{-1} , followed by an isotherm for 30 min to ensure dehydration. It is then heated at 5 K min^{-1} to 400°C .

2.3. Differential scanning calorimetry analysis

DSC analyses were performed with a TA instruments Q100 calorimeter under a 50 mL min^{-1} nitrogen gas flow. The calibration in energy was done using a standard of indium, while the calibration in temperature was done using a standard of indium, as well as a standard of benzophenone.

The starch sample (around 0.5 mg) was placed into opened aluminum pans, and an empty pan was used as reference. Both were heated from room temperature to 130°C at 10 K min^{-1} , followed by an isotherm for 30 min to ensure dehydration. They were then heated at 5 K min^{-1} to 400°C .

PLA and PBAC masses were around 5 mg. They were heated up to 50°C above their respective glass transition temperature at 10 K min^{-1} . The aluminum reference and sample couples, pan and lid, were identical to within $\pm 0.01 \text{ mg}$.

2.4. Fast scanning calorimetry analysis

FSC analyses were performed using a power compensation twin-type chip based fast scanning calorimeter Flash DSC 1 from Mettler Toledo. The twin-type chip sensor based on MEMS technology is made of a sample and a reference sides. Both sides are independent furnaces. The temperature is measured through sixteen thermocouples, eight for each side. The temperature resolution is determined by the time constant of the sensor which is about 1 millisecond, namely about thousand times less than standard DSC (Mathot et al., 2011). Therefore, the relaxation times induced by the heating in the glass-forming liquid can be measured, as they are of same order of magnitude than temperature resolution (Dhotel, Rijal, Delbreilh, Dargent, & Saiter, 2015). Samples were placed on the sensitive area of a MultiSTAR UFS 1 MEMS chip sensors. To do so, samples were previously cut in small pieces. A Huber TC100 intra

cooler was used to cool samples down to -90°C and thus operate high cooling rates. Samples were continuously flushed with a $20\text{ mL}\cdot\text{min}^{-1}$ nitrogen flow gas to avoid water condensation from the environment and to optimize the program temperature applied (Mathot et al., 2011). The thermal contact between the sample and the chip was improved by using a thin layer of silicone oil. If possible, the sample masses were estimated from the step change in heat flow at the glass transition, by comparing the value of the heat capacity step ΔC_p from the one obtained through FSC and the one obtained through standard DSC for a wholly amorphous sample (Dhotel et al., 2015). Heat capacities of $0.51\text{ J}\cdot\text{g}^{-1}\cdot\text{K}^{-1}$ (Monnier et al., 2015) and $0.27\text{ J}\cdot\text{g}^{-1}\cdot\text{K}^{-1}$ (Bizot et al., 1997) have been used for PLA and anhydrous starch, respectively. Prior to FSC analysis, starch film was always dried at 130°C during 10 min.

The sample shapes were observed with a universal EPI-illuminator optical microscope and a digital camera system from Nikon Corporation in reflection mode. Perimeter and surface area were measured with ImageJ software. Finally, the thickness of each sample was figured out from the density.

3. Results and discussions

3.1. Thermal degradation

Fig. 1 shows thermogravimetric and differential scanning calorimetry analyses of starch films. As observed in Fig. 1(A), dehydration takes place in the starch from ambient temperature up to 130°C . The weight loss during this phase is related to the moisture content. After the isothermal of 30 min to complete the dehydration of starch, the weight loss suddenly drops at a temperature of 290°C , which corresponds to the thermal degradation of the starch. Prior to the DSC analysis, an isothermal at 130°C has also been performed as shown in Fig. 1(B). Decrease of the heat flow is measured from ambient temperature up to 130°C . Once the content of moisture is lost, classic increase of the heat flow related to the starch as a function of temperature is observed up to 220°C . Then, above 220°C , the heat flow decreases to reach an endothermic peak with a maximum located at around 290°C . Thus, initial thermal degradation of the starch starts at 220°C . The initial decrease might be related to breaking of inter-chain weak bonds. Then, endothermic peak might be related to the cleavage of macromolecular chains, resulting in its thermal degradation.

3.2. Glass transition

By means of DSC, at a low scanning rate such as depicted in Fig. 1(B), anhydrous amorphous starch degrades before to reach the glass transition. The relative low scanning rates used by means of DSC might lead to unwanted thermal reactions during heating. A well-known example comes from polyacrylonitrile (PAN). Over the temperature range $200\text{--}300^{\circ}\text{C}$, three major exothermic reactions occur on the PAN in addition of its own melting. As a consequence, the melting temperature of PAN cannot be easily measured without using plasticizing agent (Gupta, Paliwal, & Bajaj, 1998). Nevertheless, Furushima et al. have reported glass transition and melting of PAN by using different high scanning rates by FSC. They inhibited exothermic reactions, cold crystallization and reorganization of PAN by using scanning rate higher than $250\text{ K}\cdot\text{s}^{-1}$ (Furushima et al., 2014).

As a second example, non-isothermal crystallization of PLA leads to concomitant formation of highly ordered α crystals and less ordered δ crystals upon relative low cooling by DSC (Wasanasuk & Tashiro, 2011). However, Androsch et al. have successfully inhibited crystallization of PLA upon cooling by using sufficient high cooling rates. Besides, even if the melt is cooled faster than the critical cooling rate to suppress crystallization, they have also detected the presence of nuclei in PLA (Androsch et al., 2016). Therefore, high scanning rates of FSC can inhibit or shift nucleation, crystallization or any unwanted reactions with regard to various polymer investigations. In this way, inhibition of the thermal degradation occurring prior to the glass transition by means of FSC has been investigated.

Premelting are usually used in order to improve the thermal contact between the analyzed sample and the membrane of the chip sensor by FSC. The premelting consists of heating the sample up to the liquid-like state or liquid state (Monnier, Saiter, & Dargent, 2017; Schawe, 2015). However, premelting of anhydrous amorphous starch film fails due to its thermal degradation. The only way to improve the thermal contact, in addition of the thin layer of oil, has been to approach the glass transition by successive heating and cooling scans up to the glass transition. Fig. 2 shows heat flows of anhydrous amorphous starch film by means of FSC. As depicted, three successive scans have been used (cycle 1, 2 and 3) in order to improve the thermal contact and reach the glass transition on the subsequent heating (cycle 4). On the fourth scan, a step in the heat flow is clearly distinguished upon heating and located around 333°C . This step seems to be related to the glass transition. Then, the subsequent cooling (cycle 4) depicts a slight decrease of the glass transition. On the cycle 5, the heat flow increases up to 330°C . Then, it drops up to 380°C . By superimposing the

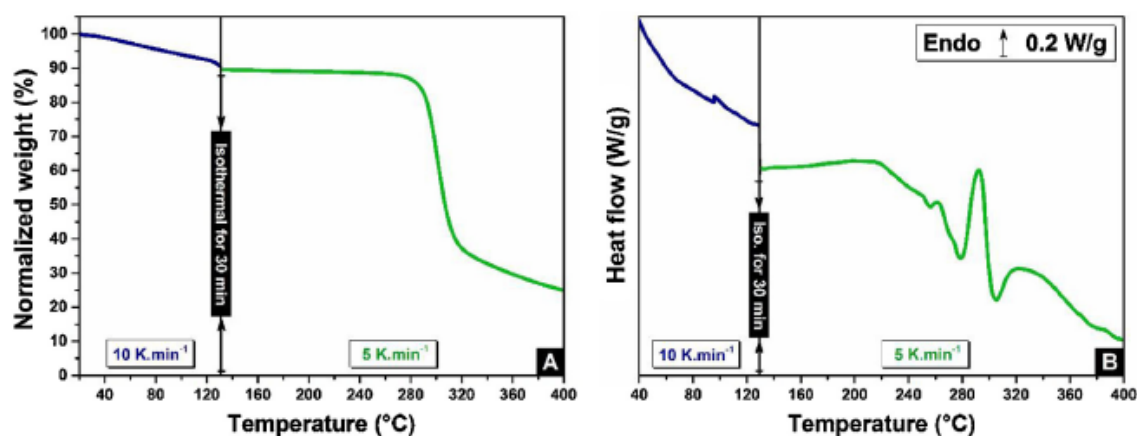


Fig. 1. Thermogravimetric (A) and differential scanning calorimetry (B) analyses of starch films. First, starch was heated up to 130°C at $10\text{ K}\cdot\text{min}^{-1}$. Dehydration was sensed through isothermal for 30 min. Then, starch was heated up to 400°C at $5\text{ K}\cdot\text{min}^{-1}$.

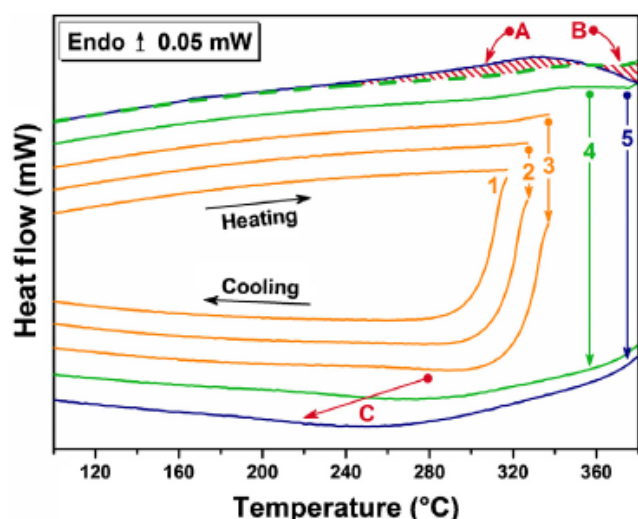


Fig. 2. FSC heat flows of anhydrous starch. First, the sample was heated up to 340 °C after 3 progressive scanning ramps with an increment of 10 °C, from 320 °C to 340 °C (cycle 1, 2 and 3). Each heating is followed by the subsequent cooling, as highlighted by the numbered vertical arrows. This is done to improve the thermal contact. The cycle 4 displays a step in the heat flow. Heating of the cycle 4 has been translated on the glassy state of the heating cycle 5 (Dashed line). With regards to the cycle 5: (A and B) endothermic and exothermic events related to thermal degradation, respectively; (C) decrease of the glass transition from around 280 °C to 220 °C resulting from thermal degradation. All scanning rates were 2000 K s⁻¹.

previous heating of the cycle 4, two thermal events can be distinguished: one endothermic (A) and one exothermic (B), respectively. We can clearly see that the glassy line increases up to the step observed in the heat flow. Then, the liquid line clearly decreases. Finally, the last cooling (cycle 5) displays another glass transition temperature lower than the previous one (C). Liu et al. argued that thermal decomposition mechanism of anhydrous starch above 300 °C comes from chemical dehydration, in which thermal condensation between hydroxyl groups of starch chains forms ether segments as well as water molecules and other small molecular species (Liu et al., 2013). Therefore, the thermal degradation species induced lead to a lower glass transition on the subsequent cooling. As a consequence, the two thermal events depicted on the heating of the cycle 5 above 300 °C might be related to thermal degradation.

By using a scanning rate of 2000 K s⁻¹ by means of FSC, degradation of anhydrous amorphous starch films, occurring before its glass transition, seems inhibited. From the experimental observation in Fig. 2, the endothermic step upon heating on the cycle 4 seems to be related to glass transition of anhydrous amorphous starch. However, in order to certify this thermal event, structural relaxation has also been investigated. A glass-forming liquid is out of equilibrium when it is cooled down due to the impossibility of the liquid to equilibrate in the available time imposed by the cooling rate (Kovacs, 1964). However, molecular mobility exists in the glassy state due to its metastable nature. Thus, hold below its glass transition, any glass-forming liquids will slowly evolve towards thermodynamic equilibrium (Cangialosi, Alegría, & Colmenero, 2016; Struik, 1977). This phenomenon is the so called structural relaxation or physical aging (Boucher et al., 2011; Cangialosi, Boucher, Alegría, & Colmenero, 2012; Koh et al., 2016). This phenomenon also happens when the cooling rate used to form the glass is lower than the subsequent heating (Gao & Simon, 2015; Saiter, Hess, D'Souza, & Saiter, 2002). Such behavior has led to the concept of limiting fictive temperature T_f introduced by Tool and Eiclitin (Tool & Eiclitin, 1931). This concept is used to characterize the non-equilibrium state and the glass to liquid-like transition (Couderc et al., 2007). By definition, T_f is the temperature at which any properties related to the structural

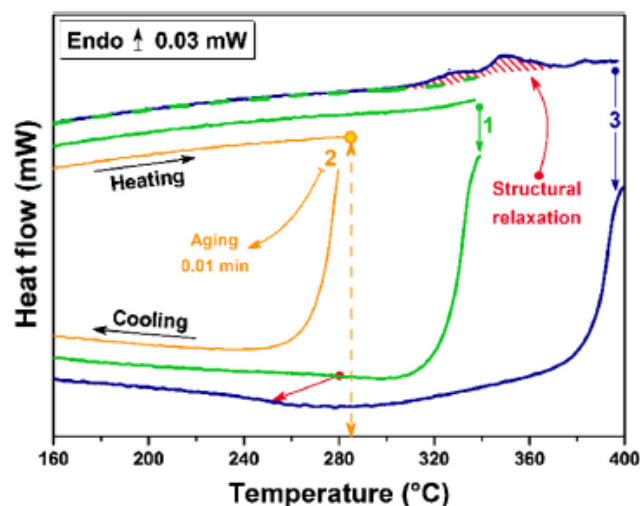


Fig. 3. FSC heat flows of anhydrous starch. The sample was heated up to 340 °C (cycle 1) to improve the thermal contact as explained before prior to age at 285 °C during 0.01 min (cycle 2). Finally, the structural relaxation (hatched area) was measured from a final heating scan up to 400 °C (cycle 3). Each heating is followed by the subsequent cooling, as highlighted by the numbered vertical arrows. Heating of the cycle 1 has been translated on the glassy state of the heating of cycle 3 (Dashed line). All scanning rates were 2000 K s⁻¹.

relaxation are at the equilibrium state. The resulting effect of structural relaxation is observed upon heating with an enthalpy recovery peak superimposed to the glass transition (Sánchez, Touzé, Saiter, Saiter, & Ribelles, 2005).

Fig. 3 shows structural relaxation investigations through physical aging. In the same manner as outlined above, successive scanning ramps up to 340 °C have been used to improve the thermal contact. Beginning of the glass transition is even measured with a rupture of the glassy state line, as shown on the heating of the cycle 1 in Fig. 3. On the following cycle 2, physical aging has been performed at an aging temperature $T_{ag} = 285$ °C during an aging time $t_{ag} = 0.01$ min. Those physical aging conditions have been optimized after successive steps at higher aging temperatures and different aging times. Thus, the annealing takes place at around 45 °C below the glass transition measured in Fig. 2. Therefore, at 285 °C the glassy state is reached and structural relaxation occurs (Struik, 1977). Besides, thanks to the high cooling rate ($\beta_c = 2000$ K s⁻¹), high level of enthalpy is induced in the glass formed (Koh, Grassia, & Simon, 2015; Monnier et al., 2017). Consequently, the glass formed presents very short relaxation times allowing to measure changes after very short times. After the aging stage, the subsequent heating curve of the cycle 3 displays a clear peak related to enthalpy recovery (red hatched area). Besides, none exothermic event related to thermal degradation has been observed up to 400 °C. However, thermal degradation seems to occur due to the decrease of the glass transition temperature upon cooling (cycle 1 and 3), from around 280 °C to 250 °C between the first and last cooling (red arrow).

Fig. 4 shows structural relaxation investigation through the limiting fictive temperature concept. As explained before, successive scanning ramps have also been performed up to 350 °C in order to improve the thermal contact. Thus, beginning of the glass transition has been reached, improving the thermal contact, while thermal degradation is avoided, as used in the previous investigations. It is worth mentioning that liquid state is even reached (green curve). The subsequent cooling ramp has been performed at 70 K s⁻¹ in order to form a glass with a lower fictive temperature than a glass formed at 2000 K s⁻¹. Due to the relative low cooling rate (70 K s⁻¹) and the very low mass used (few ng), none thermal events are observed upon cooling, except a based line (orange curve). Thus,

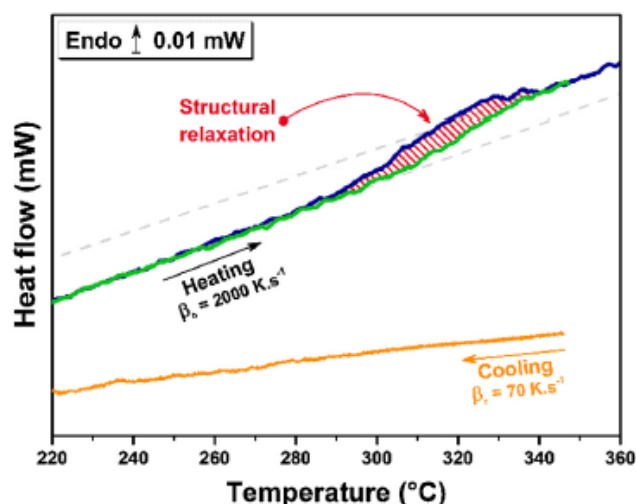


Fig. 4. FSC heat flows of anhydrous starch. The sample was heated up to 350 °C after successive progressive heating with a scanning rate of $\beta_{hc} = 2000 \text{ K.s}^{-1}$ (green curve) to improve the thermal contact as explained before. Then, after reaching 350 °C, the sample was cooled down at $\beta_c = 70 \text{ K.s}^{-1}$ (orange curve). Upon the subsequent heating, up to 360 °C at $\beta_h = 2000 \text{ K.s}^{-1}$, structural relaxation (hatched area) is observed due to the difference between β_c and β_h (blue curve). The grey dashed lines represent the extrapolated glassy and liquid like states. (For interpretation of the references to colour in this figure legend, the reader is referred to the web version of this article.)

the final heating at 2000 K.s^{-1} (blue curve) has led to structural relaxation with a broad enthalpy recovery peak superimposed to the glass transition (red hatched area). It is also important to notice that no degradation has occurred up to 360 °C. In addition, both liquid lines of the heating ramps, before and after the recovery, superimpose perfectly.

Consequently, the structural relaxation phenomena observed seem to certify that the step change in heat flow is related to the glass transition of anhydrous amorphous starch. As far as we know, it is the first measurement of glass transition for an anhydrous amorphous starch.

3.3. Thermal lag corrections, comparison with standard polymers

As explained in the introduction, thermal lag occurs by FSC due to the high scanning rates and the smearing effects induced by the technique itself. As explained by Schawe (Schawe, 2015), dynamic and static thermal lags have to be estimated to correct the thermal lag. The first one corresponds to the average value of glass transition temperatures determined from heating and cooling measurements at the same scanning rate $\beta_h = |\beta_c|$. The second one corresponds to a third of the difference in the onset melting temperatures of an indium piece placed over the sample and another one positioned directly on the reference chip sensor. Unfortunately, due to the thermal degradation of anhydrous starch, dynamic thermal lag corrections have not been possible. Therefore, an alternative one has been proposed. The goal is to estimate a glass transition temperature for an anhydrous amorphous starch film, which would be measured by standard DSC. Thus, the thermal lag correction is not based on heat transfer delay between the heater and the sample, but it can only be based on the comparison of the glass transition temperature difference ΔT measured by means of standard DSC at 0.17 K.s^{-1} and FSC at 2000 K.s^{-1} upon heating.

In addition to the glass transition temperature, other parameters define a glass-forming liquid. One of the most commonly used is the fragility index m (Angell, 1991). This index measures the rapidity with which glass-forming liquid properties change as the glassy state is approached. More precisely, it characterizes the decrease of

Table 1

Glass transition parameters of the starch, as well as PLA and PBAC used to investigate the thermal lag correction induced by the high scanning rates of the FSC: glass transition temperature measured by means of FSC $T_{g,FSC}$, glass transition temperature measured by means of DSC $T_{g,DSC}$, glass transition temperature difference ΔT between FSC and DSC and fragility index m . Thickness L_{FSC} of the analyzed samples by means of FSC are also displayed. a (Delpouve, De Ibreilh, Stoclet, Saiter, & Dargent, 2014); b (Mano, Gómez Ribelles, Alves, & Salmerón Sanchez, 2005); c (Qin & McKenna, 2006); d (Rijal, De Ibreilh, & Saiter, 2015).

	$T_{g,FSC}$ (°C)	$T_{g,DSC}$ (°C)	ΔT (°C)	m	L_{FSC} (μm)
Starch	327 ± 5	0	0	>170	9
PLA	74 ± 1	58 ± 1	16 ± 2	155 ^a , 166 ^b	6
PBAC	160 ± 1	146 ± 1	14 ± 2	132 ^c , 170 ^d	8

the relaxation times of any glass forming-liquid as approaching the glass transition. Thus, glass forming-liquids are classified as strong and fragile, which depict Arrhenius and non-Arrhenius behavior, respectively. This difference of relaxation time when approaching the glass transition might induce a difference of heat transfer delay by FSC due to the high scanning rates. According to the nature and the ability of a glass forming-liquid to turn into glass, different thermal lag might be involved. Thus, it might be possible to observe different ΔT from a glass-forming liquid to another according to its fragility index.

Naturally, the fragility index of the anhydrous starch is unknown. Nevertheless, Borde et al. have shown from hydrated amylopectin (6% and 16% water) a fragility index m of 169 and 114, respectively (Borde, Bizot, Vigier, & Buleon, 2002). In addition, Bouthegourd et al. have estimated a fragility index value of 151 for a hydrated starch (13% water) (Bouthegourd, Esposito, Lourdin, Saiter, & Saiter, 2013). Thus, a value of m superior to 170 can be easily estimated for an anhydrous amorphous starch. Consequently, PLA and PBAC have been chosen as standards in this work with regards to their relative high fragility index m value ranging from around 130 to 170, as summarized in Table 1. The goal is to assess the ΔT value for those standards in order to give a glass transition temperature as accurate as possible for an anhydrous amorphous starch which would be measured by means of DSC.

First, anhydrous amorphous starch and amorphous PLA have been analyzed on the same chip sensor. To do so, PLA has been pre-melted in order to improve its thermal contact, and then starch film has been placed next to PLA, as shown in Fig. 5(A). Finally, successive scanning ramps have been performed, as depicted in Fig. 5(B). Thermal stability of PLA is clearly observed for all scans upon heating, as well as cooling, with a glass transition temperature of 74 °C and 66 °C, respectively. On the 5th ramp, the glass transition temperature of the anhydrous starch is once again observed at around 330 °C upon heating, as well as on the cooling at around 300 °C. From three different analyses on three different samples, an average glass transition temperature not corrected $T_g = 327 \pm 5$ °C has been estimated upon heating.

In a second time, concomitant analyses of PLA and PBAC have been performed with a similar procedure. Fig. 6(A) shows FSC heat flows of PLA and PBAC analyzed on the same chip sensor. As measured in Fig. 5, PLA depicts a glass transition of 74 °C. PBAC glass transition takes place at higher temperature: 160 °C. As explained above, the thermal lag correction is based on the comparison between the glass transition temperatures measured upon DSC at 0.17 K.s^{-1} and FSC at 2000 K.s^{-1} . Thus, the glass transition temperatures of individual PLA and PBAC have been measured by means of DSC, as presented in Fig. 6(B). The glass transition temperatures measured are 58 °C and 146 °C, respectively. In addition, thicknesses of the analyzed samples by FSC have been evaluated by taking into account their respective mass, density and geometrical shape in order to certify the thermal lag correction. Indeed, due to the high scanning rates used by FSC, it is well established in

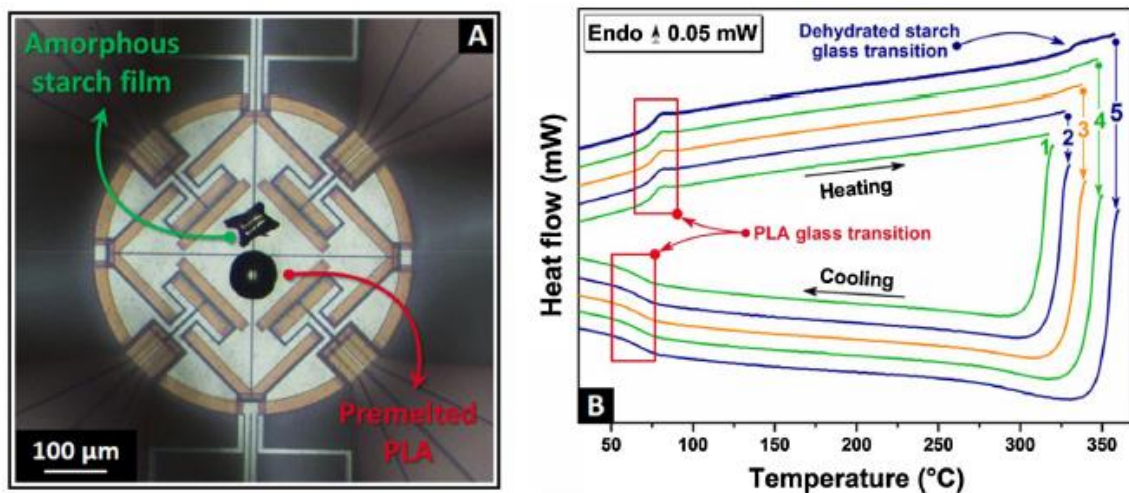


Fig. 5. Optical microscope picture (A) and FSC heat flows (B) of PLA and starch on a same FSC chip sensor. The samples were heated up to 350°C after 5 progressive scanning ramps, with an increment of 10°C. Each heating is followed by the subsequent cooling, as highlighted by the numbered vertical arrows. Glass transitions of PLA upon heating and cooling are highlighted by red rectangular. All scanning rates were 2000K s⁻¹. (For interpretation of the references to colour in this figure legend, the reader is referred to the web version of this article.)

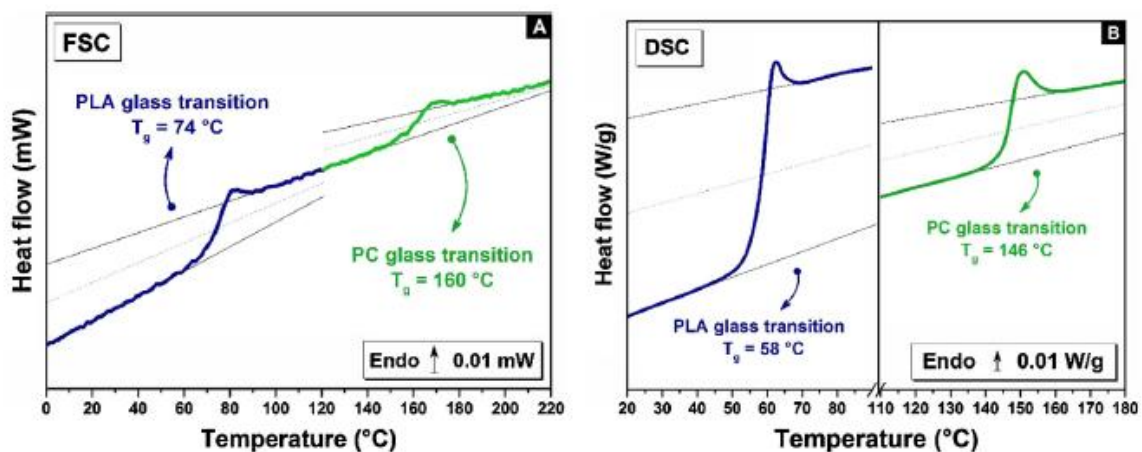


Fig. 6. FSC heat flows (A) and DSC heat flows (B) of PLA and PBAC. The scanning rates were 2000K s⁻¹ and 10K min⁻¹, respectively for FSC and DSC.

literature that thermal lag correction becomes significant for sample having a thickness higher than 10 μm (Schawe, 2015). Thus, thicker samples lead to incorrect measurements. The thicknesses measured are all below 10 μm, as reported in Table 1. Consequently, for samples having a similar thickness, namely a similar thermal lag, and presenting different values of fragility index, a constant ΔT has been measured between both techniques. Independently of the fragility index, the ΔT is approximately equal to 15°C. Thus, a thermal lag correction of 15°C has to be subtracted on the raw FSC measurements in order to assess the glass transition temperature of an anhydrous amorphous starch which would be measured upon standard DSC. A glass transition temperature of 312 ± 7°C is then proposed for an anhydrous amorphous starch. Such result agrees with the investigations of Bizot et al. on hydrated amorphous starches (Bizot et al., 1997). By using different water contents, they have been able to extrapolate a glass transition temperature of 316°C for an anhydrous amorphous starch through the Couchman's model. Consequently, thanks to the FSC, this study shows that experiment and theory join together.

4. Conclusion

To our knowledge, it is the first time that glass transition of anhydrous amorphous starch has been measured. Thanks to the FSC,

a scanning rate of 2000 K s⁻¹ has permitted to observe the heat capacity change at the glass transition on duration short enough to avoid the thermal degradation of the biopolymer. In addition, structural relaxation has been performed through physical aging and the concept of limiting fictive temperature. Both cases have depicted enthalpy recovery peaks on the subsequent heating curves. As a consequence the determination of the glass transition for an anhydrous amorphous starch has been possible, and a glass transition temperature of 312 ± 7°C is proposed for an anhydrous amorphous starch. This value correlates with previous investigations on hydrated starches with an extrapolated value of 316°C. This work demonstrates that FSC open new perspectives for numerous polysaccharides and biopolymers for which the problem of water sensitivity and degradation is common.

Acknowledgment

The authors gratefully acknowledge the Normandy Region, France, for the financial support to Xavier Monnier thesis as well as for FSC equipment.

References

- Androsch, R., Di Lorenzo, M. L., & Schick, C. (2016). Crystal nucleation in random l/d-lactide copolymers. *European Polymer Journal*, 75, 474–485. <http://dx.doi.org/10.1016/j.eurpolymj.2016.01.020>
- Androsch, R., Iqbal, H. M. N., & Schick, C. (2015). Non-isothermal crystal nucleation of poly(l-lactic acid). *Polymer*, 81, 151–158. <http://dx.doi.org/10.1016/j.polymer.2015.11.006>
- Androsch, R., Rhoades, A. M., Stölte, L., & Schick, C. (2015). Density of heterogeneous and homogeneous crystal nuclei in poly(butylene terephthalate). *European Polymer Journal*, 66, 180–189. <http://dx.doi.org/10.1016/j.eurpolymj.2015.02.013>
- Angell, C. A. (1991). Relaxation in liquids, polymers and plastic crystals—Strong/fragile patterns and problems. *Journal of Non-Crystalline Solids*, 131, 13–31. [http://dx.doi.org/10.1016/0022-3093\(91\)90266-9](http://dx.doi.org/10.1016/0022-3093(91)90266-9)
- Bizot, H., Le Bail, P., Leroux, B., Davy, J., Roger, P., & Buleon, A. (1997). Calorimetric evaluation of the glass transition in hydrated, linear and branched poly(hydroxy)lucosaccharides. *Carbohydrate Polymers*, 32(1), 33–50. [http://dx.doi.org/10.1016/s0144-8617\(96\)00146-4](http://dx.doi.org/10.1016/s0144-8617(96)00146-4)
- Borde, B., Bizot, H., Vigier, G., & Buleon, A. (2002). Calorimetric analysis of the structural relaxation in partially hydrated amorphous polysaccharides. I. Glass transition and fragility. *Carbohydrate Polymers*, 48(1), 83–96. [http://dx.doi.org/10.1016/s0144-8617\(01\)00217-X](http://dx.doi.org/10.1016/s0144-8617(01)00217-X)
- Boucher, V. M., Cangialosi, D., Alegría, A., Colmenero, J., González-Irún, J., & Liz-Marzán, L. M. (2011). Physical aging in PMMA/silica nanocomposites: Enthalpy and dielectric relaxation. *Journal of Non-Crystalline Solids*, 357(2), 605–609. <http://dx.doi.org/10.1016/j.jnoncrysol.2010.05.091>
- Bouhagourd, E., Esposito, A., Lourdin, D., Saiter, A., & Saiter, J. M. (2013). Size of the cooperative rearranging regions vs. fragility in complex glassy systems: Influence of the structure and the molecular interactions. *Physica B: Condensed Matter*, 425, 83–89. <http://dx.doi.org/10.1016/j.physb.2013.05.029>
- Cangialosi, D., Boucher, V. M., Alegría, A., & Colmenero, J. (2012). Enhanced physical aging of polymer nanocomposites: The key role of the area to volume ratio. *Polymer*, 53(6), 1362–1372. <http://dx.doi.org/10.1016/j.polymer.2012.01.033>
- Cangialosi, D., Alegría, A., & Colmenero, J. (2016). Effect of nanostructure on the thermal glass transition and physical aging in polymer materials. *Progress in Polymer Science*, 54–55, 128–147. <http://dx.doi.org/10.1016/j.progpolymsci.2015.10.005>
- Cebe, P., Partlow, B. P., Kaplan, D. L., Wurm, A., Zhuravlev, E., & Schick, C. (2015). Using flash DSC for determining the liquid state heat capacity of silk fibroin. *Thermochimica Acta*, 615, 8–14. <http://dx.doi.org/10.1016/j.tca.2015.07.009>
- Couchman, P. R. (1987). The glass transition of compatible blends. *Polymer Engineering & Science*, 27(9), 618–621. <http://dx.doi.org/10.1002/pen.760270903>
- Coudrec, H., Delbreilh, L., Saiter, A., Grenet, J., De Souza, N., & Saiter, J. M. (2007). Relaxation in poly-(ethylene terephthalate glycol)/montmorillonite nanocomposites studied by dielectric methods. *Journal of Non-Crystalline Solids*, 353(47–51), 4334–4338. <http://dx.doi.org/10.1016/j.jnoncrysol.2007.03.046>
- Delpouve, N., Delbreilh, L., Stoclet, G., Saiter, A., & Dargent, E. (2014). Structural dependence of the molecular mobility in the amorphous fractions of polylactide. *Macromolecules*, 47(15), 5186–5197. <http://dx.doi.org/10.1021/ma500839p>
- Dhotel, A., Rijal, B., Delbreilh, L., Dargent, E., & Saiter, A. (2015). Combining Flash DSC, DSC and broadband dielectric spectroscopy to determine fragility. *Journal of Thermal Analysis and Calorimetry*, 121(1), 453–461. <http://dx.doi.org/10.1007/s10973-015-4650-9>
- Furushima, Y., Nakada, M., Takahashi, H., & Ishikiriya, K. (2014). Study of melting and crystallization behavior of polyacrylonitrile using ultrafast differential scanning calorimetry. *Polymer*, 55(13), 3075–3081. <http://dx.doi.org/10.1016/j.polymer.2014.05.015>
- Furushima, Y., Kumazawa, S., Umetsu, H., Toda, A., Zhuravlev, E., & Schick, C. (2017). Melting and recrystallization kinetics of poly(butylene terephthalate). *Polymer*, 109, 307–314. <http://dx.doi.org/10.1016/j.polymer.2016.12.053>
- Gao, S., & Simon, S. L. (2015). Measurement of the limiting fictive temperature over five decades of cooling and heating rates. *Thermochimica Acta*, 603, 123–127. <http://dx.doi.org/10.1016/j.tca.2014.08.019>
- Gordon, M., & Taylor, J. S. (1952). Ideal copolymers and the second-order transitions of synthetic rubbers. I. Non-crystalline copolymers. *Journal of Applied Chemistry*, 2(9), 493–500. <http://dx.doi.org/10.1002/jctb.5010020901>
- Gupta, A. K., Paliwal, D. K., & Bajaj, P. (1998). Melting behavior of acrylonitrile polymers. *Journal of Applied Polymer Science*, 70(13), 2703–2709. [http://dx.doi.org/10.1002/\(SICI\)1097-4628\(19981226\)70:13<2703::AID-APP15>3.0.CO;2-2](http://dx.doi.org/10.1002/(SICI)1097-4628(19981226)70:13<2703::AID-APP15>3.0.CO;2-2)
- Koh, Y. P., Grassia, L., & Simon, S. L. (2015). Structural recovery of a single polystyrene thin film using nanocalorimetry to extend the aging time and temperature range. *Thermochimica Acta*, 603, 135–141. <http://dx.doi.org/10.1016/j.tca.2014.08.025>
- Koh, Y. P., Gao, S., & Simon, S. L. (2016). Structural recovery of a single polystyrene thin film using Flash DSC at low aging temperatures. *Polymer*, 96, 182–187. <http://dx.doi.org/10.1016/j.polymer.2016.04.047>
- Kovacs, A. J. (1964). Transition vitreuse dans les polymères amorphes. Etude phénoménologique. In *Fortschritte Der Hochpolymeren-Forschung*, pp. 394–507. Berlin, Heidelberg: Springer. Retrieved from <http://link.springer.com/chapter/10.1007/BFb0050366>
- Levine, H., & Slade, L. (1988). *Water as a plasticizer: Physico-chemical aspects of low moisture polymeric systems*. Retrieved March 2, 2017, from https://www.researchgate.net/profile/Harry_Levine2/publication/301564755_Water_as_a_plasticizer_Physico-chemical_aspects_of_low_moisture_polymeric_systems/links/571a3af08ae7f552a472c03/Water-as-a-plasticizer-Physico-chemical-aspects-of-low-moisture-polymeric-systems.pdf
- Liu, X., Wang, Y., Yu, L., Tong, Z., Chen, L., Liu, H., & Li, X. (2013). Thermal degradation and stability of starch under different processing conditions. *Starch Stärke*, 65(1–2), 48–60. <http://dx.doi.org/10.1002/star.201200198>
- Lourdin, D., Colonna, P., & Ring, S. G. (2003). Volumetric behaviour of maltose-water, maltose-glycerol and starch-sorbitol-water systems mixtures in relation to structural relaxation. *Carbohydrate Research*, 338(24), 2883–2887. <http://dx.doi.org/10.1016/j.carres.2003.09.006>
- Mano, J. F., Gómez Ribelles, J. L., Alves, N. M., & Salmerón Sanchez, M. (2005). Glass transition dynamics and structural relaxation of PLLA studied by DSC: Influence of crystallinity. *Polymer*, 46(19), 8258–8265. <http://dx.doi.org/10.1016/j.polymer.2005.06.096>
- Mathot, V., Pyda, M., Pijpers, T., Vanden Poel, G., van de Kerkhof, E., van Herwaarden, S., et al. (2011). The Flash DSC 1, a power compensation twin-type, chip-based fast scanning calorimeter (FSC): First findings on polymers. *Thermochimica Acta*, 522, 36–45.
- Monnier, X., Delpouve, N., Basson, N., Guinault, A., Domenek, S., Saiter, A., et al. (2015). Molecular dynamics in electrospun amorphous plasticized polylactide fibers. *Polymer*, 73, 68–78. <http://dx.doi.org/10.1016/j.polymer.2015.07.047>
- Monnier, X., Saiter, A., & Dargent, E. (2017). Physical aging in PLA through standard DSC and fast scanning calorimetry investigations. *Thermochimica Acta*, 648, 13–22. <http://dx.doi.org/10.1016/j.tca.2016.12.006>
- Noel, T. R., Ring, S. G., & Whittam, M. A. (1991). Kinetic aspects of the glass-transition behaviour of maltose-water mixtures. *Carbohydrate Research*, 212, 109–117. [http://dx.doi.org/10.1016/0008-6215\(91\)84049-K](http://dx.doi.org/10.1016/0008-6215(91)84049-K)
- Orford, P. D., Parker, R., Ring, S. G., & Smith, A. C. (1989). Effect of water as a diluent on the glass transition behaviour of malto-oligosaccharides, amylose and amylopectin. *International Journal of Biological Macromolecules*, 11(2), 91–96. [http://dx.doi.org/10.1016/0141-8130\(89\)90048-2](http://dx.doi.org/10.1016/0141-8130(89)90048-2)
- Qin, Q., & McKenna, G. B. (2006). Correlation between dynamic fragility and glass transition temperature for different classes of glass forming liquids. *Journal of Non-Crystalline Solids*, 352(28–29), 2977–2985. <http://dx.doi.org/10.1016/j.jnoncrysol.2006.04.014>
- Rijal, B., Delbreilh, L., & Saiter, A. (2015). Dynamic heterogeneity and cooperative length scale at dynamic glass transition in glass forming liquids. *Macromolecules*, 48(22), 8219–8231. <http://dx.doi.org/10.1021/acs.macromol.5b01152>
- Rolland-Sabaté, A., Guildas, S., Jaillais, B., & Colonna, P. (2011). Molecular size and mass distributions of native starches using complementary separation methods: Asymmetrical Flow Field Fractionation (A4F) and Hydrodynamic and Size Exclusion Chromatography (HDC-SEC). *Analytical and Bioanalytical Chemistry*, 399(4), 1493–1505. <http://dx.doi.org/10.1007/s00216-010-4208-4>
- Roos, Y. H. (1995). *Phase transitions in foods*. Academic Press.
- Sánchez, M. S., Touzé, Y., Saiter, A., Saiter, J. M., & Ribelles, J. L. G. (2005). Influence of the chemical structure on the kinetics of the structural relaxation process of acrylate and methacrylate polymer networks. *Colloid and Polymer Science*, 283(7), 711–720. <http://dx.doi.org/10.1007/s00396-004-1207-z>
- Saiter, A., Hess, M., D Souza, N. A., & Saiter, J. M. (2002). Entropy and fragility in vitreous polymers. *Polymer*, 43(26), 7497–7504. [http://dx.doi.org/10.1016/s0032-3861\(02\)00631-6](http://dx.doi.org/10.1016/s0032-3861(02)00631-6)
- Schawe, J. E. K. (2015). Measurement of the thermal glass transition of polystyrene in a cooling rate range of more than six decades. *Thermochimica Acta*, 603, 128–134. <http://dx.doi.org/10.1016/j.tca.2014.05.025>
- Schick, C., & Mathot, V. (Eds.). (2016). *Fast scanning calorimetry*. In: Cham: Springer International Publishing. <http://link.springer.com/10.1007/978-3-319-31329-0>; Retrieved from
- Struik, L. C. E. (1977). Physical aging in plastics and other glassy materials. *Polymer Engineering & Science*, 17(3), 165–173. <http://dx.doi.org/10.1002/pen.760170305>
- Toda, A., Androsch, R., & Schick, C. (2016). Insights into polymer crystallization and melting from fast scanning chip calorimetry. *Polymer*, 91, 239–263. <http://dx.doi.org/10.1016/j.polymer.2016.03.038>
- Tool, A. Q., & Eicidin, C. G. (1931). Variations caused in the heating curves of glass by heat treatment. *Journal of the American Ceramic Society*, 14(4), 276–308. <http://dx.doi.org/10.1111/j.1151-2916.1931.tb16602.x>
- Wasanasuk, K., & Tashiro, K. (2011). Crystal structure and disorder in poly(l-lactic acid) β form (α' form) and the phase transition mechanism to the ordered α form. *Polymer*, 52(26), 6097–6109. <http://dx.doi.org/10.1016/j.polymer.2011.10.046>



ELSEVIER

Contents lists available at ScienceDirect

Polymer

journal homepage: www.elsevier.com/locate/polymer

Local and segmental motions of the mobile amorphous fraction in semi-crystalline polylactide crystallized under quiescent and flow-induced conditions



Xavier Monnier^{a,*}, Laurence Chevalier^a, Antonella Esposito^a,
Lucia Fernandez-Ballester^b, Allisson Saiter^a, Eric Dargent^a

^a Normandie Univ, UNIROUEN Normandie, INSA Rouen, CNRS, Groupe de Physique des Matériaux, 76000 Rouen, France

^b Department of Mechanical and Materials Engineering, University of Nebraska at Lincoln, Lincoln, NE 68588, United States

ARTICLE INFO

Article history:

Received 7 July 2017

Accepted 8 August 2017

Available online 12 August 2017

Keywords:

Polylactide

Amorphous fractions

Flow-induced crystallization

Spherulite

Fast scanning calorimetry

Physical aging

ABSTRACT

The molecular dynamics of the constrained and unconstrained mobile amorphous fractions in semi-crystalline polylactide (PLA) was investigated in the presence of both flow-induced crystalline structures and spherulites by fast scanning calorimetry (FSC) through cooperativity and physical aging concepts. First, the shear rate conditions leading to flow-induced crystallization were characterized by examining the relaxation of shear-induced precursors. At a temperature of 150 °C, the critical relaxation time is so long that cooling down the sheared melt to the crystallization temperature does not affect significantly the precursors. Therefore, highly oriented structures develop. The arrangement of the crystalline fraction, either in flow-induced crystalline structures or spherulites, has no influence on the molecular dynamics of the mobile amorphous fraction, whereas the crystallinity degree was proved to play a significant role. Two kinds of molecular dynamics were distinguished, respectively associated to the α and secondary relaxations. The molecular dynamics related to the α relaxation of the mobile amorphous fraction was investigated in terms of cooperativity: a clear dependence on the coupling and the confinement by the crystals was observed, because a classic decrease of the cooperativity length was found when comparing amorphous to semi-crystalline PLA. On the contrary, the molecular dynamics related to the secondary relaxations of the mobile amorphous fraction was not modified by the presence of the crystals, as observed from close physical aging investigations below the glass transition. The different length-scale of the α and secondary relaxations seems to be the reason why the crystalline environment influences the macromolecular motions rather than the molecular or local motions.

© 2017 Elsevier Ltd. All rights reserved.

1. Introduction

When polymers crystallize, the macromolecular chains that initially are in 3D random coil conformations arrange segments of their chains into lamellar crystals [1]. Semi-crystalline polymers can be obtained by either quiescent or prestressed crystallization pathways. Crystallization is quiescent when the process is only thermally activated, whether performed upon cooling from the melt or upon heating from the glassy state to a given temperature [2,3]. Quiescent crystallization is also possible in the presence of nucleating agents, which allow tailoring crystal morphology and

lamellae orientation [4]. Prestressed crystallization emerges from specific conditions, such as memory effects [5], cross-nucleation [6,7] or thermo-mechanical history [8]. The latter case is of importance for processing, as semi-crystalline polymers are frequently subjected to intense shear and/or elongational flows in the molten state prior to crystallization. Over the last few decades, numerous works have investigated the initial stages of flow-induced crystallization [9–14] as well as the final oriented semi-crystalline microstructure [15–19]. Melt flow of sufficient intensity results in local alignment and stretch of chain segments which can induce the formation of oriented nucleation precursors. Flow-induced precursors are thought to be metastable quasi-crystalline aggregates that can persist at high temperatures for long times, even above the nominal melting point. The main consequences of the presence of oriented flow-induced precursors are

* Corresponding author.

E-mail address: xavier.monnier1@univ-rouen.fr (X. Monnier).

a significant acceleration of the crystallization kinetics and a transition from an overall isotropic morphology (spherulites) to anisotropic flow-induced crystalline structures. As a result of the oriented crystalline morphology that can develop after flow, final physical properties are also significantly impacted.

Flow-induced crystallization has been frequently investigated on polyolefins — particularly polyethylene and polypropylene — because of their commercial relevance. Due to environmental concerns, several studies have recently focused on flow-induced crystalline structures in polylactide (PLA) [20–25], a biosourced and biodegradable thermoplastic polyester. Quiescent crystallization of PLA leads to the concomitant formation of highly ordered α crystals and less ordered δ crystals [26]. It is established that quiescent crystallization performed at temperatures higher than 120 °C leads to α crystals, whereas below 100 °C δ crystals are obtained. In the intermediate range of temperature, concomitant crystallization of both α and δ crystals occurs [27]. The influence of shear or elongational flow onto the crystalline structures that develop in PLA has been mainly investigated in order to improve physical attributes, such as oxygen barrier [28] or mechanical properties [29]. It should be mentioned that, in some cases, semi-crystalline microstructures similar to flow-induced crystalline structures have also been obtained in PLA-based composite materials [30,31] and in PLA-based formulations containing nucleating agents [32,33] or nano-fibrils [34].

Most of the existing studies, whether on polyolefins or PLA, are focused on characterizing the crystalline fraction, and not on the confinement of the amorphous fractions by flow-induced crystalline structures. In addition, the lifetime of flow-induced precursors in PLA has not yet been explored. The recent development of fast scanning calorimetry (FSC) has represented a real breakthrough for the study of polymer crystallization [35,36], polymer melting [37,38] and amorphous polymer properties [39,40]. Fast scanning techniques allow analyzing a few ng of a sample by using rates as fast as thousands of Kelvin per second [41]. As a consequence, the analysis of amorphous fractions confined by crystals at the scale of semi-crystalline superstructures is now possible.

The crystallization of polymers is a kinetic process that results in the formation of nano-phasic structures where crystalline and amorphous regions coexist [42]. The final morphology results from a competition between crystallization and vitrification. For decades now, most semi-crystalline polymers have been described in the literature with a three-phase model [43,44]. In fact, between the crystalline and the amorphous fractions, an incomplete decoupling may exist that defines an additional fraction called the rigid amorphous fraction (RAF) [45,46]. This fraction is due to the fact that polymer chains are much longer than the typical dimensions of polymer crystals [47,48]. RAF is commonly defined by opposition to the mobile amorphous fraction (MAF) in that its mobility is drastically restricted due to the geometrical constraints at the interface with the crystals [49,50]. Regarding the MAF, constrained and unconstrained MAF — depicted as intra- and inter-spherulitic amorphous phases respectively — have recently been reported for semi-crystalline polyesters such as PET [51] and PLA [43,52,53]. Constrained and unconstrained MAF were revealed by differential scanning calorimetric measurements through the concept of cooperative rearranging regions (CRR) [54] as well as structural relaxation (i.e. physical aging) [55].

The purpose of this paper is to investigate the relaxation of shear-induced precursors leading to flow-induced crystallization of PLA, so that the amorphous fractions constrained within different semi-crystalline microstructures can be investigated through glass transition and physical aging by means of FSC. The presence of crystals affects the molecular dynamics of the MAF; therefore, a question arises: what is the role of crystalline morphology?

2. Materials and methods

2.1. Materials and sample preparation

PLA pellets (grade 4042D, containing about 96% of *l*-lactide and 4% of *d*-lactide) were provided by NatureWorks. The number-average and weight-average molecular weights were $\langle M_n \rangle = 116$ kDa and $\langle M_w \rangle = 188$ kDa respectively, as measured by gel permeation chromatography (GPC). Prior to use, PLA pellets were dried overnight at 60 °C to prevent degradation. The pellets were then thermo-compressed between two hot plates during 5 min at a pressure of 1 bar and a temperature of 180 °C. The temperature was selected below the equilibrium melting temperature T_m^0 (ranging from 199 °C to 207 °C [56]) and above the nominal melting temperature T_m (ranging from 160 to 170 °C [57,58]). The samples were then quickly quenched in cold water and dried, obtaining self-standing films with thicknesses ranging between 200 and 300 μm . A single glass fiber with a diameter of 17 ± 1 μm was sandwiched between two PLA films and the assembly was then placed between two microscope cover-glasses.

2.2. Procedure for fiber pulling experiments

A homemade device was used to pull the fiber through the molten polymer at a constant linear velocity of 10 mm s^{-1} for 1 s. The shear rate at the interface between the fiber and the melt was estimated to be close to 1000 s^{-1} , according to Monasse et al. [15]. The different steps of the fiber pulling procedure were performed as follows. First, the as-prepared sandwich was transferred into a Mettler FP 82 hot stage and held at 180 °C for 5 min to erase any previous thermal and mechanical history. Then, the assembly was cooled to a given pull-out temperature T_{po} and held there for 3 min before pulling the fiber to impose flow onto the melt. From this point, two different procedures were followed: one to investigate the precursors' relaxation (protocol 1) and another one to probe the amorphous fraction present in flow-induced highly oriented structures (protocol 2). For experiments that followed protocol 1, shear rate was applied by pulling the fiber at different temperatures ($T_{po} = 157.5$ °C, 160 °C, 162.5 °C, 165 °C, 167.5 °C and 170 °C). The assembly was then held at T_{po} for a specific relaxation time — ranging from few seconds to few hours — prior to quenching to a suitable crystallization temperature ($T_c = 130$ °C). Depending on the extent of precursors' relaxation, either a spherulitic or an oriented flow-induced crystalline structures was observed as crystallization proceeded. For experiments that followed protocol 2, shear precursors were induced by fiber pulling at $T_{po} = 150$ °C. Next, the sample was immediately quenched to the same crystallization temperature of $T_c = 130$ °C to prevent any significant precursor relaxation. Then, isothermal crystallization was allowed to proceed for 90 min. Note that for protocol 2, the fiber was completely pulled out from the melt in order to allow the sample preparation that is required for subsequent thermal analysis. For more clarity, schematization of both protocols are displayed in supporting information.

2.3. Morphological observations

Morphological observations during and after isothermal crystallization were performed with a universal EPI-illuminator polarized optical microscope (POM) equipped with Nikon M Plan x2.5/x5/x10 objective lenses and connected with a digital camera system from Nikon Corporation in transmission mode.

Additional observations of the flow-induced crystalline structures were performed by scanning electronic microscopy (SEM). Flow-induced crystalline structures were isolated by

ultramicrotomy on an Ultracut UCT Leica-microsystem with a glass knife; this step allowed reaching the center of the structure by cutting along the pulling direction. The crystalline structure was then isolated by etching the sample in a water-methanol (1:2 by volume) solution containing 0.025 mol/L of sodium hydroxide at room temperature during 24 h, followed by rinsing in distilled water. Finally, the sample was coated with 10 nm of gold with a Cressington Sputter Coater prior to observations with a Dual-BEAM LEO1530-ZEISS scan electron microscope at an accelerating voltage of 5 kV.

2.4. Fast scanning calorimetric measurements

FSC analyses were performed using a power compensation twin-type chip-based fast scanning calorimeter Flash DSC 1 (Mettler Toledo) equipped with a Huber TC100 intra-cooler. Cross sections of both flow-induced crystalline structures and spherulites were obtained by ultramicrotomy. Serial sections of 500 nm thickness were obtained with an Ultracut UCT Leica-microsystem with a dry-glass knife. The samples were placed on the sensitive area of a MultiSTAR UPS 1 MEMS chip sensor. A thin layer of silicone oil was used to promote adhesion of the sample onto the chip and to improve thermal contact. Samples were continuously flushed with a 20 mL min⁻¹ flow of gaseous nitrogen to prevent condensation from environmental moisture and to ensure temperature control. Sample mass was estimated from the step change in heat flow at the glass transition: the heat capacity step ΔC_p obtained by FSC at $|\beta_c| = \beta_h = 1500 \text{ K s}^{-1}$ was compared to the value obtained by conventional DSC at $|\beta_c| = \beta_h = 0.17 \text{ K s}^{-1}$, that is to say 0.51 J/(g.K) for a completely amorphous PLA according to the literature [58].

Before FSC experiments, the shape of the samples was observed by optical microscopy on a microscope cover-glass in transmission mode. After FSC experiments, the shape of the samples adhered on the chip sensor was examined in reflection mode. The perimeter and the surface area were measured with the software ImageJ.

3. Results and discussion

3.1. Quiescent and prestressed crystallization of PLA

Flow-induced crystallization in PLA has been reported in the presence of steady [20,24] or oscillating [22,25] shear conditions during injection molding, and by pulling fibers within a polymer melt [21,31]. The latter procedure is the easiest way to produce shear flows with shear rates up to $\approx 1500 \text{ s}^{-1}$ [31]. However, to our knowledge, the lifetime of shear-induced precursors in PLA has not been previously investigated. Due to their metastability, the existence of shear-induced precursors is time and temperature dependent, as already observed for other polymers such as PP, PBu, PEO or PS [11,12]. In this work, the lifetime and relaxation behavior of PLA shear-induced precursors was investigated in the temperature range where melting of semi-crystalline PLA is typically reported [57,58] to mimic flow conditions typical of industrial processing. The relaxation temperature map in Fig. 1 depicts the relaxation time of PLA shear-induced precursors (t^*) measured at different pull-out temperatures (T_{po}) and the type of morphology that develops after cooling to the crystallization temperature (protocol 1). Longer relaxation times, i.e. above the "transition zone" in Fig. 1, lead to only spherulites because the precursors completely relax, whereas for shorter relaxation times the precursors are still present, which results in cylindrical flow-induced crystalline structures near the fiber, i.e. in the region that was subjected to the highest shear rate. At intermediate times, i.e. in the "transition zone", there is much less enhanced nucleation near the fiber surface due to partial relaxation of flow-induced precursors,

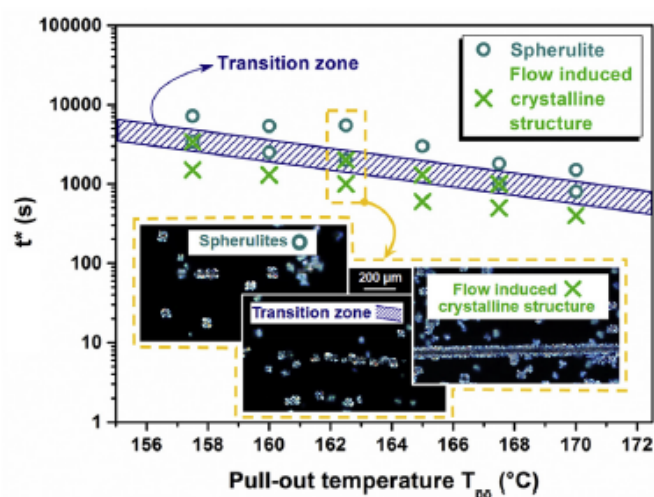


Fig. 1. Holding time (t^*), after pulling the fiber, as a function of the pull-out temperature (T_{po}). The holding time t^* is related to the relaxation of the precursors, and their lifetime is then observed after crystallization at $T_c = 130 \text{ }^\circ\text{C}$. For "longer" relaxation times (circles), the precursors relax and spherulites (SPE) are obtained. For "shorter" relaxation times, the precursors lead to flow-induced crystalline structures (crosses). For intermediate times, i.e. in the transition zone (dashed area), there is still a few flow-induced crystalline structures near the fiber surface due to some remaining precursors. The images were recorded by polarized optical microscopy at $T_{po} = 162.5 \text{ }^\circ\text{C}$.

which results in a significant reduction of oriented structures. These different behaviors are illustrated by POM images recorded at $T_{po} = 162.5 \text{ }^\circ\text{C}$. It should be noted that at higher pull-out temperature, the critical relaxation time t_c^* for precursors decay becomes shorter, in agreement with relaxation studies performed on other polymers [12,14]. Extrapolating from the relaxation temperature map of PLA precursors given in Fig. 1, a pull-out temperature $T_{po} = 150 \text{ }^\circ\text{C}$ is a judicious choice to obtain shear-induced precursors that do not significantly relax during cooling to the crystallization temperature $T_c = 130 \text{ }^\circ\text{C}$, because they would need at least a few hours to noticeably relax. This is the reason why the fiber pulling procedure to obtain the highest density of shear-induced precursors was performed at $T_{po} = 150 \text{ }^\circ\text{C}$ (protocol 2), with the purpose of examining the amorphous phase present within highly oriented structures and comparing its characteristics with the amorphous phase in conventional spherulites. The crystallization time $t_c = 90 \text{ min}$ also ensured that the cylindrical structure is not embedded within a "sea" of spherulites, facilitating its isolation to perform calorimetric experiments.

Fig. 2 shows POM and SEM pictures of semi-crystalline PLA subjected to protocol 2, in which the fiber is fully pulled out of the polymer melt. Fig. 2(A) shows that flow-induced precursors resulted in flow-induced crystalline structures, in the form of a cylindrical structure whose diameter reached approximately $100 \text{ }\mu\text{m}$ after a crystallization time $t_c = 90 \text{ min}$. The shear rate strongly decreases as the distance from the fiber increases, therefore no precursors were induced away from the pull-out region, and only spherulites were observed. Note that the diameter of the spherulites also reached approximately $100 \text{ }\mu\text{m}$. Fig. 2(B) shows the differences between flow-induced crystalline structures and spherulites through the contrast between amorphous and crystalline areas: lamellar growth in cylindrical flow-induced crystalline structures mostly occurred in the direction perpendicular to the flow [31]— that is to say that flow-induced crystalline structures are anisotropic, whereas spherulites developed radially.

The differences between flow-induced crystalline structures and spherulites, as well as their influence on the mobile amorphous

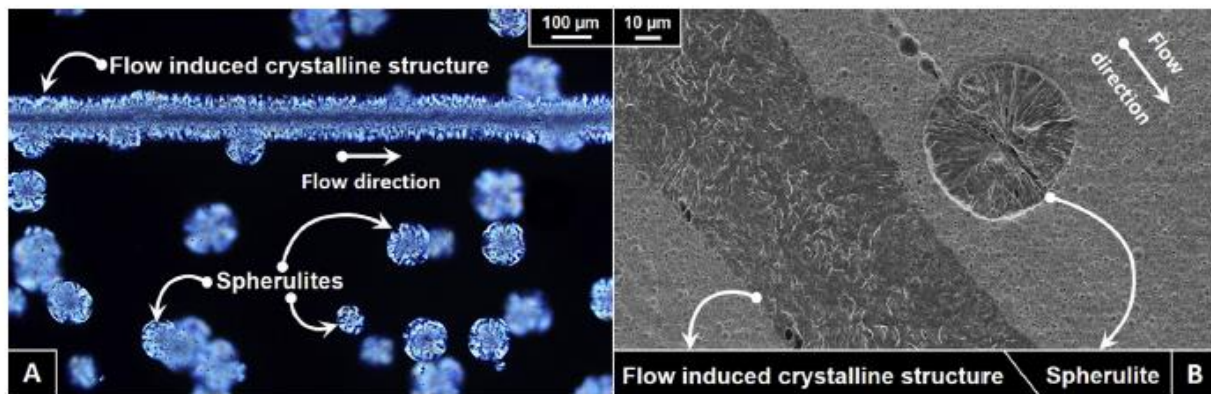


Fig. 2. Polarized optical (A) and scanning electron (B) micrographs of spherulites and flow-induced crystalline structures ($T_{po} = 150\text{ }^{\circ}\text{C}$; $t^* \lll t_c$; $T_c = 130\text{ }^{\circ}\text{C}$; $t_c = 90\text{ min}$).

fraction, were further investigated by FSC at the micro-scale, i.e. at the typical length-scale of semi-crystalline structures. Fig. 3 (A–B) shows cross sectional slices of both flow-induced crystalline structures and spherulites as obtained by ultramicrotomy prior to FSC analysis. In both slices, the semi-crystalline structure (dashed ellipse) is surrounded by an amorphous matrix. Two approaches were used to investigate the amorphous fraction. In the first approach, the whole sample (semi-crystalline structure along with surrounding amorphous matrix) was analyzed (SCA systems). In the second approach, only a portion of the semi-crystalline structure was isolated and analyzed, as indicated by the dashed polygon in Fig. 3(A–B) (SC systems). Fig. 3(C) shows a slice of flow-induced crystalline structures after FSC analysis.

Fig. 4 reports FSC heat flows normalized to the sample mass and the heating rate recorded during the first and second heating ramps from $20\text{ }^{\circ}\text{C}$ to $220\text{ }^{\circ}\text{C}$ both for a slice of flow-induced crystalline structures and spherulites. Fig. 4(A) shows the results of SCA systems, whereas Fig. 4(B) shows the results of SC systems. For all systems, the first heating ramp includes two thermal events: an endothermic step typical of the glass transition within the amorphous fraction, followed by an endothermic event related to the melting of the crystalline fraction. The second heating ramp reveals that all the systems were perfectly quenched upon cooling ($\beta_c = 1500\text{ K s}^{-1}$), as indicated by the increase in the magnitude of the heat flow step at the glass transition and the absence of the melting peak, that are typical of a fully amorphous material.

Melting occurs with a broad peak for both flow-induced

crystalline structures and spherulites, either within SCA or SC systems. When PLA is crystallized at $130\text{ }^{\circ}\text{C}$, only highly ordered α crystals are formed [26]. In addition, the use of high scanning rates (1500 K s^{-1}) prevents structural reorganization of the crystals, which means that the broadening of the melting peaks is, in this case, only due to the complexity of the investigated semi-crystalline structures. Table 1 summarizes the values of enthalpy associated to the melting peaks observed during the first heating ramps in Fig. 4, along with the physical properties measured at the glass transition. The glass transition (measured at the mid-point) of completely amorphous PLA was found to be $70.9\text{ }^{\circ}\text{C}$, with a step in heat capacity of 0.51 J/(g.K) . This value was taken as a reference to estimate the mass of the sliced sample deposited onto the chip sensor, as described in section 2.4. The mass of the sample was then used to correlate the step in heat capacity observed for the semi-crystalline systems with their respective degree of crystallinity. The glass transition temperature of the SCA systems reaches $72.7\text{ }^{\circ}\text{C}$ and $72.9\text{ }^{\circ}\text{C}$ respectively, with a step of heat capacity that drops to 0.35 J/(g.K) and 0.37 J/(g.K) for flow-induced crystalline structures and spherulites, respectively. The glass transition temperature of the SC systems reaches $74.2\text{ }^{\circ}\text{C}$ and $74.1\text{ }^{\circ}\text{C}$ respectively, with a step in heat capacity that drops to 0.32 J/(g.K) and 0.30 J/(g.K) for flow-induced crystalline structures and spherulites, respectively. Independently of the semi-crystalline morphology (flow-induced crystalline structures and spherulites), the only parameter that differs is the amount of surrounding amorphous fraction, which explains the decrease in the step of heat capacity when comparing

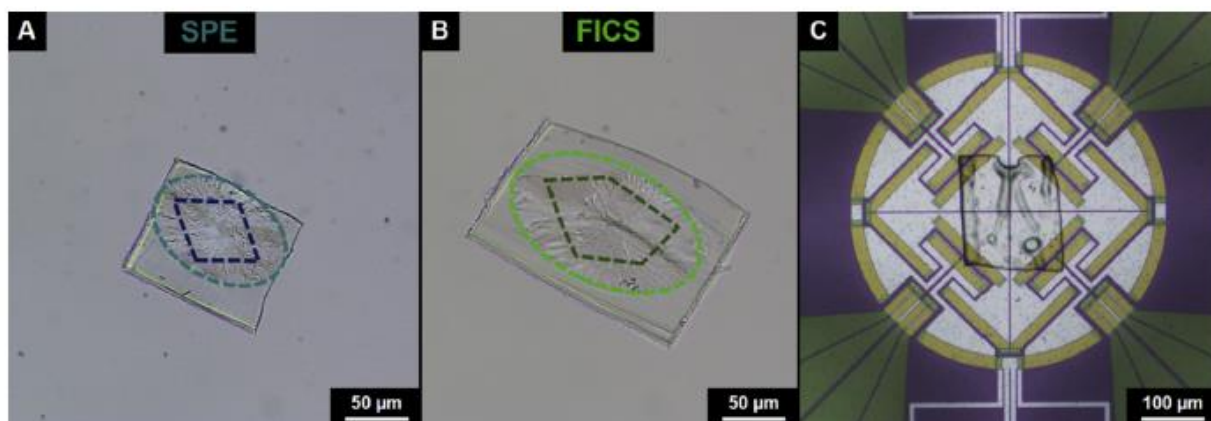


Fig. 3. Optical micrographs of slices of a spherulite (SPE) (A) and a flow-induced crystalline structure (B) obtained by ultramicrotomy prior to FSC analysis, as well as an example of a flow-induced crystalline structure slice placed on the FSC chip sensor after analysis (C). First, the sample within the ellipse plus the surrounding amorphous fraction were analyzed (SCA system), then a fresh slice was used to further isolate the dashed polygon within the semi-crystalline structures (SC system). The slices were 500 nm thick.

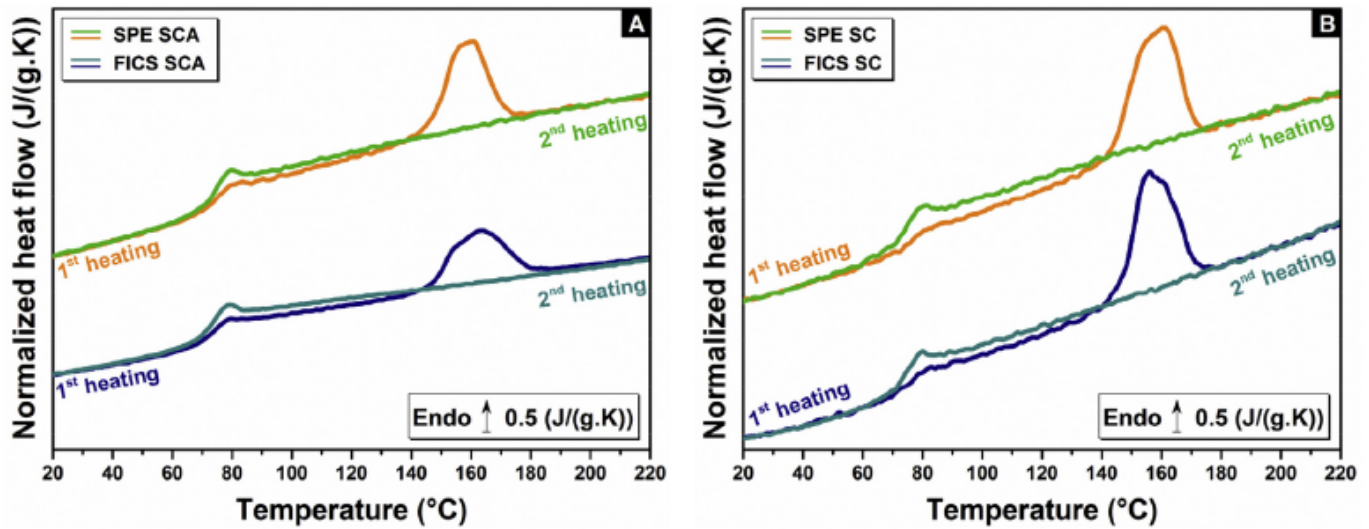


Fig. 4. FSC normalized heat flows of the first and second heating ramp from 20 °C to 220 °C for spherulites (SPE) and flow-induced crystalline structures: (A) SCA vs. (B) SC systems. SPE = spherulite, FICS = flow-induced crystalline structure, SCA = semi-crystalline structure and the surrounding amorphous phase, SC = semi-crystalline structure.

Table 1

Thermal and microstructural properties measured while heating completely amorphous, flow-induced crystalline structures (FICS) and spherulites (SPE), both for SCA and SC systems: glass transition temperature T_{gmid} , heat capacity step ΔC_p , enthalpy of melting ΔH_m , mobile amorphous fraction X_{MAF} , crystalline fraction X_c , and rigid amorphous fraction X_{RAF} .

	T_{gmid} (°C ± 1)	ΔC_p (J/(g.K) ± 0.05)	ΔH_m (J/g ± 3)	X_{MAF} (% ± 5)	X_c (% ± 5)	X_{RAF} (% ± 10)
Amorphous	71	0.51	0	100	0	0
SPE SCA	73	0.35	24	69	18	13
FICS SCA	73	0.37	18	73	13	14
SPE SC	74	0.32	37	63	27	10
FICS SC	74	0.30	33	59	24	17

SCA and SC systems. In addition, the increase of the mid-point glass transition temperature of the SCA and SC systems with respect to completely amorphous PLA (2 °C and 3 °C respectively) is due to the steric hindrances generated by the presence of the crystalline fraction. This is why intra-spherulitic amorphous phase is called constrained MAF. The glass transition of SCA systems is halfway between the glass transition temperature of the amorphous and SC systems due to the presence of both inter-spherulitic and intra-spherulitic regions. From the enthalpy of melting reported in Table 1, the crystalline fraction X_c was determined according to the following equation:

$$X_c = \frac{\Delta H_m}{\Delta H_m^0} \quad (1)$$

in which ΔH_m is the enthalpy of melting and ΔH_m^0 is the enthalpy of melting of a 100% crystallized PLA (136 J/g) which was obtained using the recent formula proposed by Righetti et al. [59]. From the crystalline fraction X_c and the step of heat capacity at the glass transition ΔC_p , the mobile amorphous fraction X_{MAF} and the rigid amorphous fraction X_{RAF} were estimated according to the following equations:

$$X_{\text{MAF}} = \frac{\Delta C_p}{\Delta C_p^0} \quad (2)$$

$$1 = X_{\text{MAF}} + X_{\text{RAF}} + X_c \quad (3)$$

in which $\Delta C_p^0 = 0.51 \text{ J/(g.K)}$ [58] is the heat capacity step of completely amorphous PLA. The values are summarized in Table 1. By comparing flow-induced crystalline structures or spherulites from SCA on one side or SC systems on the other side, it is interesting to observe that flow-induced crystalline structures or spherulites approaches have no influence on the apportionment of microstructural fractions. Nevertheless, SCA systems develop $X_{\text{MAF}} \approx 70\%$ and $X_c \approx 15\%$, whereas SC systems rather develop $X_{\text{MAF}} \approx 60\%$ and $X_c \approx 25\%$, on average. Therefore, independently of the approach used to investigate the microstructure, an average value of $X_{\text{RAF}} \approx 15\%$ was found. Apparently, the structural anisotropy induced in the liquid like-state plays no role on the apportionment of the different fractions. As observed by Righetti et al. [43,50], the establishment of the RAF depends on the crystallization temperature, i.e. on the molecular mobility of the polymer chains. These results show that the shear conditions imposed prior to crystallization only affected the crystallization kinetics and the morphology of the final crystalline structure, with no influence on the amount of the RAF (which appears to be influenced only by the temperature conditions).

3.2. Cooperative motions in amorphous and crystallized PLA at the glass transition

Prior to FSC analysis, a visual estimation of the main microstructural areas developed in SCA systems was performed by optical microscopy. The ratio of amorphous to semi-crystalline surface areas was evaluated for both morphologies (flow-induced crystalline structures and spherulites) from the POM images shown in Fig. 3 (A–B). Table 2 reports the fraction of surrounding amorphous matrix, namely unconstrained MAF, for flow-induced crystalline structures and spherulites samples (35% and 50% respectively). However, MAF (X_{MAF}) measured by FSC, reach 69% and 73% for flow-induced crystalline structures and spherulites, respectively. Thus, from POM observations and FSC analysis, a discrepancy of 34% and 23% in the amorphous fractions was evidenced between flow-induced crystalline structures and spherulites. This discrepancy is related to the fraction of constrained MAF (X_{CMAF}) within flow-induced crystalline structures and spherulites, as reported in

Table 2

Visual estimation of amorphous and semi-crystalline sample areas on the slices of spherulites (SPE) and flow-induced crystalline structures (FICS) in Fig. 3 (A–B). Prior to thermal analysis, the total sample area A_{tot} , the semi-crystalline sample area A_{sc} as well as the ratio of amorphous (A matrix) to semi-crystalline (SC structure) sample areas of the slice have been estimated by picture analysis. They highlight the unconstrained (X_{UCMAF}) and the constrained (X_{CMAF}) fractions representing the mobile amorphous fraction (X_{MAF}).

	A_{tot} (μm^2)	A_{sc} (μm^2)	A matrix (%)	SC structure (%)	$X_{MAF} = X_{CMAF} + X_{UCMAF}$ (% \pm 5)
SPE	10500 \pm 300	6800 \pm 100	35 \pm 5	65 \pm 5	69 = 34 + 35
FICS	21400 \pm 700	10800 \pm 200	50 \pm 5	50 \pm 5	73 = 23 + 50

Table 2. In the few past years, the existence of a so-called intra-spherulitic MAF has been shown for semi-crystalline polyesters such as PET and PLA [52,54,55,57,71], which behaves like a constrained MAF. Wang et al. [52] showed that semi-crystalline PLA with different crystallinity degrees has different glass transition dynamics after structural relaxation. In particular, the process occurring at lower temperature was attributed to the bulk-like glass transition, whereas the process occurring at higher temperature was attributed to the glass transition of constrained MAF, i.e. the amorphous fractions whose motions were hindered by the lamellar stacks. Later on, Delpouve et al. [54] investigated the relaxation dynamics of inter- and intra-spherulitic amorphous phases through the concept of CRR according to the thermodynamic approach proposed by Donth. The characteristic value of the cooperativity length at the glass transition (3.0 nm for a completely amorphous PLA) was found to decrease to 2.0 nm when the maximum degree of crystallinity was reached. For intermediate degrees of crystallinity, the cooperativity length associated to the dynamics of both amorphous fractions was observed to decrease linearly from 3.0 nm to 2.0 nm. It turned out that cooperativity could be correlated to the structural relaxation of the considered fractions [53]. By tracking the temperature evolution of the peaks associated to the enthalpy recovery in amorphous, partially crystallized and fully crystallized systems, they discussed the molecular dynamics of both inter- and intra-spherulitic amorphous phases, and found it in agreement with the results previously published by Wang et al. [52]. In particular for partially crystallized systems depicting double peaks, the enthalpy recovery of the inter-spherulitic amorphous fraction was found to be similar to the one observed for a completely amorphous sample, whereas the enthalpy recovery of the intra-spherulitic amorphous fraction was found to depend on degree of crystallinity. A system that is partially crystallized would show an enthalpy recovery peak related to intra-spherulitic amorphous fraction whose maximum appears at lower temperatures with respect to the same system crystallized to the maximum extent. The temperature shift was attributed to the differences induced by the crystallization process, that is to say secondary crystallization and the development of RAF [43]. In literature it has been shown that a decrease in cooperativity can be associated to a decrease in the thickness of the amorphous fraction confined within the crystal [60], as well as to isochoric [61] and multilayer [62] confinement. Thus, the molecular dynamics of the constrained MAF depends on the lamellar thickness.

In addition to the aforementioned glass transition properties, the glass transition process was also evaluated in terms of CRR. From modulated temperature DSC, the cooperativity volume $\xi_{T\alpha}^3$ at the dynamic glass transition temperature T_α is extracted from the following equation:

$$\xi_{T\alpha}^3 = \frac{(1/C_p)_{Glass} - (1/C_p)_{Liquid}}{\rho(\delta T)^2} k_B T_\alpha^2 \quad (4)$$

with k_B the Boltzmann constant, δT the average temperature fluctuation related to the dynamic glass transition of a CRR, ρ the

density of the relaxing system, and C_p the heat capacity at constant pressure. From DSC, or in this work FSC, the dynamic glass transition temperature T_α corresponds to the glass transition temperature T_g , whereas the average temperature fluctuation δT is estimated upon heating from the following equation [63]:

$$\delta T = \Delta T / 2.5 \quad (5)$$

with ΔT the temperature interval where the C_p curve from FSC varies between 16% and 84% of the heat capacity step ΔC_p . This rule has been checked for several substances in literature [63]. The different experimental parameters necessary to estimate the cooperativity volume $\xi_{T\alpha}^3$ are summarized in Table 3. In order to assess the molecular dynamics of constrained MAF, only SC systems were investigated. Such an approach cannot be used in the case of SCA systems because an average glass transition would be measured including both constrained MAF and the surrounding amorphous matrix (unconstrained MAF). With the values of glass transition temperature and heat capacity step reported above, similar values of mean fluctuation temperature, cooperativity length and volume were obtained for both flow-induced crystalline structures and spherulites. However, the mean fluctuation temperature at the glass transition for constrained MAF in flow-induced crystalline structures and spherulites is higher compared to the value obtained for completely amorphous PLA (5.4 K vs. 3.8 K). As a consequence, the cooperativity length and volume of the amorphous chains trapped within semi-crystalline structures is reduced to 1.9 nm and 7 nm³ respectively, as compared to the values of 2.6 nm and 18 nm³ that are classically observed for completely amorphous PLA [53,58]. These results are consistent with the reduction of mobility induced by the presence of lamellar stacks already reported by Wang et al. [52] and Delpouve et al. [54]. Independently of the SC system, CRR are 30% smaller with respect to completely amorphous PLA. This result suggests that constrained MAF behaves the same independently of the type of semi-crystalline morphology. Once again, the molecular dynamics of constrained MAF seems to be driven by the crystallization temperature, and therefore the competition between crystallization and vitrification, rather than by the crystalline morphology. However, another parameter should be taken into account: the degree of connection of the crystalline fraction to the surrounding amorphous fraction, i.e. the decoupling of fractions and the development of the RAF.

Table 3

Parameters obtained by FSC and used to calculate the size of the Cooperative Rearranging Regions (CRR) for completely amorphous and semi-crystalline PLA, in the case of SC systems only, for both spherulite (SPE) and flow-induced crystalline structures (FICS): mean temperature fluctuation δT , cooperativity length $\xi_{T\alpha}$ and cooperativity volume $\xi_{T\alpha}^3$.

	δT (K)	$\xi_{T\alpha}$ (nm)	$\xi_{T\alpha}^3$ (nm ³)
Amorphous	3.8 \pm 0.3	2.6 \pm 0.3	18 \pm 2
SPE SC	5.4 \pm 0.5	1.9 \pm 0.2	7 \pm 1
FICS SC	5.3 \pm 0.5	1.9 \pm 0.2	7 \pm 1

3.3. Local motions in amorphous and crystallized PLA below the glass transition

The molecular mobility of the amorphous fractions through the well-known phenomenon of structural relaxation and physical aging was then investigated. Using physical aging to reveal differences in molecular dynamics by thermal analysis is a common procedure [52,54]. In addition, the high scanning rates attainable by FSC allow accelerating the kinetics of physical aging, because glassy states with higher level of enthalpy can be formed. FSC allowed performing physical aging on a wider range of time (from milliseconds to days), reaching thermodynamic equilibrium [40].

Fig. 5 shows FSC normalized heat flows for aged PLA. Fig. 5(A) focuses on completely amorphous PLA. As aging progresses, a sequence of endothermic peaks is classically observed indicating the structural relaxation process superimposed to the glass transition. Besides, the endothermic peaks increase and shift towards high temperature as the aging time increases. Physical aging of SCA systems is more complex, as shown in Fig. 5 (B–C). The peaks of enthalpy recovery for both flow-induced crystalline structures and spherulites are clearly divided into two contributions that become more and more visible as aging time increases, indicating that a different behavior is observed for a crystalline environment. A similar behavior has already been reported in the literature for PLA as previously detailed above [53,55], explained by the existence of two amorphous fractions having their own response to structural relaxation due to their respective environment. It has also been suggested that the high-temperature contribution could be related to the enthalpy recovery of constrained MAF, whereas the low-temperature contribution would be associated to the relaxation of unconstrained MAF, i.e. the surrounding amorphous matrix.

When the SC systems are considered, only one endothermic peak for both flow-induced crystalline structures and spherulites is observed. In comparison with amorphous PLA, the enthalpy recovery peaks are broadened and shifted towards higher temperatures within a larger range of temperatures, as shown in Fig. 5 (D–E). This result could be due to the strong influence of the semi-crystalline environment on the molecular dynamics of the confined amorphous fraction, suggesting a stronger degree of confinement induced by tighter inter-lamellar stacks [53].

First of all, Fig. 6(A) shows the Gaussian fitting procedure used to track the maximum T_p of the enthalpy recovery peak for all the contributions observed in Fig. 5. The Gaussian fit was performed on the normalized heat flow subtraction (aged - rejuvenated), as shown through the example of flow-induced crystalline structures SCA aged 1 min. Fig. 6(B) reports the temperature evolution of the maximum of the enthalpy recovery peak as a function of aging time. Regarding the SCA systems, the first contribution of both flow-induced crystalline structures and spherulites behaves as unconstrained MAF in that a linear increase is observed until a plateau is reached at about 84 °C after the same aging duration. This means that the first contribution recorded for both flow-induced crystalline structures and spherulites is actually related to the surrounding amorphous matrix. As for the second contribution, SCA and SC systems show no differences: the trend is the same independently of the type of semi-crystalline morphology, and is shifted to higher temperatures as compared to the amorphous matrix. Thus, in both systems, the second contribution seems to be related to the amorphous fraction constrained within the lamellar stacks, with the same molecular dynamics.

Then, as graphically illustrated in Fig. 6(A) by the orange hatched area, the enthalpy recovery of a glass aged at a temperature T_{ag} during a time t_{ag} is calculated by integrating the difference between the scans of the aged and rejuvenated sample, according to the following equation:

$$\Delta H(T_{ag}, t_{ag}) = \int_{T_1}^{T_2} [C_p^a(T) - C_p^r(T)] dT \quad (6)$$

in which $C_p^a(T)$ and $C_p^r(T)$ are the specific heat of the aged and rejuvenated samples respectively, and T_1 and T_2 are arbitrary temperatures below and above the glass transition temperature T_g [64]. The so-called enthalpy recovery represents the energy required by the glass to reach its thermodynamic equilibrium. Under the assumption that equilibrium is reached for an infinite time, the expected total enthalpy loss ΔH_∞ extrapolated from the equilibrium melt depends on the aging temperature T_{ag} , as well as on the glass transition temperature T_g and the heat capacity step ΔC_p of the sample, according to the following relation:

$$\Delta H_\infty = \Delta C_p \cdot (T_g - T_{ag}) \quad (7)$$

Fig. 7(A) shows the evolution of the difference between the enthalpy recovery ΔH_{tag} and the total enthalpy loss ΔH_∞ as a function of aging time t_{ag} for a completely amorphous PLA, as well as for the semi-crystalline samples (both flow-induced crystalline structures and spherulites morphologies, as well as SCA and SC systems). When the crystallinity degree increases, the amorphous response decreases (Table 1). Therefore the enthalpy recovery and the total enthalpy loss values are smaller for the semi-crystalline systems with respect to the completely amorphous sample due to the decrease of MAF. To compare the kinetics and the dynamics, the structural relaxation function ϕ has been plotted as a function of the aging time. The structural relaxation function ϕ is defined as:

$$\phi(t_{ag}) = \frac{\Delta H_{tag} - \Delta H_\infty}{\Delta H_\infty}$$

in which ΔH_{tag} and ΔH_∞ are the enthalpy recovery after an aging time t_{ag} and the total enthalpy loss after an infinite aging time, respectively. This function allows normalizing the enthalpy recovery to the same amount of MAF. Fig. 7(B) shows that the evolution of enthalpy recovery is the same independently of the environment of the MAF (both type of morphology and degree of crystallinity). Besides, the whole structural relaxation process has been accelerated by the high scanning rates available in FSC [40]: all the samples reached the thermodynamic equilibrium after the same aging duration. It is worth mentioning that all systems superimpose, and depict the same physical aging kinetics. Therefore, the structural relaxation of the amorphous fraction depends neither on the microstructure, on the coupling between fractions, on the confinement by the crystals nor on the orientation of the macromolecules prior to crystallization.

Physical aging is performed at a given temperature below the glass transition. During sub- T_g structural relaxation far from the glass transition, only local molecular motions, such as the rotation of sub-segmental flexible groups along the polymer backbone take place [65]. For example, Priestley et al. [66] have shown by dielectric studies a significant decrease in the strength of the β relaxation dynamics when silica nanospheres are dispersed in a poly (methyl methacrylate) (PMMA) matrix. Such a decrease has been attributed to the hydrogen bonds between the flexible ester side-groups on PMMA and the hydroxyl groups on silica. Due to presence of silica, the hydrogen bonds inhibit the motions of the ester side-groups. Therefore, by assuming that the motions of the side-groups are the driving forces for PMMA structural relaxation, the reduction of physical aging rates far below T_g ($T_g - 88$ °C) in silica-PMMA nanocomposites have been explained and associated to a reduction of the β process. More recently, Cangialosi et al. [67]

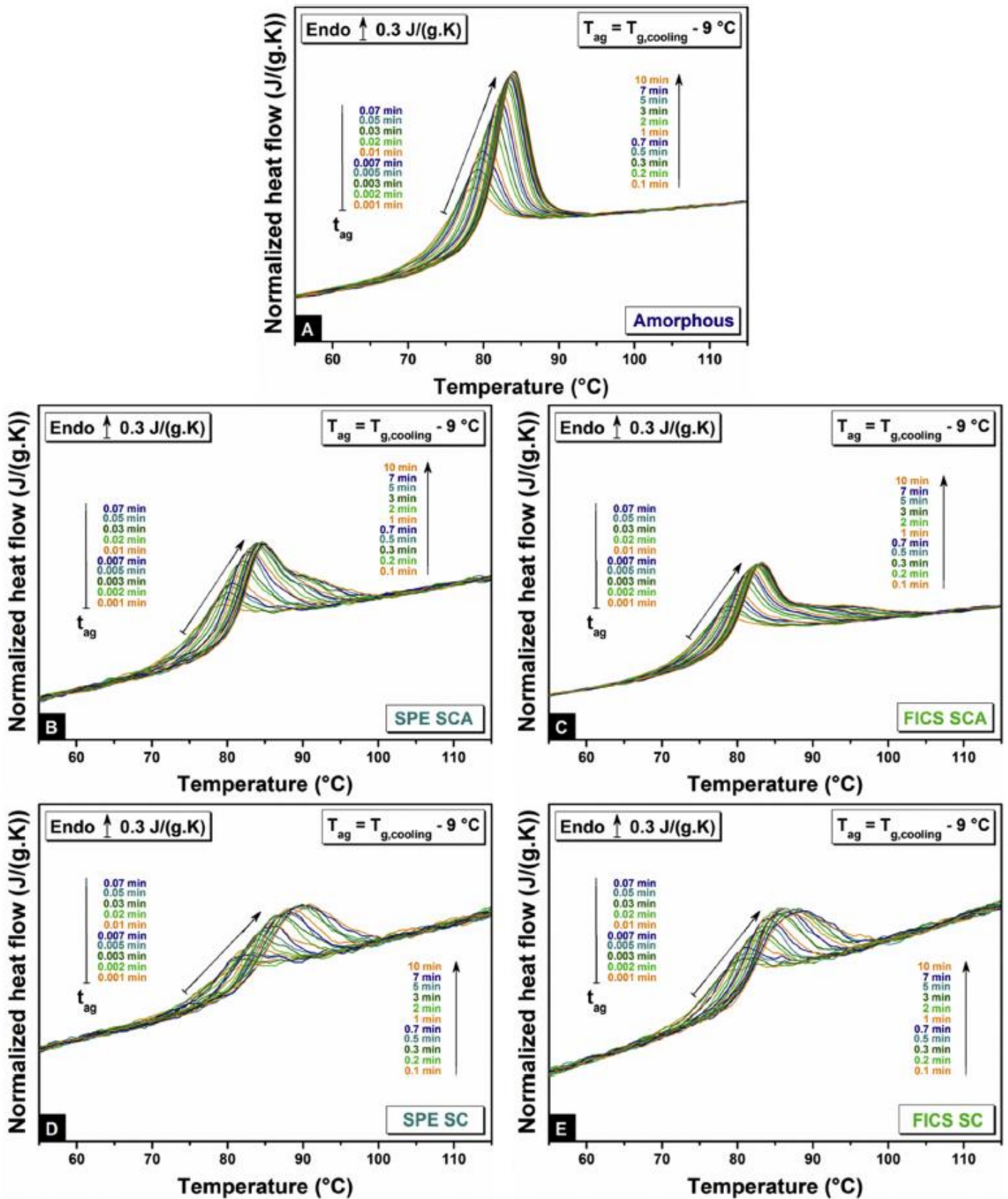


Fig. 5. Normalized heat flows recorded after physical aging of completely amorphous PLA (A), SPE SCA (B), FICS SCA (C), SPE SC (D) and FICS SC (E). Aging was performed *in situ* by PSC at a scanning rate of $|\beta_c| = \beta_h = 1500 \text{ K s}^{-1}$ at $T_{ag} = T_{g,cooling} - 9 \text{ } ^\circ\text{C} = 58 \text{ } ^\circ\text{C}$ for aging times ranging from 0.001 min to 10 min. Glass transition temperature measured upon cooling are displayed in supporting information. SPE = spherulite, FICS = flow-induced crystalline structure, SCA = semi-crystalline structure and the surrounding amorphous phase, SC = semi-crystalline structure.

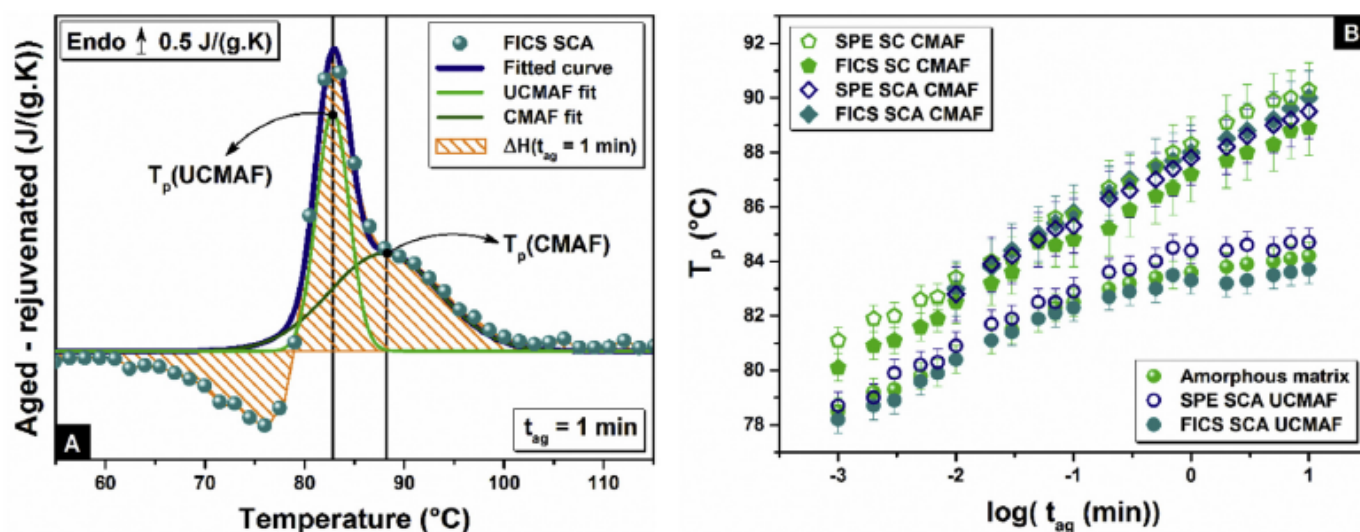


Fig. 6. (A) Normalized heat flow subtraction (aged – rejuvenated) of FICS SCA aged 1 min 9 °C below $T_{g,cooling}$. The curve illustrates how the enthalpy recovery ΔH_{ag} was calculated, as well as the fitting procedure for the maximum T_p of the enthalpy recovery peak. (B) Evolution of the maximum T_p of the enthalpy recovery peak as a function of the aging time. Spheres: completely amorphous PLA. Discs: unconstrained mobile amorphous fraction (UCMAF) within the SCA systems (FICS: filled discs, SPE: empty discs). Diamonds: constrained mobile amorphous fraction (CMAF) within the SCA systems (SPE: empty diamonds, FICS: filled diamonds). Pentagons: constrained mobile amorphous fraction (CMAF) within the SC systems (SPE: empty pentagons, FICS: filled pentagons). SPE = spherulite, FICS = flow-induced crystalline structure, SCA = semi-crystalline structure and the surrounding amorphous phase, SC = semi-crystalline structure.

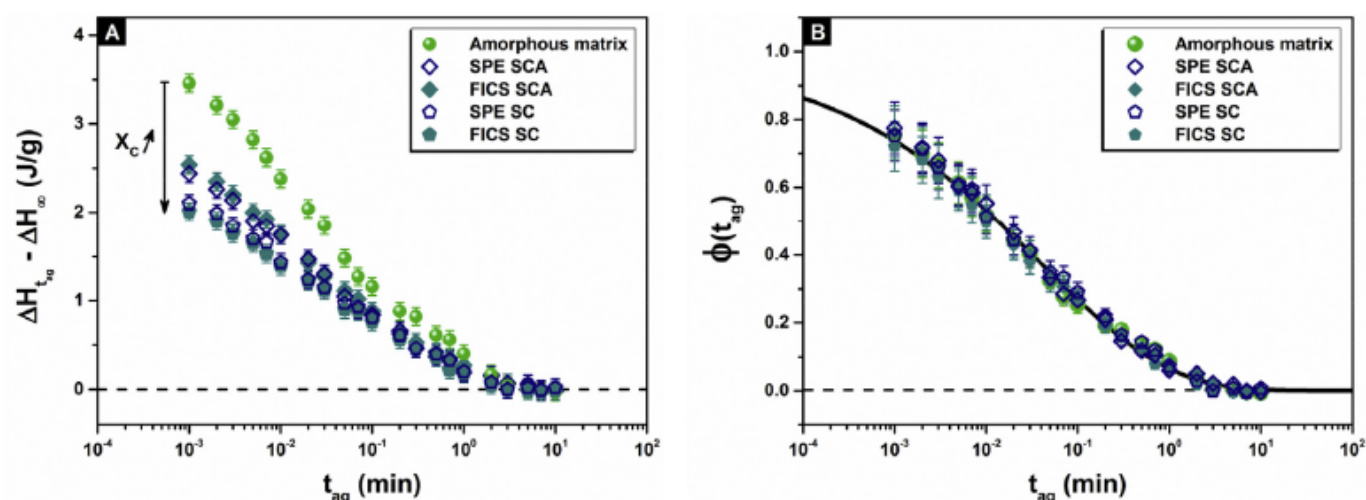


Fig. 7. Time evolution of the difference between the enthalpy recovery ΔH_{ag} and the total enthalpy loss ΔH_{∞} (A), and of the structural relaxation function ϕ (B). Spheres: completely amorphous PLA. Diamonds: SCA systems. Pentagons: SC systems. Empty symbols: SPE. Filled symbols: FICS. SCA = semi-crystalline structure and the surrounding amorphous phase, SC = semi-crystalline structure, SPE = spherulite, FICS = flow-induced crystalline structure. Black line is a guide for eyes.

observed two equilibration mechanisms during physical aging of polystyrene and polycarbonate. They reported either a single or a double decay in the enthalpy recovery, when physical aging is performed close to or far below the glass transition, respectively. The first (faster) decay has been assigned to secondary relaxations, whereas the second (slower) decay has been attributed to the α process. At the same time, Grenet et al. [68] reported experimental results that were collected on glassy Selenium both after short-term and long-term aging, which support the idea that at least two separate mechanisms of relaxation coexist in physical aging, one with very fast kinetics and the other with much slower kinetics. Therefore, according to the aging temperature (close or far to the glass transition) local motions and/or cooperative motions might be involved in the physical aging process.

In this work, differences in the structural relaxation were

observed by heating the samples through the glass transition, i.e. by measuring the results of cooperative motions during equilibrium recovery. Thus, the influence of the crystalline environment was observed on the macromolecular scale. However, no influence was highlighted during the structural relaxation, because only a single decay with the same kinetics for all systems was observed. Therefore, physical aging is assumed to be mainly driven by local motions in these aging conditions ($T_{ag} = T_{g,cooling} - 9^\circ C$). Besides, this result suggests that contrarily to α relaxation, secondary relaxations are not influenced by the crystalline environment. It is worth mentioning that Schick et al. [70] observed just a slight influence of the crystals on the local movements of MAF in the case of semi-crystalline PET by dielectric measurements. Later on, Kattan et al. showed no-dependency of the β relaxations with the degree of crystallinity on various amorphous and semi-crystalline polyesters,

by thermally stimulated depolarization current experiments [71].

To summarize, similar values of the enthalpy recovery normalized to the MAF were obtained for all the systems; however, the shape of the enthalpy recovery peaks was not the same. Amorphous PLA has a cooperativity length of 2.6 nm and sharper enthalpy recovery peaks because the relatively large cooperativity domains ease the recovery to the equilibrium upon heating. Consistently, SC PLA (both flow-induced crystalline structures and spherulites) have a reduced cooperativity length (1.9 nm) and broader enthalpy recovery peaks because the relatively small cooperativity domains delay the recovery to the equilibrium upon heating. To assess the nature of the molecular dynamics involved in the structural relaxation, between local or cooperative motions, further physical aging investigations with different aging temperatures (more or less close to the glass transition) should be performed.

4. Conclusion

The relaxation of shear-induced precursors was investigated at high temperature to mimic the industrial injection process of PLA. At 150 °C, the critical relaxation time is much larger than the time required to quench the sample to a suitable crystallization temperature, resulting in the formation of highly oriented cylindrical structures which are embedded in an amorphous PLA matrix. This observation allowed investigating the influence of the crystalline environment generated either by flow-induced crystallization or quiescent crystallization on the amorphous phase after a thermal treatment performed in optimized conditions. Slices of the semi-crystalline samples were analyzed by FSC to investigate the behavior of the amorphous phase at the same scale of the semi-crystalline structure. Thanks to the high scanning rates accessible via FSC, physical aging was accelerated, which allowed scanning up to four decades of aging time. Segmental and local relaxations were investigated through the concept of cooperativity and physical aging, respectively. A decrease of the cooperativity length in the semi-crystalline systems was observed in comparison to completely amorphous PLA, essentially due to the coupling between phases and the confinement effect of the crystals. The molecular dynamics were observed to be the same independently of the semi-crystalline morphology. The molecular dynamics were found to depend on the crystallinity degree at the macromolecular scale. However, the same enthalpy recovery was measured for all the systems, meaning that the structural relaxation is not influenced by the crystallinity degree. This result is consistent with the fact that physical aging is mainly due to local motions, and local motions are not affected by the crystalline environment (different length-scale) at this aging temperature close to the glass transition. The only influence that could be observed is the one measured during the subsequent heating ramp through the α relaxation, i.e. the glass transition. Further physical aging investigations with different aging temperatures should be performed to assess the nature of the molecular dynamics involved during the physical aging.

Acknowledgments

The authors are grateful to the Normandy Region, France, for the financial support for PhD thesis and FSC equipment.

Appendix A. Supplementary data

Supplementary data related to this article can be found at <http://dx.doi.org/10.1016/j.polymer.2017.08.021>.

References

- [1] S.Z.D. Cheng, B. Lotz, Enthalpic and entropic origins of nucleation barriers during polymer crystallization: the Hoffman–Lauritzen theory and beyond, *Polymer* 46 (2005) 8662–8681, <http://dx.doi.org/10.1016/j.polymer.2005.03.125>.
- [2] X.F. Lu, J.N. Hay, Isothermal crystallization kinetics and melting behaviour of poly(ethylene terephthalate), *Polymer* 42 (2001) 9423–9431, [http://dx.doi.org/10.1016/S0032-3861\(01\)00502-X](http://dx.doi.org/10.1016/S0032-3861(01)00502-X).
- [3] H. Li, M.A. Huneault, Effect of nucleation and plasticization on the crystallization of poly(lactic acid), *Polymer* 48 (2007) 6855–6866, <http://dx.doi.org/10.1016/j.polymer.2007.09.020>.
- [4] H. Bai, C. Huang, H. Xiu, Q. Zhang, Q. Fu, Enhancing mechanical performance of polylactide by tailoring crystal morphology and lamellar orientation with the aid of nucleating agent, *Polymer* 55 (2014) 6924–6934, <http://dx.doi.org/10.1016/j.polymer.2014.10.059>.
- [5] B.O. Reid, M. Vadlamudi, A. Mamun, H. Janani, H. Gao, W. Hu, R.G. Alamo, Strong memory effect of crystallization above the equilibrium melting point of random copolymers, *Macromolecules* 46 (2013) 6485–6497, <http://dx.doi.org/10.1021/ma400839d>.
- [6] D. Cavallo, L. Gardella, G. Portale, A.J. Müller, G.C. Alfonso, On cross- and self-nucleation in seeded crystallization of isotactic poly(1-butene), *Polymer* 54 (2013) 4637–4644, <http://dx.doi.org/10.1016/j.polymer.2013.06.051>.
- [7] D. Cavallo, L. Gardella, G. Portale, A.J. Müller, G.C. Alfonso, Kinetics of cross-nucleation in isotactic poly(1-butene), *Macromolecules* 47 (2014) 870–873, <http://dx.doi.org/10.1021/ma402396f>.
- [8] Z. Wang, Z. Ma, L. Li, Flow-induced crystallization of polymers: molecular and thermodynamic considerations, *Macromolecules* 49 (2016) 1505–1517, <http://dx.doi.org/10.1021/acs.macromol.5b02688>.
- [9] F. Azzurri, G.C. Alfonso, Lifetime of shear-induced crystal nucleation precursors, *Macromolecules* 38 (2005) 1723–1728, <http://dx.doi.org/10.1021/ma0485989>.
- [10] R.H. Somani, L. Yang, L. Zhu, B.S. Hsiao, Flow-induced shish-kebab precursor structures in entangled polymer melts, *Polymer* 46 (2005) 8587–8623, <http://dx.doi.org/10.1016/j.polymer.2005.06.034>.
- [11] F. Azzurri, G.C. Alfonso, Insights into formation and relaxation of shear-induced nucleation precursors in isotactic polystyrene, *Macromolecules* 41 (2008) 1377–1383, <http://dx.doi.org/10.1021/ma071475e>.
- [12] Y. Hayashi, G. Matsuba, Y. Zhao, K. Nishida, T. Kanaya, Precursor of shish-kebab in isotactic polystyrene under shear flow, *Polymer* 50 (2009) 2095–2103, <http://dx.doi.org/10.1016/j.polymer.2009.03.008>.
- [13] S. Kimata, T. Sakurai, Y. Nozue, T. Kasahara, N. Yamaguchi, T. Karino, M. Shibayama, J.A. Kornfield, Molecular basis of the shish-kebab morphology in polymer crystallization, *Science* 316 (2007) 1014–1017, <http://dx.doi.org/10.1126/science.1140132>.
- [14] Real-time depth sectioning: isolating the effect of stress on structure development in pressure-driven flow, *J. Rheol.* 53 (2009) 1229–1254, <http://dx.doi.org/10.1122/1.3116497>.
- [15] B. Monasse, Polypropylene nucleation on a glass fibre after melt shearing, *J. Mater. Sci.* 27 (1992) 6047–6052, <http://dx.doi.org/10.1007/BF01133748>.
- [16] J. Ju, Z. Wang, F. Su, Y. Ji, H. Yang, J. Chang, S. Ali, X. Li, L. Li, Extensional flow-induced dynamic phase transitions in isotactic polypropylene, *Macromol. Rapid Commun.* 37 (2016) 1441–1445, <http://dx.doi.org/10.1002/marc.201600185>.
- [17] P.C. Roozmond, T.B. van Erp, G.W.M. Peters, Flow-induced crystallization of isotactic polypropylene: modeling formation of multiple crystal phases and morphologies, *Polymer* 89 (2016) 69–80, <http://dx.doi.org/10.1016/j.polymer.2016.01.032>.
- [18] F.G. Hamad, R.H. Colby, S.T. Milner, Transition in crystal morphology for flow-induced crystallization of isotactic polypropylene, *Macromolecules* 49 (2016) 5561–5575, <http://dx.doi.org/10.1021/acs.macromol.6b00303>.
- [19] F. Langouche, Orientation development during shear flow-induced crystallization of i-PP, *Macromolecules* 39 (2006) 2568–2573, <http://dx.doi.org/10.1021/ma0525684>.
- [20] S. Huang, H. Li, S. Jiang, X. Chen, L. An, Crystal structure and morphology influenced by shear effect of poly(l-lactide) and its melting behavior revealed by WAXD, DSC and in-situ POM, *Polymer* 52 (2011) 3478–3487, <http://dx.doi.org/10.1016/j.polymer.2011.05.044>.
- [21] H. Xu, L. Xie, M. Hakkarainen, Beyond a model of polymer processing-triggered shear: reconciling shish-kebab formation and control of chain degradation in sheared poly(l-lactide), *ACS Sustain. Chem. Eng.* 3 (2015) 1443–1452, <http://dx.doi.org/10.1021/acssuschemeng.5b00320>.
- [22] H. Xu, G.-J. Zhong, Q. Fu, J. Lei, W. Jiang, B.S. Hsiao, Z.-M. Li, formation of shish-kebabs in injection-molded poly(l-lactide) by application of an intense flow field, *ACS Appl. Mater. Interfaces* 4 (2012) 6774–6784, <http://dx.doi.org/10.1021/am3019756>.
- [23] Y. Zhong, H. Fang, Y. Zhang, Z. Wang, J. Yang, Z. Wang, Rheologically determined critical shear rates for shear-induced nucleation rate enhancements of poly(lactide acid), *ACS Sustain. Chem. Eng.* 1 (2013) 663–672, <http://dx.doi.org/10.1021/sc400040b>.
- [24] J. Bojda, E. Piorkowska, Shear-induced nonisothermal crystallization of two grades of PLA, *Polym. Test.* 50 (2016) 172–181, <http://dx.doi.org/10.1016/j.polymertesting.2016.01.006>.
- [25] N. Najafi, M.-C. Heuzey, P. Carreau, D. Theriault, Quiescent and shear-induced

- crystallization of linear and branched polylactides, *Rheol. Acta* 54 (2015) 831–845, <http://dx.doi.org/10.1007/s00397-015-0874-7>.
- [26] K. Wasanasuk, K. Tashiro, Crystal structure and disorder in Poly(l-lactic acid) δ form (α' form) and the phase transition mechanism to the ordered α form, *Polymer* 52 (2011) 6097–6109, <http://dx.doi.org/10.1016/j.polymer.2011.10.046>.
- [27] T.-Y. Cho, G. Strobl, Temperature dependent variations in the lamellar structure of poly(l-lactide), *Polymer* 47 (2006) 1036–1043, <http://dx.doi.org/10.1016/j.polymer.2005.12.027>.
- [28] H. Bai, C. Huang, H. Xiu, Q. Zhang, H. Deng, K. Wang, F. Chen, Q. Fu, Significantly improving oxygen barrier properties of polylactide via constructing parallel-aligned shish-kebab-like crystals with well-interlocked boundaries, *Biomacromolecules* 15 (2014) 1507–1514, <http://dx.doi.org/10.1021/bm500167u>.
- [29] H. Xu, L. Xie, X. Jiang, X.-J. Li, Y. Li, Z.-J. Zhang, G.-J. Zhong, Z.-M. Li, Toward stronger transcrystalline layers in poly(l-lactic acid)/natural fiber biocomposites with the aid of an accelerator of chain mobility, *J. Phys. Chem. B* 118 (2014) 812–823, <http://dx.doi.org/10.1021/jp409021q>.
- [30] H. Xu, L. Xie, Y.-H. Chen, H.-D. Huang, J.-Z. Xu, G.-J. Zhong, B.S. Hsiao, Z.-M. Li, Strong shear flow-driven simultaneous formation of classic shish-kebab, hybrid shish-kebab, and transcrystallinity in poly(lactic acid)/natural fiber biocomposites, *ACS Sustain. Chem. Eng.* 1 (2013) 1619–1629, <http://dx.doi.org/10.1021/sc4003032>.
- [31] H. Xu, L. Xie, X. Jiang, M. Hakkarainen, J.-B. Chen, G.-J. Zhong, Z.-M. Li, Structural basis for unique hierarchical cylindrites induced by ultrahigh shear gradient in single natural fiber reinforced poly(lactic acid) green composites, *Biomacromolecules* 15 (2014) 1676–1686, <http://dx.doi.org/10.1021/bm500100z>.
- [32] H. Bai, W. Zhang, H. Deng, Q. Zhang, Q. Fu, Control of crystal morphology in poly(l-lactide) by adding nucleating agent, *Macromolecules* 44 (2011) 1233–1237, <http://dx.doi.org/10.1021/ma102439t>.
- [33] Y. Fan, J. Zhu, S. Yan, X. Chen, J. Yin, Nucleating effect and crystal morphology controlling based on binary phase behavior between organic nucleating agent and poly(l-lactic acid), *Polymer* 67 (2015) 63–71, <http://dx.doi.org/10.1016/j.polymer.2015.04.062>.
- [34] L. Xie, H. Xu, B. Niu, X. Ji, J. Chen, Z.-M. Li, B.S. Hsiao, G.-J. Zhong, Unprecedented access to strong and ductile poly(lactic acid) by introducing in situ nanofibrillar poly(butylene succinate) for green packaging, *Biomacromolecules* 15 (2014) 4054–4064, <http://dx.doi.org/10.1021/bm5010993>.
- [35] R. Androsch, H.M.N. Iqbal, C. Schick, Non-isothermal crystal nucleation of poly(l-lactic acid), *Polymer* 81 (2015) 151–158, <http://dx.doi.org/10.1016/j.polymer.2015.11.006>.
- [36] D. Cavallo, A.T. Lorenzo, A.J. Müller, Probing the early stages of thermal fractionation by successive self-nucleation and annealing performed with fast scanning chip-calorimetry, *J. Polym. Sci. Part B Polym. Phys.* 54 (2016) 2200–2209, <http://dx.doi.org/10.1002/polb.24129>.
- [37] A. Toda, R. Androsch, C. Schick, Insights into polymer crystallization and melting from fast scanning chip calorimetry, *Polymer* 91 (2016) 239–263, <http://dx.doi.org/10.1016/j.polymer.2016.03.038>.
- [38] Y. Furushima, S. Kumazawa, H. Umetsu, A. Toda, E. Zhuravlev, C. Schick, Melting and recrystallization kinetics of poly(butylene terephthalate), *Polymer* 109 (2017) 307–314, <http://dx.doi.org/10.1016/j.polymer.2016.12.053>.
- [39] Y.P. Koh, L. Grassia, S.L. Simon, Structural recovery of a single polystyrene thin film using nanocalorimetry to extend the aging time and temperature range, *Thermochim. Acta* 603 (2015) 135–141, <http://dx.doi.org/10.1016/j.tca.2014.08.025>.
- [40] X. Monnier, A. Saiter, E. Dargent, Physical aging in PLA through standard DSC and fast scanning calorimetry investigations, *Thermochim. Acta* 648 (2017) 13–22, <http://dx.doi.org/10.1016/j.tca.2016.12.006>.
- [41] J.E.K. Schawe, Measurement of the thermal glass transition of polystyrene in a cooling rate range of more than six decades, *Thermochim. Acta* 603 (2015) 128–134, <http://dx.doi.org/10.1016/j.tca.2014.05.025>.
- [42] B. Wunderlich, Reversible crystallization and the rigid–amorphous phase in semicrystalline macromolecules, *Prog. Polym. Sci.* 28 (2003) 383–450, [http://dx.doi.org/10.1016/S0079-6700\(02\)00085-0](http://dx.doi.org/10.1016/S0079-6700(02)00085-0).
- [43] M.C. Righetti, E. Tombari, Crystalline, mobile amorphous and rigid amorphous fractions in poly(l-lactic acid) by TMDSC, *Thermochim. Acta* 522 (2011) 118–127, <http://dx.doi.org/10.1016/j.tca.2010.12.024>.
- [44] M. Kattan, E. Dargent, J. Grenet, Three phase model in drawn thermoplastic polyesters: comparison of differential scanning calorimetry and thermally stimulated depolarisation current experiments, *Polymer* 43 (2002) 1399–1405, [http://dx.doi.org/10.1016/S0032-3861\(01\)00719-4](http://dx.doi.org/10.1016/S0032-3861(01)00719-4).
- [45] J. Lin, S. Shenogin, S. Nazarenko, Oxygen solubility and specific volume of rigid amorphous fraction in semicrystalline poly(ethylene terephthalate), *Polymer* 43 (2002) 4733–4743, [http://dx.doi.org/10.1016/S0032-3861\(02\)00278-1](http://dx.doi.org/10.1016/S0032-3861(02)00278-1).
- [46] I. Kolesov, R. Androsch, The rigid amorphous fraction of cold-crystallized polyamide 6, *Polymer* 53 (2012) 4770–4777, <http://dx.doi.org/10.1016/j.polymer.2012.08.017>.
- [47] R. Androsch, B. Wunderlich, The link between rigid amorphous fraction and crystal perfection in cold-crystallized poly(ethylene terephthalate), *Polymer* 46 (2005) 12556–12566, <http://dx.doi.org/10.1016/j.polymer.2005.10.099>.
- [48] A. Esposito, N. Delpouve, V. Causin, A. Dhotel, L. Delbreilh, E. Dargent, From a three-phase model to a continuous description of molecular mobility in semicrystalline poly(hydroxybutyrate-co-hydroxyvalerate), *Macromolecules* 49 (2016) 4850–4861, <http://dx.doi.org/10.1021/acs.macromol.6b00384>.
- [49] Q. Ma, G. Georgiev, P. Cebe, Constraints in semicrystalline polymers: using quasi-isothermal analysis to investigate the mechanisms of formation and loss of the rigid amorphous fraction, *Polymer* 52 (2011) 4562–4570, <http://dx.doi.org/10.1016/j.polymer.2011.08.006>.
- [50] M.C. Righetti, D. Prevosto, E. Tombari, Time and temperature evolution of the rigid amorphous fraction and differently constrained amorphous fractions in PLLA, *Macromol. Chem. Phys.* 217 (2016) 2013–2026, <http://dx.doi.org/10.1002/macp.201600210>.
- [51] N.M. Alves, J.F. Mano, E. Balaguer, J.M. Meseguer Dueñas, J.L. Gómez Ribelles, Glass transition and structural relaxation in semi-crystalline poly(ethylene terephthalate): a DSC study, *Polymer* 43 (2002) 4111–4122, [http://dx.doi.org/10.1016/S0032-3861\(02\)00236-7](http://dx.doi.org/10.1016/S0032-3861(02)00236-7).
- [52] Y. Wang, J.F. Mano, Effect of structural relaxation at physiological temperature on the mechanical property of poly(l-lactic acid) studied by microhardness measurements, *J. Appl. Polym. Sci.* 100 (2006) 2628–2633, <http://dx.doi.org/10.1002/app.22643>.
- [53] N. Delpouve, M. Arnoult, A. Saiter, E. Dargent, J.-M. Saiter, Evidence of two mobile amorphous phases in semicrystalline polylactide observed from calorimetric investigations, *Polym. Eng. Sci.* 54 (2014) 1144–1150, <http://dx.doi.org/10.1002/pen.23657>.
- [54] N. Delpouve, A. Saiter, J.F. Mano, E. Dargent, Cooperative rearranging region size in semi-crystalline poly(l-lactic acid), *Polymer* 49 (2008) 3130–3135, <http://dx.doi.org/10.1016/j.polymer.2008.04.045>.
- [55] Y. Wang, J.L. Gómez Ribelles, M. Salmerón Sánchez, J.F. Mano, Morphological contributions to glass transition in poly(l-lactic acid), *Macromolecules* 38 (2005) 4712–4718, <http://dx.doi.org/10.1021/ma047934i>.
- [56] D. Garlotta, A literature review of poly(lactic acid), *J. Polym. Environ.* 9 (2001) 63–84, <http://dx.doi.org/10.1023/A:1020200822435>.
- [57] J. Zhang, Y. Duan, H. Sato, H. Tsuji, I. Noda, S. Yan, Y. Ozaki, Crystal modifications and thermal behavior of poly(l-lactic acid) revealed by infrared spectroscopy, *Macromolecules* 38 (2005) 8012–8021, <http://dx.doi.org/10.1021/ma051232r>.
- [58] X. Monnier, N. Delpouve, N. Basson, A. Guinault, S. Domenek, A. Saiter, P.E. Mallon, E. Dargent, Molecular dynamics in electrospun amorphous plasticized polylactide fibers, *Polymer* 73 (2015) 68–78, <http://dx.doi.org/10.1016/j.polymer.2015.07.047>.
- [59] M.C. Righetti, M. Gazzano, M.L. Di Lorenzo, R. Androsch, Enthalpy of melting of α' - and α -crystals of poly(l-lactic acid), *Eur. Polym. J.* 70 (2015) 215–220, <http://dx.doi.org/10.1016/j.eurpolymj.2015.07.024>.
- [60] N. Delpouve, A. Saiter, E. Dargent, Cooperativity length evolution during crystallization of poly(lactic acid), *Eur. Polym. J.* 47 (2011) 2414–2423, <http://dx.doi.org/10.1016/j.eurpolymj.2011.09.027>.
- [61] C. Zhang, Y. Guo, R.D. Priestley, Characteristic length of the glass transition in isochorically confined polymer glasses, *ACS Macro Lett.* 3 (2014) 501–505, <http://dx.doi.org/10.1021/mz500204q>.
- [62] K. Arabeche, L. Delbreilh, R. Adhikari, G.H. Michler, A. Hiltner, E. Baer, J.-M. Saiter, Study of the cooperativity at the glass transition temperature in PC/PMMA multilayered films: influence of thickness reduction from macro- to nanoscale, *Polymer* 53 (2012) 1355–1361, <http://dx.doi.org/10.1016/j.polymer.2012.01.045>.
- [63] E. Hempel, G. Hempel, A. Hensel, C. Schick, E. Donth, Characteristic length of dynamic glass transition near T_g for a wide assortment of glass-forming substances, *J. Phys. Chem. B* 104 (2000) 2460–2466, <http://dx.doi.org/10.1021/jp991153f>.
- [64] I.M. Hodge, Enthalpy relaxation and recovery in amorphous materials, *J. Non-Cryst. Solids* 169 (1994) 211–266, [http://dx.doi.org/10.1016/0022-3093\(94\)90321-2](http://dx.doi.org/10.1016/0022-3093(94)90321-2).
- [65] L.C.E. Struik, Physical aging in plastics and other glassy materials, *Polym. Eng. Sci.* 17 (1977) 165–173, <http://dx.doi.org/10.1002/pen.760170305>.
- [66] R.D. Priestley, P. Rittigstein, L.J. Broadbelt, K. Fukao, J.M. Torkelson, Evidence for the molecular-scale origin of the suppression of physical ageing in confined polymer: fluorescence and dielectric spectroscopy studies of polymer–silica nanocomposites, *J. Phys. Condens. Matter* 19 (2007) 205120, <http://dx.doi.org/10.1088/0953-8984/19/20/205120>.
- [67] D. Cangialosi, V.M. Boucher, A. Alegría, J. Colmenero, Direct evidence of two equilibration mechanisms in glassy polymers, *Phys. Rev. Lett.* 111 (2013) 095701, <http://dx.doi.org/10.1103/PhysRevLett.111.095701>.
- [68] J. Grenet, E. Bouthegourd, A. Esposito, A. Saiter, J.M. Saiter, Is the configurational entropic model able to predict the final equilibrium state reached by Se glasses after very long ageing durations? *Philos. Mag.* 93 (2013) 2932–2946, <http://dx.doi.org/10.1080/14786435.2013.793482>.
- [70] C. Schick, J. Dobbertin, M. Pötter, H. Dehne, A. Hensel, A. Wurm, A. Ghoneim, S. Weyer, Separation of components of different molecular mobility by calorimetry, dynamic mechanical and dielectric spectroscopy, *J. Therm. Anal. Calorim.* 49 (1997) 499–511, <http://dx.doi.org/10.1007/BF01987477>.
- [71] M. Kattan, E. Dargent, J. Grenet, Relaxations IN amorphous and semi-crystalline polyesters, *J. Therm. Anal. Calorim.* 76 (2004) 379–394, <http://dx.doi.org/10.1023/B:JTAN.0000028019.88096.e3>.

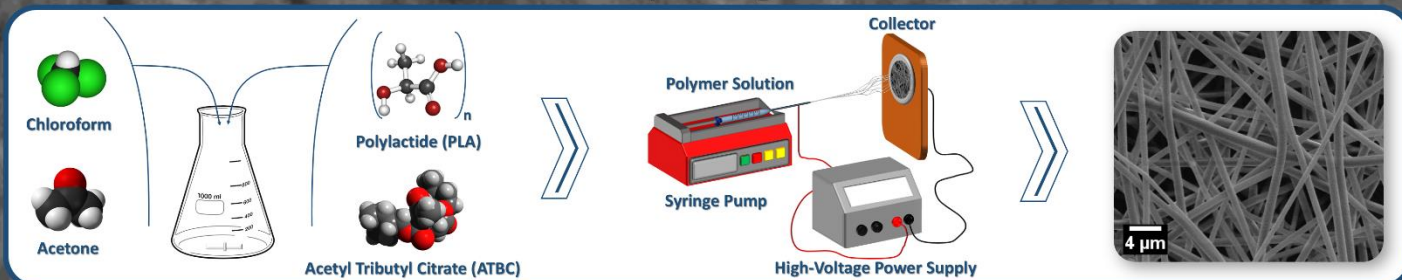
Molecular Dynamics in Electrospun Fibers of Plasticized Polylactide

X. Monnier¹, N. Delpouve¹, N. Basson⁴, A. Guinault², S. Domenek³, A. Saiter¹, P.E. Mallon⁴, E. Dargent¹

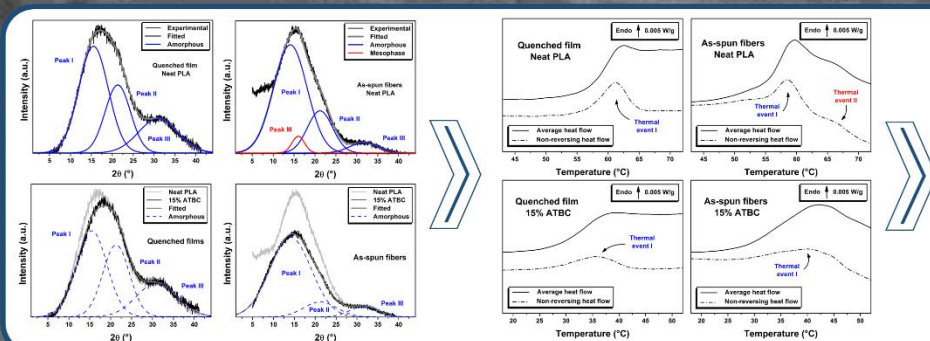
¹AMME-LECAP EA 4528 International Lab., Normandie University, Université and INSA Rouen, France; ²Laboratoire PIMM, UMR 8006, ENSAM-CNRS-CNAM, Paris, France; ³UMR1145 Ingénierie Procédés Aliments, AgroParisTech, France; ⁴Division of Polymer Science, Department of Chemistry and Polymer Science, University of Stellenbosch, South Africa

The electrospinning process can lead to non-equilibrium microstructures due to the complex processes (alignment and stretching of the molecules, rapid solvent evaporation...). It is, therefore, important to understand both the microstructure and the molecular dynamics to gain an understanding of the properties of these materials. In this study, a thermodynamic approach was used to calculate the cooperativity length using modulated temperature differential scanning calorimetry (MT-DSC) in the bulk polymer and the electrospun PLA fibers through Donth's approach^[1]. The possible correlations between the cooperativity length and the inter- and intra-chain distances in the amorphous phase, as determined by wide angle X-ray scattering (WAXS), were also investigated.

Electrospinning Process



Microstructural Investigations



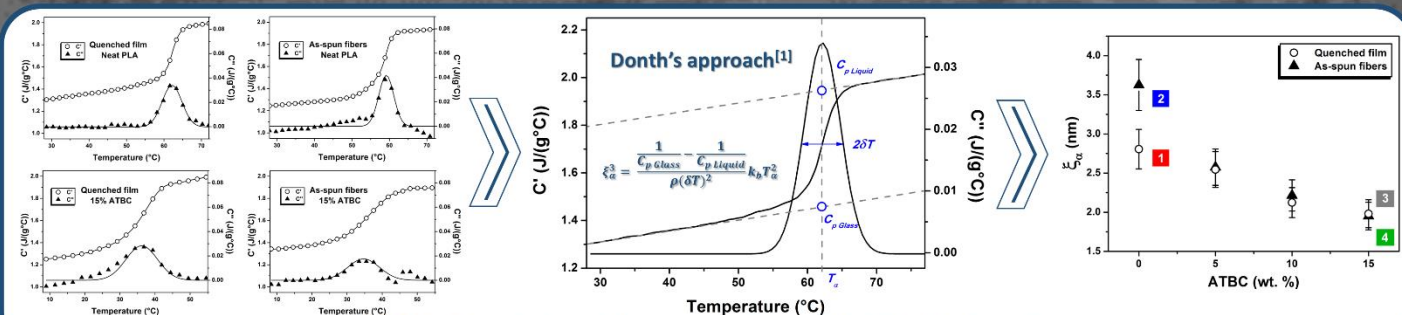
WAXS:

- Amorphous PLA : 3 chain spacings^[2]
- As-spun neat PLA fibers : mesophase^[3]
- Plasticizer :
 - redistribution of chain spacings
 - no mesophase existence

MT-DSC - Glass transition behaviors:

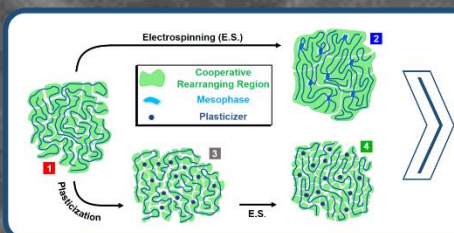
- Thermal event I :
 - structural relaxation
 - broadened by the plasticizer
- Thermal event II: melt of the mesophase

Molecular Dynamic Investigations



MT-DSC - Determination of the cooperativity length ξ_c at the glass transition

Macromolecular Organization Interpretation



Mesophase:

- higher cooperativity / higher cohesiveness
- role of anchoring points between macromolecules

Plasticizer:

- chain spacings strongly modified / smaller cooperativity
- frustrated interaction: no mesophase
- electrospinning does orientate macromolecular chains



References: [1] Donth E. J Non-Cryst Solids 1982;53:325-30 / [2] Stoclet G. et al. Macromolecules 2010;43:1488-98 / [3] Ma Q. et al. Polymer 2013;54:2544-2554

Contact: Eric Dargent, eric.dargent@univ-rouen.fr

AUTHOR'S COPY

7^{ème} JOURNÉE DES DOCTORANTS DE L'ÉCOLE DOCTORALE SPMII, 11 JUIN 2015, UNIVERSITÉ DE ROUEN, SAINT ETIENNE DU ROUVRAY, SITE DU MADRILLET

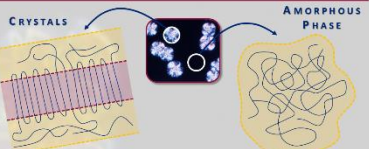
STRUCTURAL ANISOTROPY : MICROSTRUCTURE & MOLECULAR DYNAMIC INVESTIGATIONS

XAVIER MONNIER, ALLISSON SAITER, ERIC DARGENT

AMME-LECAP EA 4528 INTERNATIONAL LABORATORY, UNIVERSITÉ & INSA DE ROUEN, SITE DU MADRILLET, SAINT-ETIENNE DU ROUVRAY, FRANCE

IN POLYMER SCIENCE, THE UNDERSTANDING OF BOTH MICROSTRUCTURE AND MOLECULAR DYNAMICS IS SIGNIFICANT TO FIGURE OUT THE PHYSICAL PROPERTIES. ESPECIALLY, ONE OF THE BIG CHALLENGE IS THE UNDERSTANDING OF THE GLASS TRANSITION. THUS, THE GOAL OF THIS WORK IS TO INVESTIGATE THE MOLECULAR DYNAMICS ON POLYMER SYSTEMS SUBJECTED TO STRUCTURAL ANISOTROPY DURING THEIR PROCESSING.

JOURNEY TO THE CORE OF POLYMERS



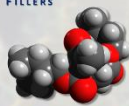
POLYMERS ARE MADE OF MACROMOLECULES : REPETITION OF STRUCTURAL ENTITIES FORMING LONG CHAINS

MICROSTRUCTURE MODIFICATIONS

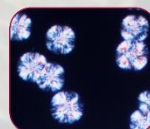
DIFFERENT POSSIBILITIES EXIST TO MODIFY THE PHYSICAL PROPERTIES OF POLYMERS, AND THUS THE GLASS TRANSITION BEHAVIOR



MINERAL FILLERS



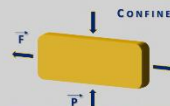
PLASTICIZERS



SPHERULITIC CRYSTALS



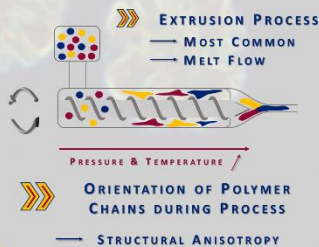
CONFINEMENT NANO-LAYERS



COMPRESSION / DRAWING

POLYMER PROCESSING MAY ALSO MODIFY THE PHYSICAL PROPERTIES

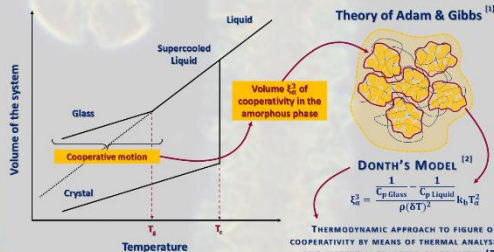
POLYMER PROCESSING



ORIENTATION OF POLYMER CHAINS DURING PROCESS

STRUCTURAL ANISOTROPY

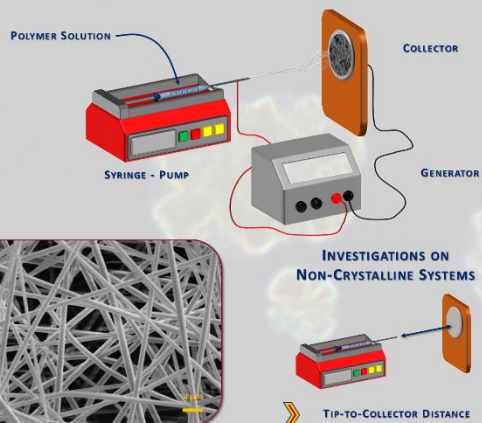
CRYSTALLIZATION & MOLECULAR DYNAMICS



MATERIALS : POLYLACTIDE



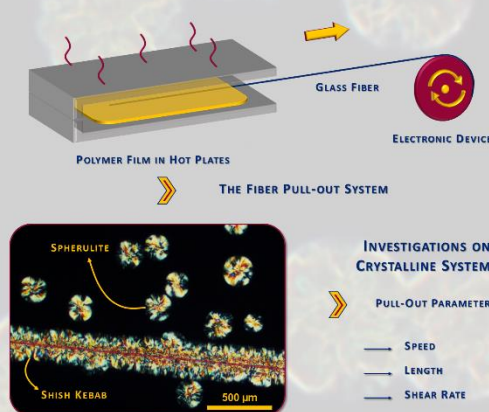
ELECTROSPINNING^[3]



INVESTIGATIONS ON NON-CRYSTALLINE SYSTEMS

TIP-TO-COLLECTOR DISTANCE

FLOW INDUCED CRYSTALLIZATION^[4]



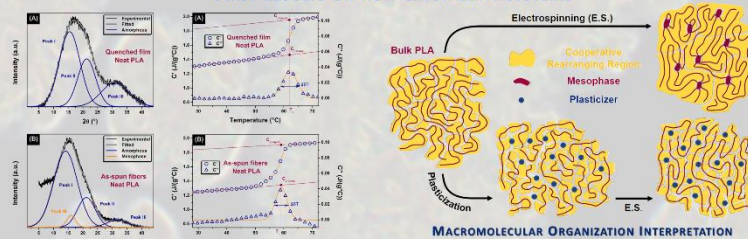
INVESTIGATIONS ON CRYSTALLINE SYSTEMS

PULL-OUT PARAMETERS

- SPEED
- LENGTH
- SHEAR RATE



FIRST RESULTS ON NON-CRYSTALLINE SYSTEMS



FROM WIDE ANGLE X-RAY SCATTERING AND MODULATED TEMPERATURE DSC, WE OBSERVED A HIGH COHESIVENESS OF MESOPHASE. IT INCREASES THE COOPERATIVITY AND PLAYS A ROLE OF ANCHORING POINTS BETWEEN MACROMOLECULES. BY ADDING PLASTICIZER, CHAIN SPACINGS ARE STRONGLY MODIFIED AND RESULT IN SMALLER COOPERATIVITY. EVEN IF THE MACROMOLECULES ARE ORIENTED, THE FORMATION OF MESOPHASE IS FRUSTRATED BY THE PLASTICIZER.



REFERENCES : [1] Adam G. & Gibbs JH. J Chem Phys 1965;43:139-46 [2] Donth E. J Non-Cryst Solids 1982;53:325-30 [3] Gareth M. Bayley et al. Polymer 2012;53:5523-39 [4] Lucia Fernandez-Ballester et al. Macromolecules 2012;45:6557-70

CONTACT : xavier.monnier@etu.univ-rouen.fr

THERMAL ANALYSIS AT THE MICRO-SCALE OF SEMI-CRYSTALLINE POLYMERS THROUGH FAST SCANNING CALORIMETRY - SKIN/CORE LAYER INVESTIGATIONS

Xavier MONNIER*, Benjamin SCHAMME*, Laurence CHEVALIER**, Laurent DELBREILH*, Lucia FERNANDEZ-BALESTER***, Allisson SAITER*, Eric DARGENT*

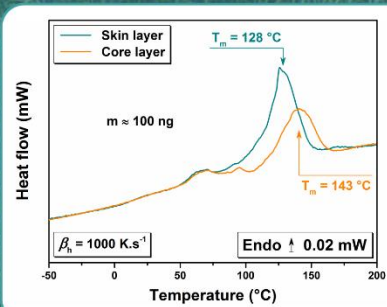
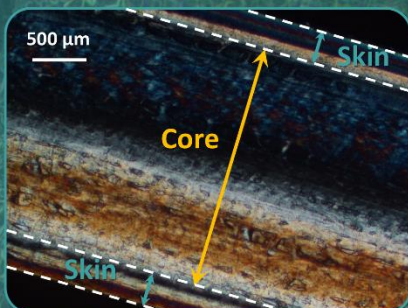


*AMME-LECAP EA 4528 International Lab, Université de Rouen Normandie, Av. de l'Université, BP12, 76801 St Etienne de Rouvray, France
 **GPM UMR 6634 CNRS UFR Sciences et Techniques, Université et INSA de Rouen, BP12, 76801 Saint Etienne du Rouvray Cedex, France
 ***Mechanical & Materials Engineering, University of Nebraska Lincoln, USA



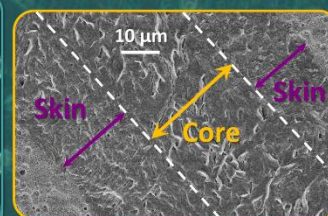
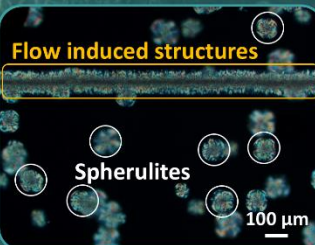
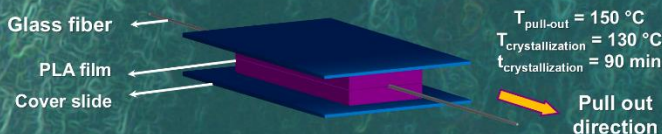
Physical properties of semi-crystalline polymers are tightly linked to their microstructures. Especially, they may be significantly influenced by the processing and the thermo-mechanical forces involved. According to the processing conditions, they can lead to trans-crystalline or skin/core structures¹. Due to the micro-scale of those structures, thermal analysis by conventional techniques, such as differential scanning calorimetry (DSC), is limited. In the recent years, the emergence of fast scanning calorimetry (FSC) has opened the possibilities of micro-to nano scale structure analysis^{2,3}. In this purpose, skin/core structures have been investigated on a commercial injected iso-polypropylene (iPP), and on polylactic acid (PLA) from flow induced structure through pull-out fiber experiment⁴. Polarized optical microscope (POM) and scanning electronic microscope (SEM) give more insight on the analysed structures.

INJECTED iPP POM AND FSC ANALYSIS

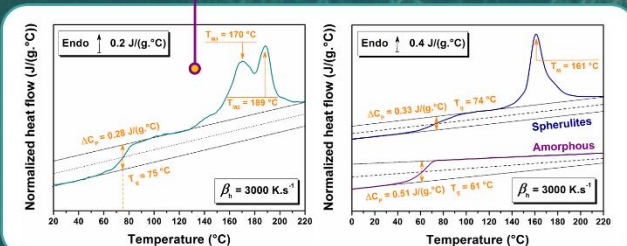
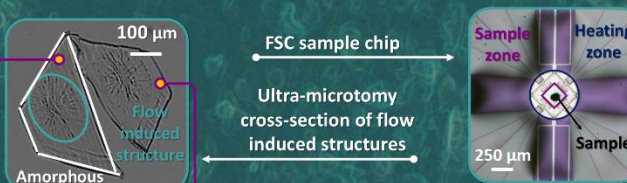


Decrease in the melting temperatures is observed from core to skin layer. It is correlated to a decrease of the crystalline lamellas in the spherulites.

PLA FLOW INDUCED-CRYSTALLIZATION POM AND SEM ANALYSIS

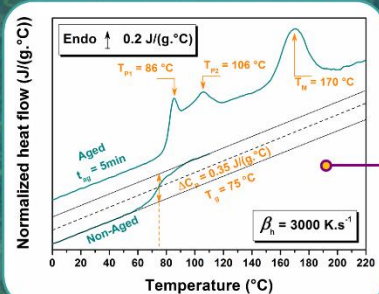


PLA FLOW INDUCED-CRYSTALLIZATION : FSC ANALYSIS



- Degree of crystallinity : 24 %
- Degree of crystallinity : 35 %
- Two melting peaks
- One melting peak

Melting temperature of PLA spherulites is around 160 °C. Flow induced structures depict an increase of 10 to 30 °C. Mass of the samples is closed to 20 ng, estimated from the amorphous heat step capacity. Such mass implies a high heating rates, more than 1000 K.s⁻¹ as used for the iPP.



Here, only one melting is observed. However, the physical aging depicts two relaxation peaks. The first one is related to the surrounding amorphous, when the second one comes from the confined amorphous.

FSC analysis on skin/core layers have been possible by means of FSC. Difference of melting have been observed from the skin and the core layers in iPP and PLA. Besides, physical aging on flow induced crystallized PLA have also been performed, and allowed us to distinguish two different relaxation modes in the amorphous phase. Consequently, these first studies on superstructures of semi-crystalline polymers such as skin/core layer show the possibilities of thermal analysis on micro-to-nano scale structures by means of FSC.

References : 1. S.S. Katti & M. Schultz, Polymer engineering and science, November 1982, vol. 22, N° 16 / 2. S. Gao et al., Macromolecules, 2013, 46, 562-570 / 3. N. Shamim et al., Journal of polymer science, Part B: Polymer physics, 2014, 52, 1462-1468 / 4. H. Xu et al., Biomacromolecules, 2014, 15, 1676-1686

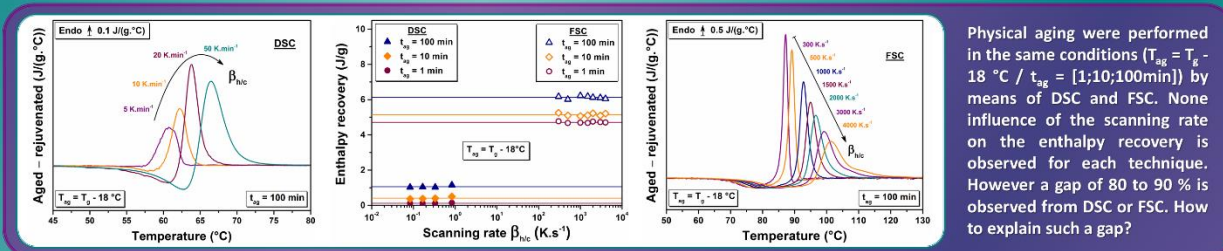
Insight and understanding of physical aging through DSC and FSC from Polylactic acid



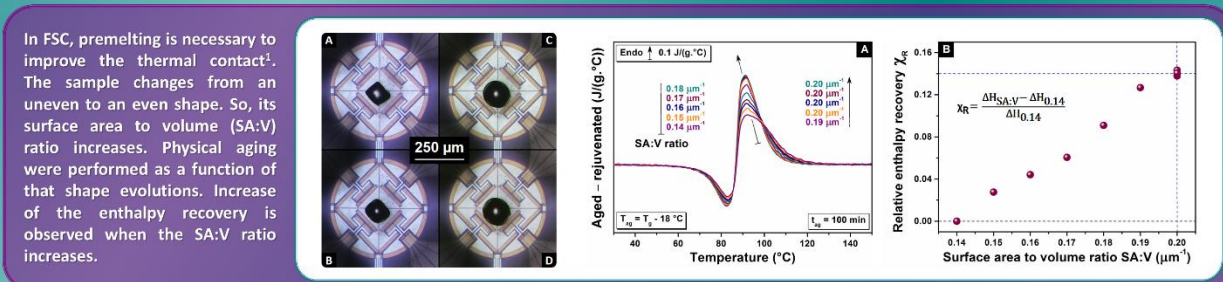
Xavier Monnier, Allisson Saiter, Eric Dargent



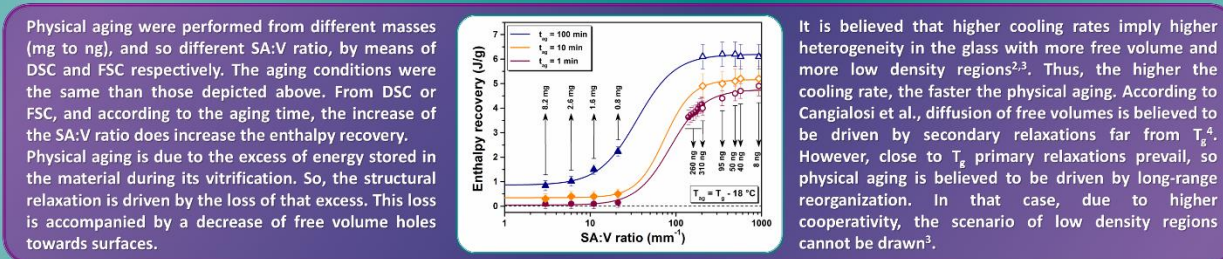
AMME-LECAP EA 4528 International Lab., Université de Rouen Normandie, Av. de l'Université, BP12, 76801 St Etienne de Rouvray, France



Physical aging were performed in the same conditions ($T_{\text{age}} = T_g - 18^\circ\text{C}$ / $t_{\text{age}} = [1;10;100\text{min}]$) by means of DSC and FSC. None influence of the scanning rate on the enthalpy recovery is observed for each technique. However a gap of 80 to 90 % is observed from DSC or FSC. How to explain such a gap?

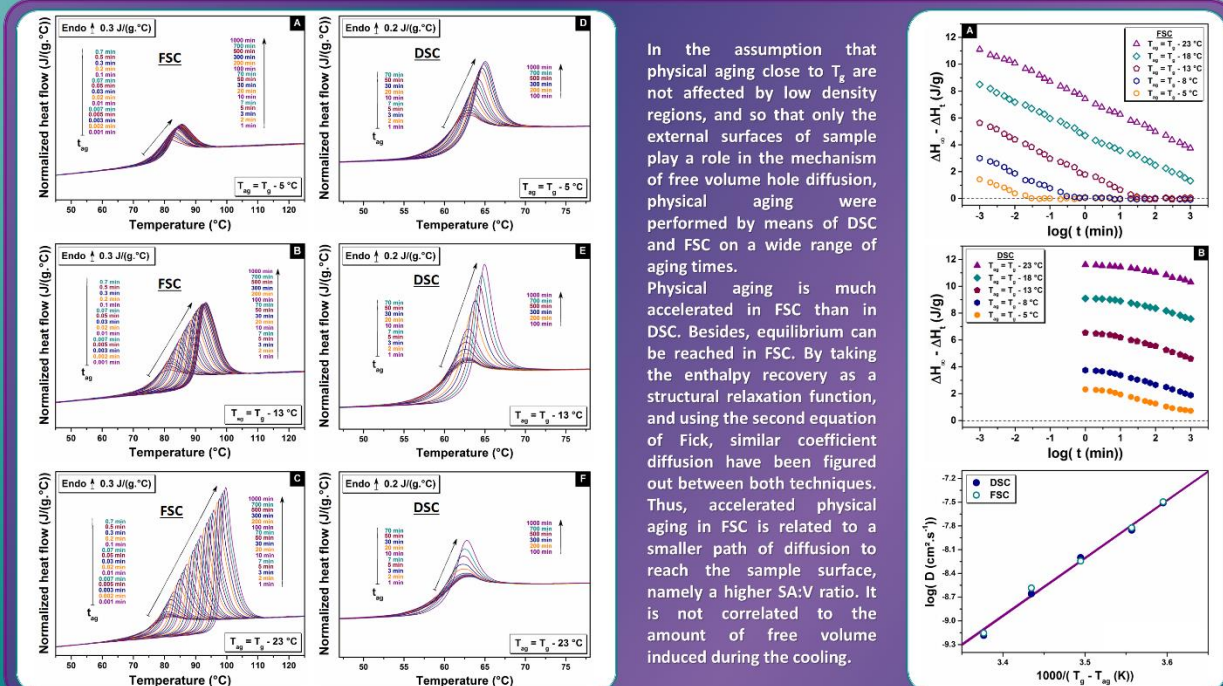


In FSC, premelting is necessary to improve the thermal contact¹. The sample changes from an uneven to an even shape. So, its surface area to volume (SA:V) ratio increases. Physical aging were performed as a function of that shape evolutions. Increase of the enthalpy recovery is observed when the SA:V ratio increases.

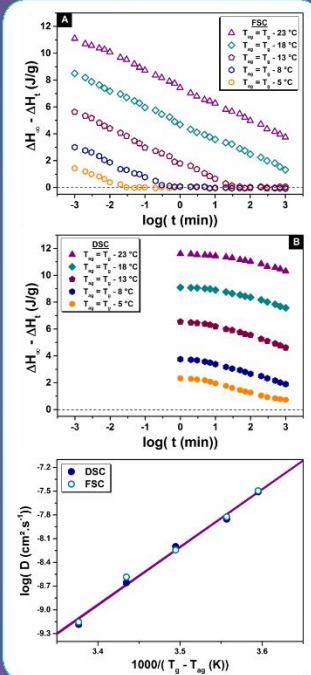


Physical aging were performed from different masses (mg to ng), and so different SA:V ratio, by means of DSC and FSC respectively. The aging conditions were the same than those depicted above. From DSC or FSC, and according to the aging time, the increase of the SA:V ratio does increase the enthalpy recovery. Physical aging is due to the excess of energy stored in the material during its vitrification. So, the structural relaxation is driven by the loss of that excess. This loss is accompanied by a decrease of free volume holes towards surfaces.

It is believed that higher cooling rates imply higher heterogeneity in the glass with more free volume and more low density regions^{2,3}. Thus, the higher the cooling rate, the faster the physical aging. According to Cangialosi et al., diffusion of free volume is believed to be driven by secondary relaxations far from T_g ⁴. However, close to T_g primary relaxations prevail, so physical aging is believed to be driven by long-range reorganization. In that case, due to higher cooperativity, the scenario of low density regions cannot be drawn⁵.



In the assumption that physical aging close to T_g are not affected by low density regions, and so that only the external surfaces of sample play a role in the mechanism of free volume hole diffusion, physical aging were performed by means of DSC and FSC on a wide range of aging times. Physical aging is much accelerated in FSC than in DSC. Besides, equilibrium can be reached in FSC. By taking the enthalpy recovery as a structural relaxation function, and using the second equation of Fick, similar coefficient diffusion have been figured out between both techniques. Thus, accelerated physical aging in FSC is related to a smaller path of diffusion to reach the sample surface, namely a higher SA:V ratio. It is not correlated to the amount of free volume induced during the cooling.



References:
 1. J.E.K. Schawe, Thermochimica Acta. 603 (2015) 128–134 / 2. L.C.E. Struik, Polymer Engineering and Science. March 1977, Vol. 17, No. 3 / 3. D. Cangialosi, M. Wübbenhorst, J. Groenewold, E. Mendes, H. Schut, A. van Veen, S.J. Picken, Phys. Rev. B. 70 (2004) 224213 / 4. D. Cangialosi, V.M. Boucher, A. Alegria, J. Colmenero, Phys. Rev. Lett. 111 (2013) 095701.
 Contacts:
 • xavier.monnier@etu.univ-rouen.fr
 • eric.dargent@univ-rouen.fr

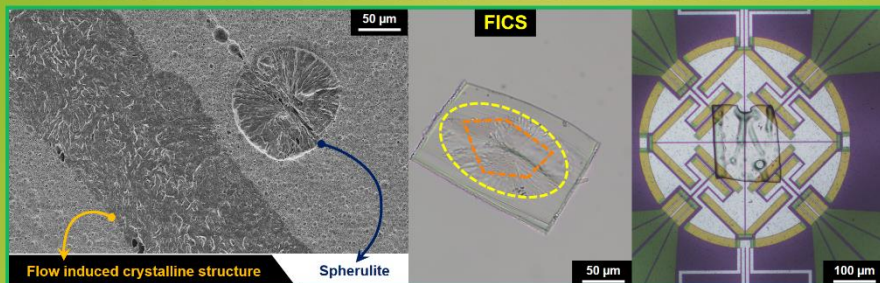
INVESTIGATIONS OF POLYLACTIDE SUBJECTED TO ANISOTROPIC AND CONFINEMENT EFFECTS BY FAST AND MODULATED TEMPERATURE DIFFERENTIAL SCANNING CALORIMETRY (FSC AND MT-DSC)



XAVIER MONNIER, ALLISSON SAITER, ERIC DARGENT
Normandie Univ, UNIROUEN Normandie, INSA Rouen, CNRS, Groupe de Physique des Matériaux, 76000 Rouen, France

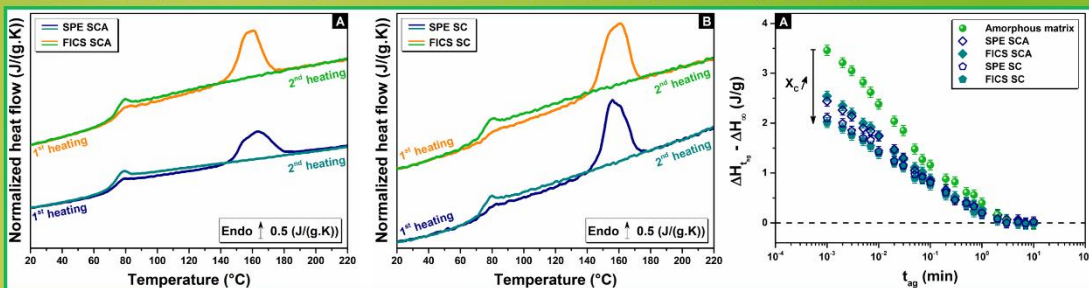


FSC ON SEMI-CRYSTALLINE SYSTEMS - FLOW INDUCED CRYSTALLINE STRUCTURES (FICS) AND SPHERULITES (SPE)

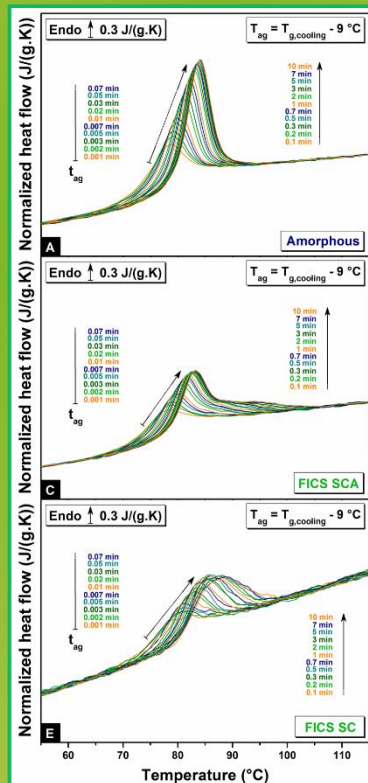


Scanning electronic microscopy; poly(lactide) (PLA) was ultramicrotomed in the longitudinal direction, etched and gold coated. FICS were induced by pulling a glass fiber out of the melt at 150 °C. Crystallization took place at 130 °C during 90 min. FICS and SPE were ultramicrotomed in the transversal direction (500 nm thick). The ellipse depicts FICS surrounding by amorphous matrix. Two analyses were performed: on the entire slices (SCA) and only on the FICS (orange polygon - SC). Samples were placed on a FSC chip membrane (around 30 nm).

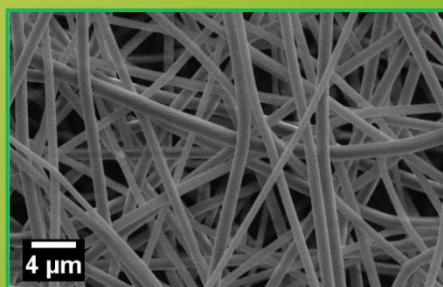
Physical aging were performed in the same conditions for amorphous and semi-crystalline systems by means of FSC. Curves of amorphous and FICS systems are displayed on the right. Characteristic endothermic peaks relative to constrained and unconstrained amorphous matrix were measured. Similar curves were measured either on FICS or SPE, independently of the analysis (SCA or SC).



When the degree of crystallinity increases, the glass transition temperature (T_g) increases. T_g is the same from FICS or SPE. Independently of SCA or SC analyses, FICS and SPE depict similar microstructures from FSC investigations: mobile amorphous fraction, rigid amorphous fraction and degree of crystallinity. In addition, the physical aging kinetic is the same for the different systems. From the glass transition and the glassy state investigations, the anisotropic effect does not influence the molecular dynamics of the amorphous phases. Only the confinement and the coupling between the amorphous and the crystals does. **REFERENCE: POLYMER 126 (2017) 141-151**



MT-DSC ON NON-CRYSTALLINE SYSTEMS - QUENCHED FILMS AND ELECTRO-SPUN FIBERS

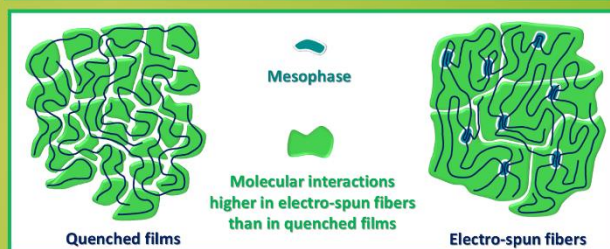
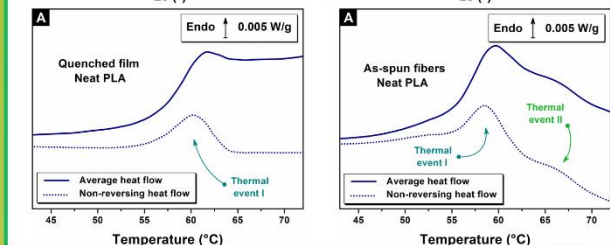
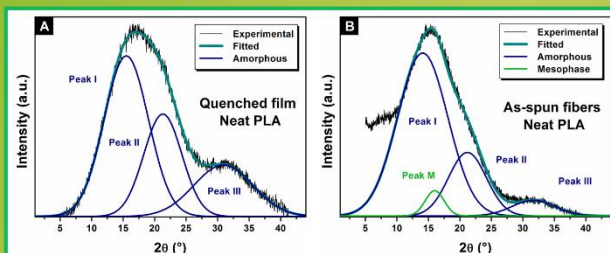
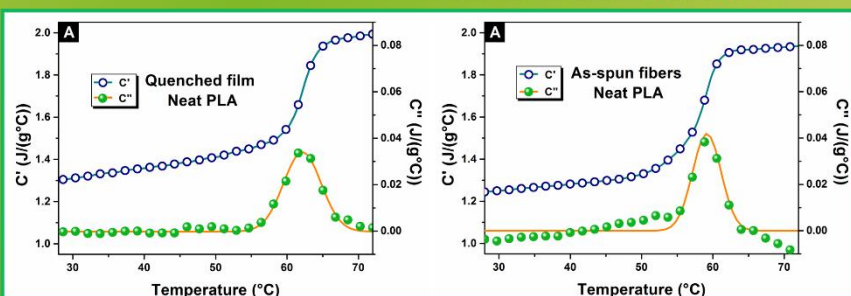


Amorphous PLA depicts two characteristics inter chain spacings and one intra chain spacing, as observed from WAXD. However, when PLA is electrospun a third inter chain spacing was observed: the mesophase (intermediate molecular arrangement between amorphous and crystal). This mesophase was also estimated by MT-DSC, by comparing amorphous quenched films and electrospun fibers (thermal event II). The thermal event I is related to the structural relaxation of amorphous PLA.

Finally, molecular dynamics, namely the molecular interactions, were investigated by MT-DSC. The heat capacity step was observed to be the same in both systems (C' signal), when the temperature fluctuation of the glass transition (FWHM of the C'' signal) was observed to be smaller for the fibers than the films. Therefore, the molecular interactions in the fibers are more significant than in the films due to the mesophase and the structural anisotropy. Schematic interpretation is done. **REFERENCE: POLYMER 73 (2015) 68-78**

Electrospinning was performed in optimized conditions to provide electro-spun fibers of PLA with an average fiber diameter of 800 ± 180 nm. Microstructures was investigated by MT-DSC, as well as wide angle X-ray diffraction (WAXD) to confirm (right curves). Molecular dynamics was then investigated by MT-DSC (curves below).

REFERENCE: POLYMER 73 (2015) 68-78



ABSTRACT.

The aim of this work is to investigate the molecular dynamics of Polylactide (PLA) subjected to structural anisotropy during its processing. To do so, two experimental set-ups were used: electrospinning and flow induced crystallization. The first one leads to non-crystalline system, while the second one leads to semi-crystalline system. For each system, the microstructure is investigated to highlight the structural anisotropy induced during the processing. Different experimental techniques are used: optical microscopy, electronic microscopy, X-ray diffraction, differential scanning calorimetry (DSC) and fast scanning calorimetry (FSC).

FSC proves to be useful. Due to the high scanning rates (1000 K.s^{-1}) and the decrease of the sample mass (few tens of nanogrammes), glass transition and physical aging kinetics are beforehand investigated in the case of a wholly amorphous PLA. It is shown that high cooling rates available by FSC allow to accelerate physical aging kinetics.

Molecular dynamics are then investigated through concept of cooperativity and phenomenon of physical aging. It is shown that preferential orientation induced during electrospinning leads to the formation of mesophase, which increase cooperativity, namely the intermolecular interactions. With regard to semi-crystalline system, molecular dynamics are only affected by the coupling between amorphous/crystal and the confinement effect of the crystals, rather than the structural anisotropy induced before the crystallization step.

Keywords: *Polylactide, nanofibers, spherulites, flow-induced crystallization, glass transition, physical aging, fast scanning calorimetry*

RÉSUMÉ.

L'objet de ce travail est d'étudier l'influence de l'anisotropie structurale, induite lors de la mise en forme d'un Polylactide (PLA), sur les dynamiques moléculaires de la phase amorphe. Deux procédés de mise en œuvre sont retenus : l'électrofilage et la cristallisation induite par flux. Le premier permet d'aboutir à un système non-cristallin, lorsque le deuxième permet d'aboutir à un système semi-cristallin. Pour chaque système, une étude microstructurale est préalablement réalisée pour mettre en avant l'anisotropie structurale induite lors de la mise en œuvre. Pour ce faire différentes techniques d'analyses sont utilisées : microscopie optique, microscopie électronique, diffraction des rayons X, calorimétrie à balayage différentielle (DSC) et calorimétrie à balayage rapide (FSC).

L'utilisation de la FSC s'avère précieuse. Du fait des vitesses extrêmement rapide (1000 K.s^{-1}) et de la diminution importante de la masse (dizaine de nanogrammes), la transition vitreuse et la cinétique de vieillissement physique sont au préalable étudiées dans le cas d'un PLA amorphe. Il est montré que les vitesses de refroidissement atteignable en FSC permettent d'accélérer les cinétiques de vieillissement physique.

Les dynamiques moléculaires sont ensuite étudiées à travers le concept de coopérativité et le phénomène de vieillissement physique. Il est montré que l'orientation préférentielle induite dans le système non-cristallin aboutit à la formation de mésophase qui augmente la coopérativité, autrement dit les interactions intermoléculaires. Dans le cas du système semi-cristallin, les dynamiques moléculaires sont influencées par le couplage amorphe/cristal et le confinement des cristaux, et non pas par l'anisotropie structurale induite avant cristallisation.

Mots-clés: *Polylactide, nanofibres, sphérolites, cristallisation induite par flux, transition vitreuse, vieillissement physique, calorimétrie à balayage rapide*